



Alghanimy, Alaa (2025) Investigating glymphatic system and AQP4 water channels with novel drugs and MRI techniques. PhD thesis.

<https://theses.gla.ac.uk/85218/>

Copyright and moral rights for this work are retained by the author

A copy can be downloaded for personal non-commercial research or study, without prior permission or charge

This work cannot be reproduced or quoted extensively from without first obtaining permission from the author

The content must not be changed in any way or sold commercially in any format or medium without the formal permission of the author

When referring to this work, full bibliographic details including the author, title, awarding institution and date of the thesis must be given

Enlighten: Theses

<https://theses.gla.ac.uk/>
research-enlighten@glasgow.ac.uk

Investigating Glymphatic System and AQP4 Water Channels with Novel Drugs and MRI Techniques

Alaa Alghanimy

B.Sc. in Radiological Sciences, M.Sc. in Medical Imaging

Submitted in fulfilment of the requirements for the Degree of
Doctor of Philosophy

School of Psychology and Neuroscience
College of Medicine, Veterinary and Life Science
University of Glasgow

Abstract

The glymphatic system serves as a vital low resistance pathway for the efficient removal of toxic waste products from the brain and its malfunction is implicated in numerous neuropathological conditions. Aquaporin-4 (AQP4) water channels are membrane-tied and highly expressed at the end-feet of astrocytic cells in the brain. They are thought to be crucial to the glymphatic clearance system, water circulation, and homeostasis of the brain. Pharmacologically targeting AQP4 presents a promising therapeutic strategy for various neurological diseases. In 2009, Huber et al. developed TGN-020, a potent AQP4 inhibitor that significantly reduced cerebral oedema in stroke models. In 2018, they introduced TGN-073, a novel AQP4 facilitator that enhanced fluid turnover and interstitial fluid clearance. This thesis investigates the effects of these AQP4 modulators, with a particular focus on TGN-073, using advanced MRI techniques and immunofluorescence staining in rat models to elucidate their potential therapeutic benefits.

The initial objective was to employ an $H_2^{17}O$ tracer to evaluate the effect of the novel AQP4 facilitator TGN-073 on glymphatic transport. Despite extensive optimization efforts, the tracer signal remained low and unreliable, precluding its use in conducting our studies. Consequently, we assessed the impact of TGN-073 on glymphatic transport using dynamic contrast-enhanced MRI. This involved catheterizing the cisterna magna to infuse the MRI contrast agent Gd-DTPA into the cerebrospinal fluid. Our findings indicated that rats treated with TGN-073 exhibited a more extensive distribution and higher parenchymal uptake of Gd-DTPA compared to the vehicle group, suggesting TGN-073's potential in enhancing glymphatic function. Following this, I developed and established an immunohistochemistry protocol for AQP4 staining using immunofluorescence, a first in our department. The aim was to optimize this technique to its fullest potential, ensuring precision and reliability for the following experiments.

Given the invasive nature of the method used to investigate the impact of TGN-073 on glymphatic transport, which requires cisterna magna cannulation, non-invasive alternatives were explored. Therefore, the impact of both AQP4 modulators, TGN-020 and TGN-073, was assessed without the necessity of

exogenous contrast agents. These evaluations utilized T_2 mapping and stimulated echo diffusion-weighted echo planar imaging (STE-DW-EPI), followed by immunofluorescence labelling of AQP4. No significant changes in the diffusion coefficient were observed across all observation times in any animal group, indicating no substantial alterations in brain microstructure. However, T_2 values significantly decreased following the administration of TGN-073, suggesting enhanced water exchange. In contrast, T_2 values significantly increased following the administration of TGN-020, while remaining unchanged in the vehicle group. These findings underscore the role of AQP4 in modulating water exchange between tissue compartments. Immunofluorescence staining revealed significantly higher AQP4 expression in the brains treated with TGN-073, contrasting with a significant decrease in AQP4 expression in the brains treated with TGN-020, compared to the vehicle-treated group.

To advance our understanding of the positive effects of AQP4 facilitators on glymphatic function, we investigated the impact of TGN-073 in a rat model of vascular cognitive impairment, specifically the bilateral common carotid artery stenosis (BCAS) model. This model, known for inducing chronic cerebral hypoperfusion and vascular dementia, represents a novel application within our institution. To our knowledge, this is the first study to evaluate glymphatic transport in BCAS rat models and to assess the impact of an AQP4 facilitator in this context. We successfully established cerebral hypoperfusion in the BCAS model, as evidenced by a significant reduction in cerebral blood flow (CBF). Our findings demonstrated glymphatic dysfunction and altered AQP4 expression associated with BCAS. Importantly, TGN-073, effectively mitigated these effects by restoring AQP4 expression, enhancing glymphatic function, and alleviating CBF reduction. This study highlights the potential of AQP4 facilitators in ameliorating the adverse effects of cerebral hypoperfusion and associated glymphatic dysfunction. TGN-073 shows promise for preventing the progression of neurodegenerative diseases and improving the quality of life for affected individuals.

Table of Contents

Abstract	ii
Table of Contents	iv
List of Tables.....	ix
List of Figures.....	x
Publications	xvi
Conference Proceedings & Awards.....	xvii
Acknowledgement	xviii
Author's Declaration	xix
Definitions/Abbreviations	xx
Chapter 1 Literature Review	1
1.1 Cerebrospinal fluid dynamics	1
1.1.1 CSF production.....	2
1.1.2 CSF circulation.....	3
1.1.3 CSF reabsorption/ drainage.....	4
1.2 The "perivascular" glymphatic system: a historical perspective	6
1.3 Glymphatic system	7
1.4 Aquaporin water channel.....	9
1.4.1 Aquaporin-4	11
1.4.2 AQP4 implication in neurological disorders	13
1.5 Meningeal lymphatic vessels	14
1.6 Glymphatic system driving force	15
1.7 Imaging the glymphatic system.....	16
1.7.1 Invasive imaging techniques	16
1.7.2 Non-invasive imaging techniques	18
1.8 Glymphatic system activation	20
1.9 Ongoing discussion regarding the glymphatic system	23
1.9.1 The important role of AQP4	23
1.9.2 The flow direction	23
1.9.3 Bulk flow vs diffusion	24
1.9.4 The validity of the glymphatic hypothesis.....	24
1.9.5 Potential sources of variable results	25
1.10 Glymphatic impairment in neurological disorders	26
1.10.1 Alzheimer's disease	27
1.10.2 Parkinson's disease	29
1.10.3 Age-related hearing loss disorder	30
1.10.4 Idiopathic normal pressure hydrocephalus	30

1.10.5	Neuromyelitis optica spectrum disorder	31
1.10.6	Amyotrophic lateral sclerosis.....	32
1.10.7	Multiple sclerosis	32
1.10.8	Vascular cognitive impairment	34
1.11	Preserving glymphatic vitality	35
1.12	Thesis aim	37
Chapter 2	Magnetic Resonance Imaging	39
2.1	Spin angular momentum.....	40
2.2	Nuclear magnetic moment	41
2.3	Radiofrequency pulses	45
2.4	MR image formation.....	48
2.4.1	Gradients and encoding	49
2.5	Relaxation times	52
2.5.1	Spin-lattice (<i>T1</i>) relaxation.....	52
2.5.2	Spin-spin (<i>T2</i>) relaxation.....	53
2.5.3	Contrast properties	55
2.6	Pulse sequences.....	58
2.6.1	Image contrast parameters	58
2.6.2	Rapid acquisition with relaxation enhancement.....	59
2.6.3	Multi slice multi echo.....	60
2.6.4	Gradient echo sequence	61
2.6.5	Diffusion MRI	63
2.6.6	Flow-sensitive alternating inversion recovery	65
2.7	Essential components in MRI scanner	66
2.7.1	Main magnet	66
2.7.2	Shim coils.....	66
2.7.3	Gradient coils.....	67
2.7.4	RF coils	67
2.7.5	Shielding.....	68
2.7.6	Electronics	68
2.7.7	Transmit-receive birdcage coil construction	70
Chapter 3	Methodology	73
3.1	Animal provider	73
3.2	Animal housing and acclimatization	73
3.3	Animal preparation for surgery	74
3.4	Animal surgeries	75
3.4.1	Femoral artery cannulation	75
3.4.2	Cisterna magna cannulation	77
3.4.3	Bilateral common carotid artery stenosis	81

3.5	Animal recovery.....	83
3.6	Drug supplier and preparation	85
3.7	MRI imaging processing	86
Chapter 4	MRI Stability.....	90
4.1	In vivo pilot study.....	90
4.1.1	Background.....	90
4.1.2	Methods.....	91
4.1.3	Results	92
4.2	Phantom study	93
4.2.1	Magnetic resonance imaging.....	94
4.2.2	T ₂ values of CuSO ₄	94
4.2.3	Transverse relaxivity of CuSO ₄	95
4.3	Magnet stability improvements.....	97
4.3.1	Active shim values	97
4.3.2	Impact of gradient runtime on MRI stability	98
4.3.3	Basic frequency drifting.....	100
Chapter 5	Oxygen-17 Tracer: Chasing MRI Clues	102
5.1	Introduction	102
5.2	MRI protocol-related adjustments	104
5.2.1	30-minute dummy scans.....	104
5.2.2	Phase-frequency swapping.....	104
5.2.3	Magnetisation transfer.....	105
5.2.4	Introduce an angle to the animal's position in the cradle.....	107
5.3	Tracer-related adjustments: Increasing H ₂ ¹⁷ O density	108
5.3.1	Methods.....	109
5.3.2	Results	111
5.3.3	Discussion.....	113
Chapter 6	The effect of a novel AQP4 facilitator, TGN-073, on glymphatic transport captured by diffusion MRI and DCE-MRI	114
6.1	Introduction	114
6.2	Methods and Materials	117
6.2.1	Animals	117
6.2.2	Drug Preparation	117
6.2.3	Animal Surgery.....	118
6.2.4	Infusion Pump Setup	120
6.2.5	Magnetic Resonance Imaging	120
6.2.6	Data Analysis.....	121
6.2.7	Statistical Analyses.....	123
6.3	Results.....	123

6.4	Discussion	126
6.5	Conclusion	129
Chapter 7	AQP4 Staining Optimization	130
7.1	Introduction	130
7.2	Fixation and preparation of brain sections	131
7.3	First test run: Assessing technique validity	132
7.3.1	Introduction	132
7.3.2	Methods and materials	132
7.3.3	Results and conclusion	134
7.4	Second test run: Assessing the validity of antibodies	135
7.4.1	Introduction	135
7.4.2	Methods and materials	136
7.4.3	Results and conclusion	137
7.5	Third test run: Optimizing AQP4 antibody dilution factor and antigen retrieval pH.....	138
7.5.1	Introduction	138
7.5.2	Methods and materials	138
7.5.3	Results and conclusion	140
7.6	Fourth test run: Retest the optimized protocol using immunofluorescence.	142
7.6.1	Introduction	142
7.6.2	Methods and materials	142
7.6.3	Results and conclusion	144
7.7	Fifth test run: Decreasing AQP4 antibody dilution.....	144
Chapter 8	Exploring the Impact of TGN-073 and TGN-020 on AQP4 Water Channels and Brain Microstructure	146
8.1	Introduction	146
8.2	Materials and methods	148
8.2.1	Animals	148
8.2.2	Study design.....	149
8.2.3	Drug Preparation	150
8.2.4	Magnetic Resonance Imaging Protocols	150
8.2.5	Immunohistochemistry	151
8.2.6	Data analysis	152
8.2.7	Statistical analysis	153
8.3	Results.....	154
8.3.1	No significant change in diffusion values was observed after administering AQP4 drugs.....	154
8.3.2	Inhibition of AQP4 resulted in increased brain T ₂ values, whereas enhancement of AQP4 led to reduced brain T ₂ values	155

8.3.3	AQP4 expression in the brain increased with TGN-073 treatment, whereas decreased with TGN-020 treatment	158
8.4	Discussion	161
8.5	Conclusion	164
Chapter 9	The Effect of AQP4 Facilitator TGN-073 on the BCAS Rat Model ..	165
9.1	Introduction	165
9.2	Materials and methods	167
9.2.1	Animals	167
9.2.2	Animal surgeries	167
9.2.3	Magnetic Resonance Imaging	168
9.2.4	Immunohistochemistry	170
9.2.5	Statistical analysis	170
9.3	Results.....	171
9.3.1	Cerebral blood flow reduction following BCAS procedure	171
9.3.2	AQP4 facilitator enhanced the glymphatic function in BCAS rats ..	172
9.3.3	AQP4 expression rescued by TGN-073 after BCAS induction	174
9.4	Discussion	177
9.5	Conclusion	180
Chapter 10	General discussion	180
10.1	Summary	181
10.2	Limitation.....	182
10.3	Future work.....	184
References.....		187

List of Tables

Table 1: The Birdcage Coil Configuration.....	70
Table 2: Presents the T_2 values for each concentration of CuSO_4	95
Table 3: Shim percentage values for the power supply before and after maintenance services.	98

List of Figures

Figure 1-1: Schematic diagram of the glymphatic pathway (Rasmussen et al., 2018).	9
Figure 1-2: Diffusion-tensor imaging along the perivascular space.*	20
Figure 1-3: the difference in glymphatic system in healthy vs AD brain (Silva et al., 2021).	29
Figure 1-4: Left: Healthy brain, with normal glymphatic influx (peri-arterial) and efflux (perivenous). AQP4 is highly expressed at astrocytic end-feet with normal convective flow of interstitial fluid and intact myelin sheath. Right: Proposed changes in multiple sclerosis with reduced glymphatic influx (peri-arterial) and efflux (perivenous). AQP4 is depolarized away from the astrocytic end feet with lower convective flow of interstitial fluid, lower brain clearance and demyelinated sheath (Alghanimy et al., 2024).	34
Figure 2-1: The splitting of the energy level into different states, also known as Zeeman Splitting. For hydrogen, $l=1/2$ (Orange dashed lines), and for Oxygen-17, $l=5/2$ (Green dashed lines).	42
Figure 2-2: The precession frequency of a hydrogen nucleus about B_0	43
Figure 2-3: The overall net magnetization, denoted as M_0	44
Figure 2-4: The Electromagnetic Spectrum from https://www.miniphysics.com/electromagnetic-spectrum_25.html	45
Figure 2-5: The view of M_0 (grey downward spiral) during the application of an RF pulse is referred to as the laboratory frame of reference.	47
Figure 2-6: The new coordinate system (x' , y' , z') corresponds to the rotating frame of reference, creating an analogy to standing on a rotating carousel. Despite the continuous rotation at the Larmor frequency, the view from the carousel perspective gives a sense of stability to the rotating frame. This perspective facilitates the identification of speed variations of the spins.	47
Figure 2-7: The sample comprises the rat brain, when a gradient is applied (indicated by the red line), the precession frequencies (ω) will vary linearly with the position in the x-direction. Upon applying an RF-pulse with frequency ω and bandwidth $\Delta\omega$, only spins within the green slice with a thickness of Δx will be excited.	49
Figure 2-8: In the context of MRI, data acquisition in k-space is a process that involves mapping the spatial frequencies of the acquired signals. The k-space grid (on the right) is a representation of these spatial frequencies, with two key gradients: the phase encoding direction (k_y) and the frequency encoding direction (k_x). A standard gradient echo sequence is illustrated on the left. The yellow colour represents the phase encode gradient, the green represents the read de-phase encode gradient, and the red indicates the read (frequency) encode gradient. During each TR, a line of k-space is filled. The information collected in k-space is later transformed into spatial domain image through Fourier transformation.	51
Figure 2-9: T_1 Relaxation. In the rotating frame (the second row), after the cessation of the 90° RF pulse, the transverse net magnetization (M_{xy}) starts to decrease, while the longitudinal net magnetization (M_z) builds up. The rate of the exponential recovery is known as T_1 relaxation time. The red arrow represents the net magnetization.	53
Figure 2-10: T_2 Relaxation. In the rotating frame (the second row), after the 90° RF pulse is turned off, the transverse net magnetization (M_{xy}) gradually decreases due to losing phase coherence between spins, resulting in signal	

decay. The exponential decay of M_{xy} is quantified by the T_2 relaxation time. The red bold arrow symbolizes the net magnetization in the xy-plane.	54
Figure 2-11: On the left: Standard spin echo sequence displaying TE and TR. On the right: A table illustrating the influence of the parameters TE and TR on MR image contrast.	59
Figure 2-12: RARE sequence.	60
Figure 2-13: MSME sequence.	61
Figure 2-14: Schematic of gradient echo sequence.	62
Figure 2-15: A schematic of the conventional spin echo DW-EP sequence is on the left, and the stimulated echo DW-EPI sequence is on the right (Avram, 2011). .	65
Figure 2-16: PASL FAIR.....	65
Figure 2-17 : A diagram illustrates the key components of an MRI scanner system.	68
Figure 2-18: Home-made transmit receive birdcage coil.	71
Figure 2-19: A 3D FLASH T1-weighted image was generated using the home-made birdcage coil as an RF pulse transmitter and receiver.	72
Figure 3-1: The anaesthetic monitoring sheet is utilized throughout the entire duration of the experiment to track and record the status of the animals under anaesthesia.	75
Figure 3-2: Real-Time Physiological Monitoring Interface.	76
Figure 3-3: epoc Blood Gas Analyser.	76
Figure 3-4: Schematic illustration of the cisterna magna cannula implementation. CM: cisterna magna.	78
Figure 3-5: a. A difference image is generated by subtracting the baseline T2-weighted image from the image acquired 20 minutes after starting the tracer infusion. The ROI is delineated in yellow, indicating the retention of the tracer. b. A T2-weighted image with the same ROI is shown to provide a clearer perspective. c. A T2-weighted image depicting the brain of a deceased rat, with a marked line indicating the extra length of tubing inserted into the cisterna magna.	79
Figure 3-6: An example of a well-positioned 2 mm tip cannula is depicted here, which is a routine step to verify cannula positioning before commencing the experiment. The sequence employed is T_2 turbo spin echo in the sagittal orientation.	80
Figure 3-7: The aCSF infusion rate began at 0.2 $\mu\text{l}/\text{min}$ and was gradually increased to 1.6 $\mu\text{l}/\text{min}$, with 5-minute intervals between each increment. Concurrently, blood pressure was carefully monitored.....	81
Figure 3-8: Under the microscope, the ties around the common carotid arteries are illustrated before the withdrawal of the blunt needle.	83
Figure 3-9: Animals postoperative monitoring sheet.	84
Figure 3-10: Animals scoring sheet.	85
Figure 3-11: Pre-processing steps for MRI images.	86
Figure 3-12: Images co-registration for pre-processing: a. depicts the image before co-registration, while b. illustrates the image after co-registration using rigid body registration. This process is essential for aligning images to a common coordinate system, enhancing the accuracy of subsequent analyses. The slice orientation is coronal, and the sequence is diffusion-weighted imaging.	87
Figure 3-13: Another example for brain co-registration, with a. before and b. after motion correction. The slice orientation is sagittal, and the sequence is T_2 -weighted imaging.....	88
Figure 3-14: Rat brain MRI images: a. before smoothing, and b. after smoothing using an anisotropic diffusion filter. The slice orientation is sagittal, and the sequence is T2-weighted imaging.	89

Figure 4-1: TACs illustrate the percentage signal change plotted against time for two brain regions: a. Brain Cortex, and b. Whole Brain.	92
Figure 4-2: a. The drawing provides a visual representation that outlines how the phantoms are arranged. b. The corresponding image of the phantoms acquired using the MSME sequence.	94
Figure 4-3: T_2 exponential decay curves of the six phantoms.	95
Figure 4-4: Linear regression analysis of the change in relaxation rate as a function of CuSO_4 concentration.	96
Figure 4-5: Localizer images in the axial view overlaid: 0 mins in red colour on top of 135 mins in blue colour. (a) Scan performed before maintenance services; a slight shift in the FOV is observed at the phantom's edges, as indicated by the arrows. (b) Scan performed after maintenance services, the shift in the FOV is no longer present, as shown by the arrows.	97
Figure 4-6: Three regions of interest (ROI) delineated at different locations relative to the receiver coil.	99
Figure 4-7: Time activity curves for each ROI depicting the percentage signal change from baseline over a 135-minute period. Blue markers represent experiments with gradients left on for 24 hours ($n=4$), while orange markers represent experiments with gradients on for 3 hours ($n=4$). Statistical significance is denoted by asterisks: *** $P < 0.001$, **** $P < 0.0001$	99
Figure 4-8: The image acquired after 135 minutes of scanning was subtracted from the baseline image, (a) without frequency adjustment and (b) with frequency adjustments. Markers indicating differences are delineated with red circles.	101
Figure 5-1: a. MRI image of the control rat's brain, acquired 20 minutes after initiating H_2^{17}O tracer infusion and subtracted from the baseline, showing no detectable presence of the tracer. b. Image from (Alshuhri et al., 2021) demonstrating successful H_2^{17}O tracer uptake in a rat brain.	103
Figure 5-2: The percentage signal change is plotted continuously over a 50-minute period, with each scan lasting approximately 3 minutes. The ROI is delineated in the brain cortex.	104
Figure 5-3: Subtracted MRI images of the rat's brain in sagittal view. (a) Original images with the phase direction oriented as anterior-posterior. (b) Images after swapping the phase direction to superior-inferior.	105
Figure 5-4: Free and bound water spectrum (Henkelman et al., 2001).	106
Figure 5-5: The images displayed here are brain localizers utilized for guidance. These localizers are oriented in the coronal plane. The pink lines indicate the number of slices that will be excited in the sagittal orientation.	107
Figure 5-6: Scatter plot of signal intensity against the number of slices, with (a) the whole brain delineated and (b) the cerebral cortex delineated. The dashed lines represent the correlation line.	107
Figure 5-7: Comparison of MRI images of the rat brain after 9 minutes of tracer infusion under different positioning conditions: a. Rat positioned flat on the cradle. b. Rat positioned with an angle of 6° cephalic. H_2^{17}O in the cisterna magna is marked with green circles.	108
Figure 5-8: a. The suggested glymphatic pathway in the rat brain. b. MRI of the rat brain 20 minutes after infusing Gd-DTPA. c. MRI of the rat brain 20 minutes after infusing H_2^{17}O . The blue arrows indicate the direction of the tracers.	109
Figure 5-9: The ROIs delineated for calculating the percentage signal change induced by different combinations of H_2^{17}O . The image used is sagittal T2-weighted RARE.	110
Figure 5-10: The images depict the rat brain enhancements after 20 minutes of starting the infusion of different combinations of H_2^{17}O	111

Figure 5-11: Percentage signal change plotted as a function of time for several brain regions.	112
Figure 6-1: Study design (protocol). Cisterna magna cannulation then intraperitoneal injection of the drug; wait half an hour and start MRI scanning. CM: cisterna magna, IP: intraperitoneal, ADC: apparent diffusion coefficient, and MRI: magnetic resonance imaging.	119
Figure 6-2: Cisterna magna cannulation. Rat was placed in the prone position in a stereotaxic frame, using tooth and ear bars for stabilisation with the head fixed to 45° (snout). A 3 cm skin incision was made in the midline of the dorsal neck to expose the occipital crest and dural membrane covering the cisterna magna. A custom-made CM cannula (22-gauge, 2 mm Tip PEEK, SAI Infusion Technologies, RCMC-03) was advanced 2 mm into the subarachnoid space (i.e. CM space). CM: cisterna magna.	120
Figure 6-3: Serial MRI images in the sagittal plane of a single representative rat's brain. Using Gd-DTPA as the paramagnetic contrast agent reveals glymphatic transport, showing higher uptake and greater parenchymal penetration throughout the brain over a period of two hours in the animal treated with the AQP4 facilitator (TGN-073) compared to a vehicle-only treated rat. The time (in minutes) indicates the progression from the start of Gd-DTPA infusion.	124
Figure 6-4: Averaged time activity curves (TAC) of three different regions of rats' brains. The percentage signal change is plotted as a function of time for the TGN-073 treated (n = 6, blue circles), vehicles (n = 6, orange circles), and artificial CSF (n = 3, grey circles) in (a) prefrontal cortex, (b) cerebellum and (c) whole brain. Pink shading on graphs indicates the period of tracer infusion. Shading on the anatomical images of the brain illustrates the location of ROIs, blue: prefrontal cortex, purple: cerebellum and orange: whole brain.	124
Figure 6-5: Boxplots of apparent diffusion coefficient in the cerebral cortex (grey), the striatum (red), and whole brain (blue). In each figure, left: TGN-073-treated group; right: vehicle group. Asterisks indicate significant differences: *P < 0.05.	126
Figure 7-1: Gravity technique for transcordial perfusion fixation.	132
Figure 7-2: a. A grayscale microscopic image of the rat brain section in coronal orientation. b. The same microscopic image utilizes the blue channel to visualize DAPI staining, revealing the successful staining of cell nuclei within the brain section. c. The same microscopic image utilizes the green channel to visualize fluorescence emitted by immunofluorescence Alexa Fluor 488, which is supposed to stain neurons. However, the image appears smeared due to nonspecific staining.	135
Figure 7-3: DAB staining of rat brain sections. a. rat brain section was stained with the anti-NeuN primary antibody and a fresh secondary antibody conjugated with horseradish peroxidase, resulting in clear staining of neurons with DAB (brown colour). b. rat brain section stained with the same anti-NeuN primary antibody but using an old secondary antibody conjugated with horseradish peroxidase, with no observable staining of neurons. Both images were counterstained with haematoxylin to highlight cell nuclei (purple colour). Brain regions are denoted as follows: 1. cerebral cortex, and 2. hippocampus.	138
Figure 7-4: The diagram illustrates the allocation of slides to different antigen retrieval solutions and AQP4 antibody dilution factors. Ab: antibody.	139
Figure 7-5: Images were obtained using a standard microscope.	141
Figure 7-6: Images were obtained using a slide scanner. The brain images were zoomed in on the substantia nigra, while the kidney images were zoomed in on the convoluted tubules and collecting ducts of the nephron. The brown colour	

represents DAB staining of AQP4, while the purple colour, resulting from haematoxylin staining, highlights cell nuclei.....	141
Figure 7-7: The diagram illustrates the allocation of slides to different AQP4 antibody dilution factors. Ab: antibody.....	143
Figure 7-8: Immunofluorescence staining of AQP4 using Alexa Fluor 488 (green) in (a) brain and (b) kidney sections from rat.....	144
Figure 7-9: Immunofluorescence staining illustrates the distribution of AQP4 in the hippocampal region of rat brain sections. The bright green signal (Alexa Fluor 488) indicates perivascular localization of AQP4 around blood vessels, while cell nuclei are counterstained with DAPI (blue). Figure (a) and (b) show staining with 1:200 and 1:400 primary antibody dilutions, respectively. The observed perivascular streaks and punctate signals suggest high AQP4 expression along astrocytic endfeet surrounding vessels, consistent with its role in glymphatic fluid transport. Notably, the AQP4 signal appeared more distinct and better defined at the 1:400 dilution, indicating enhanced specificity and reduced background staining compared to the 1:200 dilution. Scale bar = 200 μm	145
Figure 8-1: Top image: the longer diffusion time allows water molecules to travel greater distances, increasing the likelihood of interactions with structures such as cell membranes and AQP4 channels. Bottom image: with a shorter diffusion time, water molecules have less opportunity to move and interact with cellular structures. The Root Mean Square Displacement (X_{rms}) was calculated using the equation $X_{\text{rms}} = \sqrt{6D\Delta}$, where D is the diffusion coefficient ($0.8 \times 10^{-9} \text{ m}^2 \text{ s}^{-1}$) and Δ is the diffusion time.	148
Figure 8-2: Study Protocol: The study involved an initial baseline MRI scan, followed by an intraperitoneal injection of either the drug or vehicle. After a waiting period of 30 minutes, a second MRI scan was performed. Following the imaging, the rats' brains were fixed for immunofluorescence staining. DWI: Diffusion weighted imaging.	150
Figure 8-3: Normalized diffusion coefficient values within the brain cortex across a range of diffusion times spanning from 20 to 1400 milliseconds, for TGN-073, TGN-020, and vehicle groups. Blue circles: before drug administration, and red circles: after drug administration.....	155
Figure 8-4: In the TGN-020 treated group, T2 values exhibited significant increases, whereas in the TGN-073 treated group, significant decreases were observed in several brain regions. Figure d shows the locations of the ROIs. ...	157
Figure 8-5: T ₂ values compared across treatment groups (Vehicle vs TGN-020, and Vehicle vs TGN-073) for the same ROIs as in Fig. 8.4. Unlike Fig. 8.4, which focused on within-group comparisons before and after treatment, this figure presents between-group comparisons. Statistical analysis revealed no significant differences in T ₂ values in the Cortex and Hippocampus across groups, but a significant difference ($P < 0.05$) was identified in the Thalamus between Vehicle and TGN-020 recipients. The locations of the ROIs are shown in Figure 8.4d. Data are presented as box plots showing median, interquartile range, and whiskers representing minimum and maximum values.	157
Figure 8-6: AQP4 immunofluorescence staining was performed in the rat brain using Alexa Fluor 488 (green) and nuclear counterstaining with DAPI (blue). Images captured at 40x magnification. Scale bars: Cortex and thalamus, 100 μm ; hippocampus, 50 μm	159
Figure 8-7: AQP4 Immunofluorescence staining of rat brain. The figure displays a larger field of view of the brain cortex. Panels depict: a. TGN-020 recipient, b. TGN-073 recipient. Images were captured at 20x magnification.....	160
Figure 8-8: The violin plots represent the percentage of AQP4 coverage area in different brain regions. The TGN-073 recipient group is represented by green,	

the TGN-020 recipient group by red, and the vehicle recipient group by blue. * indicates $P < 0.05$, and **** indicates $P < 0.0001$ 160

Figure 9-1: study protocol timeline. 168

Figure 9-2: CBF measured using ASL-MRI before and 24 hours after BCAS or sham surgery. CBF values are presented as percentages, normalized to baseline (pre-surgery) measurements set at 100%. Blue squares represent sham-operated animals, grey squares represent BCAS-operated animals that received a vehicle, and red squares represent BCAS-operated animals that received TGN-073. 172

Figure 9-3: Serial T1-weighted MRI images in the sagittal plane of rat brains following the BCAS procedure reveal glymphatic transport using Gd-DTPA as the paramagnetic contrast agent. Over a period of two hours, BCAS-operated rats treated with the AQP4 facilitator TGN-073 exhibited higher uptake and greater parenchymal penetration of Gd-DTPA compared to those treated with a vehicle. The times (in minutes) represent changes from the start of the Gd-DTPA infusion. 173

Figure 9-4: Time-activity curves (TAC) of several regions of interest (ROIs) in rat brains. The percentage signal change is plotted as a function of time for BCAS-operated rats treated with TGN-073 (n = 3, pink circles), BCAS-operated rats treated with vehicle (n = 3, grey circles), and sham-operated rats (n = 1, blue circles). Red shading on the brain images indicates the locations of the ROIs. . 174

Figure 9-5: AQP4 immunofluorescence staining was performed on rat brain sections using Alexa Fluor 488 (green) to visualize AQP4 expression. Images were captured at 40x magnification using a confocal laser scanning microscope. Scale bars represent 100 μm . Representative images show the localization and distribution of AQP4 in the cerebral cortex, hippocampus, and thalamus, highlighting differences in expression among TGN-073 treated BCAS, vehicle BCAS, and sham groups. 176

Figure 9-6: The bar charts represent the percentage of AQP4 coverage area in different brain regions. Blue bars indicate sham animals, grey bars indicate BCAS animals that received a vehicle, and pink bars indicate BCAS animals treated with TGN-073. Statistical significance is indicated as follows: ** $P < 0.01$, *** $P < 0.001$, and **** $P < 0.0001$ 177

Publications

Alghanimy, A., Martin, C., Gallagher, L. & Holmes, W.M. (2023) 'The effect of a novel AQP4 facilitator, TGN-073, on glymphatic transport captured by diffusion MRI and DCE-MRI,' *PLOS ONE*, 18(3), pp. e0282955-.

Alghanimy, A.A., Giovannoni, G., Lechner-Scott, J., Levy, M., Yeh, E.A. & Hawkes, C.H. (2023) 'Is multiple sclerosis a glymphaticopathy?', *Multiple sclerosis and related disorders*, 80.

Alghanimy, A., Work, L.M. & Holmes, W.M. (2024) 'The Glymphatic System and Multiple Sclerosis: An Evolving Connection', *Multiple Sclerosis and Related Disorders*, p. 105456.

Conference Proceedings & Awards

Investigating glymphatic transport with novel MRI tracers and therapeutic targets. SINAPSE Annual Scientific Meeting 2021. Oral presentation.

Award: Best talk in the preclinical and optical imaging theme.

Investigating glymphatic transport with novel MRI tracers and therapeutic targets. British and Irish Chapter-ISMRM 2021. Oral presentation.

Award: Best neuro talk.

The effect of a novel AQP4 facilitator, TGN-073, on glymphatic transport captured by diffusion MRI and DCE-MRI. BRAIN & BRAIN PET 2022. Poster presentation.

The effect of a novel AQP4 facilitator, TGN-073, on glymphatic transport captured by diffusion MRI and DCE-MRI. SINAPSE Annual Scientific Meeting 2022. Oral presentation.

Award: Best presentation in the Cognitive Neuroimaging session.

The effect of a novel AQP4 facilitator, TGN-073, on glymphatic transport captured by diffusion MRI and DCE-MRI. British and Irish Chapter-ISMRM 2022. Oral presentation.

Award: Second place for best talk in all categories.

The effect of a novel AQP4 facilitator, TGN-073, on glymphatic transport captured by diffusion MRI and DCE-MRI. The 12th Neuronus Neuroscience Forum 2022. Oral presentation.

The effect of pharmacological modulation of AQP4 on glymphatic transport and brain microstructure in normal rats. BRAIN & BRAIN PET 2023. Poster presentation.

Acknowledgement

First and foremost, I would like to express my deepest gratitude to my primary supervisor, Dr. William Holmes. Your guidance and support throughout these years have been instrumental in the completion of this thesis. Your exceptional ability to teach MRI physics made the learning process both enriching and enjoyable. I have learned so much under your mentorship, not just about MRI, but also about History and culture. Thank you for always believing in me and pushing me to reach my full potential. I also extend my thanks to my second supervisor, Dr. Lorraine Work, for her valuable guidance and support. Your insights and advice have been crucial in shaping this research, and I am grateful for your contributions.

A special mention must go to the incredible individuals without whom this thesis would not have been possible. Mrs. Linda Carberry, Mrs. Lindsay Gallagher, Dr. Rosario Lopez, Dr. Karin Williams, Mr. James Mullin, and Mr. Conor Martin - you have been the backbone of this research. Your expertise, encouragement, guidance, and support have been invaluable and have greatly contributed to the quality of this research, and I am deeply grateful for everything. Lindsay, Linda, Jim, and Conor; I can't thank you enough for everything you did to make these experiments work. Your dedication and sacrifices, your willingness to go above and beyond like staying late or skipping proper meals to rush back to the experiments, have not gone unnoticed. I greatly appreciate and am deeply grateful for your relentless commitment and everything you have done.

I would also like to extend my special thanks and gratitude to my family and friends. Your consistent emotional support and belief in me have been my sources of strength. Thank you for your encouragement, understanding, and for always being there for me, especially during the tough times. Your love and support have been the driving force behind my perseverance.

Author's Declaration

I, Alaa Alghanimy, declare that, except where explicit reference is made to the contribution of others, that this thesis is the result of my own work and has not been submitted for any other degree at the University of Glasgow or any other institution.

Definitions/Abbreviations

5-CQA	5-Caffeoylquinic Acid
aCSF	Artificial cerebrospinal fluid
AD	Alzheimer's disease
ALS	Amyotrophic lateral sclerosis
AQP	Aquaporin
AQP1	Aquaporin-1
AQP4	Aquaporin-4
ASL	Arterial spin labelling
AB	Amyloid beta peptide
BBI	Blood-brain interface
BCAS	Bilateral common carotid artery stenosis
BCAO	Bilateral carotid artery occlusion
BBB	Blood-brain barrier
BP	Blood pressure
CBF	Cerebral blood flow
CCH	Chronic Cerebral Hypoperfusion
CNS	Central nervous system
CSF	Cerebrospinal fluid
DCE-MRI	Dynamic contrast-enhanced MRI
DTI	Diffusion tensor imaging
DTI-ALPS	DTI analysis along the perivascular space
DWI	Diffusion-Weighted Imaging
ECS	Extracellular space
FOV	Field of view
Gd	Gadolinium
GBCA	Gadolinium-based contrast agents
HR	Heart rate
HRP	Horseradish peroxidase
iNPH	Idiopathic normal pressure hydrocephalus
ICP	Intracranial pressure

IF	Immunofluorescence
IHC	Immunohistochemistry
ISF	Interstitial fluid
IV	Intravenous
iPAD	Intramural Peri-Arterial Drainage
LDF	Laser-Doppler Flowmetry
LSBFI	Laser Speckle Blood Flow Imaging
MMSE	Mini-Mental State Examination
MoCA	Montreal Cognitive Assessment
MRI	Magnetic resonance imaging
MS	Multiple sclerosis
NREM	Non-rapid eye movement
NMOSD	Neuromyelitis optica spectrum disorder
PD	Parkinson's disease
PET	Positron emission tomography
PFA	Paraformaldehyde
PVS	Perivascular spaces
ROI	Region of interest
SAS	Subarachnoid space
SMS	Scalp mechanical stimulation
STE-DW-EPI	Stimulated echo diffusion-weighted echo planar imaging
TAC	Time-activity curves
TBS	Tris-buffered Saline
TBI	Traumatic brain injuries
TE	Echo time
TR	Repetition time
VCI	Vascular Cognitive Impairment
WKY	Wistar Kyoto

Chapter 1 Literature Review

1.1 Cerebrospinal fluid dynamics

Being one of the most vital organs in the body, the brain requires a comprehensive protection mechanism. Various approaches contribute to safeguarding the brain, including the skull, which protects it from physical harm, cerebrospinal fluid (CSF) provides essential cushioning for the delicate brain and spinal cord while contributing to overall homeostasis. Additionally, the blood-brain barrier (BBB) serves to impede harmful molecules from entering the brain (Proulx, 2021). The brain's total water content is distributed with approximately 60% in the intracellular space and the remaining 40% in the extracellular space (ECS) in mammals. The extracellular fluid can be subdivided into three components: Interstitial fluid (ISF) constitutes 20% of the total water, while the remaining 20% is distributed between blood vessels and CSF, with each accounting for 10% of the intracranial fluid (Jessen et al., 2015; Plog & Nedergaard, 2018).

The term "cerebrospinal fluid" was coined by François Magendie in the nineteenth century to designate this crucial liquid (Magendie, 1842; Proulx, 2021). CSF is a colourless and clear liquid that occupies the brain ventricles and envelops its tissue within the subarachnoid space (SAS). This essential fluid serves various homeostatic functions, including the transport of nutrients, elimination of catabolic waste products, hydromechanical shock absorption, thermal stress management, and serving as a carrier for neurotransmitters. Predominantly composed of water (99%), CSF's remaining 1% consists of essential components such as glucose, electrolytes, neurotransmitters, and proteins (Hutton et al., 2022; Orešković & Klarica, 2010; Theologou et al., 2022).

The exploration of CSF dynamics commenced more than 15 decades ago, and understanding the precise mechanisms of CSF production, circulation, and

reabsorption remains a persistent challenge for researchers. This complexity is largely attributed to the inherent difficulty in accessing brain CSF *in vivo* without resorting to invasive procedures. Consequently, the majority of studies have historically been conducted *ex vivo* and *post-mortem*. While these studies are insightful, they are susceptible to artefacts that may potentially distort true results, such as tissue degradation and *post-mortem* changes (Weed, 1914; Davson & Segal, 1996; Key, 1875). *Ex vivo* methods alter the natural physiological conditions when they extract tissue or fluid from living organisms which impacts CSF production, reabsorption and circulation. For instance, the absence of blood circulation along with temperature fluctuations and cellular response changes outside the body creates potential misinterpretation of how CSF behaves within living organisms (Opitz et al., 2017; Mestre, Mori, et al., 2020). However, with the continuous advancement of technology and innovations in non-invasive imaging techniques, our understanding of CSF dynamics is becoming clearer.

1.1.1 CSF production

CSF is actively generated within the ventricular system of the brain, predominantly by the choroid plexuses (McComb, 1983). These structures are situated in the ependymal lining of the brain ventricles. The choroid plexus epithelial cells exhibit a division into basolateral and apical parts (Damkier et al., 2013). Additional extrachoroidal sources for CSF synthesis are proposed. For example, ISF and hydrostatic pressure exerted by cerebral blood vessels within the brain parenchyma are suggested contributors to the production of CSF (Orešković & Klarica, 2010; Hutton et al., 2022). Aquaporin1 (AQP1) water channels are widely expressed on the apical part of the choroid plexus and are suggested to play a role in CSF secretion. This proposition gains strength from observations in mice lacking AQP1, which exhibited a 20% inhibition in CSF formation compared to their wild-type counterparts (Oshio et al., 2005; Mobasheri & Marples, 2004).

In the adult human, the CSF production rate is approximately 0.4 mL/min, translating to about 565 mL/day (Bakker et al., 2016; G. Liu et al., 2020). The total CSF volume in the adult human central nervous system (CNS) ranges from approximately 254 to 331 mL (Alperin et al., 2016; Chazen et al., 2017). In

rodents, the CSF production rate differs between adult rats and mice, with rates of 0.895 $\mu\text{L}/\text{min}$ and 0.108 $\mu\text{L}/\text{min}$, respectively (Karimy et al., 2015; G. Liu et al., 2020). Notably, the adult rat brain is several times larger than the adult mouse brain, resulting in total CSF volumes of around 400 μL and 40 μL for adult rats and mice, respectively (Oshio et al., 2005; Chiu et al., 2012).

The production of CSF can be influenced by various factors, including ageing, wakefulness state, and amyloid beta peptide (AB) overproduction. In Alzheimer's disease (AD) mice models, AB overproduction led to a 33% reduction in CSF production compared to wild-type counterparts (G. Liu et al., 2020). The reduction of CSF production with age has been documented in rats and humans, as well as in mice (Chiu et al., 2012; May et al., 1990). Furthermore, gender may play a role in CSF production rates, as seen in young mice where females exhibited a 30% higher CSF production rate (108.0 nL/min) compared to males (83.9 nL/min) (G. Liu et al., 2020). This gender difference could potentially be attributed to variations in sex hormonal expression in the choroid plexus.

1.1.2 CSF circulation

The CSF follows a specific pathway within the brain ventricles and SAS. It flows from the lateral ventricles to the third ventricle through the foramina of Monro. Subsequently, it moves from the third to the fourth ventricles via the cerebral aqueduct of Sylvius. The CSF then enters the SAS via the foramen of Magendie and Luschka. The movement of CSF from the ventricles to the SAS is predominantly passive, driven by hydrostatic pressure gradients, with the pressure inside the ventricles typically higher than in the SAS, and influenced by the pulsations of nearby blood vessels (Damkier et al., 2013).

Phase-contrast imaging with velocity encoding is a widely used technique for measuring flow dynamics such as CSF (Menick, 2001). It operates by applying two phase-encoding gradients in opposite directions. Stationary protons do not produce a signal, while moving protons generate a detectable signal. Fluid flow can be quantified by selecting a region of interest, such as the aqueduct, and plotting velocity against time. The resulting graph reveals pulsatile flow, with forward flow during systole and retrograde flow during diastole. The area under

the curve for each phase represents the flow values in both directions (Battal et al., 2011). This technique has proven valuable in diagnosing neurological disorders associated with altered CSF dynamics. For instance, phase-contrast MRI has shown that patients with normal pressure hydrocephalus (NPH) exhibit higher CSF flow compared to controls with normal flow. In contrast, patients with brain atrophy due to ageing show reduced CSF flow compared to controls (Govindarajan et al., 2024).

Different theories exist regarding the primary mechanism governing CSF movement in the PVS, notably bulk flow and passive diffusion. The debate over which mechanism is dominant continues and will be explored further in this chapter. Bulk flow is an active process requiring energy, which is derived from cellular metabolism. This movement is independent of molecular size. In contrast, diffusion is a passive process relying on thermal energy from the surrounding environment and is size-dependent. Larger molecules diffuse more slowly than smaller ones (Plog & Nedergaard, 2018).

Conventionally, the ECS (includes both the ISS and the PVS) in the brain parenchyma was believed to be governed solely by diffusion, with bulk flow considered impractical due to the small and tortuous nature of the ECS (Verkman, 2013). Ex vivo measurements suggested an ECS width of around 10-20 nm (Brightman, 2002). However, in living organisms, the ECS width is a minimum of two times larger, ranging from 38 to 64 nm (Thorne & Nicholson, 2006). Additionally, there is a theory proposing that CSF direction is influenced by respiration. Inhalation induces CSF cephalic motion, while exhalation causes the opposite, leading to caudal CSF movement (Yamada et al., 2013).

1.1.3 CSF reabsorption/ drainage

The outflow of CSF from the cranial cavity has intrigued neuroscientists for decades (Proulx, 2021). The conventional theory posits that CSF primarily exits the brain into the blood circulation. According to this theory, CSF in the SAS drains into the venous sinuses in the dura mater through arachnoid projections extending from the arachnoid layer into the dural sinuses (Weed, 1914; Davson & Segal, 1996; Kido et al., 1976). These arachnoid projections come in two types based on

size: larger ones are termed arachnoid granulations, while smaller ones are referred to as arachnoid villi (Turner, 1958; Butler et al., 1983). The terms granulation and villi are sometimes used interchangeably. However, the clearance of CSF to the venous sinus through arachnoid granulations is challenged due to several factors. In humans, arachnoid granulations are absent during fetal development, gradually forming around the time of birth and increasing in quantity with age (Papaiconomou et al., 2002). This route becomes less active with ageing due to the thickening of the arachnoid membrane and the deterioration of arachnoid granulations (Pollay, 2010; Gomez et al., 1983; Mollanji et al., 2001; Papaiconomou et al., 2002).

Moreover, brain solutes encounter difficulties passing through arachnoid villi channels unless there is a significant pressure difference between CSF and the dural sinus (Welch & Pollay, 1961). Additionally, the limited opening size of arachnoid villi (up to 12 μm in diameter) restricts the passage of some macromolecules. The properties and shape of molecules may also influence their ability to traverse these channels (Welch & Pollay, 1961; Pollay, 2010). Consequently, this pathway has not been conclusively proven, and instead, it has been suggested that arachnoid granulations function as security valves that open when intracranial pressure is elevated (Gomez et al., 1973; Gomez & Potts, 1977; Welch & FRIEDMAN, 1960; Proulx, 2021).

Subsequent studies have shown that CSF tracers reach the lymphatic vessels. Various pathways have been proposed for CSF drainage into the lymphatic system, including along the perineural sheaths of cranial and spinal nerves or through the recently discovered meningeal lymphatic vessels in the dura mater (Pollay, 2010; McComb, 1983; Bradbury & Cserr, 1985; Koh et al., 2005; Aspelund et al., 2015; Louveau et al., 2017; Ueno et al., 2016; Louveau et al., 2015). Another suggested pathway is that CSF solutes reach the deep cervical lymphatic nodes via highly expressed lymphatic structures in the nasal submucosa (Faber, 1937; Walter et al., 2006). Observations in both humans and rodents indicate that CSF flows along the perineural sheath surrounding olfactory nerves to the lymphatic vessels in the nasal submucosa through the cribriform plate (Johnston et al., 2004; Ma et al., 2017).

1.2 The "perivascular" glymphatic system: a historical perspective

Pestalozzi and Durand-Fardel played instrumental roles in characterizing perivascular spaces in the 1840s (Durand-Fardel, 1843; Woollam & Millen, 1955). Subsequently, German scientist Rudolf Virchow and French scientist Charles Philippe Robin further elucidated these spaces, leading to their recognition as Virchow-Robin spaces in the 1850s (Robin, 1859; Virchow, 1851). The exploration of perivascular dynamics gained momentum in the 1970s when Cserr et al. proposed the glymphatic "perivascular" system, highlighting the bulk flow of ISF (Cserr & Ostrach, 1974). Cserr's team injected tracer (blue dextran 2000) into the caudate of a rat's brain. Microscopic examination was carried out after 15 minutes and after 24 hours; the dye was found to have been distributed by bulk flow of the ISF following the path of the cerebral blood vessels (Cserr & Ostrach, 1974).

In a subsequent study, Cserr and colleagues infused the caudate of a rat's brain with horseradish peroxidase (HRP) to investigate the bulk flow of ISF. Analysis of protein distribution was conducted between 4 and 8 hours after injection, whereupon the HRP were found in the perivascular spaces (Cserr et al., 1977). A further study by Cserr and colleagues, conducted in 1981, found perivascular ISF drains derived from bulk flow rather than diffusion. This was achieved by injecting radiolabelled isotopes of three different molecular weights into the caudate nucleus of a rat's brain. Despite variation in diffusion coefficients, the clearance rate in all cases had approximately the same half-life (Cserr et al., 1981).

In 1985, Rennels and colleagues corroborated the perivascular clearance system's existence using dogs and cats as experimental subjects, confirming its presence in larger mammals (Rennels et al., 1985). However, despite the accumulated evidence from multiple studies, the hypothesis of CSF perivascular flow was largely set aside due to a lack of confirmation by other research teams. This limitation may have arisen from the lack of sophisticated and sensitive imaging technology available at that time.

1.3 Glymphatic system

In peripheral body organs, interstitial waste is cleared through lymphatic vessels (Schmid-Schonbein, 1990), yet despite its high metabolic rate, the brain parenchyma lacks conventional lymphatic vessels typically present in other organs (Cserr et al., 1992; Abbott, 2004). Historically, it was believed that brain interstitial fluid movement relied solely on diffusion, and the removal of protein solutes from the brain was primarily attributed to degradation processes such as autophagy (Syková & Nicholson, 2008; Bossy et al., 2008). Meanwhile, certain proteins, including Amyloid β , were cleared to the bloodstream through transporters and mediators at the BBB (Deane et al., 2009; Zlokovic et al., 2010).

In the last decade, neuroscientific interest in the glymphatic system has intensified. The glymphatic system, composed of glial and lymphatic elements, derives its name from the essential role played by astroglial water channels aquaporin-4 (AQP4), facilitating CSF-ISF exchange. Its designation as 'lymphatic' stems from its functional resemblance to the peripheral lymphatic system (Iliff et al., 2012). Glymphatic system activity involves the flow of subarachnoid CSF along the perivascular space surrounding penetrating arteries. Subsequent influx of CSF into the brain interstitium is mediated by the AQP4, which is mainly expressed at the end feet of astrocytes that ensheath the perivascular spaces (Iliff et al., 2012). It is proposed that this influx results in the bulk flow of ISF, which then exits along perivenous spaces. Importantly, this bulk flow aids the removal of harmful metabolite and waste products from the brain tissue, as shown in Figure 1-1 (Iliff & Simon, 2019; Iliff et al., 2012). Brain waste products ultimately drain into the meningeal lymphatic vessels or deep cervical lymph nodes (Mestre, Mori, et al., 2020).

The glymphatic system plays a crucial role in clearing harmful proteins associated with the pathophysiology of AD, including A β and tau proteins. This observation is supported by studies involving transgenic mice, where compromised glymphatic function resulting from the deletion of the AQP4 gene leads to the accumulation of such molecules in the brain (Iliff et al., 2012, 2014). In their original study, Iliff and colleagues employed two-photon imaging combined with different fluorescent tracers injected into the cisterna magna of live mice. This approach revealed the

influx of CSF into the brain parenchyma via perivascular spaces around penetrating arteries, while interstitial fluid was drained via perivenous spaces. Additionally, they demonstrated that AQP4 knockout mice exhibited a significant reduction in the clearance of interstitial solutes. This was evident when radiolabelled AB (¹²⁵I) was injected into the striatum, revealing a ~55% decrease in clearance in AQP4 knockout mice compared to wild-type counterparts (Iliff et al., 2012).

The glymphatic system is believed to activate during sleep, either naturally or under anaesthesia (Xie et al., 2013). The observed increase in brain lactate levels during wakefulness, coupled with decreased lactate levels during sleep, suggests a role for the glymphatic system in lactate clearance. This hypothesis was investigated in mice using microdialysis to measure lactate concentrations during the light and dark phases, which correspond to sleep and wakefulness, respectively (Lundgaard et al., 2017). Consequently, factors such as the removal of AQP4, administration of anaesthesia, opening of the cisterna magna, and the application of acetazolamide, all of which contribute to a reduction in glymphatic clearance, are associated with elevated lactate levels in the brain (Lundgaard et al., 2017).

In addition to its waste-clearing function, the glymphatic system contributes to delivering essential components and nutrients, including signalling molecules, lipids, and Apolipoprotein E (APOE) to the brain (Achariyar et al., 2016; Thrane et al., 2013). Furthermore, this system possesses the capability to transport drugs directly to the brain, bypassing the BBB (Lundgaard et al., 2015). Therefore, the modulation of the glymphatic system using therapeutic drugs holds promising potential for the treatment of various neurological diseases.

Although initial glymphatic studies were conducted in rodents, subsequent studies have suggested the presence of glymphatic flow in humans (Ringstad et al., 2017; Eide & Ringstad, 2015; Iliff et al., 2012; Iliff, Lee, et al., 2013). Nonetheless, evidence remains limited due to the challenges associated with direct imaging of glymphatic activity in humans, such as the need for intracisternal or intrathecal tracer injections (Eide et al., 2018). Human glymphatic flow is significantly slower compared to that observed in rodent brains. In humans, the glymphatic signal peaked after 24 hours, whereas in rodents, the glymphatic signal reached its peak

just 2 hours after tracer administration. Both human and rodent studies employed MRI, enhanced with gadolinium-based contrast agents, to visualize glymphatic flow. However, it is important to note that in humans, contrast administration was intrathecal (lumbar region), whereas in rodents, it was intracisternal (cisterna magna region). Given the greater proximity of the cisterna magna to the brain compared to the lumbar region, the full extent of glymphatic flow in humans may therefore be underestimated (Eide et al., 2018; Iliff, Lee, et al., 2013). The effectiveness of glymphatic clearance declines with ageing, as well as in several neurological diseases, which will be discussed later in this chapter (Benveniste et al., 2019).

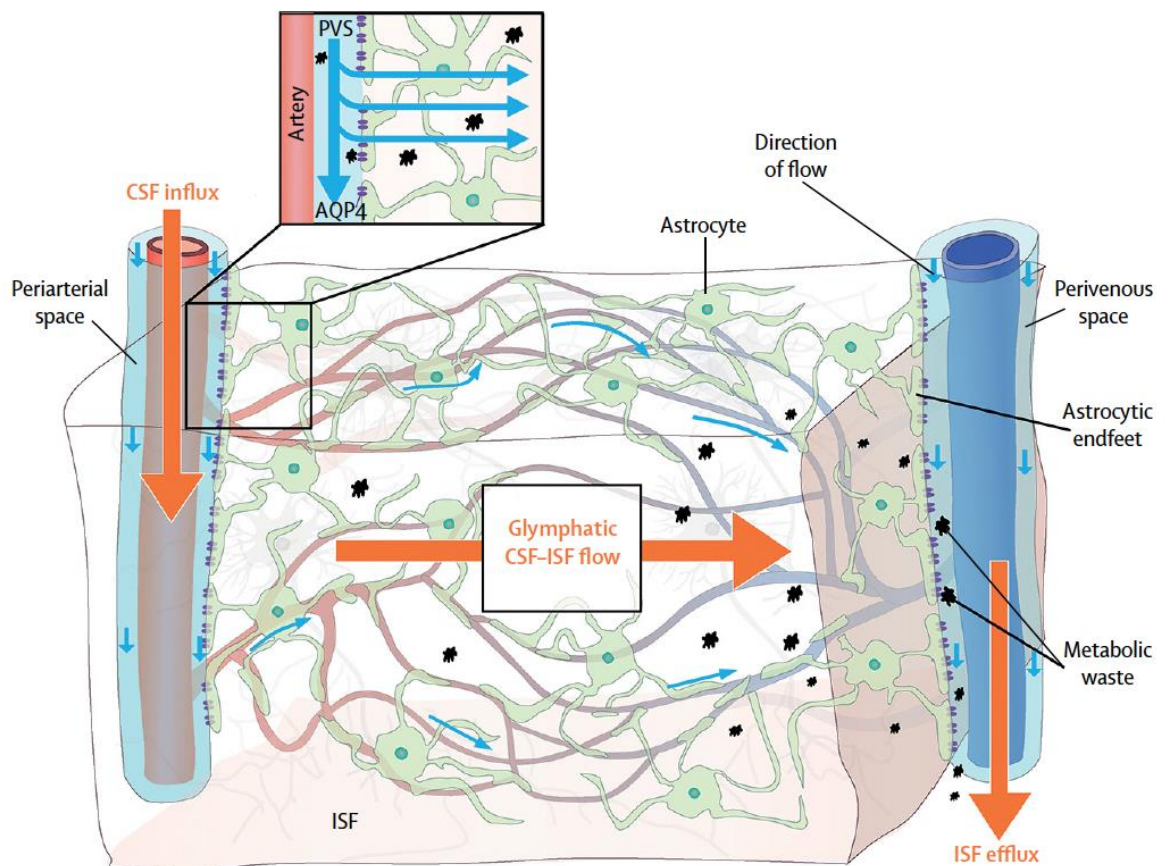


Figure 1-1: Schematic diagram of the glymphatic pathway (Rasmussen et al., 2018).

1.4 Aquaporin water channel

Aquaporin (AQP) water channels were first identified by Peter Agre and his colleagues over 30 years ago. This groundbreaking discovery earned him the Nobel Prize in Chemistry in 2003 (Agre et al., 2002; Farr et al., 2019; Mader & Brimberg,

2019; Preston et al., 1992). AQPs are small cellular plasma membrane proteins characterized by six alpha-helices connected by five linking loops. The intracellular side includes the terminal carboxyl and amino domains, and their size is approximately 30 kDa (Trillo-Contreras et al., 2022). Notably, AQPs demonstrate high water permeability, with each monomer capable of transmitting up to 3×10^9 water molecules per second (Zeidel et al., 1994; Walz et al., 1994).

The AQP family comprises 13 types of AQPs distributed throughout the mammalian body. They are categorized into three subfamilies based on their structure and permeability. First, there are the conventional or classical AQPs (AQP 0, 1, 2, 4, 5, 6, and 8), primarily permeable to water, also known as water-selective channels. Second, the aquaglyceroporins, including AQP 3, 7, 9, and 10, exhibit permeability not only to water but also to certain small substances with a neutral charge and glycerol (also called glycerol channels). Third, the superaquaporins, AQP11 and AQP12, are located in the cytoplasm, playing a role in regulating cellular water homeostasis (Trillo-Contreras et al., 2022; Beitz et al., 2004).

Additionally, there is a proposal suggesting that AQPs may act as facilitators for the transport of small gas molecules such as O_2 , CO_2 , and N_2O (Agre, 2006; Zador et al., 2009). Within the CNS, three AQPs—AQP1, AQP4, and AQP9—are identified. Their presence in the brain is crucial for maintaining water homeostasis and normal function. AQP1 is predominantly expressed in the choroidal plexus epithelia, where it plays a role in facilitating water movement associated with CSF production. AQP4 is most abundant in the CNS and is highly expressed in the membranes of astrocytes' endfeet. Finally, AQP9 is found in the substantia nigra (Papadopoulos & Verkman, 2013; Verkman et al., 2014).

Metal ions have an impact on the activity of most AQPs. For example, mercury has an impact on all AQPs, inhibiting their activity except for AQP6, which it activates (Yasui et al., 1999). Additionally, zinc has demonstrated its ability to decrease the water transportation of AQP4 by approximately 30% (Yukutake et al., 2009). Furthermore, copper has exhibited inhibitory effects on AQP4 (Yukutake et al., 2009; Yukutake & Yasui, 2010). Despite the effectiveness of metal ions in modulating AQP functions, their high toxicity limits their potential applications (Vandebroek & Yasui, 2020).

1.4.1 Aquaporin-4

Water moves through various pathways within the brain, including transportation from the blood circulation through the BBB and astrocytic foot processes into the brain parenchyma. Additionally, water moves from the parenchyma through the pial layer and subpial astrocytes into the SAS. All these pathways are believed to be essential for sustaining brain water homeostasis, and AQP4 is expressed in all of those regions (Vindedal et al., 2016). AQP4 is presumed to play a crucial role in the glymphatic system, as well as in brain health and disease (Nedergaard, 2013). These water channels are densely expressed at the vascular endfeet of astrocytes, precisely where the interstitial and perivascular spaces connect, commonly referred to as AQP4 polarisation. Whereas loss of AQP4 polarisation typically refers to the redistribution of AQP4 away from the astrocytic endfeet towards the cell body and other regions of the astrocyte. This shift has been observed in neurodegenerative diseases, response to injury, and inflammatory processes, which could impair water regulation and neurovascular coupling (Rash et al., 1998; Nielsen et al., 1997; Papadopoulos & Verkman, 2013).

Astrocytes, a predominant glial cell type in the CNS, make up over 50% of the total cellular population in the brain. It is widely believed that the number of astrocytes exceeds that of neurons by a factor of ten (Ikeshima-Kataoka, 2016). Notably, the size of the cleft or gap between astrocytic endfeet measures approximately 20 nanometres (Mathiisen et al., 2010).

Water flux through AQP4 is bidirectional and is influenced by osmotic gradients, hydrostatic pressure differences, and electrochemical forces between the two regions connected by AQP4 (Papadopoulos & Verkman, 2007; Igarashi et al., 2011). AQP4 has two primary isoforms, M1 and M23, which originate from methionine M1 (323 amino acids) and methionine M23 (301 amino acids) as their translation start sites, respectively (Lu et al., 1996). The AQP4 M23 isoform is predominantly expressed in endfeet processes, while the AQP4 M1 isoform is distributed around the plasma membrane (Smith et al., 2014).

The mechanism governing the polarised distribution of AQP4 to perivascular endfeet astrocytes remains poorly understood. It is suggested that AQP4 engaged with either α -syntrophin or agrin, both of which have demonstrated polarised AQP4 expression to astrocyte endfeet processes (Neely et al., 2001). The significance of α -syntrophin in AQP4 polarisation gained further support through experiments with α -syntrophin knockout mice, which displayed a lack of AQP4 polarisation to the perivascular space (Puwarawuttipanit et al., 2006; Mestre, Hablitz, et al., 2018).

Several research studies demonstrate that the absence of AQP4 inhibits the distribution and clearance of various interstitial substances, including tau (Ilf et al., 2014), lactate (Lundgaard et al., 2017), adeno-associated viruses (Murlidharan et al., 2016), and ApoE (Achariyar et al., 2016). The pivotal role of AQP4 is confirmed by the work of Iliff et al., revealing that the lack of AQP4 water channels leads to a reduction in CSF influx, resulting in a decrease of approximately 70% in ISF solute clearance (Iliff et al., 2012). Behavioural examinations further support these findings, indicating cognitive impairment in AQP4 knockout mice (Fan et al., 2013; Zhang et al., 2013; Skucas et al., 2011).

Computational modelling further supports the role of AQP4. In a study conducted by Asgari et al., various structures involved in fluid transport, including AQP4, gap junctions, and inter-end-feet gaps, were incorporated. Their findings illustrate that the transfer of brain solutes from neuropil to the perivascular space is facilitated by the low resistance of astrocytes to bulk flow. Importantly, the deletion of AQP4 results in a reduction of bulk flow, compromising brain solute clearance along perivenous spaces (Asgari et al., 2015). Collectively, these insights highlight the significant contribution of AQP4 in facilitating both the entry of CSF into brain tissue and the removal of interstitial solutes.

To date, to our knowledge, the only putative AQP4 facilitator that enhances water flux through these channels is TGN-073, developed by Huber and colleagues in 2018. This drug showed promising results in preclinical studies (Huber, Igarashi, et al., 2018; Peng et al., 2025). Huber et al. tested TGN-073 in mice using a specialized imaging method, $[^{17}\text{O}] \text{H}_2\text{O}$ vicinal coupling proton exchange MRI (JJVCPE), which traces water molecules. Their results clearly demonstrated that

enhancing AQP4 with TGN-073 increased fluid flow through the glymphatic system, leading to a noticeable reduction of [^{17}O] H_2O in the cortex and normal fluid flow into the CSF (Huber, Igarashi, et al., 2018). The mechanism of action of TGN-073 may involve ligand interaction with AQP4, causing a conformational shift, particularly in the protein loop spanning the H2 and HB helices. This shift may increase the channel diameter, thereby enhancing water flux (Kaptan et al., 2015). Additionally, TGN-073 was tested in the 5xFAD AD mouse model, where it was found that facilitation of AQP4 by TGN-073 reduced the accumulation of insoluble A β (Kwee et al., 2020). The effect of TGN-073 was also evaluated in mice subjected to a long-term high-fat diet. Using immunofluorescence imaging, A β labelled with HiLyte-555 was injected into the hippocampus of these mice. The results revealed a significant increase in A β clearance in mice treated with TGN-073 compared to those that received normal saline (Peng et al., 2025).

1.4.2 AQP4 implication in neurological disorders

The loss of AQP4 polarisation to the perivascular space appears to escalate with age (Zeppenfeld et al., 2017; Kress et al., 2014). Moreover, there is an observed overexpression of AQP4, coupled with its mis-localization to the parenchymal processes of astrocytes in aged brains. This observation has led to the suggestion that the increased AQP4 expression may serve as a compensatory response to the age-related deterioration of astrocytes (Zeppenfeld et al., 2017; Silva et al., 2021). In a post-mortem study of AD patients, a loss of AQP4 polarisation was observed in the cerebral cortex (Zeppenfeld et al., 2017). This observation finds support in rodent studies, where AD mouse models demonstrated reduced AQP4 polarisation alongside increased plaque formation (Yang et al., 2011; Eidsvaag et al., 2017). The loss of AQP4 polarisation is suggested to decrease A β clearance (Hoshi et al., 2012).

It was shown that the size of cerebral oedema induced by an ischemic stroke, resulting from an occlusion in the middle cerebral artery, was 35% smaller in AQP4 knockout mice compared to their wild-type counterparts. This reduction was accompanied by less neurological deterioration (Manley et al., 2000). AQP4 knockout mice also demonstrated less severe brain oedema and improved blood flow distribution during mild water intoxication, contrasting with their wild-type

counterparts (Bordoni et al., 2023). This data suggests that diminishing AQP4 could aid in decreasing cerebral oedema following an injury. This is particularly important, as oedema is recognized to play a significant role in exacerbating the situation and increasing mortality rates.

1.5 Meningeal lymphatic vessels

Shortly after the introduction of the glymphatic hypothesis in 2012 (Iliff et al., 2012), studies revealed the existence of meningeal lymphatic vessels within the dura matter, and this has helped to clarify the mechanism responsible for moving fluid from the brain's CSF to deep cervical lymph nodes (Louveau et al., 2015; Aspelund et al., 2015). Aspelund et al. found that in transgenic mice lacking these dural lymphatic vessels, the transfer of fluid from the brain parenchyma to the deep cervical lymph nodes was abolished (Aspelund et al., 2015). Meningeal lymphatic vessels have also been identified in humans. These lymphatic vessels are located within the dura mater and are particularly concentrated along the superior sagittal sinus (Visanji et al., 2018; Absinta et al., 2017).

A recent prospective study by Gabr et al. applied dynamic intravenous contrast magnetic resonance imaging (MRI), employing a standard 3T MRI scanner, to investigate dural lymphatic vessels in multiple sclerosis (MS) patients. This showed noticeable contrast enhancement within these lymphatic vessels, with signal tracking extending for approximately 33 minutes post-contrast injection, with an average peak enhancement of 109%, indicating potential disruption in meningeal lymphatic flow associated with MS pathology (Gabr et al., 2023).

In a study aimed at investigating the correlation between ageing and the deterioration of glymphatic function along with meningeal lymphatic vessels, 35 patients underwent intrathecal injection of gadodiamide. Subsequently, MRI scans were conducted before and at various intervals (4.5, 15, and 39 hours) following the contrast administration. The analysis focused on measuring changes in signal intensities in different regions, revealing a significant correlation between clearance dysfunction and ageing (Zhou et al., 2020).

The study also illustrated the interdependence of the glymphatic pathway and meningeal lymphatic vessels. Specifically, early enhancement of meningeal lymphatic vessels was associated with a faster glymphatic clearance compared to cases with late enhancement (Zhou et al., 2020). Furthermore, the research by Da Mesquita et al. demonstrated that the dysfunction of meningeal lymphatic vessels in the ageing process could lead to a higher accumulation of A β in the brain, contributing to the development of AD (Da Mesquita et al., 2018).

1.6 Glymphatic system driving force

Scholars have identified several potential drivers of glymphatic transport, including respiration (Helakari et al., 2022), vasomotion (van Veluw et al., 2020), cardiac/arterial pulsation (Iliff, Wang, et al., 2013), and CSF production and turnover (Smets et al., 2023; Rasmussen et al., 2018). A study utilizing ultrafast MR encephalography indicated that glymphatic flow is governed by multiple mechanisms rather than a singular one, such as respiration and cardiac pulsation (Kiviniemi et al., 2016).

Several studies support the notion that arterial pulsatility plays a crucial role in glymphatic movement and direction. In a mouse study, for instance, cerebral arterial pulsatility decreased by 50% following unilateral ligation of the internal carotid artery. Conversely, the administration of dobutamine increased penetrating artery pulsatility by 60%. Iliff and colleagues also observed that carotid artery ligation reduced the rate of perivascular CSF-ISF exchange, while dobutamine increased the exchange rate (Iliff, Wang, et al., 2013). Additionally, in another study, even with an intact carotid artery, subarachnoid CSF influx into brain parenchyma was disrupted due to a blockage in the brachiocephalic artery (Rennels et al., 1985).

Moreover, decreased vascular pulsatility, resulting from smooth muscle cell loss in the vessel wall during ageing, leads to glymphatic flow impairment (Kress et al., 2014). This strengthens the suggestion that arterial pulsation is a primary driving force. The alterations in arterial wall conditions seen in cardiovascular diseases may establish a causal relationship between vascular diseases and protein accumulation disorders (Nedergaard & Goldman, 2020). Hypertension, for instance—a well-known risk factor for AD, linked with amyloid- β aggregation—

stiffens the arterial wall, reducing its elasticity and pulsatility, and consequently diminishing perivascular flow (Gentile et al., 2009; Carnevale et al., 2016; Mortensen et al., 2019; Mestre, Hablitz, et al., 2018).

In the human brain, three sources of pulsatility have the potential to affect glymphatic flow: respiration (~0.25 Hz), cardiac pulsation (~1 Hz), and very low-frequency pulsation (<0.1 Hz) (Kiviniemi et al., 2016). Respiratory-related pulsatile cycles represent an additional influential factor in the driving forces of glymphatic flow. The centripetal movement of venous fluid, intensified by the respiratory rhythm, has the potential to enlarge the venous space and propel glymphatic efflux (Kiviniemi et al., 2016).

The rate of CSF production is suggested to contribute to the driving force of glymphatic flow, as evidenced by the impairment of CSF clearance observed in rodents treated with acetazolamide, a CSF production inhibitor (Lundgaard et al., 2017; Plog et al., 2015; Rasmussen et al., 2018). This connection may provide insight into the association between glymphatic dysfunction and ageing, where CSF production is reduced. In humans, the CSF production rate is four times higher at night compared to during the day, aligning with the activation of glymphatic function during the night (Nilsson et al., 1992; Xie et al., 2013).

It has been demonstrated that CSF production decreases by 50% in AD patients compared to healthy age-matched individuals (Kant et al., 2018). This reduction could potentially explain the failure of the glymphatic system to clear harmful proteins from the brain in AD patients. In conclusion, evidence supports the crucial role of arterial pulsatility as the primary driving force for the glymphatic system. Although other mechanisms may contribute to the driving force to a lesser extent, unravelling their precise roles awaits further exploration in future studies.

1.7 Imaging the glymphatic system

1.7.1 Invasive imaging techniques

The first investigation into the glymphatic system employed two-photon laser scanning microscopy, a precise and effective technique for examining specific perivascular spaces. This technique is able to image tracer transport at the

microscopic scale, providing dynamic information about glymphatic transport. For instance, Iliff et al. in 2012 demonstrated that the CSF penetrates the brain parenchyma via the perivascular spaces surrounding the arteries, and that the clearance of the ISF takes place along the perivenous spaces, revealing the presence of glymphatic pathway and flow directionality (Iliff et al., 2012). However, this technique is highly invasive, it requires sectional removal of the animal's skull (Taoka & Naganawa, 2020). Moreover, it is unsuitable for conducting brain-wide studies, particularly in deep brain tissues.

Another imaging modality capable of dynamic real-time imaging of the whole brain is positron emission tomography (PET). PET involves the injection of radiolabelled tracers, which are biologically active molecules labelled with a radioactive atom e.g. ^{11}C , ^{18}F . When these nuclei decay, they emit positrons that interact with electrons in the body, resulting in the emission of two gamma rays in the opposite direction. A PET scanner detects these gamma rays and reconstructs an image of tracer concentration. PET imaging has been utilized to evaluate glymphatic clearance in humans (Schubert et al., 2019; De Leon et al., 2017). Leon and colleagues utilized two radiolabelled tracers, ^{11}C -PiB and ^{18}F -THK5117, known for their binding to AB plaques and tau, respectively. Their findings revealed that individuals with AD exhibited reduced brain clearance compared to healthy counterparts (De Leon et al., 2017). In another investigation by Schubert et al., using ^{11}C -PiB PET to assess CSF dynamics in various patient groups, it was evident that CSF clearance was significantly reduced in individuals with AD when compared to matched controls (Schubert et al., 2019). Nevertheless, PET scans are frequently avoided due to their reliance on ionizing radiation, which can present health risks, especially when long scans are necessary, commonly observed in glymphatic studies.

In contrast, MRI is capable of dynamic real-time imaging of the whole brain without the involvement of ionizing radiation. The glymphatic system can be visualised using intrathecal injection of gadolinium-based contrast agents (GBCA). Gadolinium (Gd) is a paramagnetic substance that shortens the T1 relaxation time of tissues, making them appear brighter on T1 weighted images. In 2013, Iliff and colleagues were the first to employ MRI for monitoring glymphatic function in

rodents. Their work demonstrated that dynamic contrast-enhanced MRI can effectively reveal the presence of glymphatic pathways (Iliff, Lee, et al., 2013).

The glymphatic system was also studied in humans. Eide and Ringstad used MRI scans to assess individuals who had received intrathecal injections of GBCA. After GBCA had been injected into the subarachnoid space, signal intensity in both the grey and white matter of the brain was elevated, suggesting that Gd had entered the human brain through the glymphatic system (Eide & Ringstad, 2015). Eight healthy volunteers underwent MRI after intrathecal administration of Gd through lumbar puncture to investigate glymphatic CSF dynamics. Heterogeneity in brain regions was observed, indicating variations in both speed and amount of tracer uptake throughout the brain. Notably, Gd first reached the CSF, followed by the brain ventricles, cortex, and finally the white matter. Compared to rodents, the glymphatic flow in humans was slower, with tracer detection in the basal cisterns occurring almost two hours post-injection. The peak enhancement of the tracer was faster in the CSF (1-3 hours) compared to the brain parenchyma, where tracer uptake was still rising at the end of the 11-hour imaging period (Dyke et al., 2020).

Nagasawa and colleagues examined the brains of 27 participants who had received intravenous (IV) -GBCA injections four hours earlier. In the post-contrast heavily T₂ Weighted MRI FLAIR image, both the perivascular space and subarachnoid space exhibited elevated signal intensity, indicating the transfer of GBCA to these areas via the glymphatic system (Naganawa et al., 2017). Developing this further, a subsequent study involved subjects aged between 17 and 69 years, who underwent MRI brain scans four hours after IV-GBCA injection. The detection of contrast leakage into the CSF from the cortical veins was exclusive to subjects above the age of 37, while those younger than 37 showed no observable leak. This finding highlights a correlation between Gd leakage into the perivascular CSF and age (Naganawa et al., 2019).

1.7.2 Non-invasive imaging techniques

Ethical considerations preclude the intrathecal injection of GBCA in the majority of human patients. This fact has spurred research into MRI methods that do not require the injection of GBCA. These methods, including but not limited to T1w

perivascular spaces (PVS) automated segmentation and T2w PVS visual rating, have unveiled potential impairments in the glymphatic system among individuals with AD (Steward et al., 2019; Kamagata et al., 2022; Joseph et al., 2020; Vilor-Tejedor et al., 2021) and Parkinson's disease (PD) (Donahue et al., 2021; Chung et al., 2021; Shen et al., 2021, 2022; Ramirez et al., 2022).

To assess AQP4 water channels, Ohene et al. employed multi-echo time (TE) arterial spin labeling (ASL) to investigate water permeability across the blood-brain interface (BBI) in mouse brains. The results revealed that AQP4 knockout mice exhibited a 31% higher exchange time compared to their wildtype counterparts (Ohene et al., 2019). This method could be a valuable approach for investigating the functionality of these channels.

Another non-invasive MRI technique employed to assess glymphatic flow is Diffusion-Weighted Imaging (DWI). In the brains of rats, an ultra-long echo time (TE), a small b value, and multi-directional DWI were utilized to evaluate CSF movement within perivascular spaces. The findings indicated a remarkable 300-fold acceleration of perivascular fluid during each heartbeat, underscoring the substantial influence of pulsation on glymphatic flow (Harrison et al., 2018).

Taoka et al. (2017) have introduced a novel approach that allowed the indirect assessment of glymphatic activity based on diffusion tensor imaging (DTI) (Taoka et al., 2017). It uses mathematical techniques to eliminate the impact of major white matter fibre diffusivity, in order to assess the minor diffusion component within the perivascular spaces' orientation. This DTI analysis "along the perivascular space" (DTI-ALPS) serves as an index of diffusivity measured along the perivascular space's direction, which is perpendicular to the dominant white matter fibres, Figure 1-2. Thus, indicating the extent of diffusion within the white matter adjacent to the lateral ventricle body (Taoka et al., 2017). This method has proved robust across various scanners, which indicates a high degree of reproducibility under a consistent imaging protocol (Taoka et al., 2022). Since the introduction of this method, it has been widely used in studies of neurological and metabolic disorders (Ma et al., 2021; Si et al., 2022; Yang et al., 2020; Andica et al., 2023).

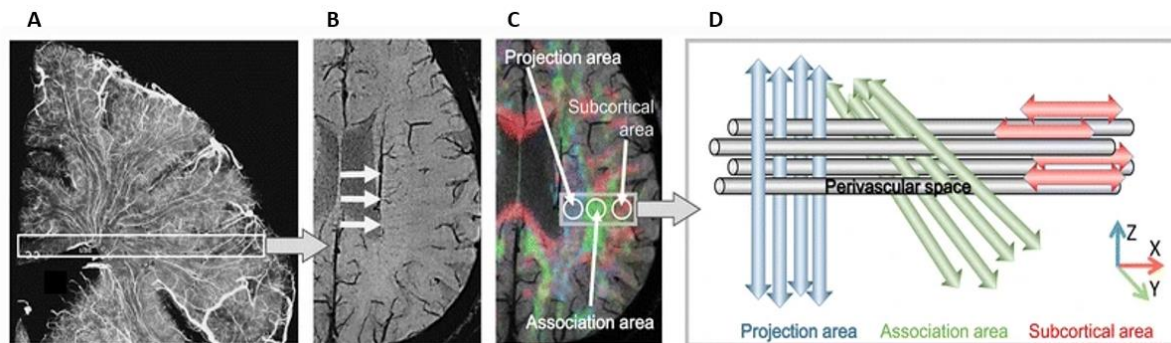


Figure 1-2: Diffusion-tensor imaging along the perivascular space.*

*The DTI-ALPS method involves the analysis of diffusion tensor images along the perivascular space. A, a radiograph, shows parenchymal vessels within a brain slice at the level of the lateral ventricle body. B, an axial susceptibility weighted imaging (SWI) indicates the lateral orientation of parenchymal vessels. C, combines DTI with SWI to show the distribution of different types of fibres and highlights three regions of interest for the measurement of diffusivity along three directions (x, y, z). D, schematically illustrates the relationship between perivascular space direction and fibre directions, with perivascular space perpendicular to both projection and association fibres. Adapted from a previous publication (Taoka et al., 2017) with permission granted by Dr. Toshiaki Taoka and the publishing journal.

1.8 Glymphatic system activation

Several years ago, the detrimental effects of acute sleep insufficiency on cognitive activities, such as memory deficit, attention, and learning, became widely recognized (Lim & Dinges, 2010). Prolonged sleep deprivation can have severe consequences and may even be fatal (Rechtschaffen et al., 1983; Shaw et al., 2002). Chronic sleep disturbance has emerged as a significant risk factor for the development of neurodegenerative diseases like AD (Moran et al., 2005). The revelation that the glymphatic system is primarily active during sleep sheds light on the longstanding mystery surrounding the function of sleep (Krueger et al., 2016; Reddy & van der Werf, 2020).

Lee et al. demonstrated that glymphatic function predominantly increases during the slow-wave period of sleep (Lee et al., 2015). Specifically, the third phase of non-rapid eye movement (NREM) sleep, associated with slow waves, exhibited higher brain clearance (Ju et al., 2017) and glymphatic flow (Hauglund et al., 2020). It has been proposed that the enhancement of glymphatic activity during sleep results from an increase in the volume of the interstitial space due to a reduction in noradrenergic tone. Sleeping resulted in a 60% increase in the volume

of interstitial space in mice. Conversely, during wakefulness, increasing the level of norepinephrine reduces the volume of the interstitial space, leading to a reduction in CSF influx and ISF solutes efflux (Xie et al., 2013).

Sleep induced by anaesthesia demonstrates a similar effect on glymphatic clearance as natural sleep. For instance, dexmedetomidine anaesthesia, an alpha₂ agonist, reduces norepinephrine release from the locus coeruleus, mimicking the deep sleep stage and enhancing slow-wave sleep (Purdon et al., 2015). In rats, this anaesthesia was tested and showed increased glymphatic function (Benveniste et al., 2017), and improved drug delivery to the brain via intrathecal injection (Lilius et al., 2019).

In a study conducted by Taoka et al., gadodiamide was intravenously injected into 24 rats eight times over a 2-week period, with variations in the time and duration of anaesthesia during contrast administration. Five weeks after the final administration, the animals were euthanized, and a quantitative assessment was conducted. The lowest contrast concentration was observed in rats that received gadodiamide in the morning under prolonged anaesthesia duration. This observation can be attributed to the nocturnal nature of rats, as their glymphatic systems are expected to be more active during the day (Taoka et al., 2018).

Another study investigated whether CSF in the SAS directly exits the cranial cavity or recirculates in the brain parenchyma via perivascular spaces. Fluorescence tracers were administered into the cisterna magna in three groups of mice: awake, and anesthetized with two different types of anaesthetics. The study demonstrated that in awake mice, the glymphatic perivascular CSF influx into brain parenchyma is diminished, and CSF in the SAS is drained immediately to the lymphatic system. However, both groups with anesthetized mice exhibited a larger amount of tracers in the perivascular spaces, indicating higher CSF influx (Ma et al., 2019).

Research conducted on mice indicated that the clearance of AB through the glymphatic system was twice as effective during sleep compared to the awake state (Xie et al., 2013). In contrast, sleep impairment causes an elevation of AB deposition in both animals (Kang et al., 2009) and humans (Branger et al., 2016).

Moreover, a study in humans revealed that interruptions during NREM sleep result in elevated levels of A β in CSF (Ju et al., 2017).

According to a PET study in humans, a single night of sleep deprivation is capable of increasing A β deposition in healthy individuals (Shokri-Kojori et al., 2018). In a recent study by Eide et al., where human brains were imaged using MRI after the intrathecal administration of gadobutrol to explore the impact of one night of sleep deprivation on brain clearance. The findings revealed that a single night of sleep disturbance resulted in impaired molecular clearance in various brain regions, including the white matter and cerebral cortex. Interestingly, normal sleep on the following night was unable to compensate for the impaired brain clearance the night before (Eide et al., 2021).

The perivascular space appears enlarged in neurological disorders like AD compared to healthy individuals (Ramirez et al., 2015). Interestingly, sleep deprivation is linked to the enlargement of perivascular spaces (Berezuk et al., 2015; Del Brutto et al., 2019). Opel et al., demonstrated an inverse correlation between the size of enlarged perivascular spaces and the number of sleeping hours (Opel et al., 2019).

Moreover, body posture during sleep influences glymphatic clearance (Lee et al., 2015; Reddy & van der Werf, 2020). Lee et al. (2015) reported that in rodents, sleeping in a lateral position, rather than in the supine or prone positions, promotes brain clearance. Their study employed multiple imaging modalities, including dynamic contrast-enhanced MRI (DCE-MRI) and A β labelled with both fluorescence and radioactive tracers. Among all sleeping postures, lateral posture was associated with reduced retention of neurotoxic solutes in the interstitial space and enhanced CSF influx (Lee et al., 2015). Indeed, there is a connection between sleep posture and neurodegenerative disorders (Simka et al., 2019; Levendowski et al., 2019). While healthy individuals prefer sleeping in a lateral (decubitus) position, individuals with neurodegenerative diseases tend to sleep on their back (supine) position (Levendowski et al., 2019).

1.9 Ongoing discussion regarding the glymphatic system

1.9.1 The important role of AQP4

The glymphatic system's dependency on AQP4 has been supported by various studies, where mis-localization or depletion of AQP4 leads to impairment in this system (Ilyff et al., 2012, 2014; Xie et al., 2013). Despite this, the glymphatic hypothesis, including the role of AQP4, remains a subject of debate (Smith & Verkman, 2019; Abbott et al., 2018; Hladky & Barrand, 2014; Smith & Verkman, 2018; Spector et al., 2015). For instance, a study conducted by Smith et al. found that AQP4 deletion did not impact the transport of tracers from the SAS to the brain (Smith et al., 2017).

However, a similar study by Ilyff et al. demonstrated that the delivery of fluorescent albumin injected into the cisterna magna was defective, and the clearance of ISF solute was markedly diminished in AQP4 knockout mice (Ilyff et al., 2012). Additionally, five independent research groups re-evaluated the importance of AQP4 in the glymphatic system. Their findings demonstrated that the CSF influx was greater in wild-type mice compared to four different *Aqp4* knockout lines, as well as a line lacking perivascular AQP4 localization (*Snta1* knockout) (Mestre, Hablitz, et al., 2018).

1.9.2 The flow direction

The concept that glymphatic flow clears ISF to peri-venous spaces has faced contradictions from different perspectives. For example, it has been suggested that ISF solutes are cleared to brain ventricles instead of peri-venous spaces (Bedussi et al., 2015). Others have proposed that ISF solutes are cleared to the Intramural Peri-Arterial Drainage (iPAD), indicating that brain solutes are drained along the arterial basement membrane, contrary to the direction of blood flow (Bakker et al., 2016; Carare et al., 2008; Albargothy et al., 2018).

Computational models have also challenged the notion that arterial pulsatility drives glymphatic flow (Asgari et al., 2016; Rey & Sarntinoranont, 2018). However, relying on mathematical models for accurate measurements is questionable. For example, these models used histological parameters for perivascular dimensions,

which can be affected by the collapse of the PVSs during fixation, thus compromising real flow estimations. In vivo studies have shown that PVSs are approximately ten times larger than computational model estimates (Mestre, Tithof, et al., 2018; Mestre, Mori, et al., 2020). This potentially explains why computational models concluded that arterial pulsation cannot drive bulk flow.

1.9.3 Bulk flow vs diffusion

The concept of glymphatic bulk flow has also been challenged, with suggestions that brain solute transport is dominated by diffusion (Asgari et al., 2016; Holter et al., 2017; Jin et al., 2016). For instance, Smith et al., demonstrated a molecular size dependence in brain solute transport, pointing towards a diffusive mechanism (Smith et al., 2017). It is essential to note that their crude method of tracer injection into brain parenchyma, involving glass pipettes, might induce traumatic brain injuries (TBI), and TBI have been reported to inhibit CSF influx (Iliff et al., 2014). Moreover, two paramagnetic contrast agents with different molecular weights, Gd-DTAP (938 Da) and GadoSpin (200 kDa), were intrathecally injected into separate groups of rats. Despite their size difference, they exhibited a similar rate of perivascular influx, providing support for the glymphatic bulk flow (Iliff, Lee, et al., 2013).

1.9.4 The validity of the glymphatic hypothesis

It is suggested that increased intracranial pressure (ICP) resulting from cisterna magna injection of the tracer leads to elevated CSF influx, implying that glymphatic influx is an artefact of tracer injection. However, it's crucial to note that the change in ICP during physiological activities such as sneezing or changing body posture (10-40 mmHg) surpasses that observed during tracer intracisternal injection (1-3 mmHg) (Mestre, Mori, et al., 2020). Evidence supports the idea that the introduction of tracers does not impact CSF flow. For instance, the average speed of CSF flow within the perivascular space remained consistent even with a nearly sixfold difference in the infusion rate (Mestre, Tithof, et al., 2018; Bedussi et al., 2018).

The observed glymphatic flow following cisterna magna injection has also been a subject of debate. It is argued that despite the infusion rate not causing negative

impacts on ICP, the bulk flow might be driven by the pressure generated during injection rather than arterial pulsation, considering the potential increase in overall CSF volume (Crocì et al., 2019; Keith Sharp et al., 2019; van Veluw et al., 2020; Vinje et al., 2020; Kedarasetti et al., 2020; Faghieh & Sharp, 2021; Smith & Verkman, 2018; Smith et al., 2017). However, this theory was tested using a new *in vivo* method, wherein tracer particles are infused into the cisterna magna utilizing a dual syringe protocol with equal volumes of fluid injected and withdrawn simultaneously. This approach showed no change in CSF volume, and no substantial rise in ICP. Particle tracking revealed fluid flow patterns similar to those observed in previous single-syringe injection experiments in every aspect (Raghunandan et al., 2021). Furthermore, the researchers demonstrated that the driving force behind glymphatic transport is arterial pulsation. This conclusion was supported by the finding that CSF flow in perivascular spaces of pial arteries strongly correlates with heart rate rather than respiration rate (Raghunandan et al., 2021).

1.9.5 Potential sources of variable results

The controversy surrounding the glymphatic hypothesis, including the role of AQP4, may be attributed to variabilities between studies. These variations include the use of different ages, anaesthetic substances, types of tracers, and routes of tracer injection (Mestre, Hablitz, et al., 2018; Hablitz et al., 2019). Moreover, properties of tracers beyond molecular weight, such as conformation, size, shape, and their physical and chemical behaviour, could also contribute to their glymphatic flow and exchange between CSF and ISF (Iliff, Lee, et al., 2013).

Based on a meta-analysis conducted to investigate variabilities in glymphatic studies in rodents, it was noted that the tracer injection rate and choice of anaesthetic materials are the main factors contributing to the heterogeneous findings. For instance, Avertin anaesthesia (tribromoethanol) was exclusively used by Smith's group, which holds an opposing opinion to the glymphatic hypothesis (Mestre, Hablitz, et al., 2018). The mechanism of action of Avertin remains unclear. In addition, its usage is prohibited in many countries in Europe, while in the US, it is allowed only for terminal procedures (Arras et al., 2001; Meyer & Fish, 2005). It is worth noting that many studies questioning the glymphatic theory

are not conducted in live animals but are instead based on computational modelling (Jin et al., 2016; Asgari et al., 2016; Faghieh & Sharp, 2018).

1.10 Glymphatic impairment in neurological disorders

The glymphatic system is responsible for maintaining brain health, and plays an important role in various neurological conditions. Ageing is a factor that significantly increases the risk of various neurological conditions; studies of both animals and humans have shown a strong connection between ageing and dysfunction of the glymphatic system and meningeal lymphatic vessels (Kress et al., 2014; Benveniste et al., 2019; Zhou et al., 2020). This connection may be attributed to age-related alterations in the cerebral vascular system (Balbi et al., 2015; Frost et al., 2016; Love & Miners, 2016; Sun et al., 2018). With increasing age, cerebral arteries become increasingly stiff, which leads to the retention of fluid in expanded perivascular spaces. This, in turn, can block perivascular pathways through the basement membrane, and impair functioning of the glymphatic system (Sun et al., 2018; Zhou et al., 2020). Furthermore, the amplitude of arterial pulsation tends to decrease with advancing age. Since arterial pulsations are significant drivers of the glymphatic system, this phenomenon may contribute to that system's disruption (Iliff, Wang, et al., 2013).

Ageing is accompanied by several structural changes that can impact the CNS and overall well-being. These changes include, but are not limited to, a decrease in CSF production, ventricular shrinkage, and brain atrophy. These alterations may contribute to glymphatic impairment and the accumulation of A β with ageing. Aged mice have demonstrated a significant deterioration in glymphatic function, up to 90% compared to their younger counterparts (Kaur et al., 2020). Furthermore, following intracisternal and intraventricular injection, aged mice exhibited a considerable delay in tracer delivery to the cervical lymphatic system and blood flow compared to the young group (Ma et al., 2017). In humans, enlarged perivascular spaces are emerging as a sign of glymphatic impairment. In cognitively normal aged individuals, Wang et al. utilized various MRI sequences, including T₂-weighted imaging to visualize enlarged perivascular spaces and T₂-fluid attenuated inversion recovery (FLAIR) imaging to assess white matter hyperintensities. Additionally, they employed PET with the radiotracers ¹⁸F-

flortaucipir and ^{18}F -florbetapir to investigate tau and A β deposition, respectively. They reported that enlarged perivascular spaces in the basal ganglia correlate with age and white matter hyperintensity, while those in the centrum semiovale correlate with tau accumulation in the brain (Wang et al., 2021).

1.10.1 Alzheimer's disease

AD is one of the most distressing neurodegenerative diseases. It is characterized by the deposition of A β , forming senile plaques, and the presence of abnormally hyperphosphorylated tau protein in the form of neurofibrillary tangles in the brain cortex. These pathological changes contribute to neuronal loss and neurovascular disorders, ultimately leading to neuronal cell death (Hardy & Selkoe, 2002; Zlokovic, 2011). Ageing is a major risk factor for developing AD, with the probability escalating even further in advanced age, particularly in individuals aged 75 and older (Association, 2018).

Glymphatic impairment is closely associated with AD, where it may contribute to an increase in the accumulation of A β (Xu et al., 2015) and tau (Holth et al., 2017, 2019; Harrison et al., 2020) proteins. Sleep disturbances accompanying AD pathology may exacerbate glymphatic deterioration through a feed forward process, because the glymphatic system is most active during sleep (i.e. a process involves a mutually reinforcing cycle where sleep disturbances and glymphatic system deterioration intensify each other, ultimately accelerating the progression of AD (Winer et al., 2019).

AQP4 knockout mice, crossbred with AD mice models (APP/PS1), exhibited higher accumulations of soluble and insoluble A β in brain parenchyma and blood vessels (cerebral amyloid angiopathy) compared to AD animal models expressing normal AQP4 (Xu et al., 2015). Loss of AQP4 perivascular polarisation was observed in AD patients but not in the normal group, indicating that AQP4 mislocalization could be an early marker of AD. The similarity in AQP4 dysfunction in AD between rodents and humans was confirmed in post-mortem AD patients, revealing altered AQP4 expression similar to what has been observed in mice (Zeppenfeld et al., 2017). Figure 1-3 illustrates the difference in glymphatic function between healthy brains and those affected by AD.

The normal structure of perivascular spaces, in healthy conditions, is thin, linear and difficult to visualise by MRI. However, in some pathologies perivascular spaces dilate and so become easy to detect (Brown et al., 2018). In AD for example, structural MRI scans may reveal dilated perivascular spaces indicating potential glymphatic dysfunction (Taoka & Naganawa, 2021; Kim et al., 2022). In their original paper, Taoka et al. used their new DTI-ALPS technique to evaluate the human glymphatic system in AD patients. By analysing diffusivity in specific brain regions, they calculated an ALPS index and correlated it with Mini-Mental State Examination (MMSE) scores. Results showed lower water diffusivity along perivascular spaces in more severe cases of AD, which suggests glymphatic system impairment (Taoka et al., 2017).

Human studies showed that the elimination of A β is reduced both with AD (Mawuenyega et al., 2010) and advancing age (Patterson et al., 2015). In both conditions, the rate of production of A β stays substantially the same. This indicates that an impairment in the A β clearing process may lead to the A β accumulation and pathology initiation. The clearance of interstitial A β is accomplished by different approaches. Local A β elimination via degradation and phagocytosis (Pomilio et al., 2016; Wyss-Coray et al., 2003; Ries & Sastre, 2016). A β also drains into the blood circulation across the BBB (Shibata et al., 2000). Further, A β cleared by the glymphatic system via the exchange between ISF and CSF along the perivascular spaces (Iliff et al., 2012; Xie et al., 2013). The relationship between A β accumulation and glymphatic impairment appears to be a reciprocal relationship. Not only does glymphatic dysfunction lead to A β deposition, but the injection of ^{125}I -A β_{1-40} into healthy mice CSF also leads to the impairment of glymphatic flow, suggesting that A β by itself may be responsible for glymphatic disruption (Peng et al., 2016).

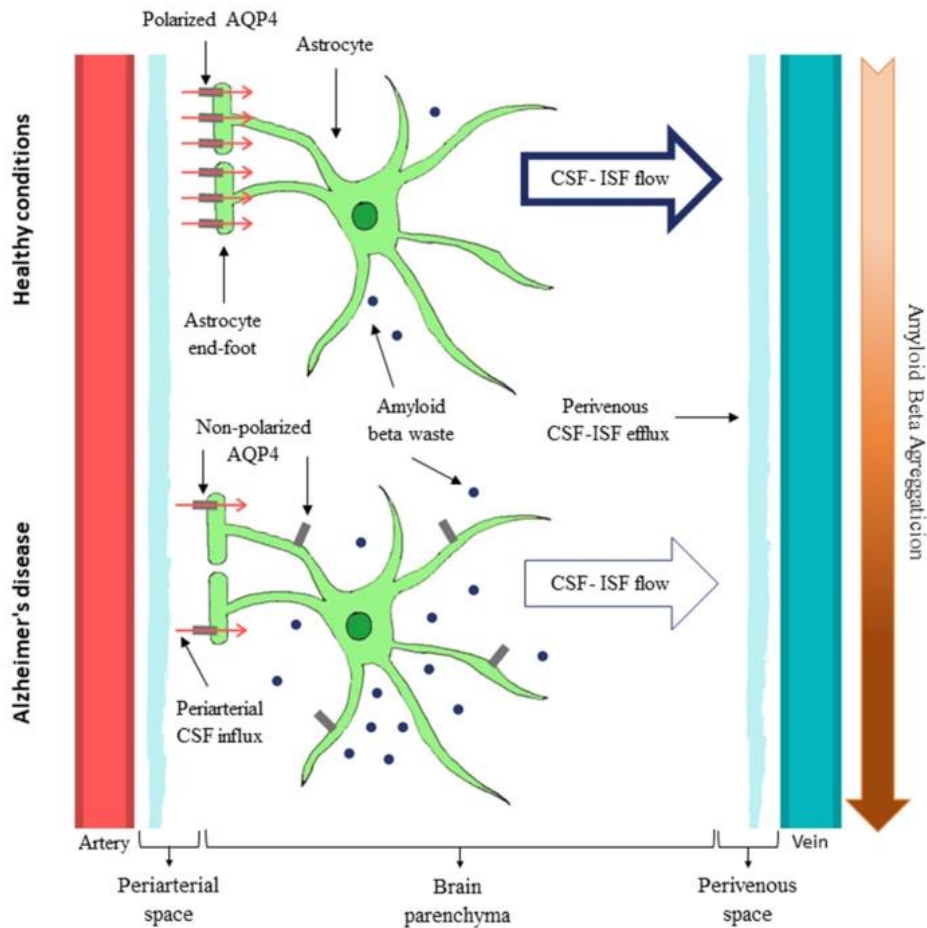


Figure 1-3: the difference in glymphatic system in healthy vs AD brain (Silva et al., 2021).

1.10.2 Parkinson's disease

It has been suggested that glymphatic system function might be impaired in PD, potentially as a result of the accumulation of alpha-synuclein protein and decline of dopaminergic neurons (Sundaram et al., 2019; Verghese et al., 2022). Both factors are associated with sleep disruption (Sundaram et al., 2019). Recent findings from neuroimaging research employing DTI-ALPS assessment indicate compromised glymphatic function in people with PD (McKnight et al., 2021; Si et al., 2022; Cai et al., 2023). A recent study by He et al. applied the DTI-ALPS approach and found glymphatic dysfunction to be associated with the severity of PD, autonomic function and motor symptoms. He and colleagues also found that the ALPS index served as a predictor for accelerated decline in both motor and cognitive functions (He et al., 2023). In a recent study involving Parkinson's mouse models, it has been shown that the pharmacological enhancement of slow-wave sleep for several months can lower α -synuclein deposition. Additionally, this

intervention increases the expression of AQP4 to perivascular spaces. These findings suggest a potential significant increase in glymphatic function, emphasizing its relevance in the context of PD (Morawska et al., 2021).

1.10.3 Age-related hearing loss disorder

The literature has shown that age-related hearing loss disorder is often associated with cognitive decline and an elevated risk of dementia (Ford et al., 2018; Loughrey et al., 2018). Xu et al. sought to assess the performance of the glymphatic system in individuals with age-related hearing loss disorder, also known as presbycusis, compared with a group of healthy individuals. This assessment was carried out using the DTI-ALPS technique. Results indicated that presbycusis patients who also had cognitive impairment were significantly more likely to display compromised glymphatic activity than presbycusis patients without cognitive impairment, and healthy controls. Moreover, there was a notable correlation between age-related-hearing-impaired individuals' glymphatic system dysfunction and their scores on the Montreal Cognitive Assessment (MoCA). This suggests that the DTI-ALPS index could be a valuable tool for tracking disease progression or evaluating treatment outcomes in presbycusis patients, by serving as an indicator of changes in glymphatic activity (Xu et al., 2023).

1.10.4 Idiopathic normal pressure hydrocephalus

Scholars have also examined the glymphatic impairment in patients with idiopathic normal pressure hydrocephalus (iNPH). The use, in MRI, of intrathecal injection of a GBCA as a CSF tracer, accompanied by multiple MRI examinations spanning a 24-hour period, revealed indications of delayed glymphatic clearance in individuals with iNPH when contrasted with healthy controls (Ringstad et al., 2017). The enhancement of glymphatic activity reached its highest point during the night, and this was attributed to the activation of glymphatic function during sleep (Ringstad et al., 2017). Another study by Ringstad et al. has used repeated MRI scanning to assess glymphatic system activity in individuals with iNPH dementia, revealing brain-wide distribution of a CSF tracer introduced via intrathecal administration. In the iNPH dementia group, clearance of the tracer

substance was observed to be slower compared to healthy individuals, possibly due to compromised glymphatic transport (Ringstad et al., 2018).

Due to the invasiveness associated with the intrathecal injection of MRI contrast agents in earlier research, several studies have used MRI without contrast agent injections to assess glymphatic function in iNPH (Yokota et al., 2019; Bae et al., 2021; Georgiopoulos et al., 2023). For example, Georgiopoulos et al. conducted DTI-MRI in patients with iNPH, who showed significantly reduced ALPS index scores compared with healthy counterparts. Notably, a sex-related discrepancy was detected among healthy controls, with females displaying higher ALPS index scores than males, yet this particular variation was not evident within the iNPH patient group. Moreover, there existed a moderate correlation between the ALPS index and measures of motor function, while a positive correlation was established with MMSE scores. These findings collectively indicate that the ALPS index holds promise as a tool for the evaluation of iNPH severity (Georgiopoulos et al., 2023).

1.10.5 Neuromyelitis optica spectrum disorder

Research evidence has indicated a connection between the glymphatic system and autoimmune demyelinating diseases when individuals with neuromyelitis optica spectrum disorder (NMOSD) tested positive for antibodies targeting AQP4 (Pittock & Lucchinetti, 2016). Thus, it is reasonable to infer that inhibition of the AQP4 channel by its antibodies generates impairment of the glymphatic system, which would significantly contribute to development of the characteristic inflammatory lesions seen in the pathophysiology of NMOSD. Cacciaguerra et al. found dilation of PVSs in the centrum semiovale to be more pronounced, and the DTI-ALPS index was lower, in individuals with NMOSD compared to healthy subjects. Furthermore, this enlargement showed correlation with both reduced cognitive function and brain atrophy. Cacciaguerra et al. proposed that the observed perivascular space impairments in NMOSD may be associated with compromised glymphatic system function (Cacciaguerra et al., 2022).

1.10.6 Amyotrophic lateral sclerosis

A retrospective study by Liu et al. investigated glymphatic function in early-stage amyotrophic lateral sclerosis (ALS) patients using the ALPS-DTI index (Liu et al., 2023). Their findings revealed that early-stage ALS patients had substantially lower ALPS index values than healthy controls. These researchers also found correlations between the ALPS index, sleep disturbances and clinical disability in early-stage ALS patients. Also, periodic limb movements and sleep efficiency were predictive factors for the ALPS index. Liu and colleagues' research supports the hypothesis that glymphatic dysfunction plays a role in ALS, where it correlates with sleep disturbances, and suggests it has promise as an early diagnostic marker for ALS. Furthermore, it may be that enhancing glymphatic function early in the disease progression could slow down neurodegeneration in ALS (Liu et al., 2023). Further research into glymphatic dysfunction in pre-symptomatic neurodegenerative diseases, would be helpful.

1.10.7 Multiple sclerosis

There is significant research interest in understanding the intricate relationship between CSF dynamics, glymphatic function, and the pathogenesis of MS, and scholars have suggested that change in the flow of CSF within brain tissue may be a factor in the development of MS (Fournier et al., 2018). Using high-resolution MRI scans of the spinal cord in mice, Fournier et al. identified parenchymal CSF circulation within the spinal cord. In a model of MS known as experimental autoimmune encephalomyelitis, they observed a reduction in the parenchymal CSF circulation within the spinal cord (Fournier et al., 2018).

The human study aligns with the previously mentioned animal study. Here, Schubert et al. used dynamic ^{11}C -PiB PET to identify changes in CSF clearance, it was observed that CSF clearance in the lateral ventricle was substantially reduced among MS patients, compared to the healthy group. These findings suggest the presence of pathological alterations in CSF dynamics and glymphatic impairment (Schubert et al., 2019).

Carotenuto et al. recently conducted a retrospective study, to explore the role of the glymphatic system in clinical disability, disease progression, demyelination,

and neurodegeneration in individuals with MS. Their study included MS patients (relapsing-remitting RRMS and progressive MS) and age- and sex-matched healthy controls. All participants underwent neurological and MRI exams. Several measurements were made, including DTI-ALPS index, a proxy for glymphatic function. Findings were that MS patients generally had impaired glymphatic function compared to healthy controls, with more pronounced impairment in progressive MS than are found in RRMS. This glymphatic dysfunction was associated with greater disability, demyelination and neurodegeneration, which indicates its importance in the MS disease process (Carotenuto et al., 2022).

Additional analysis revealed an inverse relationship between the ALPS index and duration of the disease during the initial 4-year period of MS with no significant correlation afterwards (Carotenuto et al., 2022). These findings suggest that dysfunction in the glymphatic system could potentially cause the build-up of neuroinflammatory and neurotoxic substances, leading to the progressive loss of myelin and neurons. Figure 1-4 illustrates the proposed pathological alteration in the glymphatic system in MS in comparison to a healthy glymphatic system.

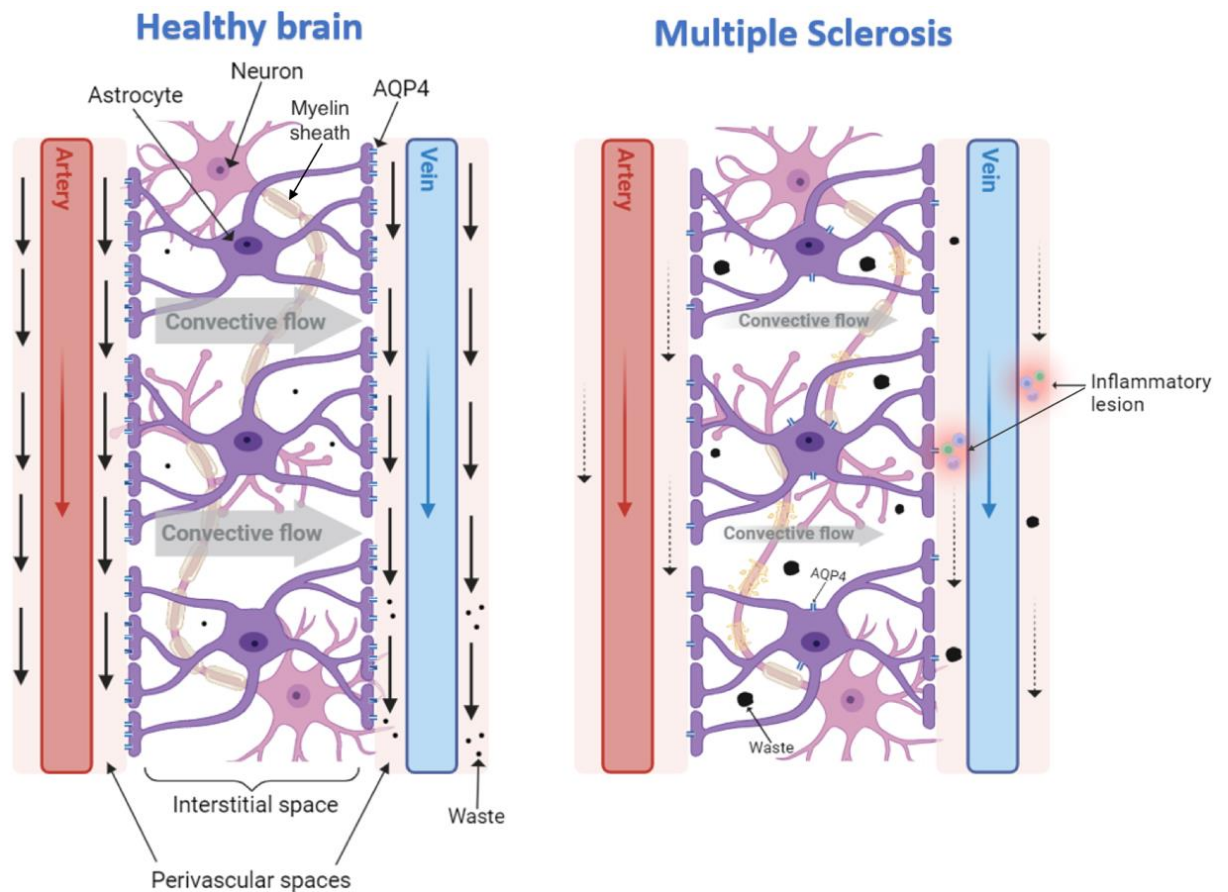


Figure 1-4: Left: Healthy brain, with normal glymphatic influx (peri-arterial) and efflux (perivenous). AQP4 is highly expressed at astrocytic end-feet with normal convective flow of interstitial fluid and intact myelin sheath. Right: Proposed changes in multiple sclerosis with reduced glymphatic influx (peri-arterial) and efflux (perivenous). AQP4 is depolarized away from the astrocytic end feet with lower convective flow of interstitial fluid, lower brain clearance and demyelinated sheath (Alghanimy et al., 2024).

1.10.8 Vascular cognitive impairment

Vascular Cognitive Impairment (VCI) is a neurological disorder with a spectrum of severity, spanning from mild cognitive impairment to vascular dementia (Gorelick et al., 2011), which is widely recognized as the second most common form of dementia, following AD (T O'Brien & Thomas, 2015). VCI develops as a consequence of cerebrovascular diseases. Glymphatic function was non-invasively evaluated in humans with VCI. In VCI patients, the ALPS-index was lower than in normal individuals, indicating impaired glymphatic function (Song et al., 2022).

Chronic Cerebral Hypoperfusion (CCH) emerges as a key underlying pathology in VCI, often arising from carotid stenosis (T O'Brien & Thomas, 2015). CCH may instigate various neuropathologies, including white matter inflammation,

demyelination, and increased cerebral amyloid deposition (Dichgans & Leys, 2017).

CCH may lead to glymphatic impairment, given that the primary driving force of glymphatic flow is cerebral arterial pulsation (Iliff, Wang, et al., 2013). This suggestion gained support when mouse models with CCH, induced by bilateral common carotid artery stenosis (BCAS), demonstrated both glymphatic and cognitive impairment. Interestingly, pharmacological enhancement of blood circulation resulted in an improvement in both glymphatic function and cognition (Cao et al., 2022).

To the best of our knowledge, no studies have investigated the effect of BCAS on glymphatic function using dynamic contrast-enhanced MRI (DCE-MRI). Therefore, in the final experiment of this thesis, we aim to address this gap and examine whether the novel AQP4 facilitator has the potential to rescue both glymphatic and AQP4 functions.

1.11 Preserving glymphatic vitality

The glymphatic system is integral for optimal brain function and cognition, as it plays a crucial role in removing brain solutes and harmful proteins (Plog & Nedergaard, 2018). Given its significance, the incorporation of certain healthy lifestyle practices can positively influence glymphatic flow, contributing to overall brain health. This section will discuss briefly specific healthy lifestyle practices that might support glymphatic function, promote cognitive well-being, and potentially mitigate the risk of neurodegenerative conditions.

Dietary habits exert a significant impact on health, with the capacity to markedly increase or diminish the likelihood of developing various diseases (Kylkilahti et al., 2021). While the Mediterranean diet has been shown to reduce the incidence of AD (Scarmeas et al., 2009; Bianchi et al., 2021), diets high in fat and carbohydrates have demonstrated the opposite effect (Samadi et al., 2019). Incorporating 5-Caffeoylquinic Acid (5-CQA) into the diet of AD mouse models demonstrated promising results by inhibiting A β levels. The intervention also increased the perivascular polarisation of AQP4, accompanied by memory

improvements. These findings suggest that 5-CQA supports glymphatic function (Ishida et al., 2020).

Omega-3 polyunsaturated fatty acid has demonstrated neuroprotective effects in preventing neurodegenerative diseases, and the use of Omega-3 as a dietary supplement is linked to a decreased risk of developing AD (Calon & Cole, 2007). Mice received fish oil, rich in omega-3, showed preserved perivascular polarisation of AQP4, lower A β deposition, and overall higher glymphatic clearance (Ren et al., 2017; Zhang et al., 2020). Moreover, in humans, the consumption of omega-3-rich fish meat has been linked to a decreased incidence of dementia (Kalmijn et al., 1997; Barberger-Gateau et al., 2007; Morris et al., 2005).

Exercise has a positive impact on CNS health (Andel et al., 2008; Stuckenschneider et al., 2018) and glymphatic function (He et al., 2017; von Holstein-Rathlou et al., 2018; Yin et al., 2018). In mice, physical activity demonstrated beneficial effects on brain clearance, with higher CSF flux to the deep cervical lymph nodes observed in the group engaged in running exercise compared to the control group (He et al., 2017; von Holstein-Rathlou et al., 2018). Additionally, exercise improved cognitive function, decreased A β levels and increased AQP4 polarisation (He et al., 2017). In another study, AD mouse models aged 3 months underwent a two-month period of voluntary wheel exercise. The results indicated that mice subjected to exercise exhibited lower A β burden, AQP4 depolarisation, and memory deficits compared to their counterparts of the same age that did not undergo the exercise (Liu et al., 2022).

As mentioned earlier, the glymphatic system activates during sleep. Therefore, it is logical to assume that maintaining a healthy sleep pattern will contribute to the protection and optimal function of the glymphatic system. A five-year longitudinal study conducted in the United States, involving a cohort aged 65 years and older, examined the relationship between sleep disruption and dementia. The findings revealed that both sleeping less than 5 hours and experiencing a sleep latency (time taken to fall asleep) of more than 30 minutes increase the risk of developing dementia (Robbins et al., 2021).

1.12 Thesis aim

Targeting AQP4 pharmacologically is a promising approach for treating several neurological diseases (Verkman et al., 2014, 2017; Tang & Yang, 2016; Tradtrantip et al., 2017). In 2009, Huber et al. developed TGN-020, an AQP4 inhibitor (Huber et al., 2009). The effectiveness of the drug was demonstrated in murine models of ischemic stroke. The study highlighted significant reductions in cerebral oedema (from 21% to 12%) and cortical infarction (from 30% to 20%) compared to the control group (Igarashi et al., 2011). Expanding on their work, Huber et al. introduced TGN-073, a novel AQP4 facilitator, in 2018. This facilitator displayed enhanced fluid turnover and improved ISF clearance around the BBB in the brains of mice (Huber, Igarashi, et al., 2018). In the course of this thesis, AQP4 modulators will be further investigated in rat models, with a particular focus on the novel AQP4 facilitator, TGN-073. The effect of this drug will be explored in both normal and diseased rat brains. The primary objectives of the thesis are as follows:

- Chapter 2. As MRI is the primary imaging modality employed in this thesis, this chapter provides a detailed exploration of the underlying principles and physics of the technique. It outlines the process by which images are generated, as well as the key components and electronics essential for the MRI machine's operation. The chapter concludes with the construction of the MRI volume (birdcage) coil.
- Chapter 3. This chapter outlines the methodology followed throughout this thesis, detailing the general procedures used in live animal experiments, including the sourcing of animals, animal surgeries, drug preparation, and the standard imaging processing.
- Chapter 4. Both quantitative and qualitative MRI techniques will be employed in live rats in this thesis; thus, signal stability is of paramount importance. This chapter explores several enhancements made to the MRI scanner to improve its stability.
- Chapter 5. The initial plan was to investigate the dynamics of glymphatic flow using H_2^{17}O as a CSF tracer. In this chapter, several improvements were implemented to enhance the signal from the Oxygen-17 tracer, building upon a previously established MRI technique. The chapter

concluded that Oxygen-17 was insufficient to induce a significant reduction in the ^1H signal on T_2 -weighted imaging. As a result, the decision was made to proceed with the standard MRI contrast agent, gadolinium-DTPA.

Chapter 6. Glymphatic dysfunction resulting from pharmacological or genetic impairment of AQP4 has been investigated. However, to the best of our knowledge, no studies have assessed the enhancement of glymphatic function through pharmacological facilitation of AQP4. This chapter seeks to address this gap in the literature by investigating the impact of the novel AQP4 facilitator, TGN-073, on glymphatic transport, employing DCE-MRI and diffusion MRI.

Chapter 7. Complementing MRI with histological analysis is beneficial for advancing our understanding of AQP4's role in the glymphatic system. This chapter details the optimization of AQP4 immunofluorescent staining, a technique newly established in our department.

Chapter 8. In furthering the investigation, a non-invasive assessment of the impact of both AQP4 modulators, TGN-020 and TGN-073, was conducted without the necessity of exogenous contrast agents. This evaluation utilized a state-of-the-art MRI sequence: stimulated echo diffusion-weighted echo planar imaging (STE-DW-EPI).

Chapter 9. To advance our understanding of the positive impact of the AQP4 facilitator on glymphatic function, the impact of TGN-073 was explored in VCI rat models, specifically focusing on BCAS models, a well-established model known for inducing chronic cerebral hypoperfusion and vascular dementia. To our knowledge, this experiment represents the first investigation of the impact of BCAS on glymphatic function using DCE-MRI, as well as the effect of AQP4 facilitation on glymphatic function in these models.

Chapter 10. The thesis concludes with a general discussion that includes a summary of the findings, the limitations encountered during the execution of the experiments, and suggestions for future work.

Chapter 2 Magnetic Resonance Imaging

Studying the glymphatic system using an optimal imaging technique holds promise for improving disease outcomes and developing innovative therapeutic approaches. Examining brain-wide glymphatic function in vivo is primarily possible using techniques like MRI, which enables deep tissue imaging across extensive regions of the brain (Kudo et al., 2018). In contrast, other techniques, such as two-photon microscopy, are limited to imaging only superficial structures, typically within a depth range of 1 to 1.5 mm (Cahalan & Parker, 2005; Iliff et al., 2012). MRI stands out as a leading imaging technique, primarily due to its numerous advantages, particularly its lack of ionizing radiation, making it safe for longitudinal or repetitive studies. MRI offers superior temporal and spatial resolution of brain-wide glymphatic pathways (Iliff, Lee, et al., 2013), providing diverse contrast images with the flexibility to utilize either endogenous or exogenous contrast for specific functional characterizations (Lee et al., 2015).

This chapter aims to comprehensively explore the theoretical foundations of MRI, ranging from the fundamental principles of nuclear magnetic resonance to MR image formation. Emphasis will be placed on imaging sequences and techniques relevant to the context of this thesis. The content draws from these sources (McRobbie et al., 2017; Levitt, 2013; Callaghan, 1993; Cercignani et al., 2018). Any information derived from alternative sources will be clearly stated. The chapter will conclude with a hands-on mini experiment. This practical exercise involves crafting an essential MRI component: a handmade birdcage coil, providing a tangible link between the theoretical knowledge presented and its real-world application.

2.1 Spin angular momentum

Spin angular momentum, commonly referred to as spin, is a fundamental characteristic inherent in elementary particles, such as electrons, protons, and neutrons. In contrast to classical angular momentum associated with the orbital motion of macroscopic objects, spin is an intrinsic form of angular momentum. It is a quantum mechanical property that contributes to the total angular momentum of a particle. Despite its name, spin doesn't imply actual rotation; rather, it is a quantum property with profound implications for the behaviour of particles in the microscopic world. The concept of spin contributes significantly to the magnetic properties of particles. The spin of an atomic nuclei is characterized by its quantization, meaning it can only take discrete values, typically in multiples of $\hbar/2$, where \hbar is the reduced Planck's constant. This can be explained by the following:

$$L = \hbar \sqrt{I(I + 1)} \quad 2-1$$

$$\hbar = \frac{h}{2\pi} \quad 2-2$$

$$h = 6.63 \times 10^{-34} \text{ m}^2 \text{ kg s}^{-1} \quad 2-3$$

where L is Spin Angular Momentum Magnitude, I is nuclear spin quantum number, and h is Planck's constant. The spin quantum number (I) for hydrogen nuclei (^1H), given its single proton, is $1/2$. The nuclear magnetic quantum number m_I is calculated as follows:

$$m_I = -I, -I + 1, -I + 2, \dots \quad 2-4$$

The number of energy levels equals $2I+1$. For ^1H , the number of energy levels is 2 spin states, with $m_I = -\frac{1}{2}, \frac{1}{2}$.

The angular momentum component along z-axis:

$$I_z = m_I \hbar \quad 2-5$$

2.2 Nuclear magnetic moment

A magnetic moment refers to the nucleus's ability to interact with an external magnetic field. It is a vector quantity, representing both the strength and direction of the object's magnetic properties. Similar to all charged particles, when the nucleus undergoes rotational motion, it generates a magnetic field. The relationship between the nuclear magnetic moment (μ) and the nuclear spin angular momentum is expressed through the gyromagnetic ratio (γ), a constant specific to each nucleus. For instance, γ for ^1H is 42.58 MHz T^{-1} . The nuclear magnetic moment is calculated as follows:

$$\mu = \gamma I_z = \gamma m_I \hbar \quad 2-6$$

While overall magnetization of the sample, represented as M , equals:

$$M = \sum_i \mu_i \quad 2-7$$

The nucleus initially exists in a degenerate nuclear ground state. However, when subjected to an external static magnetic field (B_0) along the z-direction, it undergoes splitting into distinct nuclear energy levels (m_I). The energy associated with each specific level (i.e. Zeeman effect) can be expressed as.

$$E = -\mu B_0 \quad 2-8$$

$$E = -\gamma m_I \hbar B_0 \quad 2-9$$

Where E is the energy. The extent of the splitting is dependent on the strength of the magnetic field. Spins that align with the magnetic field exhibit lower energy levels, whereas those aligning against the field experience higher energy levels, as illustrated in the figure below.

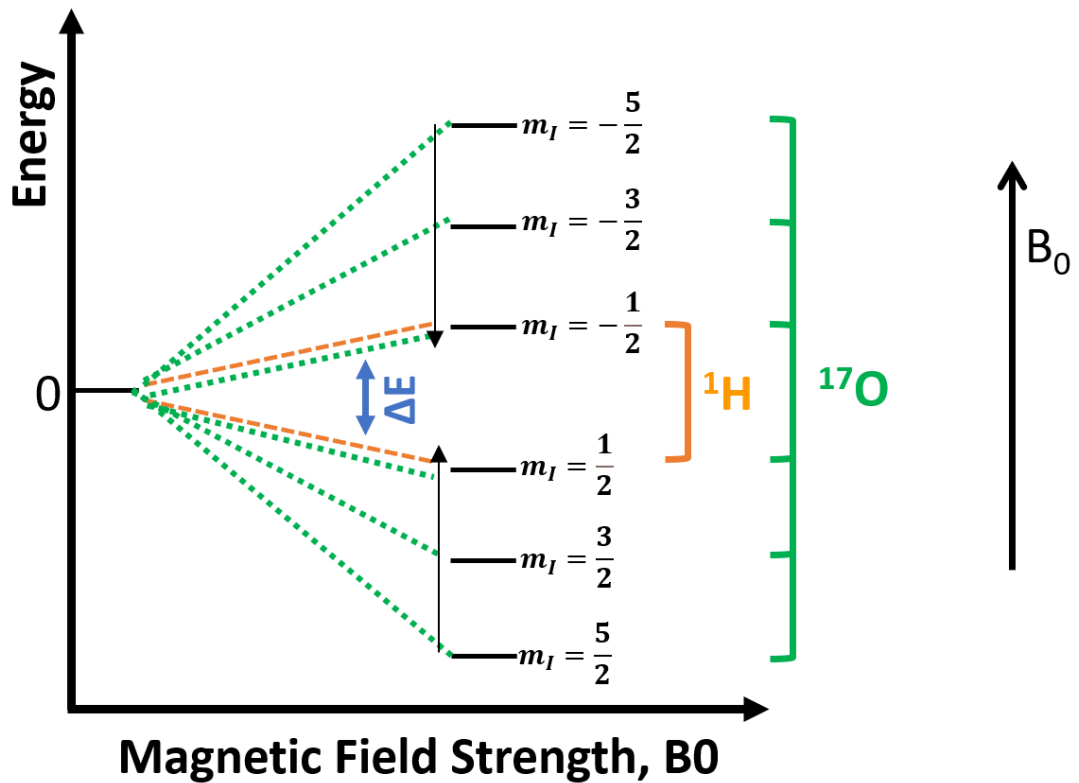


Figure 2-1: The splitting of the energy level into different states, also known as Zeeman Splitting. For hydrogen, $l=1/2$ (Orange dashed lines), and for Oxygen-17, $l=5/2$ (Green dashed lines).

The energy difference between the two states can be calculated as follows:

$$\Delta E = E_{(-\frac{1}{2})} - E_{(\frac{1}{2})} \quad 2-10$$

$$\Delta E = \left[-\left(-\frac{1}{2}\right)\gamma\hbar B_0 \right] - \left[-\left(\frac{1}{2}\right)\gamma\hbar B_0 \right] \quad 2-11$$

$$\therefore \Delta E = \gamma\hbar B_0 \quad 2-12$$

While Planck's equation is expressed as:

$$\Delta E = h f \quad 2-13$$

Where f is the frequency.

With the reduced Planck's constant, Planck's equation can be expressed as:

$$\Delta E = \hbar \omega_0 \quad 2-14$$

Where ω_0 is the angular frequency, related to f by $\omega = 2\pi f$

The Larmor equation can be derived by combining these two equations: 2-12 and 2-14,

$$\hbar \omega_0 = \gamma \hbar B_0 \quad 2-15$$

$$\therefore \omega_0 = \gamma B_0 \quad 2-16$$

Thus, the strength of the static magnetic field is directly proportional to the Larmor frequency of the spins. From equation 2-16, the Larmor precession frequency ω_0 of a hydrogen nucleus placed in an external magnetic field B_0 with a strength of 7 Tesla (the typical strength used in our experiments) is approximately 300 MHz, Figure 2-2.

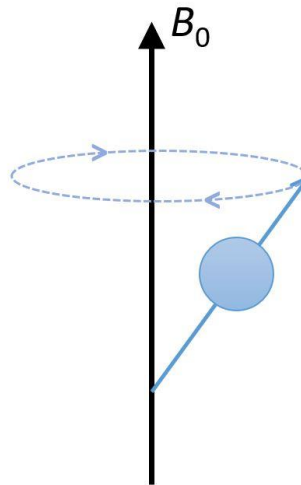


Figure 2-2: The precession frequency of a hydrogen nucleus about B_0 .

The energy difference between the two spin states is relatively small. The distribution of spins in each state is given by the Boltzmann distribution. The population of nuclei in the spin-up state (N_{\uparrow}) with the lower energy level, exceeds that of spins in the higher energy state (N_{\downarrow}). Thus, the net magnetization $M = (N_{\uparrow} - N_{\downarrow}) \mu$, represented by the bold blue arrow in Figure 2-3.

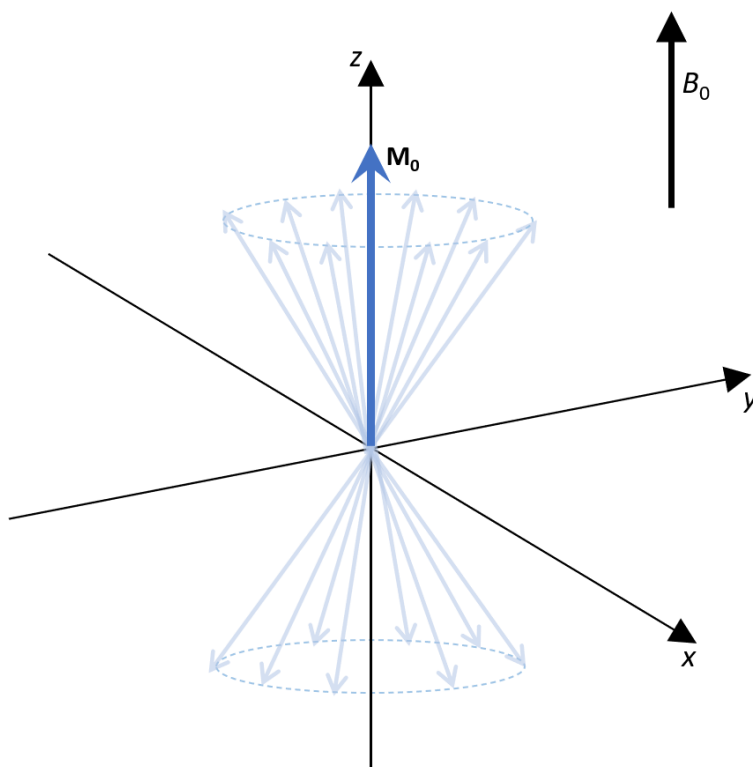


Figure 2-3: The overall net magnetization, denoted as M_0 .

The relationship between temperature and the corresponding energy is described by the Boltzmann equation, as illustrated below:

$$\frac{N_{\uparrow}}{N_{\downarrow}} = e^{\frac{-\Delta E}{K_B T}} \quad \text{2-17}$$

Where K_B is the Boltzmann constant ($1.3805 \times 10^{-23} \text{ J K}^{-1}$) and T is the temperature in Kelvin.

At thermal equilibrium, the net magnetization is expressed by the Curie law of temperature-dependent paramagnetism:

$$M_0 = \frac{N(\gamma \hbar)^2 B_0}{4K_B T} \quad \text{2-18}$$

Where N is the total number of spins, i.e. proton density in the sample.

2.3 Radiofrequency pulses

Radiofrequency (RF) radiation, a type of electromagnetic radiation, is characterized by its long wavelengths within the electromagnetic spectrum (Figure 2-4, highlighted in red). Classified as non-ionizing radiation, RF is generally considered safe. The crucial distinction from ionizing radiation lies in the low energy of RF photons, which lacks the strength or energy to strip tightly bound electrons from atoms, avoiding any ionization process. It's important to recognize that the potential for harm tends to increase with shorter wavelengths, as they bring in more energetic radiation.

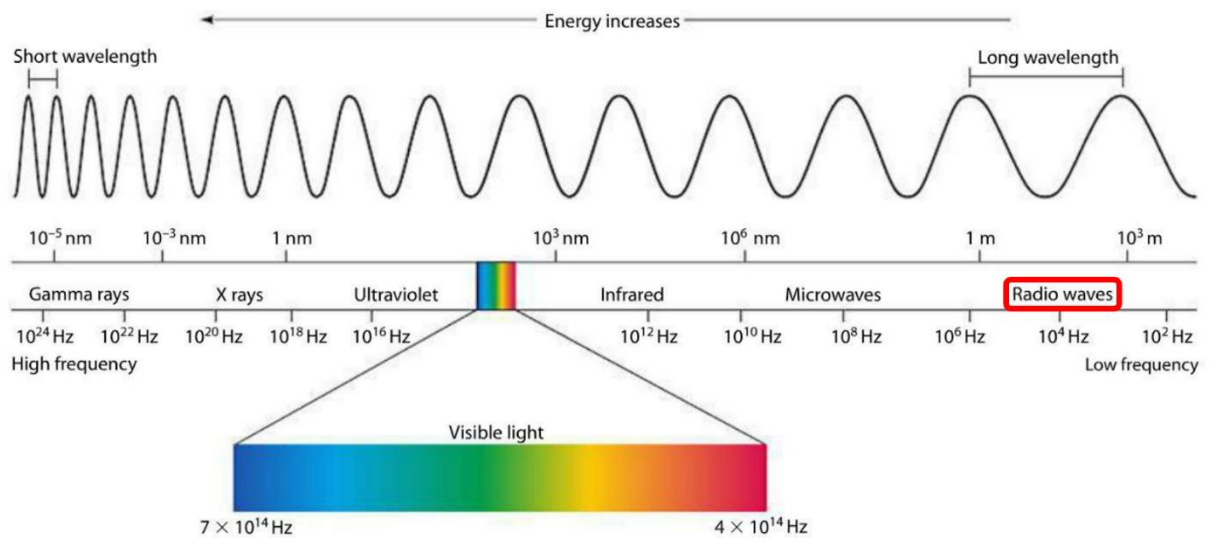


Figure 2-4: The Electromagnetic Spectrum from https://www.miniphysics.com/electromagnetic-spectrum_25.html

When ^1H nuclei are subjected to a static magnetic field, B_0 , they undergo precession about the B_0 direction. The introduction of an oscillating magnetic field, denoted as B_1 , perpendicular to B_0 , results in the additional precession of nuclear magnetic moments about the B_1 direction. This brief oscillating field, referred to as an RF pulse, is a crucial component in MR imaging processes. Following the cessation of the RF pulse, the net magnetization, M , gradually returns to its equilibrium state. The frequency of the oscillating magnetic field, B_1 , represented as ω_1 , governs the precession of the net magnetization around the B_1 field. The relationship:

$$\omega_1 = \gamma B_1 \quad \mathbf{2-19}$$

Indicates that the B_1 field can apply a constant directional torque when its frequency (ω_1) closely aligns with the precession frequency (ω_0) associated with the external magnetic field, B_0 , i.e. $\omega_1 = \omega_0$.

The flip angle, α , refers to the angle by which the net magnetisation is tipped away from equilibrium by an RF pulse. The magnitude of the flip angle is directly influenced by both the strength and duration of the applied RF pulse as follows:

$$\alpha = \omega_1 t_p = \gamma B_1 t_p \quad \mathbf{2-20}$$

Where t_p is the pulse duration. The flip angle is a crucial parameter in MRI as it influences the amount of signal that is generated during the imaging process. α can have any value, the two common flip angles are the 90-degree and 180-degree. A 90-degree flip angle is often used for excitation, causing the magnetic moments to rotate perpendicular to the static magnetic field, while a 180-degree flip angle is employed for inversion recovery sequences. The choice of flip angle affects the contrast and quality of the MR image.

To understand the influence of an RF pulse on the net magnetization, a useful approach is to adopt a rotating frame of reference. While the net magnetization may precess at a high frequency, such as 300 MHz (in our system) within the laboratory frame of reference, the observation from this stationary standpoint results in a complex motion, Figure 2-5. However, introducing the concept of a rotating frame and undergoing a coordinate transformation from the laboratory frame (x, y, z) to a reference frame (x', y', z') that is rotating at the B_1 frequency provides a more insightful perspective, Figure 2-6. This transformation effectively renders the net magnetization stationary, eliminating the effect of the B_0 field.

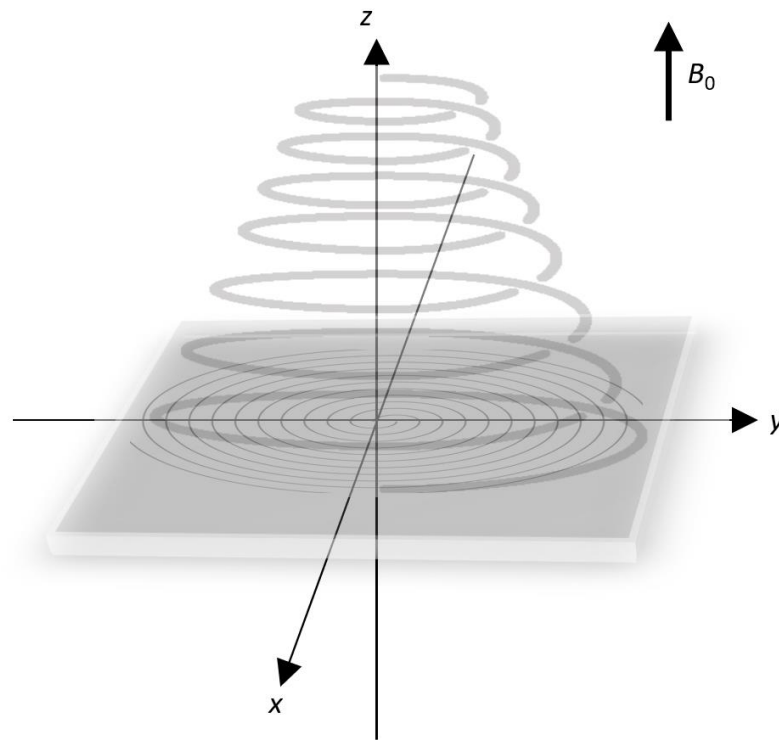


Figure 2-5: The view of M_0 (grey downward spiral) during the application of an RF pulse is referred to as the laboratory frame of reference.

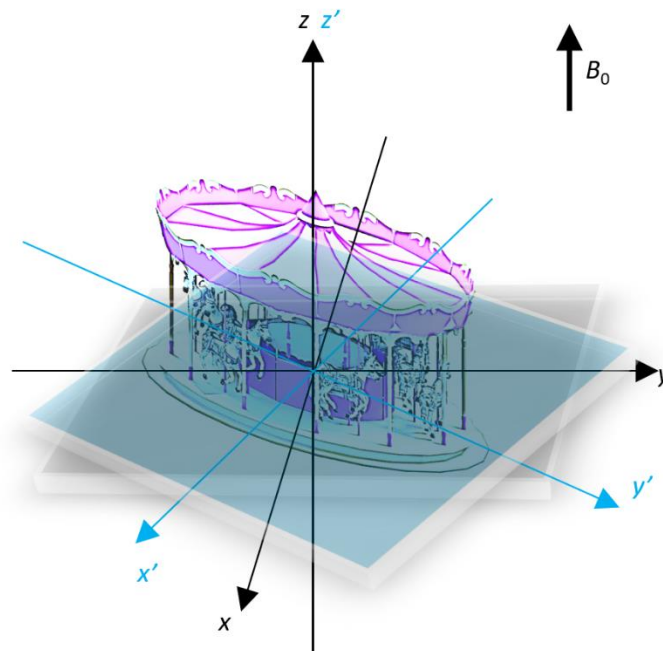


Figure 2-6: The new coordinate system (x' , y' , z') corresponds to the rotating frame of reference, creating an analogy to standing on a rotating carousel. Despite the continuous rotation at the Larmor frequency, the view from the carousel perspective gives a sense of stability to the rotating frame. This perspective facilitates the identification of speed variations of the spins.

2.4 MR image formation

When on resonance, following the application of an RF pulse that tips the net magnetization, M_0 , to possess a component precessing in the transverse plane (M_{xy}) at the frequency ω_0 , an oscillating magnetic field is formed. This dynamic field, in turn, induces an alternating small electrical current within a nearby receiver coil. This exemplifies Faraday's Law of Induction, which states that a changing magnetic field within the proximity of a conductor results in the generation of an electromotive force (emf) according to the equation:

$$emf = -N \frac{d\Phi}{dt} \quad \mathbf{2-21}$$

Where N is the number of loops, Φ is the magnetic flux, and $d\Phi/dt$ denotes its rate of change with respect to time. In this context, the current produced in the coil is directly proportional to the rate of change in the magnetic flux.

The MRI signal generated by precession of M_{xy} , denoted as S , is a complex number encompassing both real and imaginary components. The signal incorporates amplitude and phase information. The phase of the signal can be expressed in Euler form as:

$$S \propto e^{(i\varphi)} \quad \mathbf{2-22}$$

Where φ represents the phase angle, which at a given time (t), is calculated as follows:

$$\varphi = \omega_0 t \quad \mathbf{2-23}$$

Equation 2-22 can be rewritten as

$$S \propto e^{(i\omega_0 t)} \quad \mathbf{2-24}$$

$$\therefore S \propto e^{(i\gamma B_0 t)} \quad \mathbf{2-25}$$

2.4.1 Gradients and encoding

The concept of a gradient in MRI, involves introducing an extra linear variation in the strength of the B_0 . Gradients (G) can be applied along any or all of the three orthogonal directions (x , y , and z), and defined as:

$$G_x = \frac{\partial B_z}{\partial x} \quad G_y = \frac{\partial B_z}{\partial y} \quad G_z = \frac{\partial B_z}{\partial z} \quad \text{2-26}$$

For instance, when implementing a gradient in the x -direction (G_x), it either increases or decreases the magnitude of the B_0 field at various points along the x -axis. As a result, the precession frequency of the spins in the sample will be encoded based on their position. Figure 2-7 illustrates the main static magnetic field, B_0 (dashed line) and the field with the x -gradient incorporated (red line). The strength of the gradient field is quantified in millitesla per meter (mT m^{-1}).

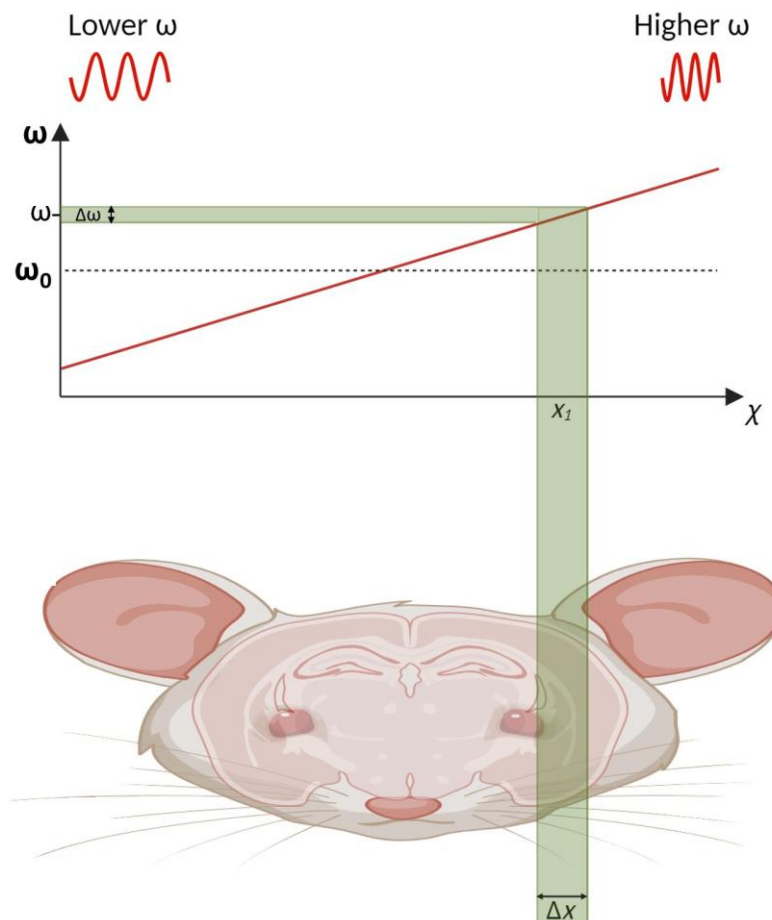


Figure 2-7: The sample comprises the rat brain, when a gradient is applied (indicated by the red line), the precession frequencies (ω) will vary linearly with the position in the x -direction.

Upon applying an RF-pulse with frequency ω and bandwidth $\Delta\omega$, only spins within the green slice with a thickness of Δx will be excited.

In the laboratory frame of reference, when applying a gradient along the x-axis, Figure 2-7, the magnetic field (B) is calculated as follows:

$$B = B_0 + G_x \cdot x_1 \quad 2-27$$

In the rotating frame of reference, on the other hand, when the net magnetization appears stationary due to the disappearance of the B_0 effect, the calculation of B is as follows:

$$B = G_x \cdot x_1 \quad 2-28$$

Now, Equation 2-25 can be rewritten, with the signal depending on the x_1 position, as follows:

$$S \propto e^{(i\gamma G_x x_1 t)} \quad 2-29$$

K-space is a foundational concept in MRI, where data is acquired in the time domain. The determination of k-space is dependent on phase and frequency encoding data. K-space serves as a mathematical representation of spatial frequencies. The transition from k-space data to the final spatial image is achieved through Fourier transformation, where data is transformed from the time domain to the frequency domain, and then the magnitude is taken.

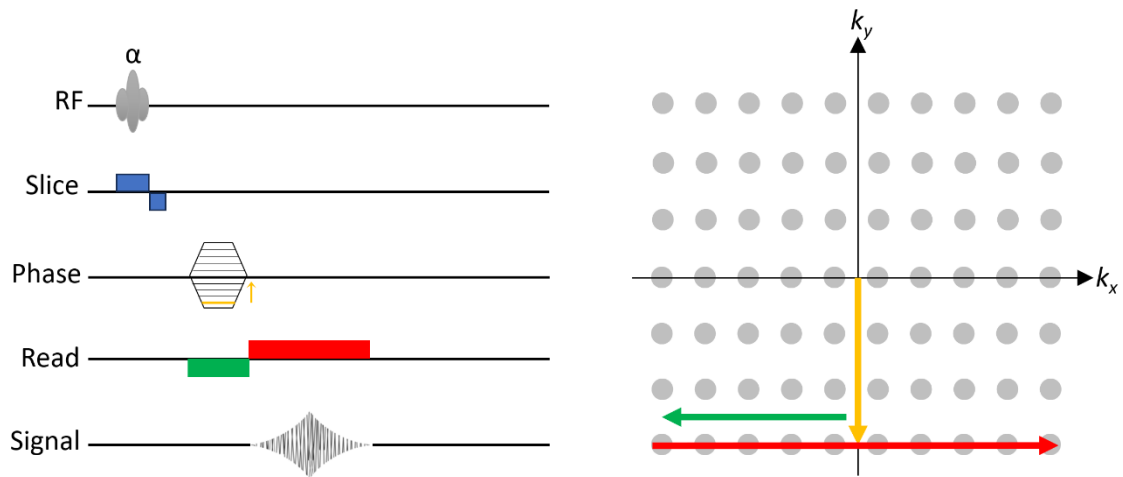


Figure 2-8: In the context of MRI, data acquisition in k-space is a process that involves mapping the spatial frequencies of the acquired signals. The k-space grid (on the right) is a representation of these spatial frequencies, with two key gradients: the phase encoding direction (k_y) and the frequency encoding direction (k_x). A standard gradient echo sequence is illustrated on the left. The yellow colour represents the phase encode gradient, the green represents the read de-phase encode gradient, and the red indicates the read (frequency) encode gradient. During each TR, a line of k-space is filled. The information collected in k-space is later transformed into spatial domain image through Fourier transformation.

For the 1-dimensional image, the total signal of a sample is the sum over all x at a given time t with a G_x gradient is applied in the x -direction:

$$S_{(G_x, t)} = \int_{-\infty}^{\infty} \rho(x_1) e^{i\gamma G_x t \cdot x} dx \quad 2-30$$

$$k_x = \frac{1}{2\pi} \gamma G_x \cdot t \quad 2-31$$

Where $\rho(x_1)$ represents the sample's spin density at position x_1 . The relationship between the k-space (spatial domain) and Fourier transform (frequency domain) is expressed by rewriting equation 2-30 incorporating the substitution 2-31:

$$S_{(k)} = \int_{-\infty}^{\infty} \rho(x) e^{i2\pi k_x \cdot x} dx \quad 2-32$$

For the 2-dimensional image:

$$S_{(k_x, k_y)} = \int_{-\infty}^{\infty} \int_{-\infty}^{\infty} \rho(x, y) e^{i2\pi(k_x \cdot x + k_y \cdot y)} dx dy \quad \mathbf{2-33}$$

The inverse Fourier transform:

$$\rho(x, y) = \int_{-\infty}^{\infty} \int_{-\infty}^{\infty} S_{(k_x, k_y)} e^{-i2\pi(k_x \cdot x + k_y \cdot y)} dk_x dk_y \quad \mathbf{2-34}$$

2.5 Relaxation times

After exciting the spins with an RF pulse to induce a flip into the transverse plane, they undergo a relaxation process back to their equilibrium position once the RF pulse is terminated. This relaxation involves two primary aspects: spin-lattice and spin-spin relaxation, which occur concurrently but independently.

2.5.1 Spin-lattice (T_1) relaxation

The T_1 relaxation process is known as longitudinal relaxation, attributed to the realignment of the net magnetization with the main magnetic field, M_z , until it reaches its equilibrium state, where M_z equals M_0 . It is also termed Spin-Lattice relaxation, as this relaxation occurs when the spins release their absorbed energy to their surroundings (lattice). This recovery process follows an exponential pattern, Figure 2-9.

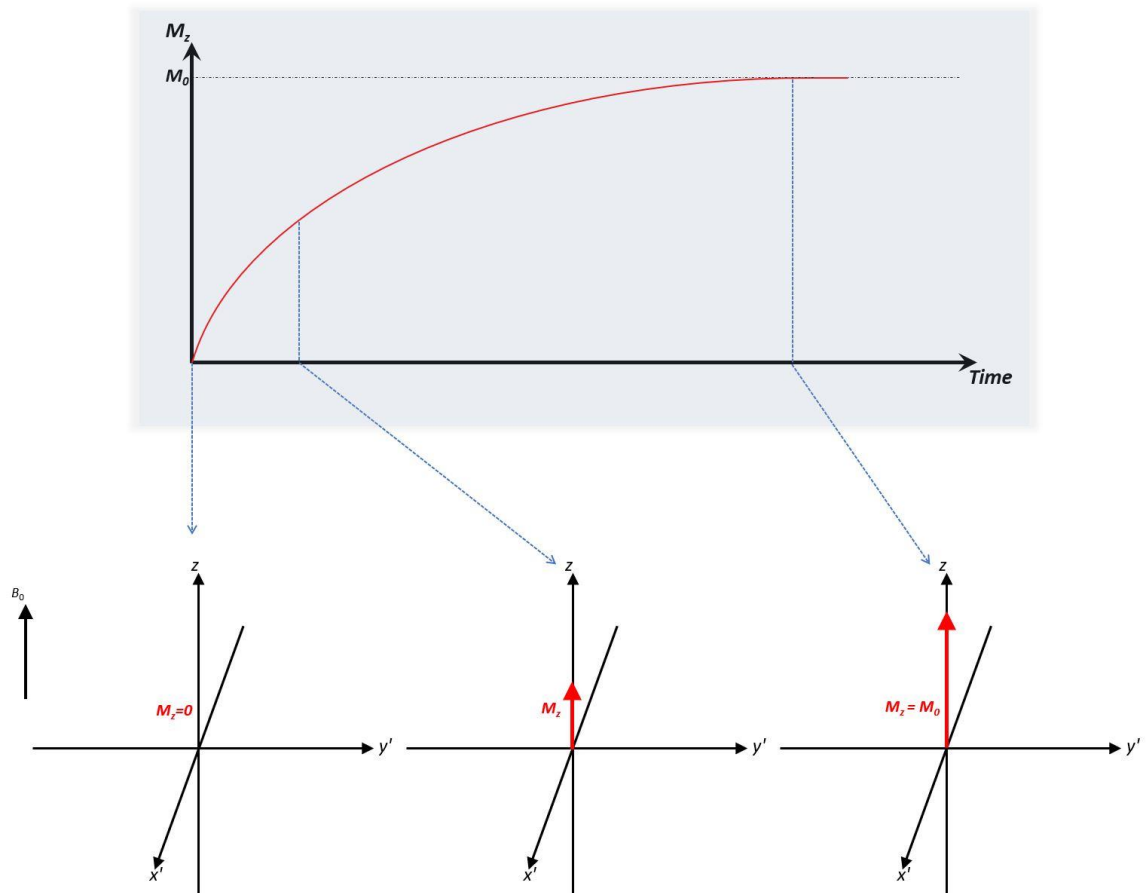


Figure 2-9: T_1 Relaxation. In the rotating frame (the second row), after the cessation of the 90° RF pulse, the transverse net magnetization (M_{xy}) starts to decrease, while the longitudinal net magnetization (M_z) builds up. The rate of the exponential recovery is known as T_1 relaxation time. The red arrow represents the net magnetization.

After the cessation of the 90° RF pulse, the spins release their energy to the surrounding lattice and gradually realign with the main magnetic field, reaching their ground energy state, i.e. equilibrium magnetization, M_0 . This recovery process follows an exponential curve and can be expressed as:

$$M_z(t) = M_0 \left(1 - e^{-\frac{t}{T_1}}\right) \quad \mathbf{2-35}$$

Where M_z is the longitudinal magnetization at time t , and T_1 is the longitudinal relaxation time.

2.5.2 Spin-spin (T_2) relaxation

Spin-spin relaxation arises from interactions among neighbouring spins (dipole-dipole interaction), leading to changes in the magnetic field for each spin based

on their magnetic moments in relation to each other. Consequently, individual spins may precess at rates higher or lower than the Larmor frequency, causing dephasing of the transverse net magnetization and a gradual reduction of the net magnetization in the xy -plane. This phenomenon is also known as transverse relaxation and is clearly observed in the rotating frame, Figure 2-10.

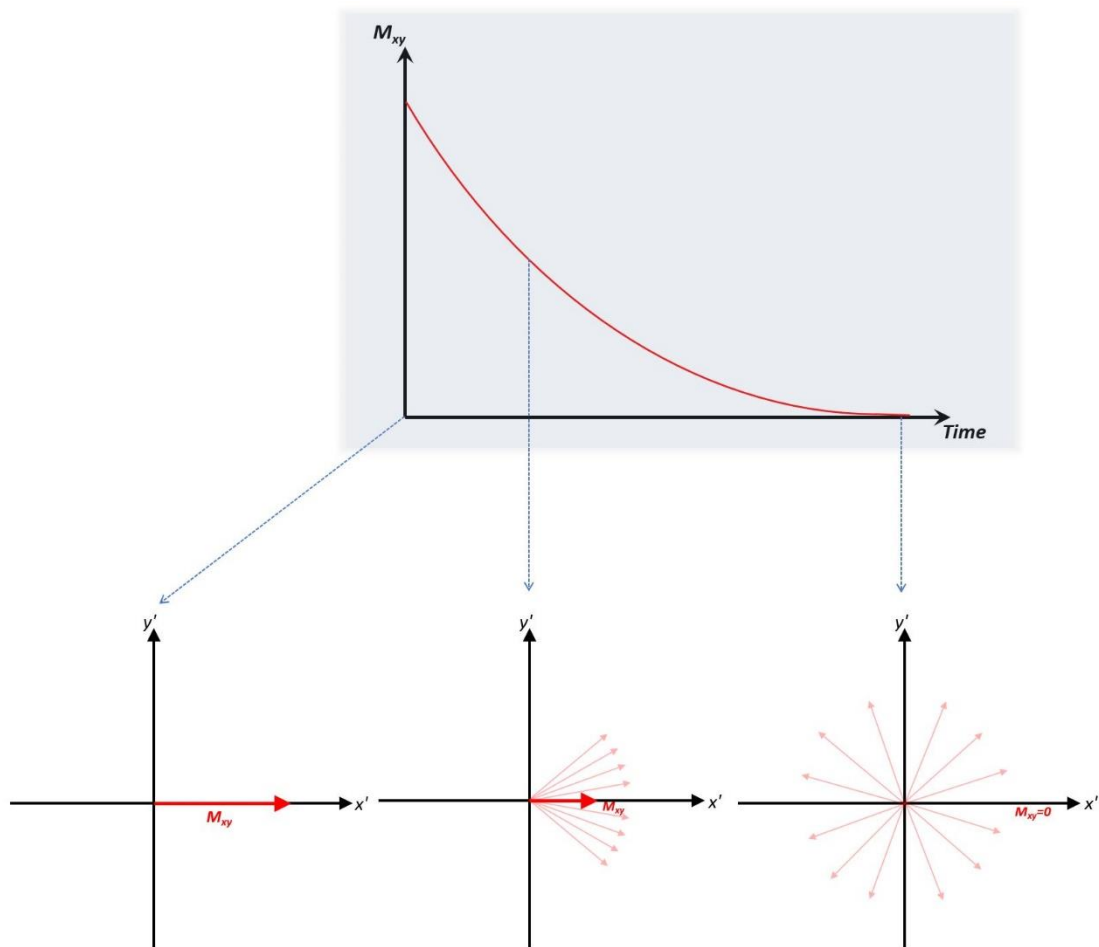


Figure 2-10: T_2 Relaxation. In the rotating frame (the second row), after the 90° RF pulse is turned off, the transverse net magnetization (M_{xy}) gradually decreases due to losing phase coherence between spins, resulting in signal decay. The exponential decay of M_{xy} is quantified by the T_2 relaxation time. The red bold arrow symbolizes the net magnetization in the xy -plane.

The dephasing, signifying the decline of the transverse net magnetization, M_{xy} , follows an exponential decay curve, and this decay is characterised by the relaxation time constant T_2 :

$$M_{xy}(t) = M_0 e^{\frac{-t}{T_2}}$$

Where $M_{xy}(t)$ is the transverse net magnetization at time t , and M_0 is the initial transverse magnetization following a 90° RF pulse.

Another type of transverse relaxations is T_2^* relaxation, which encompasses the effects of not only dipole-dipole interactions but also static magnetic field inhomogeneity. The additional contribution of magnetic field inhomogeneity to T_2^* relaxation results in even faster dephasing of spins, leading to a more rapid decay of the signal. The T_2^* relaxation rate is calculated using the formula:

$$\frac{1}{T_2^*} = \frac{1}{T_2} + \frac{1}{T_2'} \quad \text{2-37}$$

Where T_2' is the additional contribution from external magnetic field inhomogeneity to the transverse relaxation process. The T_2^* relaxation decay can be expressed as follows:

$$M_{xy}(t) = M_0 e^{\frac{-t}{T_2^*}} \quad \text{2-38}$$

T_2 relaxation decay results from intrinsic spin properties, rendering it an irreversible process. On the other hand, T_2^* relaxation decay is influenced by extrinsic factors, specifically magnetic field inhomogeneity, and can be reversed by applying a refocusing 180° RF pulse.

2.5.3 Contrast properties

Magnetic susceptibility is an inherent feature of all materials, quantifying how much a material becomes magnetized when exposed to a strong magnetic field, B_0 , based on its electron arrangement. There are four main types of magnetic susceptibilities: Diamagnetic substances: These have weak susceptibility and lack unpaired electrons, thus generating an internal field opposing the applied magnetic field (e.g., oxygenated blood). Paramagnetic substances: With a stronger susceptibility due to the presence of unpaired electrons, they align their internal field with the primary B_0 and increase the effective magnetic field. Examples include Gadolinium (Gd) chelates, a common MRI contrast agent with seven unpaired electrons, and deoxyhaemoglobin. Superparamagnetic substances: These exhibit behaviour between paramagnetic and ferromagnetic substances.

Hemosiderin is an example. Finally, ferromagnetic substances: When exposed to an external magnetic field, they become highly magnetized and strongly attracted to it. Examples include cobalt, nickel, and iron.

The appearance of a particular tissue in MR images is determined by its relaxation times. However, the T_1 and T_2 relaxation times of the tissue can be altered by changes in its local magnetic field, often induced by the introduction of contrast agents. These agents consist of substances with different magnetic susceptibilities. The relaxivities (r_1 and r_2) of MRI contrast agents define their effects on tissues, altering the relaxation rates of the tissues. The relaxation rate constants are calculated as follows:

$$R_1 = \frac{1}{T_1} \qquad R_2 = \frac{1}{T_2} \qquad \mathbf{2-39}$$

Where R_1 is the longitudinal relaxation rate, and R_2 is the transverse relaxation rate. Gd has the effect of reducing the T_1 relaxation time (increasing R_1) in adjacent tissues. This outcome manifests as a bright signal in T1-weighted images. The relaxivity of a contrast agent is a measure of its strength and plays a crucial role in determining the sensitivity of MRI signal detection. It is affected by various factors like temperature and the strength of the applied magnetic field. Consequently, the relaxation rate (R_1 or R_2) of tissues undergoes changes based on tracer concentration. This relationship can be expressed by the equations:

$$\frac{1}{T_1} = \frac{1}{T_1^0} + r_1 [C] \qquad \frac{1}{T_2} = \frac{1}{T_2^0} + r_2 [C] \qquad \mathbf{2-40}$$

Where T_1^0 and T_2^0 represent the baseline relaxation times (i.e. in the absence of the contrast agent), r_1 is the relaxivity constant associated with T_1 relaxation, r_2 is the relaxivity constant associated with T_2 relaxation, and $[C]$ denotes the contrast agent concentration. Relaxivity constants are often derived from the slope of the linear regression obtained by plotting the tissue relaxation rate against the concentration of the contrast agent. Hence, the relaxivity of a contrast agent can define the specific concentration required to elicit an observable effect on a biological medium.

Rearranging Equations 2-40:

$$\frac{1}{T_1} - \frac{1}{T_1^0} = r_1 [C] \qquad \frac{1}{T_2} - \frac{1}{T_2^0} = r_2 [C] \qquad \mathbf{2-41}$$

$$\therefore \Delta R_1 = r_1 [C] \qquad \Delta R_2 = r_2 [C] \qquad \mathbf{2-42}$$

2.5.3.1 Oxygen-17

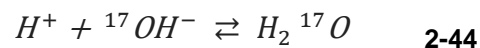
Hydrogen nuclei with a nuclear spin of $I=1/2$ are dipolar nuclei. The distribution of nuclear charge in these nuclei forms a symmetrical, spherical shape, remaining largely unaffected by the surrounding electron environment. In contrast, quadrupolar nuclei, like Oxygen-17 (^{17}O), with a nuclear spin of $I=5/2$ and 6 different energy levels, exhibit an asymmetrical distribution of nuclear charge. This asymmetry exerts a noticeable effect on the neighbouring electron clouds. ^{17}O , a notably scarce yet stable isotope, presents itself as a promising tracer candidate for MRI applications due to its capacity to generate an MRI signal. However, its natural abundance is quite low at 0.037%, making it approximately 2700 times lower than hydrogen, which has a natural abundance of 99.9%. Additionally, the gyromagnetic ratio of ^{17}O is approximately seven times smaller than that of hydrogen, measuring at 5.8 MHz/Tesla compared to hydrogen's 42.58 MHz/Tesla. Given the inherent challenges posed by its low abundance and reduced gyromagnetic ratio, the sensitivity of MRI to detect ^{17}O is extremely lower than that of the hydrogen nucleus. Consequently, the enrichment of ^{17}O is crucial in MRI applications (Zhu et al., 2005; Zhu & Chen, 2017). Nevertheless, its utilization is constrained by its high cost (Kudo et al., 2018). ^{17}O imaging can be achieved through both direct and indirect techniques. However, the direct technique faces challenges, including the need for specialized hardware to detect the signal and its inherently weak nature. In contrast, the indirect technique, utilizing ^{17}O -enriched water as a tracer to shorten the T_2 relaxation of ^1H protons, offers more advantages. It does not require special hardware, yields a stronger signal, and exhibits relaxation independent of field strength (Tailor et al., 2003; Taoka & Naganawa, 2020).

The shortening effect on the T_2 relaxation of ^1H is induced by the presence of ^{17}O nuclei, arising from the scalar coupling between ^1H and ^{17}O . This relationship can be expressed as follows:

$$\frac{1}{T_{2,H}} \approx \frac{1}{T_{2,H}^{(16)}} + \frac{35}{12} P \tau J^2 \quad \text{2-43}$$

In which $T_{2,H}^{(16)}$ represents the transverse relaxation time of protons in water (H_2^{16}O), P is the water enrichment fraction of ^{17}O , τ is the exchange lifetime of protons, and J is the ^{17}O - ^1H scalar coupling constant (Zhu et al., 2005).

The hydrogen protons in H_2^{16}O and H_2^{17}O can freely exchange between the two molecules which magnifies this effect (Meiboom, 1961):



Consequently, the transverse relaxation time of water is shortened, resulting in a darker appearance in T_2 -weighted imaging (Igarashi et al., 2014).

2.6 Pulse sequences

2.6.1 Image contrast parameters

In MRI, the image contrast is affected by various parameters, which can be categorized into two types: inherent contrast parameters and external contrast parameters. The former, including the tissue's T_1 and T_2 relaxation times, are intrinsic and beyond our control. On the other hand, the external contrast parameters, such as echo time (TE), repetition time (TR), and flip angle, are adjustable parameters which can be deliberately optimized to enhance image contrast.

TR, or Time to Repeat, refers to the time interval between two successive RF pulses for the same slice. On the other hand, TE, or Time to Echo, refers to the

time interval from the initial RF pulse to the centre (peak) of the signal echo, Figure 2-11.

In MRI, image weighting is adjustable based on the values of TE and TR used in the pulse sequence. Modifying these parameters allows for the emphasis of T_1 , T_2 , or proton density contrasts in the resulting images, Figure 2-11. To produce T_1 -weighted images, it is necessary to keep both TE and TR short. This choice minimizes the T_2 effect with a short TE while accentuating the T_1 effect with a short TR. Conversely, for T_2 -weighted images, both TE and TR should be long. Finally, for proton density-weighted images, a balance between T_1 and T_2 weightings can be achieved by selecting a short TE and a long TR.

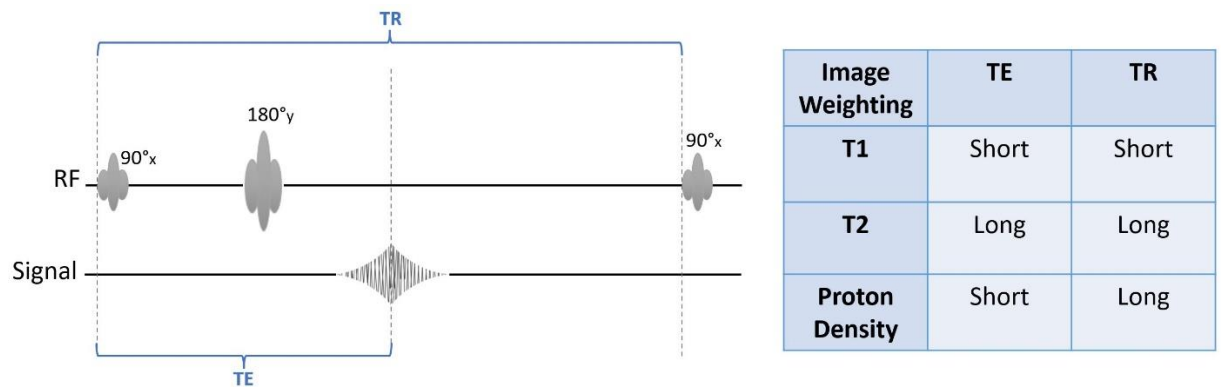


Figure 2-11: On the left: Standard spin echo sequence displaying TE and TR. On the right: A table illustrating the influence of the parameters TE and TR on MR image contrast.

2.6.2 Rapid acquisition with relaxation enhancement

Rapid Acquisition with Relaxation Enhancement (RARE), also known as Fast Spin Echo (FSE) or Turbo Spin Echo (TSE), was first introduced by Hennig et al. in 1986 (Hennig et al., 1986). This technique employs a series of 180° slice-selective refocusing pulses following the initial 90° RF pulse, which flips the spins from longitudinal magnetization (M_z) to transverse magnetization (M_{xy}). In contrast to the conventional spin echo sequence, which typically produces only a single echo per TR, this technique generates multiple echoes per one TR, leading to a drastic reduction in acquisition time, Figure 2-12. Each echo has a different phase encoding, enabling the filling of multiple lines of k-space within a single TR. The number of refocusing pulses, referred to as the 'echo train length' or 'echo train

factor,' usually ranges from 4 to 32. In specific cases, such as single-shot RARE, it may extend to as many as 64 refocusing pulses. In our experiments, the echo train length was set to 12. The echo train length is inversely correlated with acquisition time; thus, a higher echo train length leads to faster imaging. MR image contrast is determined by the echoes that fill the centre of K-space; in the case of the RARE sequence, the image weighting is determined by the effective TE. This sequence is used in Chapters 4 and 5.

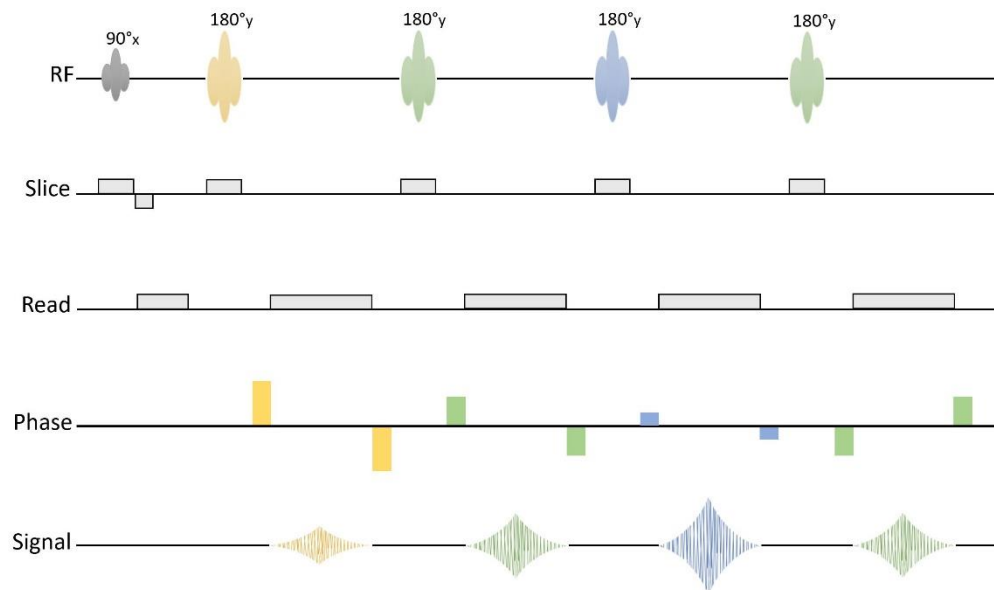


Figure 2-12: RARE sequence.

2.6.3 Multi slice multi echo

The Multi Slice Multi Echo (MSME) technique is employed for T_2 mapping. In contrast to T_2 -weighted imaging, which provides qualitative insights, T_2 mapping facilitates the quantification of T_2 relaxation times in sampled tissues. The MSME technique operates similarly to FSE imaging but employs a distinct approach. Instead of acquiring different lines of k-space for the same slice by varying the phase-encode gradient, MSME fills the same line of k-space in several different slices, each with different TEs, Figure 2-13. Consequently, each voxel from every slice can be fitted to a T_2 exponential decay curve following Equation 2-36. This technique is used in Chapters 4 and 8.

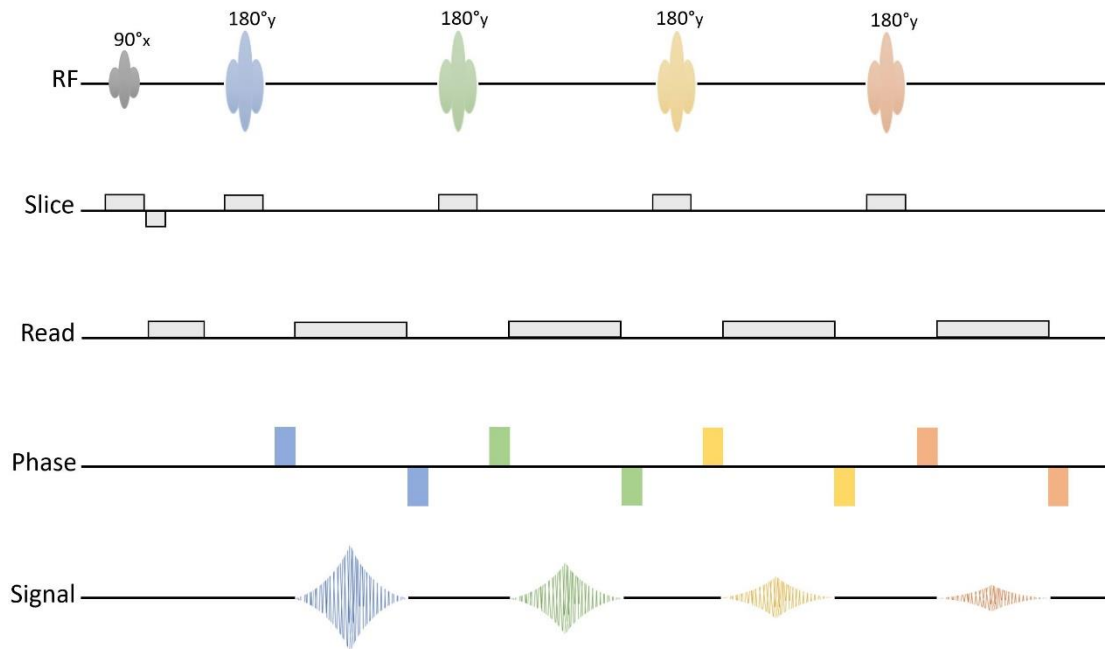


Figure 2-13: MSME sequence.

2.6.4 Gradient echo sequence

In gradient echo sequences, an RF pulse with an angle (α) less than 90° is typically used. The signal decay in this sequence depends on T_2 and additionally on T_2^* , the latter being influenced by static magnetic field inhomogeneities. Unlike in spin echo pulse sequences, where a 180° refocusing pulse helps compensate for T_2^* effects, gradient echo sequences lack this additional refocusing pulse. Due to the use of an RF pulse less than 90° and the absence of a 180° refocusing pulse, gradient echo imaging is generally faster than spin echo imaging.

Figure 2-14 shows a schematic of the gradient echo sequence. The read dephasing gradient is employed to dephase the transverse magnetization created by the free induction decay, followed by the read rephasing gradient. This gradient is doubled in size and applied in the opposite direction to the read dephasing gradient, thereby generating the gradient echo.

In gradient echo sequences, to obtain a T_1 -weighted image, a short TE and a large flip angle should be used. Conversely, to generate a T_2^* -weighted image, a small flip angle and a long TE can be employed. The choice of a small flip angle for T_2^* -weighted image minimizes the T_1 weighting effect, allowing the longitudinal

magnetization to approach full relaxation faster. The Ernst angle determines the optimal flip angle (α) values to achieve the highest signal under specific imaging parameters and tissue characteristics.

$$\alpha_{Ernst} = \cos^{-1} \left(e^{-\frac{TR}{T_1}} \right) \quad \mathbf{2-45}$$

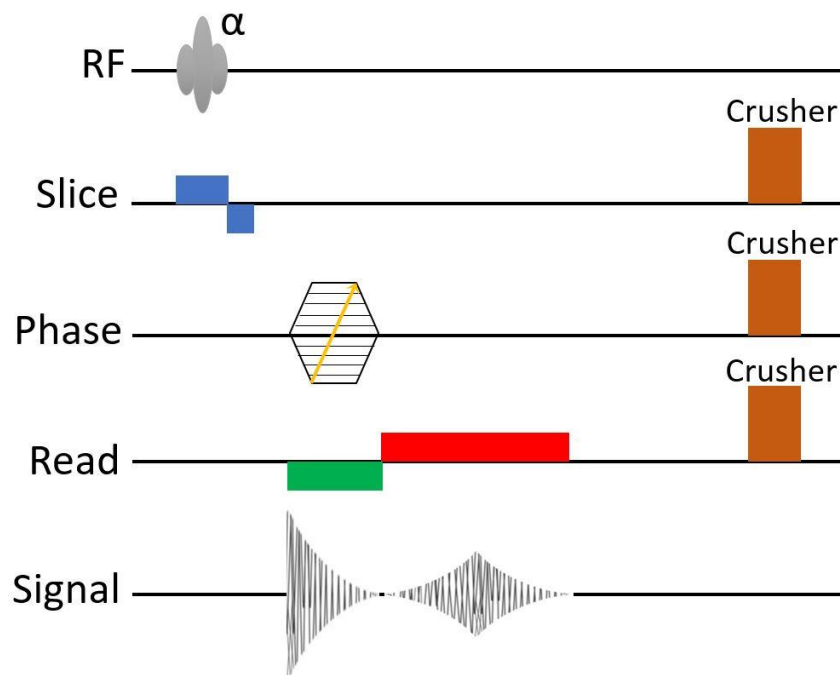


Figure 2-14: Schematic of gradient echo sequence.

In a fast low angle shot (FLASH) sequence, a T_1 -weighted gradient echo imaging sequence, the TE is typically a few milliseconds, while the TR is in the tens of milliseconds. In the FLASH sequence, if the TR is equal to or less than the transverse relaxation time (T_2^*), the spins from the previous excitation might not have enough time to lose their phase coherence before the next excitation. This can lead to the accumulation of transverse net magnetization and introduce artefacts in the images. To mitigate this issue, crusher or spoiler gradients are often employed to dephase the residual transverse magnetization, Figure 2-14. These gradients help ensure that the spins are adequately dephased before the next excitation. This sequence is used in Chapters 6 and 9.

2.6.5 Diffusion MRI

Diffusion-weighted imaging (DWI) is an important technique in MRI, owing to its exceptional sensitivity in promptly detecting various pathologies, such as ischemic strokes. Notably, the significance of DWI is underscored by its ability to reveal subtle changes in tissue microstructure without the need for contrast injection. DWI, introduced by Stejskal and Tanner in 1965, operates by applying two diffusion-sensitizing gradients separated by a 180° inversion pulse to detect the Brownian (random) motion of water molecules, Figure 2-15. If the molecules remain motionless, their signal output would be high due to the cancellation of phase shift. In contrast, movable molecules will experience an uncanceled phase shift, resulting in signal loss. The degree of signal loss corresponds to increased molecular diffusivity. Consequently, on a DWI, regions with high diffusion exhibit darker appearances, while areas with restricted diffusion appear brighter (Stejskal & Tanner, 1965; Taoka & Naganawa, 2020).

The signal intensity in DWI is calculated as follows:

$$S = S_0 e^{-bD} \quad 2-46$$

Where S_0 is the signal intensity when no diffusion gradients are applied ($b = 0$), representing the reference image. b is the b-value, and D represents the diffusion coefficient, measured in $\text{mm}^2 \text{s}^{-1}$. The diffusion coefficient can be calculated by rearranging equation 2-46:

$$D = -\frac{1}{b} \ln\left(\frac{S}{S_0}\right) \quad 2-47$$

The effective diffusion sensitization in DWI is governed by the b-value, which relies on both the strength and duration of the applied diffusion-sensitizing gradients:

$$b = \gamma^2 G^2 \delta^2 \left(\Delta - \frac{\delta}{3}\right) \quad 2-48$$

Here, G represents the magnitude of the diffusion-sensitizing gradients, δ is the duration of these gradients, and Δ is the time between these gradients, Figure 2-15. Δ is commonly referred to as either 'big delta,' 'observation time,' or 'diffusion time.' From this equation, it is clear that diffusion sensitization correlates positively with G , δ , and Δ .

Throughout this thesis, two types of Diffusion-Weighted Echo-Planar Imaging (DW-EPI) sequences were employed. Conventional spin echo DW-EPI was used in Chapter 6; however, this technique allows for only a short diffusion time because the signal decay depends on the T_2 relaxation time, Figure 2-15. In contrast, the novel stimulated echo DW-EPI used in Chapter 8 allows for very long diffusion times without risking signal loss, as the signal decay depends on the T_1 relaxation time, Figure 2-15.

In a stimulated echo sequence, following the initial 90° RF pulse, another 90° RF pulse is applied instead of the 180° refocusing RF pulse. This 90° pulse inverts the transverse net magnetization to the longitudinal magnetization, where the phase shift is stored during the mixing time (TM). Subsequently, another 90° RF pulse is applied to flip the longitudinal net magnetization back to the transverse magnetization to generate the echo. The echo is formed during the time interval encompassing TE plus TM.

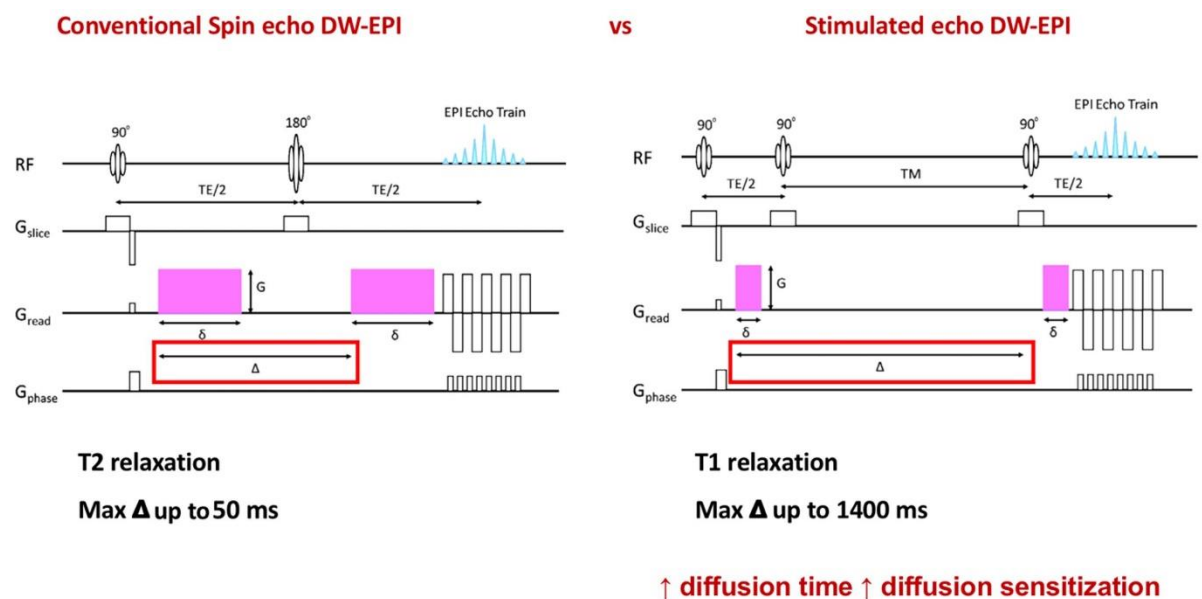


Figure 2-15: A schematic of the conventional spin echo DW-EP sequence is on the left, and the stimulated echo DW-EPI sequence is on the right (Avram, 2011).

2.6.6 Flow-sensitive alternating inversion recovery

The FAIR (Flow-sensitive Alternating Inversion Recovery) sequence is a specialized MRI technique developed for non-invasive assessment of cerebral blood perfusion. Applying the principles of pulsed arterial spin labelling (PASL), the FAIR sequence employs alternating inversion of magnetization between labelled and control conditions to tag arterial blood water protons, Figure 2-16. Subsequently, this tagged blood water flows into the imaging region, enabling the measurement of perfusion without the necessity of contrast agents.

Cerebral blood flow (CBF) can be calculated from the non-selective and slice-selective inversion recovery images using the following formula:

$$CBF = \lambda \left(\frac{1}{T_{1\text{ selective}}} - \frac{1}{T_{1\text{ nonselective}}} \right) \quad 2-49$$

Here, λ represents the blood-brain partition coefficient. FAIR technique is valuable for studying brain perfusion and has applications in various neurological conditions, including stroke, neurodegenerative diseases, and brain tumours. This sequence is used in Chapter 9.

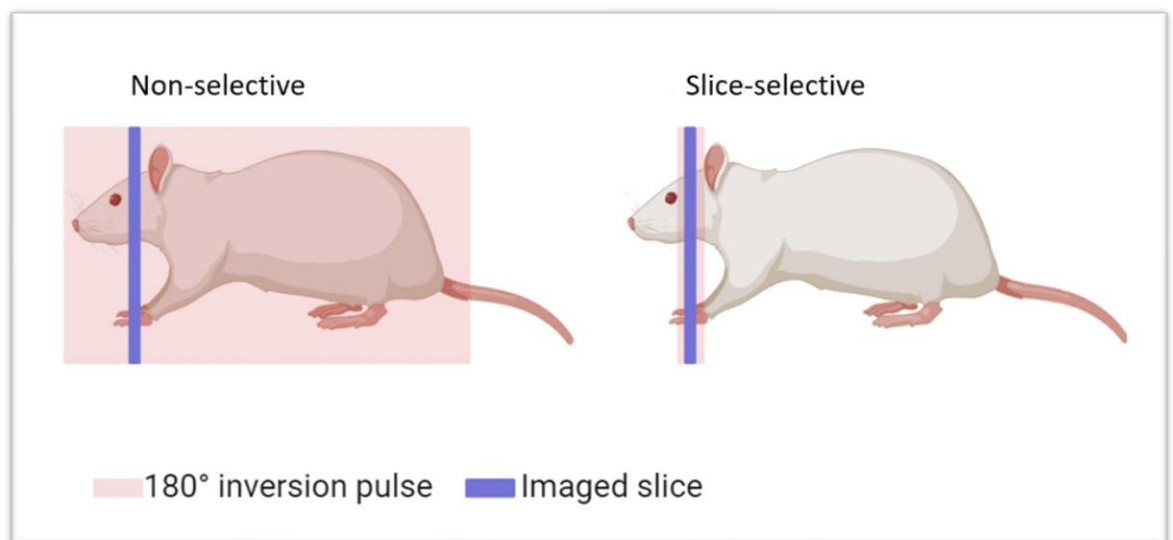


Figure 2-16: PASL FAIR

2.7 Essential components in MRI scanner

2.7.1 Main magnet

There are three primary types of magnets used in MRI systems. The first type is permanent magnets, which are made of ferromagnetic materials and operate without requiring an external power supply. However, they have certain drawbacks, including their substantial weight and a relatively low magnetic field strength, typically up to 0.5 T. The second type is resistive magnets, constructed from electromagnet materials. However, they are associated with significant drawbacks, including the generation of a relatively low magnetic field, typically up to 0.3 T, and a high susceptibility to field inhomogeneity.

The final and most widely used magnet in MRI systems is the superconducting magnets. Superconducting coils are made of a niobium-titanium alloy. These coils consist of thousands of turns, with wires extending up to 400 kilometres in length. Niobium-titanium coils must be maintained at an extremely low temperature, close to absolute zero at around 4 Kelvin, to preserve their superconductivity. Therefore, cryogenics, such as the use of liquid helium, are essential. This type of magnet offers distinct advantages over other types, characterized by exceptional homogeneity and the ability to generate exceedingly strong magnetic fields, reaching up to 18 T. Figure 2-17 illustrates the main components of a standard MRI system. All experiments conducted during my PhD utilized 7 T preclinical MRI scanners, namely the Bruker PharmaScan with a bore size opening of 16 cm and the Bruker Biospec with a bore size opening of 30 cm. Controlled by ParaVision 5.1 and 6.0.1 software (Bruker Bio Spin, Ettlingen, Germany), respectively.

2.7.2 Shim coils

Several limitations, such as factors related to the construction of the main magnet and variations in magnetic susceptibilities within the imaged object, can contribute to inhomogeneity in the main magnetic field of an MRI system. A decrease in static magnetic field homogeneity leads to broadened linewidths of

peaks and an overall reduction in the sensitivity of the main magnetic field. To correct field distortions and enhance main magnetic field homogeneity, shimming is employed, and it can be either active or passive. Passive shims, typically thin sheet metal pieces, primarily serve to compensate for main magnetic inhomogeneity, while active shims consist of electromagnetic coils that require current to operate.

2.7.3 Gradient coils

Gradient coils in an MRI system play a crucial role in spatial encoding of the signal by having a direct current passed through them. These coils vary the strength of the main magnetic field linearly with position and are positioned in all three orientations: x, y, and z. The steeper the gradient, the higher the achievable resolution. Gradient coils serve a dual purpose, enabling spatial localization and contributing to shimming for the enhancement of main magnetic field homogeneity, a process known as 'gradient offset.' These coils can be adjusted either manually or automatically for each sample, compensating for any field distortion induced by the sample. The z-axis gradient employs a Maxwell coil configuration, while the x and y-axis gradients utilize saddle coil configurations. Our Bruker PharmaScan features a gradient inner diameter of 90 mm, a gradient strength of 300 mT/m, and a gradient slew rate of 6840 T/m/s. While our Bruker Biospec features a larger gradient inner diameter of 114 mm, higher gradient strength of 440 mT/m, and a gradient slew rate of 3440 T/m/s.

2.7.4 RF coils

RF coils consist of two primary components: the RF transmitter coil and the RF receiver coil, although some designs incorporate a single coil that can serve both functions. The RF transmitter coil is responsible for generating RF radiation (B_1 field) with a frequency close to the Larmor precession of the spins, enabling the excitation of spins from longitudinal magnetization (B_0) to transverse magnetization. In our experiments, we used a volume coil with a birdcage configuration for RF pulse transmission. To receive the MRI signal, we employed a surface coil, which was a four-channel phased array coil specifically designed for imaging the rat's brain.

2.7.5 Shielding

To mitigate the fringe field (magnetic field outside the magnetic bore) generated by the MRI scanner, active shield coils are employed. These coils, located outside the primary magnetic field coils within the helium apparatus, generate a magnetic field counteracting the main magnetic field (B_0). This helps create a more uniform magnetic field within the imaging region, reducing distortions in the resulting images and improving image quality. Additionally, the magnet room incorporates a Faraday cage to shield against external RF interference, preventing signals from electronic devices and radio signals outside the room from affecting the imaging process. These measures not only enhance image quality but also contribute to the safety of both patients and staff by minimizing exposure to stray magnetic fields and RF interference.

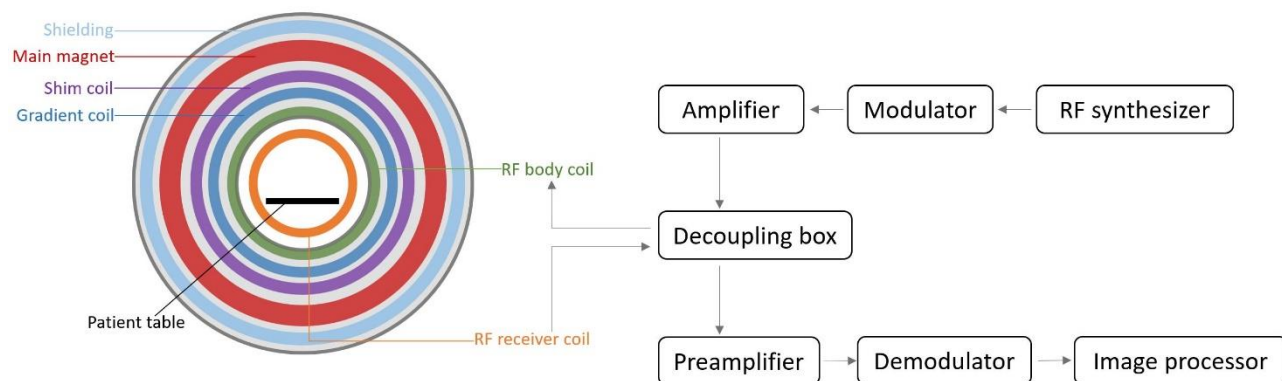


Figure 2-17 : A diagram illustrates the key components of an MRI scanner system.

2.7.6 Electronics

The process of generating an RF pulse, receiving the MR signal, and digitizing it involves several intricate steps:

2.7.6.1 RF synthesizer (oscillator)

The RF synthesizer plays a crucial role in MRI imaging by generating an oscillating electrical signal matched to the Larmor frequency of the object being imaged.

2.7.6.2 Modulator

The RF modulator takes an electrical signal and modulates it onto a specific RF carrier wave by modifying properties such as its amplitude and phase.

2.7.6.3 Amplifier

The RF amplifier amplifies the RF pulses sent from the modulator to the necessary power levels for excitation of the nuclear spins in the imaged object. It increases the amplitude of the RF pulse to the required strength. The specific power levels required can vary depending on factors such as the field strength of the MRI system and the imaging sequence being used. In our systems the amplifiers are 300-1000 watts.

2.7.6.4 Decoupling box

The duplexer, typically employing cross diodes, serves to switch the receiver coil off resonance during RF transmission and the transmitting coil off resonance during acquisition time. This switching is crucial to prevent the high-power transmit pulse from damaging the sensitive receiver components.

2.7.6.5 Preamplifier

In MRI systems, the preamplifier is crucial due to the minute magnitude of the received signal from the imaged object, typically around 0.001 watt. The preamplifier amplifies the signal by increasing its power, allowing for accurate detection and processing.

2.7.6.6 Demodulator

In an MRI system, quadrature detection (demodulator) utilizes a heterodyne detector to downconvert the received MRI signal for digitization and sampling. Since the signal oscillates at a high frequency (e.g., 300 megahertz at 7 Tesla), exceeding the processing capability of the ADC converter, the demodulator mixes the received signal with a reference frequency generated by the oscillator. This downconversion process results in a lower frequency signal, typically in the audible range, facilitating further processing.

2.7.6.7 Image digitizer

The analog-to-digital converter (ADC), also known as the image digitizer, converts the analog MRI signal into a digital output. This conversion process is achieved by computer systems to effectively read and interpret the images generated by the MRI system.

2.7.7 Transmit-receive birdcage coil construction

In 1985, Hayes and colleagues introduced birdcage coils for MRI systems, demonstrating their ability to produce a highly uniform RF magnetic field. This resulted in a strong signal with low noise (Hayes et al., 1985). The birdcage coil stands out as the predominant RF-transmit device in both clinical and preclinical MRI applications. In cylindrical superconducting scanners, this configuration is the standard for all body coils. These coils are composed of two circular conductive loops known as end rings (ER), linked by an even number of straight conductive elements known as rungs or legs. The quantity of legs varies based on the coil's size, typically spanning from 8 to 32. Additionally, birdcage coils incorporate capacitors positioned between conducting elements, and their arrangement is adjusted to achieve specific frequency characteristics. Table 1 presents the coil configuration utilized in constructing my birdcage coil, as calculated by the Penn State Birdcage Builder software, version 1.0.

Table 1: The Birdcage Coil Configuration.

Birdcage coil dimension	
Number of legs	8
Coil radius (cm)	0.7
Leg length (cm)	2
Leg width (cm)	0.1
RF shield radius	0
ER length (cm)	0.55

ER width (cm)	0.2
Resonant frequency	Low pass
Capacitance (pF)	10

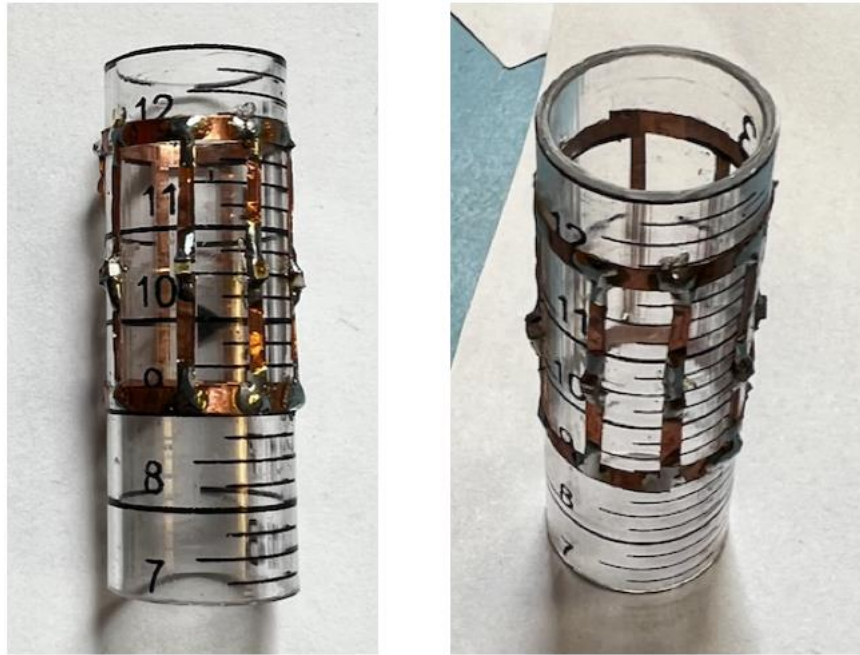


Figure 2-18: Home-made transmit receive birdcage coil.

The coil (Figure 2-18) was tested to assess its capability to both transmit and receive RF pulses and generate images. To evaluate its performance, we imaged a plastic screw immersed in a solution of $\text{CuSO}_4 \cdot 2\text{H}_2\text{O}$. The coil successfully produced a high-resolution image, as depicted below, Figure 2-19. Notably, the image reveals clear details of the screw (indicated by the arrow), demonstrating the coil's effectiveness in imaging. The imaging sequence used with this coil was 3D FLASH T1-weighted. Scanning parameters included: FOV 4x2 cm, matrix size 400x200, TR 100 ms, TE 3.8 ms, FA 15°, NEX 2, and acquisition time 40 s.

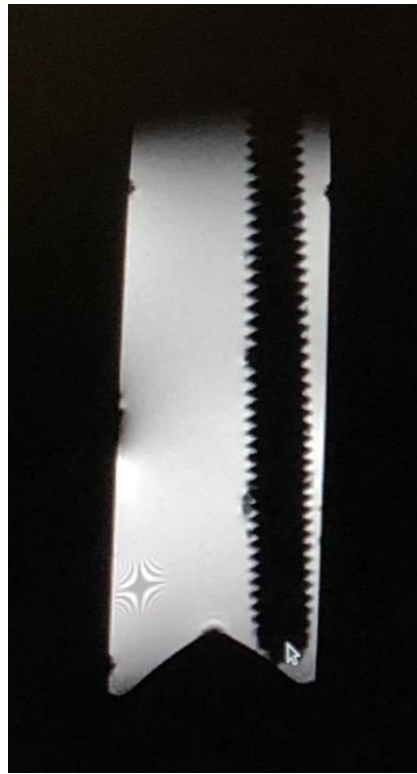


Figure 2-19: A 3D FLASH T1-weighted image was generated using the home-made birdcage coil as an RF pulse transmitter and receiver.

Chapter 3 Methodology

Surgical procedures were performed by Mrs. Lindsay Gallagher and Mr. Conor Martin, while I was responsible for conducting all MRI imaging, data analysis, infusion preparation, and dosing. Additionally, I performed all phantom studies and handled all aspects of histology staining and analysis.

All animal studies and surgical procedures in this thesis were conducted with approval from the University of Glasgow internal Animal Welfare and Ethical Review committee and the UK Home Office. These experiments were carried out in accordance with the regulations outlined in the Animals (Scientific Procedures) Act 1986 (ASPA) and the European Union legislation protection for animal used in scientific procedures, Directive 2010/63/EU. Furthermore, throughout the duration of the thesis, the principles of the three Rs (replace, reduce, refine) were strictly adhered to.

3.1 Animal provider

Two strains of male rats were employed in this thesis: Wistar rats, sourced from Charles River Laboratories, and Wistar Kyoto (WKY) rats, which were bred at the University of Glasgow.

3.2 Animal housing and acclimatization

The animals were housed in the animal care unit at the University of Glasgow and allowed one week for acclimatization upon their arrival. They were maintained in groups in cages, with a maximum of five rats per cage, and provided with ad libitum access to food and water. Room temperature, ventilation, and humidity were automatically controlled and maintained within specific ranges: humidity at $53 \pm 5\%$, temperature at $21 \pm 2^\circ\text{C}$, and a standard 12-hour dark/light cycle.

3.3 Animal preparation for surgery

Initially, rats were induced with 5% isoflurane inside an induction chamber, utilizing a mixture of 30% O₂ and 70% N₂O as carrier gases for non-recovery procedures, and a mixture of 30% O₂ and 70% air for recovery procedures. Once the rats lost consciousness and were deeply anesthetized (as evidenced by the lack of hindlimb withdrawal reflex to toe pinch), they were transferred to a facemask, and the isoflurane concentration was reduced to 1.5%-2.5%, maintaining the same volume of carrier gases. Anaesthetic concentrations and animal's physiological parameters (ex: respiration rate, heart rate, and blood pressure) were continuously monitored and documented throughout the entire duration of the experiments, ensuring they remained within optimal ranges, Figure 3-1. To prevent corneal damage, a protective eye cream was always applied. Additionally, a homeothermic blanket system with a rectal thermocouple probe was employed to mitigate the risk of hypothermia (Polystat® Cole-Parmer). During the surgical procedures, an additional heat source, provided by a heating lamp, was employed. Core body temperature was continuously monitored throughout the entire experiments and maintained at $37.0 \pm 0.5^{\circ}\text{C}$.

Next, the fur over all planned surgical regions was shaved, followed by thorough cleaning and sterilization of these areas. The animal was then transferred to a sterilized surgical area within the theatre room. Depending on the procedure, the animal was either intubated for recovery procedures or underwent a tracheotomy for non-recovery procedures, allowing for artificial ventilation and maintenance of anaesthesia. For this purpose, a 13G feeding tube was utilized, connected to the ventilator (Harvard Apparatus Inspira ASV Advanced Safety Animal Ventilator 55-7059 Volume. USA or 7025 Rodent Ventilator - Volume Controlled, manufactured by Ugo Basile S.R.L. Italy).

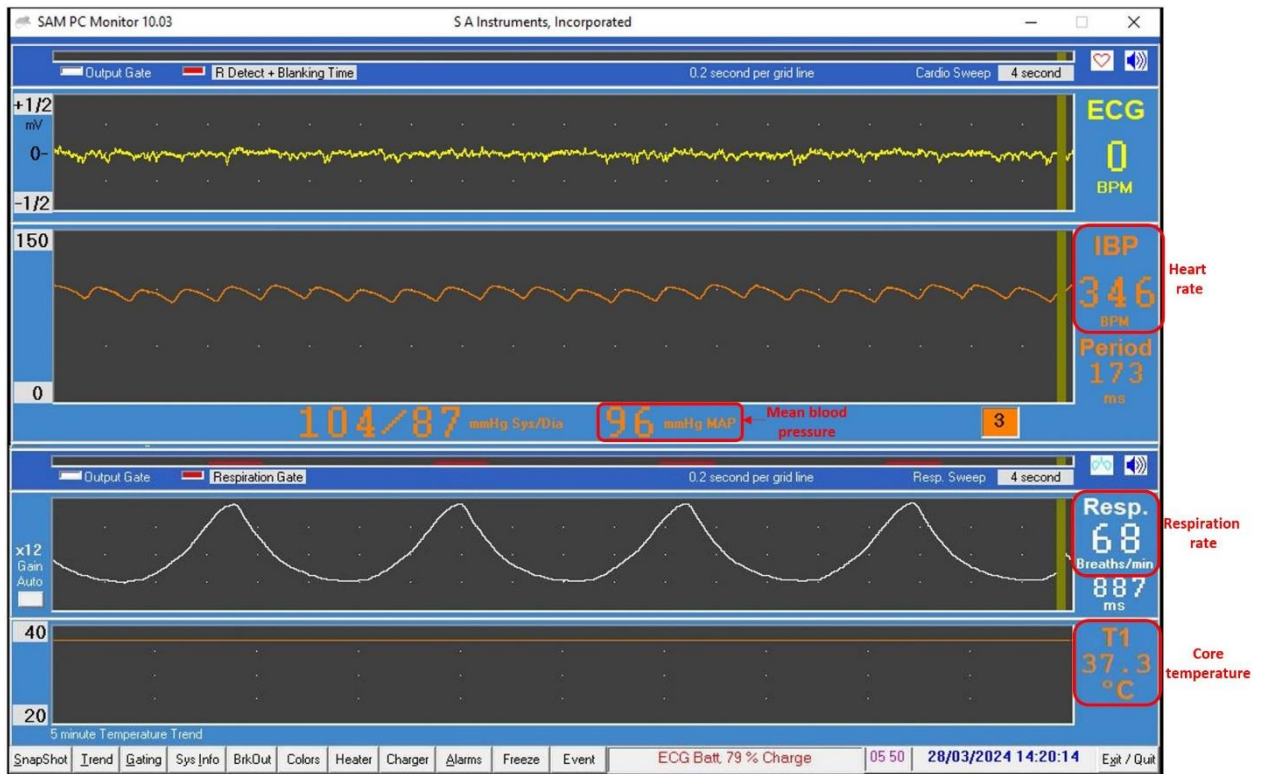


Figure 3-2: Real-Time Physiological Monitoring Interface.



Figure 3-3: epoc Blood Gas Analyser.

3.4.2 Cisterna magna cannulation

3.4.2.1 Implementing the cisterna magna cannula

The purpose of cisterna magna cannulation is to allow the infusion of contrast into the brain's CSF for MR imaging and directly assess the glymphatic flow. The rat is placed in a prone orientation within a stereotaxic frame, securing the head with tooth and ear bars. Next, the head is tilted at a 120° angle, directing the snout downward. After sterilizing the area, a 2 cm incision is carefully made in the midline of the dorsal neck to access the cisterna magna. The underlying muscle layers are then diligently dissected and separated to expose the occipital crest and the dural membrane covering the cisterna magna. Swabs are used to manage any bleeding that may occur. The cisterna magna should be positioned directly beneath the atlanto-occipital membrane, appearing within an inverted triangle formed by the bone, with the cerebellum situated above and the medulla below, Figure 3-4.

A custom-made cisterna magna cannula (22-gauge, 2 mm Tip PEEK, SAI Infusion Technologies, RCMC-03) is connected to a polyethylene tube and primed with artificial CSF (aCSF) composed of NaCl (140 mmol/L), NaH₂PO₄ (12 mmol/L), KCl (3 mmol/L), CaCl₂ (2.5 mmol/L), and NaHCO₃ (12 mmol/L) at a pH of 7.4. The cannula is then carefully advanced 2 mm into the subarachnoid space. Determination of the optimal length of the cisterna magna cannula will be addressed in the next section. After insertion, the cannula is secured in place using SurgiBond or Vetbond adhesive to prevent movement or leakage. Subsequently, the muscles are carefully repositioned, and the overlying skin is sutured to prevent bleeding or dehydration. To confirm accurate cannula placement, it's crucial to observe CSF pulsations within the cannula.

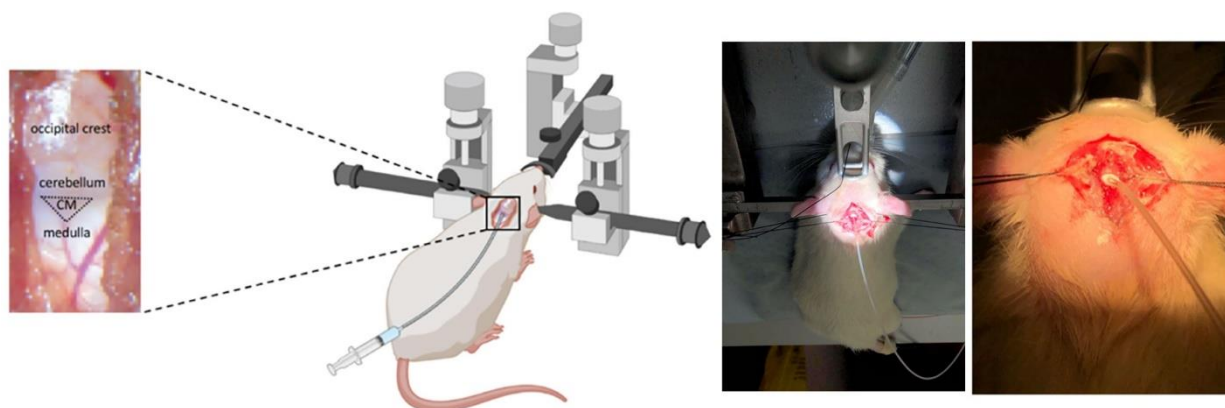


Figure 3-4: Schematic illustration of the cisterna magna cannula implementation. CM: cisterna magna.

3.4.2.2 Determining the appropriate length of the cannula

In the original study by Iliff et al., they were the first to image glymphatic dynamics in the rat brain using contrast-enhanced MRI (Iliff, Lee, et al., 2013). They achieved this by advancing the cisterna magna cannula into the intrathecal space with a short distance of only 1 mm. Inspired by their methodology, we adopted a similar cannula length of 1 mm in our initial pilot study. However, advancing the cannula by only 1 mm into the cisterna magna appears to be insufficient, as the cannula's tip did not reach the cisterna magna (subarachnoid space). As a result, the tracer may not adequately distribute to the brain via the proposed glymphatic pathway. The delineated region of interest (ROI) in Figure 3-5a-b illustrates the tracer's confinement outside the brain, indicating that the majority of the tracer is located outside the subarachnoid space.

To address the uncertainty surrounding the appropriate length of the cisterna magna cannula, an in vivo experiment was conducted using rat cadavers, adhering to the principles of Replacement, Reduction, and Refinement (the three Rs) to minimize the use of live animals. A 15 cm length of polyethylene tubing, with an inner diameter of 0.58 mm and an outer diameter of 0.96 mm, was filled with cod liver oil and securely sealed with superglue at both ends. Afterward, the tubing was advanced 6 mm into the cisterna magna and secured with superglue, following which a T_2 -weighted image was acquired in the sagittal plane. Figure 3-5c illustrates that 4 out of the 6 mm of tubing penetrated the brain, indicating that

the optimal length of the cannula should be 2 mm. As a result, a customized cisterna magna cannula with a 2 mm tip was standardized and employed consistently across all experiments. Figure 3-6 demonstrates that with the 2 mm tip, the cannula is precisely positioned within the cisterna magna.

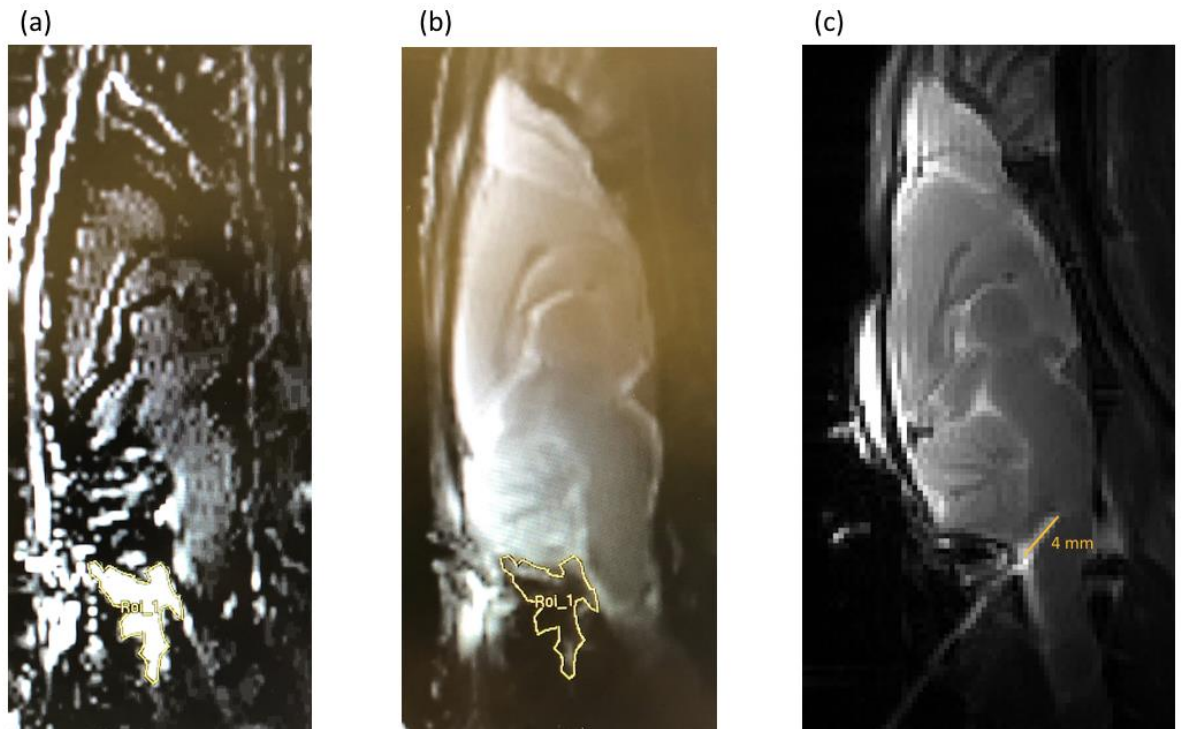


Figure 3-5: a. A difference image is generated by subtracting the baseline T2-weighted image from the image acquired 20 minutes after starting the tracer infusion. The ROI is delineated in yellow, indicating the retention of the tracer. b. A T2-weighted image with the same ROI is shown to provide a clearer perspective. c. A T2-weighted image depicting the brain of a deceased rat, with a marked line indicating the extra length of tubing inserted into the cisterna magna.

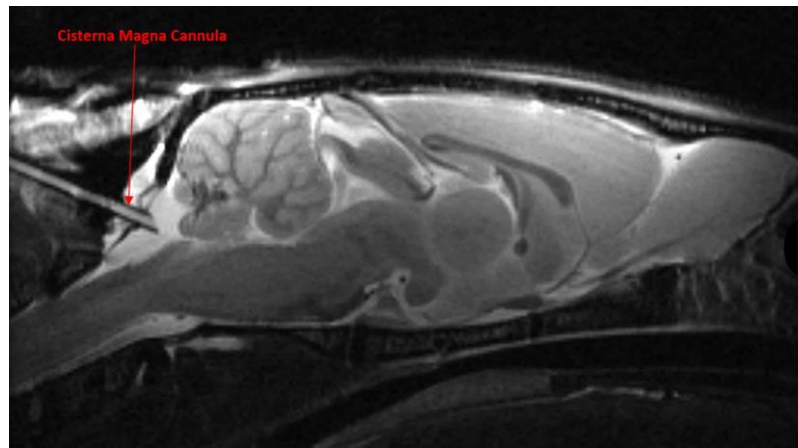


Figure 3-6: An example of a well-positioned 2 mm tip cannula is depicted here, which is a routine step to verify cannula positioning before commencing the experiment. The sequence employed is T₂ turbo spin echo in the sagittal orientation.

3.4.2.3 Determining the appropriate infusion rate

The size of the CSF compartment decreases with the size of the species. Therefore, when infusing contrast into the brain, considerable care must be taken to prevent an increase in ICP. This can be accomplished by adjusting the infusion rate to closely match the CSF production rate. In rodents under normal conditions, the CSF compartment volume is approximately 250 μL in rats and 40 μL in mice (Lee et al., 2021; Ma et al., 2008). Additionally, the CSF production rate is around 1.7 $\mu\text{L}/\text{min}$ in rats and 0.35 $\mu\text{L}/\text{min}$ in mice (Chiu et al., 2012; Karimy et al., 2015; Pardridge, 2016; Alshuhri et al., 2020). The following measures are considered safe for contrast media injection with minor changes in ICP: 20 to 80 μL infused at a rate of 0.5 to 3 $\mu\text{L}/\text{min}$ for rats, and 1 to 10 μL infused at a rate of 0.1 to 2 $\mu\text{L}/\text{min}$ for mice (Ding et al., 2018; Koundal et al., 2020; Xue et al., 2020).

A 3.0 $\mu\text{L}/\text{min}$ infusion rate in rat brains was deemed safe, only causing a slight perturbation in ICP with an elevation of approximately 6.3% from baseline (Bedussi et al., 2017). However, based on further investigations, a lower infusion rate of 1.6 $\mu\text{L}/\text{min}$ was chosen to avoid any increase in ICP (Yang et al., 2013; Cai et al., 2020). This decision was informed by the proximity of the 1.6 $\mu\text{L}/\text{min}$ infusion rate to the natural production rate of CSF in rats. Iliff and colleagues successfully utilized the 1.6 $\mu\text{L}/\text{min}$ infusion rate in their original study, where they injected MRI contrast media into the cisterna magna to investigate glymphatic flow in rat brains, demonstrating its safety and efficacy (Iliff, Lee, et al., 2013). Therefore,

before adopting the same infusion rate, we wanted to ensure that this rate would not induce any blood pressure instability in our animals, minimizing potential confounding factors that could adversely affect glymphatic flow.

The microinfusing pump (Carnegie Medicie CMA|100 Microinjection Pump with CMA|111 Syringe Selector) was utilized in this thesis for all intracisternal tracer infusions. To ensure precision, the accuracy of the infusion pump was evaluated. This assessment involved setting a specific flow rate and time period and carefully measuring the amount of solution delivered. To investigate the impact of intracisternal fluid infusion on blood pressure, a long line of aCSF extending from the microinfusing pump was connected to the cisterna magna cannula. The infusion protocol involved starting with a flow rate of 0.2 $\mu\text{L}/\text{min}$ and incrementally increasing it up to 1.6 $\mu\text{L}/\text{min}$. Each increment was spaced by a 5-minute interval over a period of 40 minutes. Throughout the experiment, the animal's blood pressure was continuously monitored and recorded, Figure 3-7. Notably, the blood pressure remained within normal ranges and was not negatively impacted even at the highest infusion rate of 1.6 $\mu\text{L}/\text{min}$.

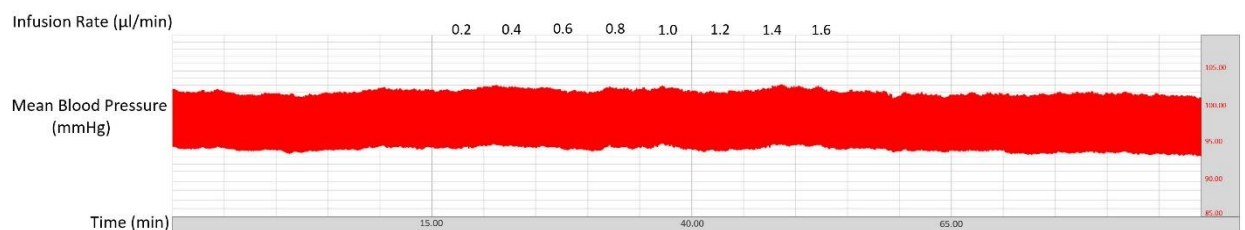


Figure 3-7: The aCSF infusion rate began at 0.2 $\mu\text{L}/\text{min}$ and was gradually increased to 1.6 $\mu\text{L}/\text{min}$, with 5-minute intervals between each increment. Concurrently, blood pressure was carefully monitored.

3.4.3 Bilateral common carotid artery stenosis

Bilateral carotid artery occlusion (BCAO) has been widely used in rat models; however, it often leads to acute and severe effects, with a mortality rate as high as 50% due to the abrupt drop in cerebral blood flow (Li et al., 2015; Wang et al., 2014). In contrast, we employ a bilateral common carotid artery stenosis (BCAS) surgical procedure, which involves narrowing the carotid arteries, resulting in a partial reduction of blood flow to the brain, known as cerebral hypoperfusion.

This procedure is primarily performed in animal research settings to mimic certain aspects of human diseases where blood flow reduction is gradual or intermittent, such as certain types of vascular dementia or transient ischemic attacks. The BCAS procedure in rats has demonstrated low mortality, with a 100% survival rate (Matin et al., 2016). Here, BCAS surgery is performed on rats, followed by MRI imaging. Cerebral blood flow is measured using ASL-MRI before and after the surgery. Additionally, imaging enhanced with contrast media will be conducted to assess glymphatic flow.

The BCAS surgery is performed following these steps: An aseptic environment is established to minimize the risk of infection. The surgical areas are shaved and sterilized to ensure cleanliness and prevent contamination. Next, a local analgesic (a subcutaneous injection of 0.5% bupivacaine) is administered, allowing sufficient time for the onset of action before proceeding. Following this, a midline incision, approximately 1 cm in length, is made along the neck to access the surgical site. The right common carotid artery is carefully exposed, and a blunt needle, with a diameter of 27-gauge and a length of 0.5 cm, is positioned adjacent to it. The carotid artery and the needle are securely tied together using two silk sutures (4-0), ensuring the ligatures are spaced 1-2 mm apart from each other, Figure 3-8. With caution, the needle is then extracted to create a partially blocked or narrowed section of the artery, inducing stenosis. The same procedure is repeated on the left common carotid artery. Finally, the wound is closed with sutures. Similar surgeries are conducted for sham procedures, which omit the securing ties on the arteries while maintaining the same surgical approach.

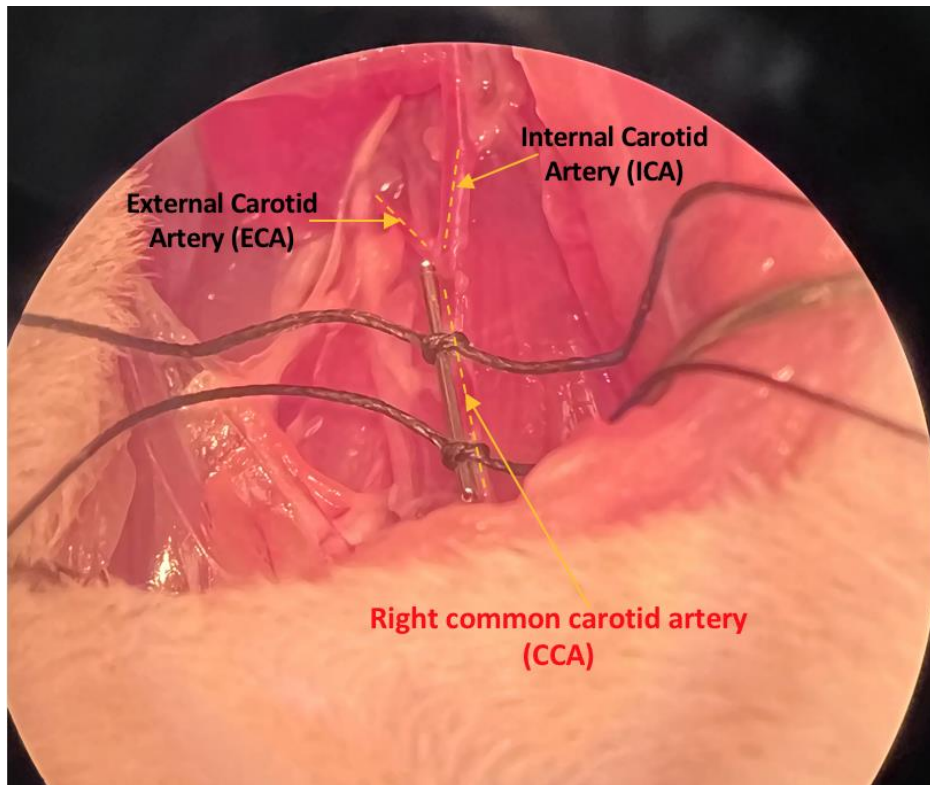


Figure 3-8: Under the microscope, the ties around the common carotid arteries are illustrated before the withdrawal of the blunt needle.

3.5 Animal recovery

Following surgery, before the rat is recovered, it receives subcutaneous injections of sterile saline for hydration and carprofen (5mg/kg) for analgesia. Next, the rat is weaned off the ventilator and allowed to fully recover. It is then transferred to a clean recovery cage placed on a warm surface to prevent hypothermia. The cage is lined with sterile absorbent bedding, and water and a soft diet are provided. During the initial recovery period, lasting up to 3 hours, the rat is closely monitored for any signs of distress, pain, abnormal behaviour, or bleeding. The animal's postoperative condition is documented regularly on a specific recovery monitoring sheet, Figure 3-9. Once the rat is fully conscious and exhibiting normal behaviour, including movement, grooming, eating, defecating, and urinating, the cage is returned to the animal's room. The following morning, the rat's postoperative behaviour and appearance are assessed and neurologically scored in accordance with the Principles of Laboratory Animal Care (PPL) before proceeding with the experiment, Figure 3-10. All recovered animals demonstrated normal behaviour and appeared to be thriving, with no mortality recorded (0%).

ANIMAL IDENTIFICATION		Score						
APPEARANCE								
Normal		0						
Slightly unkempt appearance		1						
Shining coat		2						
Slightly hunched		1						
Markedly hunched		4						
BODYWEIGHT LOSS								
Normal - < 5%		0						
Body wt. 5-10%		1						
Body wt. 10-15%		2						
Body wt. 15-19%		3						
Body wt. ≥20% (or BCS 1)		4						
CLINICAL SIGNS								
Diarrhoea		2						
Intermittent abnormal breathing		1						
Laboured respiration		3						
Dull, pale eyes		2						
Semi-closed eyes		2						
Less inquisitive than normal		2						
Little interaction with peers		3						
Barrel-rolling/frequent or unremitting fits (over period of >2 hours)		4						
PROVOKED BEHAVIOUR								
Normal		0						
Minor depression/exaggeration		1						
Moderate change		2						
Reacts violently or very little		4						
TOTAL								

JUDGEMENT

0	Normal
1 – 5	Animal will be monitored.
6 – 9	Monitor frequently, consider termination. If not terminated, seek second opinion from NACWO and/or NVS.
≥10 or any single score of 4	Clear suffering, terminate.

(BCS: Body Condition Score)

Figure 3-10: Animals scoring sheet.

3.6 Drug supplier and preparation

The AQP4 facilitator, TGN-073 (N-[3-(benzyloxy)pyridin-2-yl] benzenesulfonamide), and the AQP4 inhibitor, TGN-020 (2-(Nicotinamido)-1,3,4-thiadiazole), were purchased in bulk from Key Organics, Ltd., Camelford, Cornwall, UK. A 10 mM gamma-cyclodextrin solution (Sigma-Aldrich, St. Louis, Missouri, USA) and a 5% dimethyl sulfoxide (DMSO) solution (Sigma-Aldrich, St. Louis, Missouri, USA) are utilized to enhance the solubility of the drugs (Debaker et al., 2020). A total of 250 µL of DMSO and 4750 µL of sterile H₂O were added to gamma-cyclodextrin. The drug was added to the suspension and the mixture was

stirred with a magnet on a magnetic stirrer set at 500 rpm for 30 minutes before injection.

In Chapters 6 and 8, for the TGN-073/TGN-020 treatment groups, the drugs were intraperitoneally injected using a 25G needle at a dosage of 200 mg/kg, calculated based on body weight (20ml/kg), and administered 30 minutes prior to starting the MRI study. However, in Chapter 9, the animals were administered the drug immediately after undergoing the BCAS surgery. Meanwhile, the vehicle group received only gamma-cyclodextrin and DMSO dissolved in sterile water, without the drugs.

3.7 MRI imaging processing

In this thesis, standardized pre-processing steps for MRI images were consistently applied across all experiments, a topic that will be discussed herein, Figure 3-11. However, the post-processing of MRI images was tailored to the unique requirements of each experiment, which will be elaborated accordingly. All MRI image data processing was conducted using MATLAB software (MATLAB R2019a, MathWorks Ltd., UK), unless stated otherwise. Additionally, in-house codes were developed for analysis.

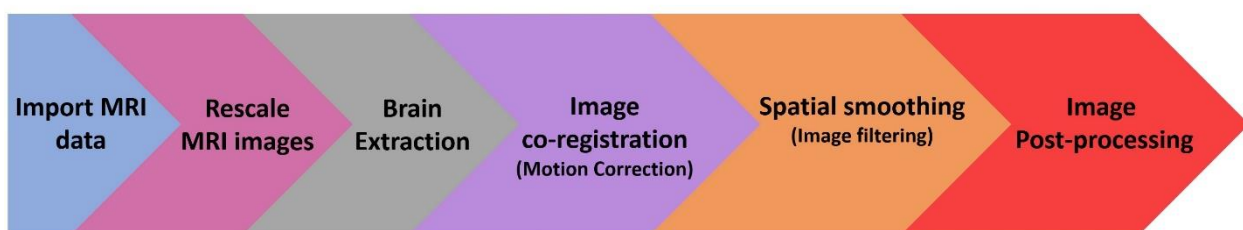


Figure 3-11: Pre-processing steps for MRI images.

The goal of MRI pre-processing is to enhance image quality and optimize the data for further analysis. Initially, MRI images are exported in DICOM format for processing. Following this, a rescaling of the image data is employed by multiplying the images by a scaling factor. This step aims to restore their original signal intensity, ensuring accurate representation of the imaging data. Next, a

mask is manually applied to remove surrounding non-brain structures and extract the brain. This step is crucial for facilitating proper image processing tasks, such as improved co-registration and reduced computational complexity.

Despite implementing several measures to minimize head motion in rats during MRI scanning, some motion remained unavoidable due to the long scanning time; sometimes lasting over 120 minutes. Rigid body registration was applied to mitigate motion artefacts. Co-registration was conducted using MATLAB's interactive Registration Estimator, available in the Image Processing Toolbox. This involved aligning all subsequent images to the initial image to compensate for inter-scan head motion. Figure 3-12 and Figure 3-13 show rat brain images both before and after co-registration.

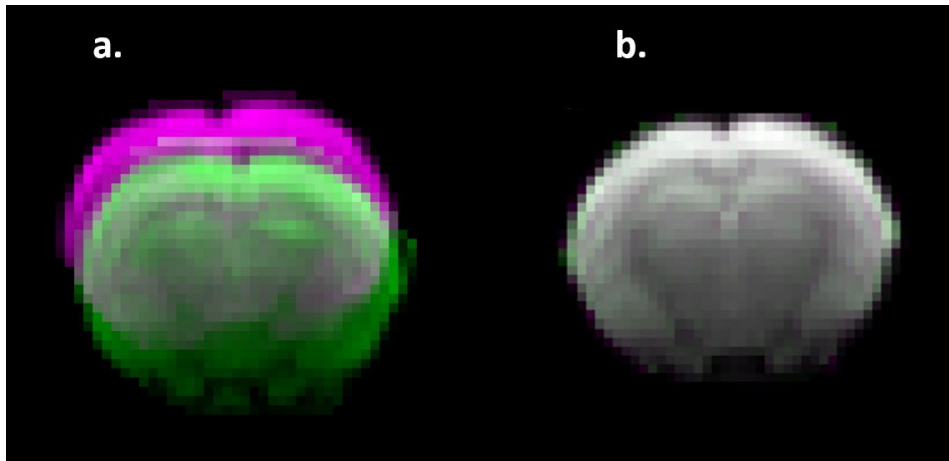


Figure 3-12: Images co-registration for pre-processing: a. depicts the image before co-registration, while b. illustrates the image after co-registration using rigid body registration. This process is essential for aligning images to a common coordinate system, enhancing the accuracy of subsequent analyses. The slice orientation is coronal, and the sequence is diffusion-weighted imaging.

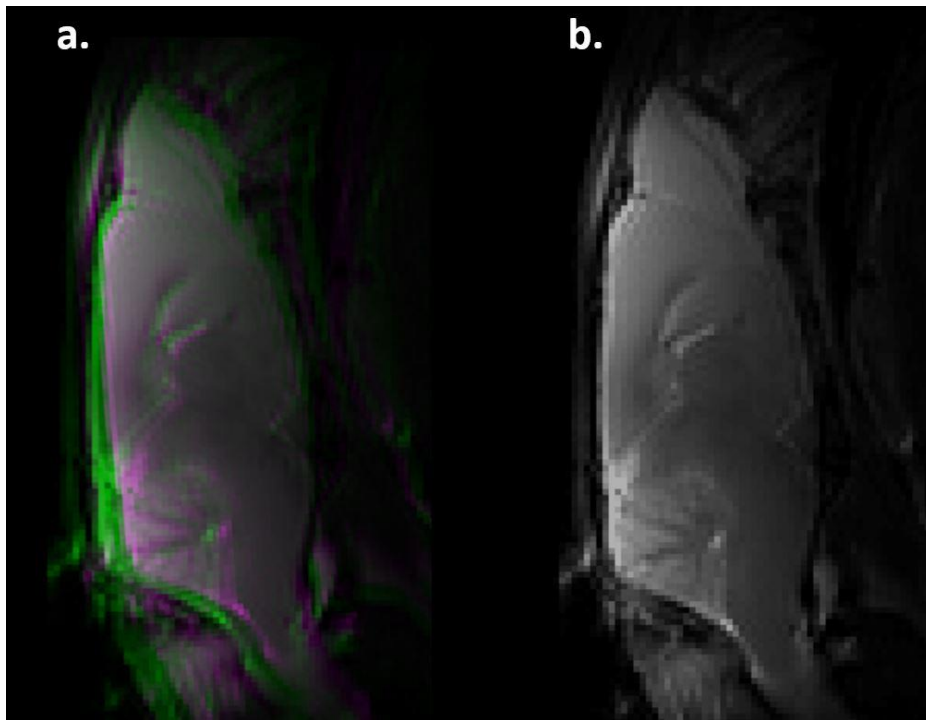


Figure 3-13: Another example for brain co-registration, with a. before and b. after motion correction. The slice orientation is sagittal, and the sequence is T_2 -weighted imaging.

To enhance image quality and reduce noise, the images underwent smoothing using the Perona-Malik diffusion (anisotropic diffusion) filter. This filter was selected specifically for its ability to improve the signal while preserving important image features, such as edges and boundaries, Figure 3-14. Finally, regions of interest were manually delineated for further processing. A thorough visual inspection is always conducted to ensure adequate pre-processing.

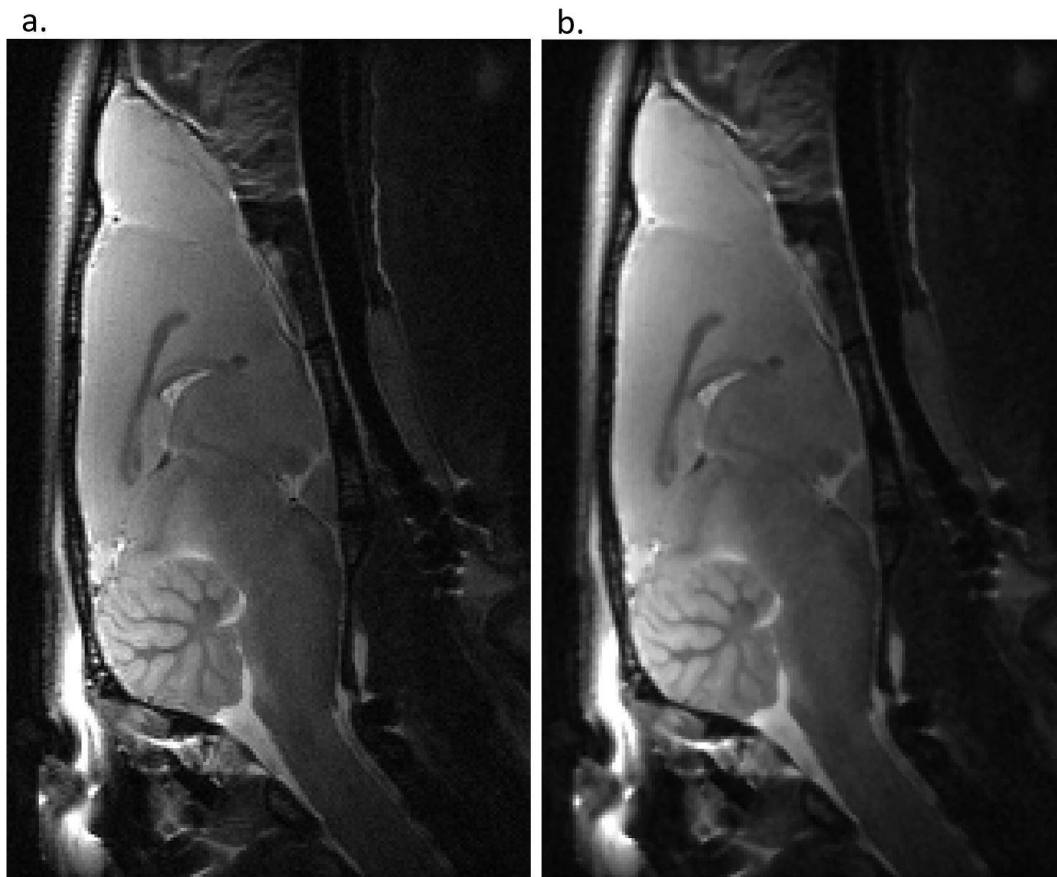


Figure 3-14: Rat brain MRI images: a. before smoothing, and b. after smoothing using an anisotropic diffusion filter. The slice orientation is sagittal, and the sequence is T2-weighted imaging.

Chapter 4 MRI Stability

In this chapter, the enhancements made to the MRI scanner aimed at improving its stability are explored. These modifications were prompted by observations during a pilot study, where the signal was expected to remain stable, but instead, fluctuations in signal intensity were detected. To address this issue, a thorough investigation was conducted to identify the underlying causes and implement corrective measures.

MRI scanner instability can arise from various sources, such as the magnet, gradients, or shims, resulting in signal fluctuations (McRobbie et al., 2017). Ensuring scanner stability is essential for reproducible, high-quality imaging, particularly for quantitative MRI techniques such as T_2 mapping, arterial spin labelling, and diffusion MRI, as well as for detecting small signal changes induced by oxygen-17 tracers (Rogers et al., 2017; Pang et al., 2022). These methods, to be used in upcoming experiments, rely on stable signal intensities and precise measurements to detect subtle biological changes (Khodabakhshi et al., 2024).

4.1 In vivo pilot study

4.1.1 Background

In this pilot study, the stability of the MRI system was assessed in vivo using the T_2 -weighted RARE sequence, employing aCSF. The primary objective was to ensure that the infusion of aCSF, predominantly composed of water (99%) (Hutton et al., 2022), into the cisterna magna did not induce any changes in signal intensity from the baseline. Notably, aCSF is not expected to affect the ^1H MRI signal. Establishing a stable baseline is imperative because, in the subsequent chapter, we will utilize water enriched with the oxygen-17 isotope (^{17}O) as an MRI tracer. Even minor signal fluctuations can significantly affect the results, given that ^{17}O

induces minimal signal changes. Therefore, ensuring the stability, precision and robustness of the MRI system is of paramount importance.

4.1.2 Methods

4.1.2.1 Animal procedure

An adult male Wistar rat was utilized (Charles River). Initially, surgical procedures were performed, including cisterna magna cannulation for the infusion of the MRI tracer, which in this case, was aCSF, and femoral artery cannulation for continuous monitoring of physiological parameters and arterial blood gas analysis. For detailed surgical procedures, please refer to the methodology chapter.

4.1.2.2 Magnetic resonance imaging

Imaging was performed using the 7 Tesla Bruker PharmaScan. The scanning protocol was as follows: first, a localizer scan was performed to adjust slice orientation and positioning. A 2D T_2 -weighted imaging RARE sequence was employed in the sagittal plane for the study. Sequence parameters were as follows: TR = 3000 ms, TE = 61.3 ms, NA = 4, flip angle = 90° , FOV = 6 cm, RARE factor = 12, acquisition time = 3 min 12 s, acquisition matrix = 200, slice thickness = 1.5 mm, slice gap = 1.5 mm, number of slices = 8.

Five baseline scans were conducted instead of only one to measure the noise relative to the true signal change induced by CSF tracers. Then, a total volume of 50 μl of aCSF was delivered intracisternally at an infusion rate of 1.6 μl per minute, while concurrent dynamic T_2 -weighted imaging of the glymphatic system was carried out and continued over a duration of two hours.

4.1.2.3 MRI data analysis

MRI image data processing was conducted using MATLAB software. MRI data pre-processing followed the steps outlined in the methodology chapter. Subsequently, all time series images obtained after the initiation of aCSF infusion were subtracted from the averaged baseline image. To correct for any signal variations due to the nonuniform sensitivity of the surface RF receiver coil, the subtracted images were normalized by dividing them by the average baseline. The percent

change in signal intensity was then calculated. These steps can be expressed mathematically as follows:

$$P(i, j, k) = \left(\frac{t_0(i, j, k) - t(i, j, k)}{t_0(i, j, k)} \right) \times 100 \quad 4-1$$

Where P represents the percentage signal change, t_0 is the signal intensity value of the averaged baseline image, t is the signal intensity value of the subsequent image, and (i, j, k) represents the voxel location.

Mean percentage signal intensity changes were extracted from regions of interest drawn within the cerebral cortex and the whole brain. Plotting these percentage signal changes as a function of time yielded the time-activity curves (TAC) for each region. Statistical analysis and graphs were plotted using Excel 2016 (Microsoft Windows).

4.1.3 Results

The TACs of both the whole brain and cerebral cortex revealed abnormal signal variations, as depicted in Figure 4-1. The percentage signal change induced by infusing aCSF plotted against time exhibited significant fluctuations of up to 9%, contrary to the expected 0% change. This discrepancy is particularly concerning because the signal change induced by $H_2^{17}O$ is approximately 10%, similar to the observed fluctuations without it. Therefore, further investigation was deemed necessary.

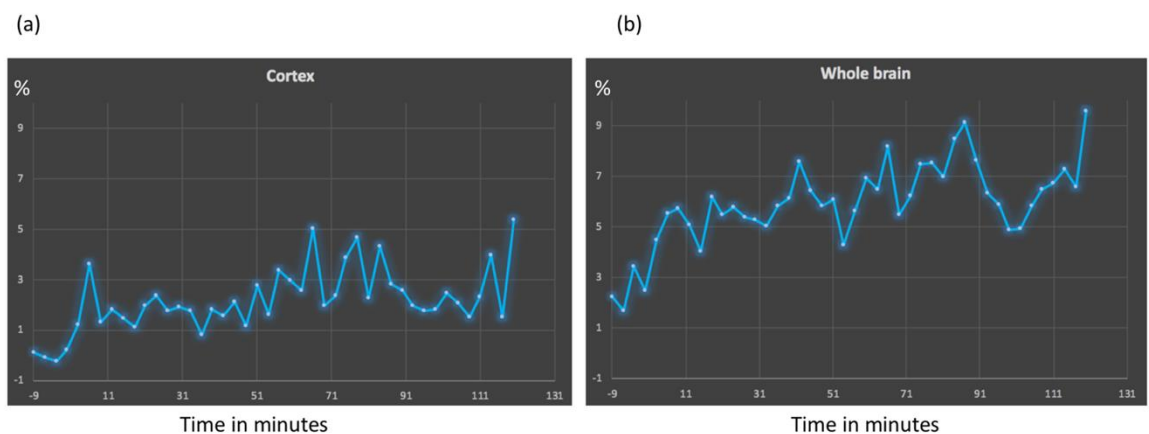


Figure 4-1: TACs illustrate the percentage signal change plotted against time for two brain regions: a. Brain Cortex, and b. Whole Brain.

Next, a series of phantom experiments was conducted to assess and improve magnet stability. Phantoms simulating rat brains were made and used instead of real rats, ensuring adherence to the principles of the 3Rs. These experiments employed a similar MR imaging sequence and quantitative data analysis methodology used in this *in vivo* study, unless specified otherwise. By ensuring consistency in methodology, any observed changes can be confidently attributed to improvements in magnet stability rather than variations in experimental procedures.

4.2 Phantom study

The primary objective is to determine the T_2 values of various concentrations of copper sulphate (CuSO_4) to identify the concentration that closely matches the T_2 value of the rat's cerebral cortex. Using a phantom containing CuSO_4 added to water instead of pure water is crucial due to the significantly shorter T_2 value of the cerebral cortex compared to the much longer T_2 value of pure water. In our 7 T magnet, the T_2 values are 55 ms for the cerebral cortex while 3000 ms for pure water.

CuSO_4 is paramagnetic, with longitudinal (r_1) and transverse (r_2) relaxivities of 0.602 and 0.730 L mmol⁻¹ s⁻¹ in a 3 T magnet, respectively (Thangavel & Saritaş, 2017). Compared to other materials such as glycerine and saline, CuSO_4 solution has been shown to produce the best contrast for T_2 -weighted sequences (Sales et al., 2016). There are numerous advantages to using CuSO_4 in MRI phantoms, including its high stability, solubility, and similarity in relaxation time to biological tissues (Thangavel & Saritaş, 2017).

Here, CuSO_4 was diluted in distilled water to produce solutions with concentrations ranging from zero to 10 g/L. Five plastic microcentrifuge tubes were filled with CuSO_4 solutions, starting at a concentration of 0.625 g/L and increasing progressively by a 2:1 ratio up to a concentration of 10 g/L in the fifth tube. Additionally, one tube was filled with pure water.

4.2.1 Magnetic resonance imaging

The MSME sequence was employed to generate T_2 mapping of each tube, using the following sequence parameters: TE = 20 ms, TR = 8000 ms, NEX = 1, number of echoes = 35, echo spacing = 20 ms, slice thickness = 2 mm, FOV = 35 x 35 mm, and matrix size of 96 x 96. This configuration yielded an in-plane resolution of 0.365 x 0.365 mm. The total scan time for the sequence was 9 minutes and 12 seconds.

4.2.2 T_2 values of CuSO_4

To measure T_2 values for each concentration of CuSO_4 , circular regions of interest were delineated on the MSME images using the Image Sequence Analysis (ISA) tool package (Paravision 6.0.1), Figure 4-2b. The water phantom (zero CuSO_4 concentration) exhibited the highest signal intensity, as water typically possesses the highest T_2 values. Conversely, the phantom with the highest CuSO_4 concentration (10 g/L) displayed the lowest signal intensity. T_2 exponential decay curves, as depicted in Figure 4-3, were fitted using the T_2 relaxation equation (2-36, Chapter 2). Table 2 presents T_2 values for each phantom, revealing a clear trend of decreasing T_2 values with increasing CuSO_4 concentration.

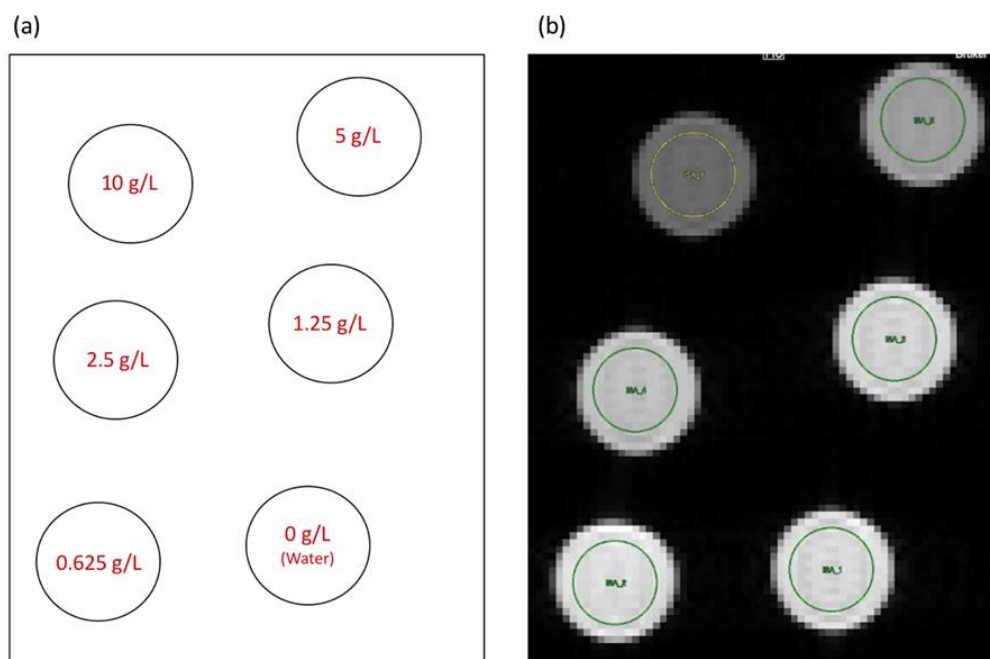


Figure 4-2: a. The drawing provides a visual representation that outlines how the phantoms are arranged. b. The corresponding image of the phantoms acquired using the MSME sequence.

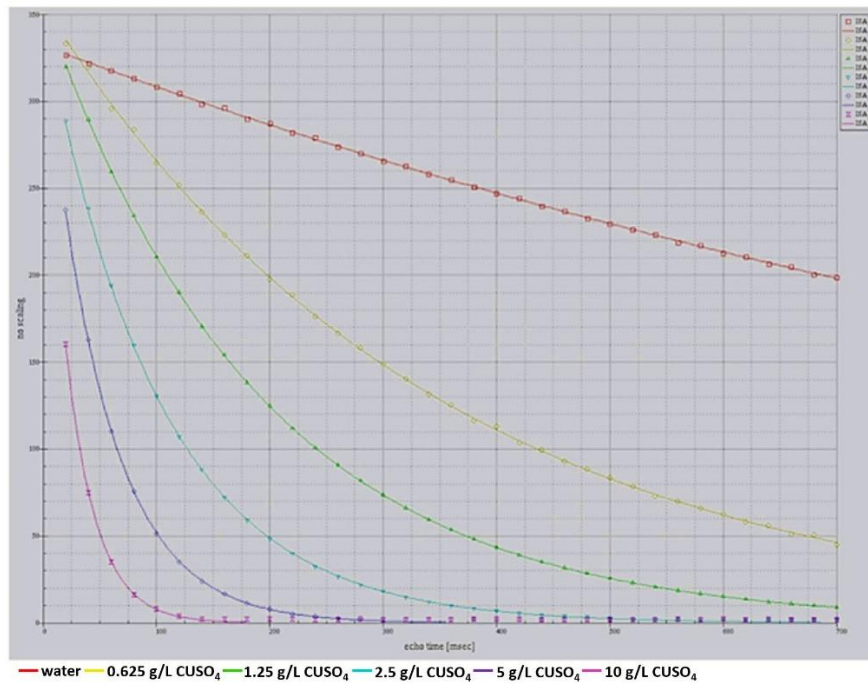


Figure 4-3: T₂ exponential decay curves of the six phantoms.

Table 2: Presents the T₂ values for each concentration of CuSO₄.

CuSO ₄ concentration in distilled water g L ⁻¹	CuSO ₄ concentration in distilled water mmol L ⁻¹	T ₂ value in seconds
0	0	1.36409
0.625	2.50312	0.344167
1.25	5.00625	0.190239
2.5	10.0125	0.101612
5	20.025	0.0528257
10	40.05	0.026666

4.2.3 Transverse relaxivity of CuSO₄

The relaxivity of a substance is a measure of its effectiveness in inducing changes in relaxation rates, reflecting its ability to influence the MRI signal. It quantifies how efficiently the substance interacts with surrounding protons to alter the relaxation behaviour, more details discussed in chapter two, section 2.5.3.

To determine the transverse relaxivity (r_2) of CuSO_4 at 7 tesla, the change in transverse relaxation rate (ΔR_2) was plotted against CuSO_4 concentrations (Figure 4-4). The slope of the regression line represents the r_2 of CuSO_4 , calculated as $0.9188 \text{ L mmol}^{-1} \text{ s}^{-1}$. Additionally, the linear regression analysis indicates a significant positive correlation between ΔR_2 and CuSO_4 concentration, with an R-squared value of 1.

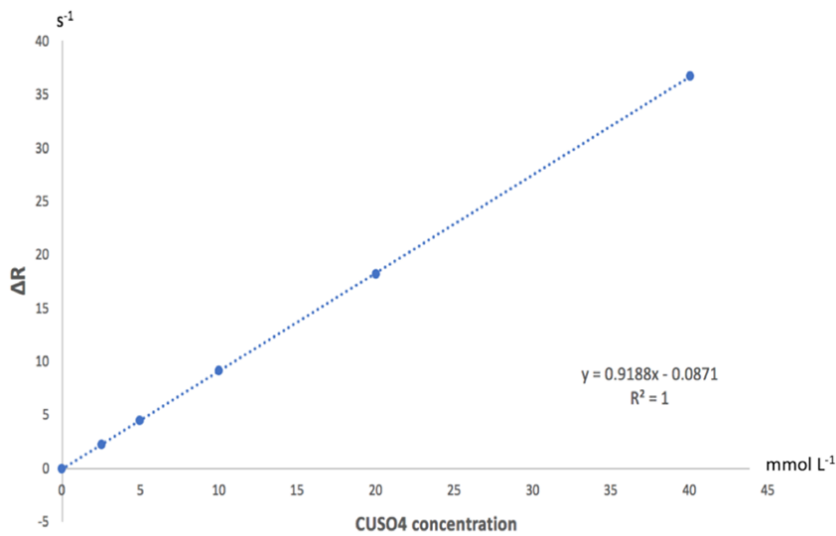


Figure 4-4: Linear regression analysis of the change in relaxation rate as a function of CuSO_4 concentration.

To determine the ideal concentration $[C]$ of CuSO_4 to match the T_2 value of the rat cerebral cortex, which has been determined in our system to be 55 ms, equation 2-42 is utilized after rearranging it as follows:

$$[C] = \frac{\Delta R_2}{r_2} \quad 4-2$$

Therefore, utilizing 4.7 g/L ($18.99 \text{ mmol L}^{-1}$) of CuSO_4 would yield a T_2 value of 55 ms. This concentration was used in distilled water to prepare the rat-head phantom, with the solution contained within a 50-mL centrifuge tube measuring 12 cm in length and 3 cm in diameter.

4.3 Magnet stability improvements

4.3.1 Active shim values

A slight shift in the field of view (FOV) was observed in the images of the phantom after running scans for more than two hours. This was evident when comparing the phantom localizer images in the axial view at the beginning and end of the scanning session. The images were overlaid in Figure 4-5a, and the arrows indicate the observed shifting. Upon examination, it was noted that the active (resistive) shim values were higher than expected, particularly in the y-axis, Table 3, even after resetting all values to zero. This raised concerns about potential negative effects on signal quality and FOV accuracy due to inaccurate shimming. Subsequent maintenance services were carried out by the manufacturer to address these issues. Afterward, a similar test was conducted, revealing the disappearance of the FOV shifting, Figure 4-5b. Additionally, there was a reduction in the active shim values, particularly in the y-gradient, indicating improved accuracy and stability, Table 3.

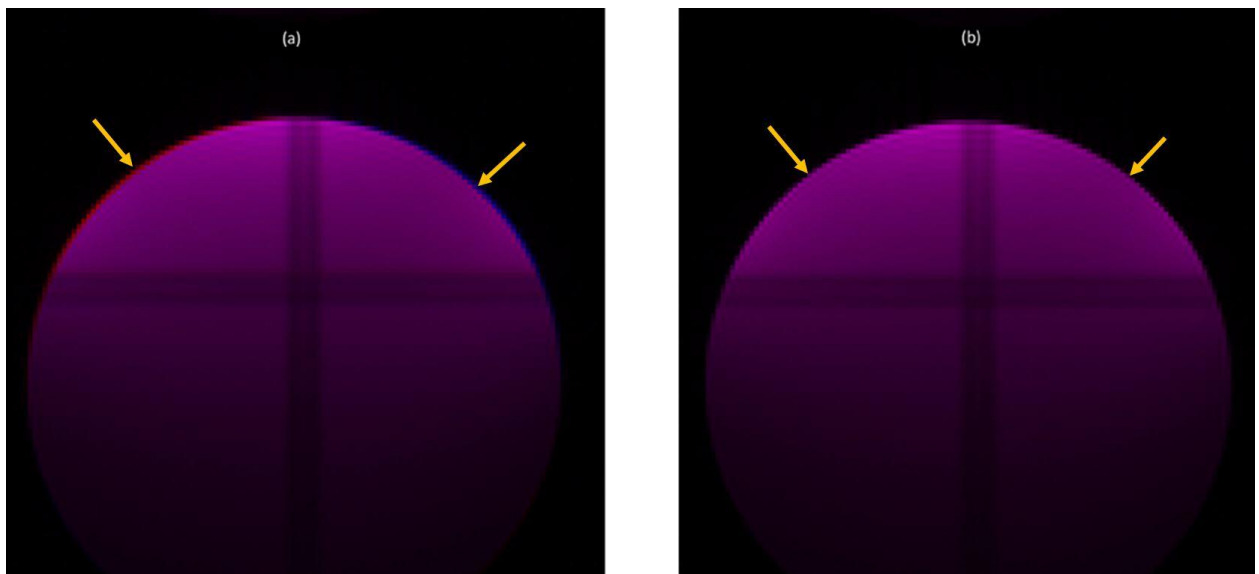


Figure 4-5: Localizer images in the axial view overlaid: 0 mins in red colour on top of 135 mins in blue colour. (a) Scan performed before maintenance services; a slight shift in the FOV is observed at the phantom's edges, as indicated by the arrows. (b) Scan performed after maintenance services, the shift in the FOV is no longer present, as shown by the arrows.

Table 3: Shim percentage values for the power supply before and after maintenance services.

	Readings before maintenance	Readings after maintenance
X	12.7± 0.6	11.3± 0.4
Y	20± 5	9.5± 0.4
Z	8± 1	5.5± 0.5

4.3.2 Impact of gradient runtime on MRI stability

In the department, it has been standard practice to power off the gradient system at the end of the day and restart it the following morning. To investigate the effect of this practice on MRI stability, a series of phantom experiments were conducted using the same sequence and data analysis employed in the in-vivo pilot study, 4.1.2. Four experiments were conducted with the gradient system powered off overnight and switched on the morning of the scanning day, while another four experiments were conducted with the gradient system left on overnight (i.e., for 24 hours). Each experiment involved acquiring a total of 45 serial T₂-weighted RARE images, with a total scan time of 135 minutes. Three circular regions of interest were manually delineated on the phantom images, maintaining consistent size and location across all images (see Figure 4-6). The percentage signal change was plotted as a function of time using TACs, Figure 4-7.

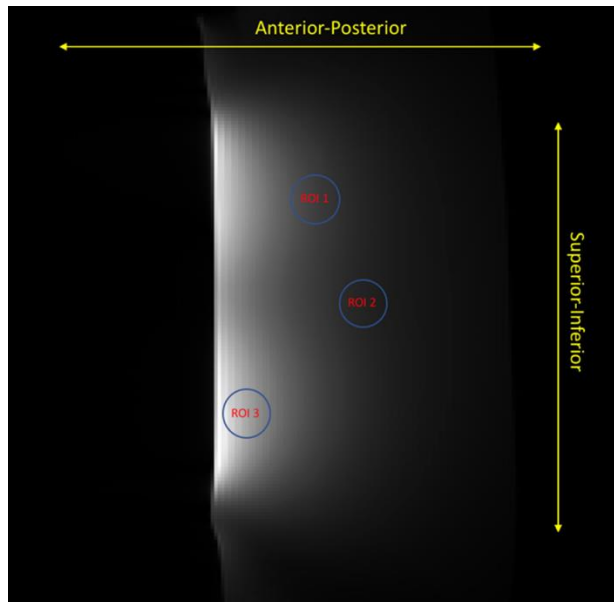


Figure 4-6: Three regions of interest (ROI) delineated at different locations relative to the receiver coil.

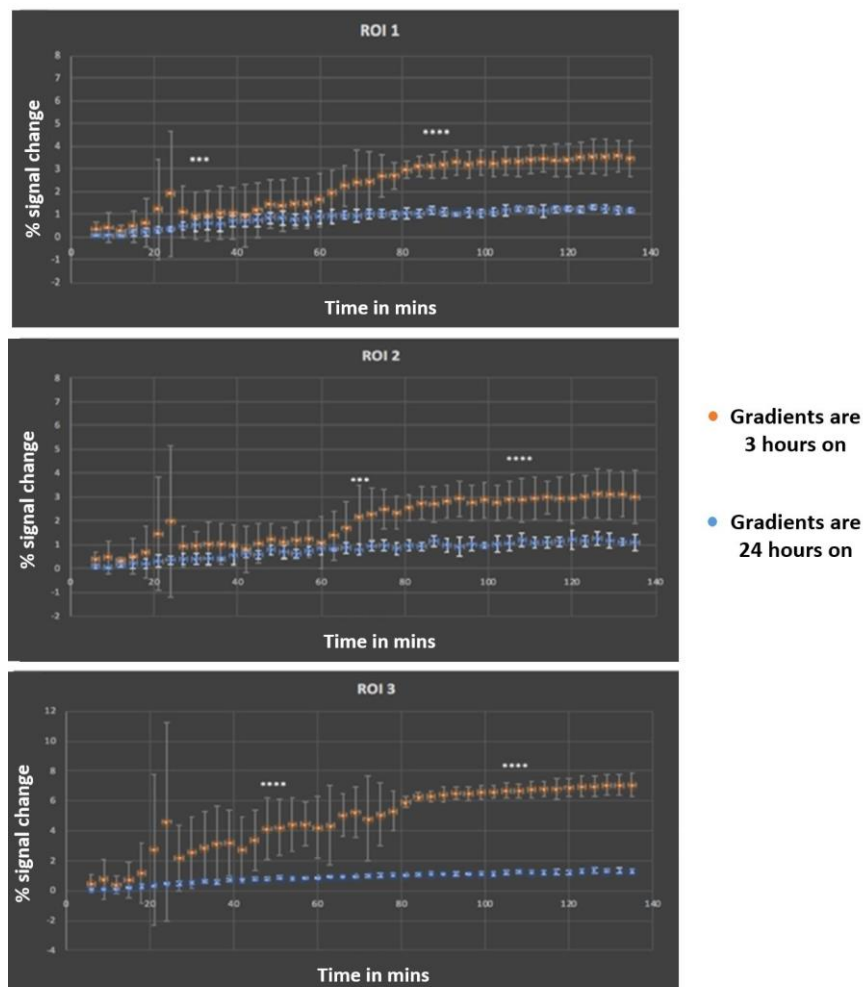


Figure 4-7: Time activity curves for each ROI depicting the percentage signal change from baseline over a 135-minute period. Blue markers represent experiments with gradients left on for 24 hours ($n=4$), while orange markers represent experiments with gradients on for 3 hours ($n=4$). Statistical significance is denoted by asterisks: *** $P < 0.001$, **** $P < 0.0001$.

Significant signal drift was observed when the gradients were switched on approximately 3 hours before scanning on the same day, as shown by the orange curves in Figure 4-7. Conversely, the signal remained quite stable when the gradients were left on for 24 hours, as illustrated by the blue curves.

The reason for signal instability could be attributed to several factors. One possibility is instabilities in the main magnet, as the gradient coils are situated inside the magnet. When the gradients are switched on in the same day, the temperature of the magnet may experience slight fluctuations. In contrast, leaving the gradients on overnight allows them to warm up and reach a stable temperature. Since the main magnet produces the B_0 field, which is slightly dependent on temperature, switching the gradients off and then on causes a change in the magnet's temperature before it reaches thermal equilibrium.

As a result, experiments conducted during the time before achieving equilibrium may be negatively affected. This effect is illustrated in Figure 4-7, where the signal drifts when the gradients are switched on 3 hours before scanning, eventually reaching a steady state around 80 minutes after the start of scanning. In conclusion, leaving the gradients on for 24 hours before scanning reduces signal fluctuations and leads to a more stable signal.

4.3.3 Basic frequency drifting

In MRI, precise tuning of the excitation pulse frequency to match the resonance frequency of the ^1H nucleus ($\omega_1 = \omega_0$) is essential. However, during scanning, a drift in the resonance frequency of the nucleus (the basic frequency) was observed. At the beginning of the scanning session, the basic frequency was measured at 300.3436570 Hz, while after 135 minutes of scanning, it was recorded at 300.3436338 Hz. This change in Larmor frequency caused a small shift in the FOV in the frequency direction, leading to a displacement of two pixels as indicated by the marker delineated by the red circle in Figure 4-8a.

As the gyromagnetic ratio is constant, any observed drift in the Larmor frequency during MRI scans is likely attributed to instabilities in the main magnetic field

strength. To mitigate this issue, adjusting the transmitted RF pulse was performed to ensure alignment with the centre of the Larmor frequency for each sequence during the scanning session. This step effectively minimized drifting FOV, as depicted in Figure 4-8b. Meanwhile, the time required for each adjustment was very small, with only an additional 8 seconds per sequence.

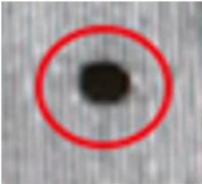
frequency direction	without frequency adjustment (a)	with frequency adjustment (b)
		
		

Figure 4-8: The image acquired after 135 minutes of scanning was subtracted from the baseline image, (a) without frequency adjustment and (b) with frequency adjustments. Markers indicating differences are delineated with red circles.

In conclusion, signal and FOV drifts were successfully eliminated. These improvements have resulted in a more stable signal and enhanced image quality.

In the next chapter, implementing all the improvements made in this chapter, a series of in vivo experiments will be conducted to enhance the signal change induced by intracisternal infusion of $H_2^{17}O$.

Chapter 5 Oxygen-17 Tracer: Chasing MRI Clues

The oxygen isotope ^{17}O has a quadrupolar nucleus. When incorporated into water molecules, ^{17}O induces a reduction in the T_2 relaxation times of the bonded hydrogen protons due to scalar dipole coupling. This effect is further intensified by the rapid chemical exchange of ^1H atoms between H_2^{16}O and H_2^{17}O , as discussed in Section 2.5.3.1 in Chapter 2. Here, a CSF tracer, H_2^{17}O , is indirectly detected by observing the ^1H signal reduction on T_2 -weighted imaging. However, a drawback of using H_2^{17}O as a CSF tracer is that the effect of ^{17}O on the ^1H MRI signal is small. In this chapter, various strategies aimed at enhancing the signal intensity change induced by H_2^{17}O are elucidated. The chapter concludes with experimental investigations where H_2^{17}O is mixed with various substances to make it denser (heavier) and potentially follow a pathway similar to the glymphatic system proposed in the literature.

5.1 Introduction

The primary aim of this thesis is to develop and validate innovative preclinical MRI techniques while investigating the impact of novel drugs targeting AQP4 water channels. The objective is to enhance brain clearance and gain deeper insights into the glymphatic system. For the first study, the plan was to examine the effect of the novel AQP4 facilitator, TGN-073, on glymphatic flow in normal rat brains by utilizing H_2^{17}O as an MRI tracer instead of standard GBCAs. This choice is motivated by the anticipation that using water labelled with ^{17}O will offer a more accurate measurement of the true glymphatic pathway. This is because it can pass AQP4 channels in a manner analogous to the movement of CSF and ISF via these channels.

A similar approach to the pilot study described in the previous chapter was employed, incorporating all adjustments to improve magnet stability. In this

study, however, water labelled with the ^{17}O isotope (H_2^{17}O , 90% enriched in Oxygen-17, 19 Da) (NUKEM Isotopes Imaging GmbH, Alzenau, Germany) was used as an MRI tracer, infused intracisternally, instead of aCSF. Despite this change, the signal intensity change induced by ^{17}O was minimal, with only a 2% signal change observed in the first control animal (Figure 5.1a). In contrast, using similar animal strains and imaging techniques, Alshuhri et al. reported approximately a 10% signal change, demonstrating successful H_2^{17}O tracer uptake in rat brains (Figure 5.1b) (Alshuhri et al., 2021). Consequently, various refinements were implemented, categorized into two subtypes: protocol-related and tracer-related adjustments, which will be discussed in detail.

The decision to use live animals instead of phantoms in these investigations was made to account for dynamic physiological effects that cannot be replicated by phantoms. This includes the influence of respiration on scanning, which can introduce motion artefacts, and variations in tissue positioning that are specific to living organisms. Furthermore, the process of infusing H_2^{17}O into the CSF, and its subsequent distribution within the CSF compartments, is influenced by the complex physiological environment of living animals, which cannot be accurately simulated in phantoms. Nonetheless, adherence to the principles of the three Rs was always maintained, for instance, one animal was utilized for all protocol-related adjustments.

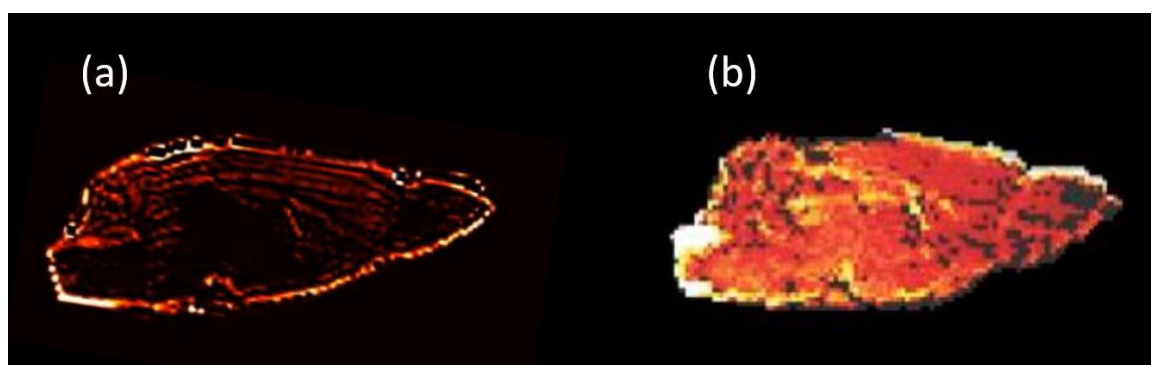


Figure 5-1: a. MRI image of the control rat's brain, acquired 20 minutes after initiating H_2^{17}O tracer infusion and subtracted from the baseline, showing no detectable presence of the tracer. b. Image from (Alshuhri et al., 2021) demonstrating successful H_2^{17}O tracer uptake in a rat brain.

5.2 MRI protocol-related adjustments

5.2.1 30-minute dummy scans

Signal instability could arise from various sources, including factors such as animal physiology and gradient instability. To mitigate these factors, dummy scans were performed for up to 30 minutes after placing the animal in the magnet and before initiating the actual scanning process. This preliminary step proved beneficial in achieving a stable signal state, as illustrated in Figure 5-2. One possible reason for this improvement is that allowing 30 minutes after connecting the cisterna magna cannula to the infusion pump may aid in stabilizing ICP and allowing the gradient to reach thermal equilibrium, thereby promoting a steady state signal.

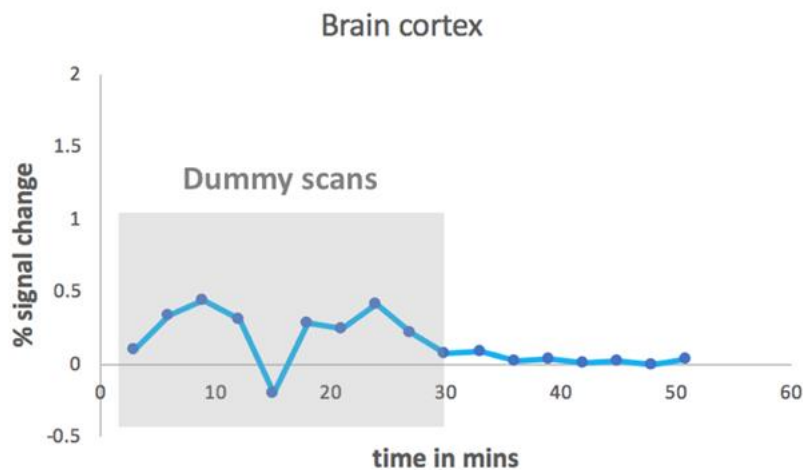


Figure 5-2: The percentage signal change is plotted continuously over a 50-minute period, with each scan lasting approximately 3 minutes. The ROI is delineated in the brain cortex.

5.2.2 Phase-frequency swapping

Motion artefacts were observed during the imaging of the rat brain, primarily due to movement caused by respiration, Figure 5-3a. This problem is exacerbated when using artificial ventilation in anesthetized rats. Motion artefacts, also known as phase mis-mapping artefacts, typically result from periodic movement of the anatomy (Westbrook & Talbot, 2018), leading to degraded image quality characterized by ghosting or blurring. These artefacts are commonly seen on MRI images in the phase encoding direction.

To address this issue, several remedies can be employed. Increasing the number of excitations (NEX) can help minimize motion artefacts. In our sequence, the NEX was doubled compared to the default sequence ($2 \gg 4$). Most importantly, switching the phase and frequency encoding directions enables the removal of motion artefacts observed in the phase encode axis (Weishaupt et al., 2003). To mitigate motion artefacts resulting from respiration here, which occur in the same direction as the phase encoding, the phase and frequency encoding directions were swapped. This adjustment effectively reduced the artefact, Figure 5-3b.

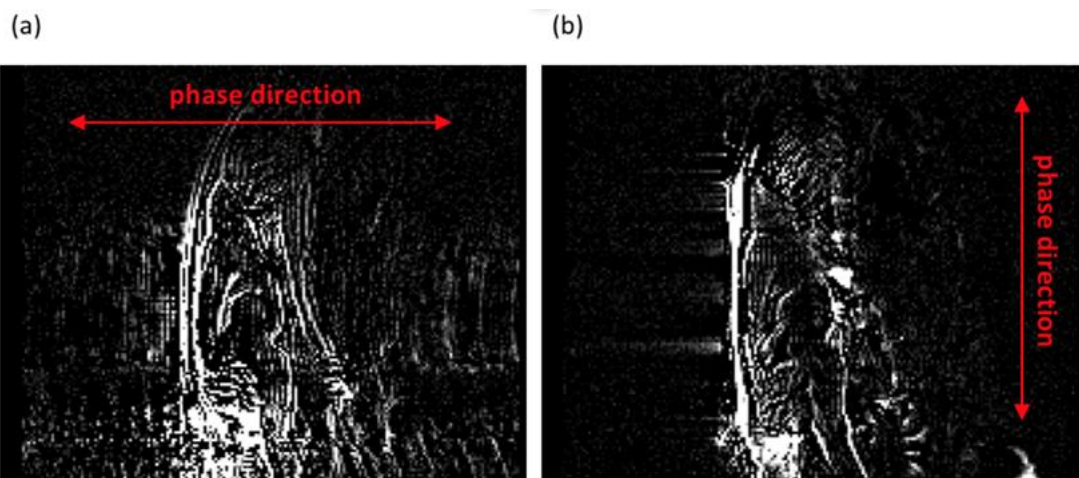


Figure 5-3: Subtracted MRI images of the rat's brain in sagittal view. (a) Original images with the phase direction oriented as anterior-posterior. (b) Images after swapping the phase direction to superior-inferior.

5.2.3 Magnetisation transfer

Chemical exchange magnetization transfer (MT) occurs when two populations, such as bound (hydrated) water molecules and bulk (free) water molecules, exchange magnetization. Bound water molecules might experience chemical exchange and dipole-dipole interactions with macromolecular hydrogen nuclei, in addition to interacting with free water on their outer surface (Henkelman et al., 2001; Ulmer et al., 1996). In multi-slice MRI experiments, in the slices that are not being slice selected, free water molecules will experience off-resonance RF frequencies, thus will not be excited. However, bound water molecules may experience on-resonance frequencies due to their broad spectrum of resonance frequencies becoming partially saturated, Figure 5-4. The rapid exchange

between bound and free water molecules leads to partially saturated free water. This in turn will reduce the longitudinal magnetisation (net magnetisation) of free water, reducing the acquired signal once the slice containing these water molecules is selected for imaging (McRobbie et al., 2017).

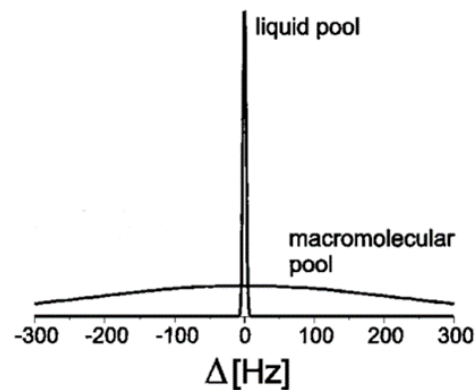


Figure 5-4: Free and bound water spectrum (Henkelman et al., 2001).

An *in vivo* study was conducted to investigate the MT effect in our experiments, as this effect does not appear with phantoms. The rat's brain was imaged using different numbers of slices (i.e. two, four, six and eight) (Figure 5-5) and the signal intensity was compared in the cerebral cortex and whole brain in the middle slice (Figure 5-6). The analysis revealed a strong negative correlation between the number of slices and signal intensity ($r = -0.8$). Specifically, reducing the number of slices from eight to two resulted in a significant signal gain of approximately 38%. Additionally, decreasing the number of RF excitation pulses induced less heat to the animal. In summary, lower numbers of slices led to lower MT and higher signal intensity. To optimize our T2-weighted RARE sequence, we reduced the number of slices from eight to two.

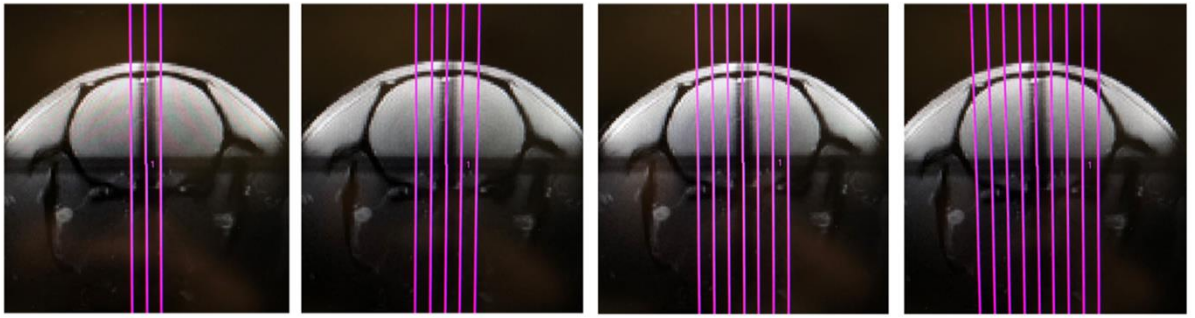


Figure 5-5: The images displayed here are brain localizers utilized for guidance. These localizers are oriented in the coronal plane. The pink lines indicate the number of slices that will be excited in the sagittal orientation.

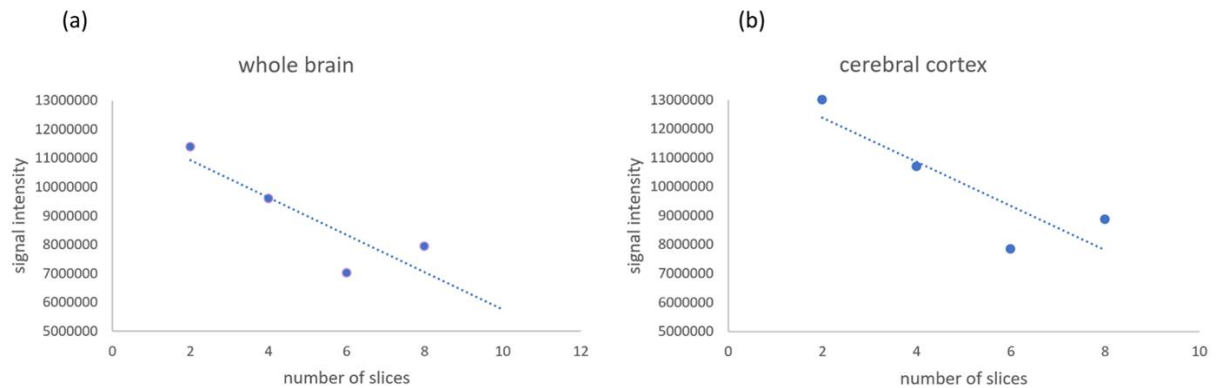


Figure 5-6: Scatter plot of signal intensity against the number of slices, with (a) the whole brain delineated and (b) the cerebral cortex delineated. The dashed lines represent the correlation line.

5.2.4 Introduce an angle to the animal's position in the cradle

When rats are positioned flat on the MRI cradle, MRI tracer infusion into the cisterna magna appears to result in immediate tracer escape, as depicted in Figure 5-7a. Instead of following the intended glymphatic pathway to the brain parenchyma, tracers may flow directly to the spinal cord. Lee et al. demonstrated that only a small portion of CSF tracers actually reach the brain parenchyma following injection through the cisterna magna cannula. This limited distribution is attributed to the presence of multiple efflux pathways from the cisterna magna, including drainage routes such as the spinal cord and vagus nerve, which divert CSF tracers away from the cranium (Lee et al., 2015).

Thus, maximizing the amount of tracer reaching the brain parenchyma to enhance the signal change induced by H_2^{17}O is crucial. Introducing a slight angle (6° cephalic) to the rat's positioning, with the head lower than the rest of its body, was implemented, Figure 5-7b. This angle aims to prevent the majority of the tracer from flowing directly out of the cranium. This adjustment helped retain most of the tracer and directed it toward the brain parenchyma. Throughout the experiment, close monitoring of the animal's physiology ensured that the introduced angle did not have any adverse effects; blood pressure and respiration remained stable.

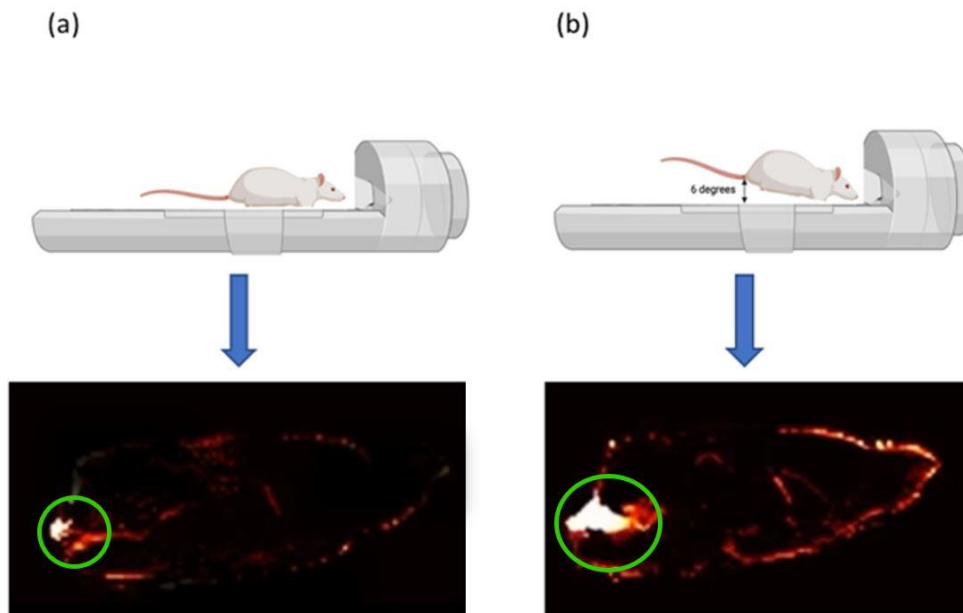


Figure 5-7: Comparison of MRI images of the rat brain after 9 minutes of tracer infusion under different positioning conditions: a. Rat positioned flat on the cradle. b. Rat positioned with an angle of 6° cephalic. H_2^{17}O in the cisterna magna is marked with green circles.

5.3 Tracer-related adjustments: Increasing H_2^{17}O density

The MRI tracer H_2^{17}O appears to deviate from the proposed glymphatic pathway in the brain, Figure 5-8a. While the typical glymphatic pathway involves CSF tracer running ventrally (as depicted in Figure 5-8b), H_2^{17}O instead flows dorsally toward the top of the brain (as depicted in Figure 5-8c). It may then be drained out of the brain via the superior sagittal sinuses before entering the brain parenchyma. It's worth noting that glymphatic studies often use heavier tracers, such as Gd-

DTPA, which have a higher molecular weight compared to H_2^{17}O (938 versus 19, respectively). Therefore, the aim of this experiment was to increase the density of H_2^{17}O by mixing it with high-molecular-weight, yet biologically safe, compounds, with the hypothesis that increasing the tracer density might enable H_2^{17}O to follow a pathway similar to that observed when using Gd-DTPA.

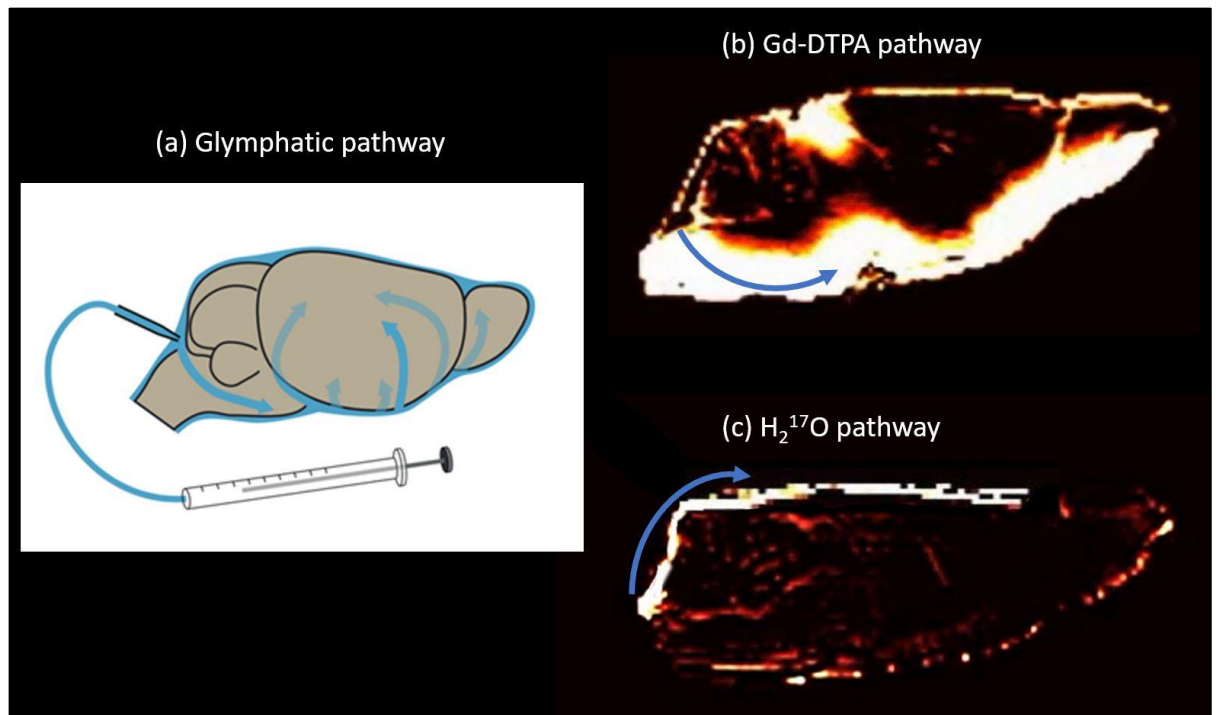


Figure 5-8: a. The suggested glymphatic pathway in the rat brain. b. MRI of the rat brain 20 minutes after infusing Gd-DTPA. c. MRI of the rat brain 20 minutes after infusing H_2^{17}O . The blue arrows indicate the direction of the tracers.

5.3.1 Methods

Male Wistar rats (Charles River), aged 20 to 24 weeks old and weighing 300-380 g, were used in this experiment. Each rat underwent three surgical procedures: cisterna magna cannulation to enable MRI tracer infusion, femoral artery cannulation for blood gas analysis and direct BP and HR measurements, and tracheotomy for artificial ventilation.

H_2^{17}O (90% enriched oxygen-17) was combined with various compounds to enhance its density. In the first group (n=3), rats received H_2^{17}O mixed with evaporated aCSF, which is enriched with salts like NaCl and KCl. This involved heating 50 μl

of aCSF overnight to evaporate the water, leaving salt deposits that were then mixed with 50 μl of H_2^{17}O . The second group ($n=3$) received H_2^{17}O mixed with double the amount of evaporated aCSF (100 μl), resulting in a higher salt concentration. In the third group ($n=3$), rats received H_2^{17}O mixed with dextran ($\text{C}_6\text{H}_{10}\text{O}_5$) $_n$, a complex carbohydrate with a molecular weight of 4500, composed of glucose molecules linked through α -1,6 glycosidic bonds. 50 μg of dextran, purchased in solid form (Sigma Aldrich, CAS# 9004-54-0), were mixed with 50 μl of H_2^{17}O . The fourth group ($n=3$) served as the control and received 50 μl of H_2^{17}O without any additional compounds. Throughout these preparations, the pH of all MRI tracers was maintained within a neutral range (7 to 7.4). Rats were randomly assigned to each group.

A dynamic T_2 -weighted RARE sequence was employed to continuously capture the glymphatic flow over a two-hour period, starting from the initiation of cisterna magna infusion. All previous adjustments made to improve magnet stability and refine the MRI protocol are incorporated. Data analysis followed the procedures outlined in section 4.1.2. In summary, after pre-processing the MRI images, baseline subtraction, normalization, and percentage signal change calculations were performed for multiple ROIs, as shown in Figure 5-9.

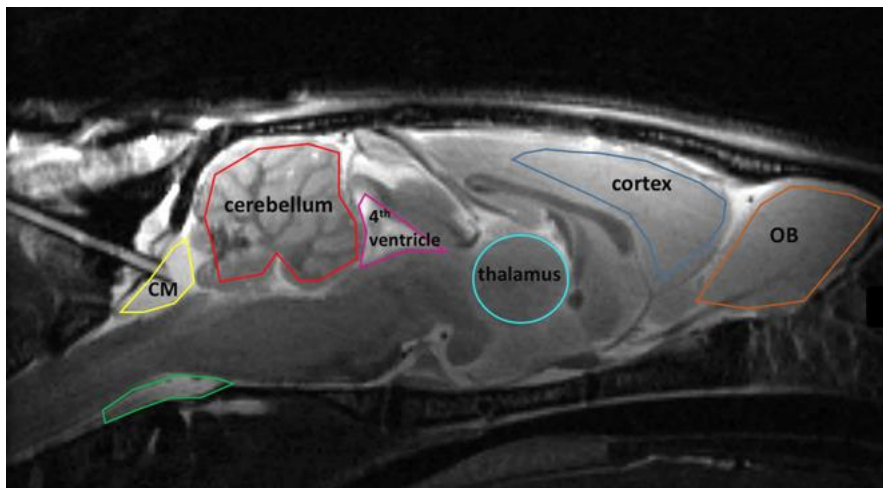


Figure 5-9: The ROIs delineated for calculating the percentage signal change induced by different combinations of H_2^{17}O . The image used is sagittal T_2 -weighted RARE.

5.3.2 Results

When H_2^{17}O is mixed with compounds such as salt and dextran, it exhibits an increase in density and subsequently sinks below the brainstem and spinal cord, as delineated in green in Figure 5-10. Due to its high molecular weight, dextran induces the highest level of tracer sedimentation, followed by the tracer combined with double the amount of aCSF. This observation, particularly the direction of H_2^{17}O + dextran flow, bears resemblance to the pathway followed by GBCAs. However, despite these characteristics, the uptake of the tracer by the brain remains very low.

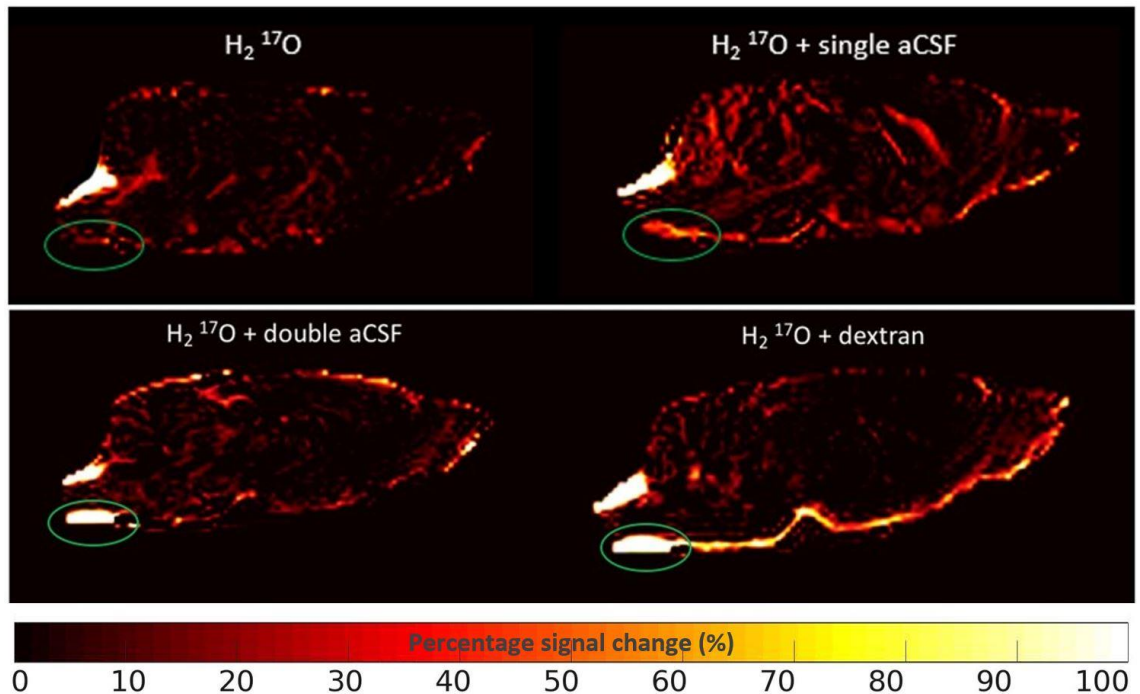


Figure 5-10: The images depict the rat brain enhancements after 20 minutes of starting the infusion of different combinations of H_2^{17}O .

When employing TACs (representing percentage signal change over time) for quantitative analysis of cerebral uptake, the results were profoundly disappointing. Both salt and dextran combined with H_2^{17}O failed to show any significant enhancements, as depicted in Figure 5-11.

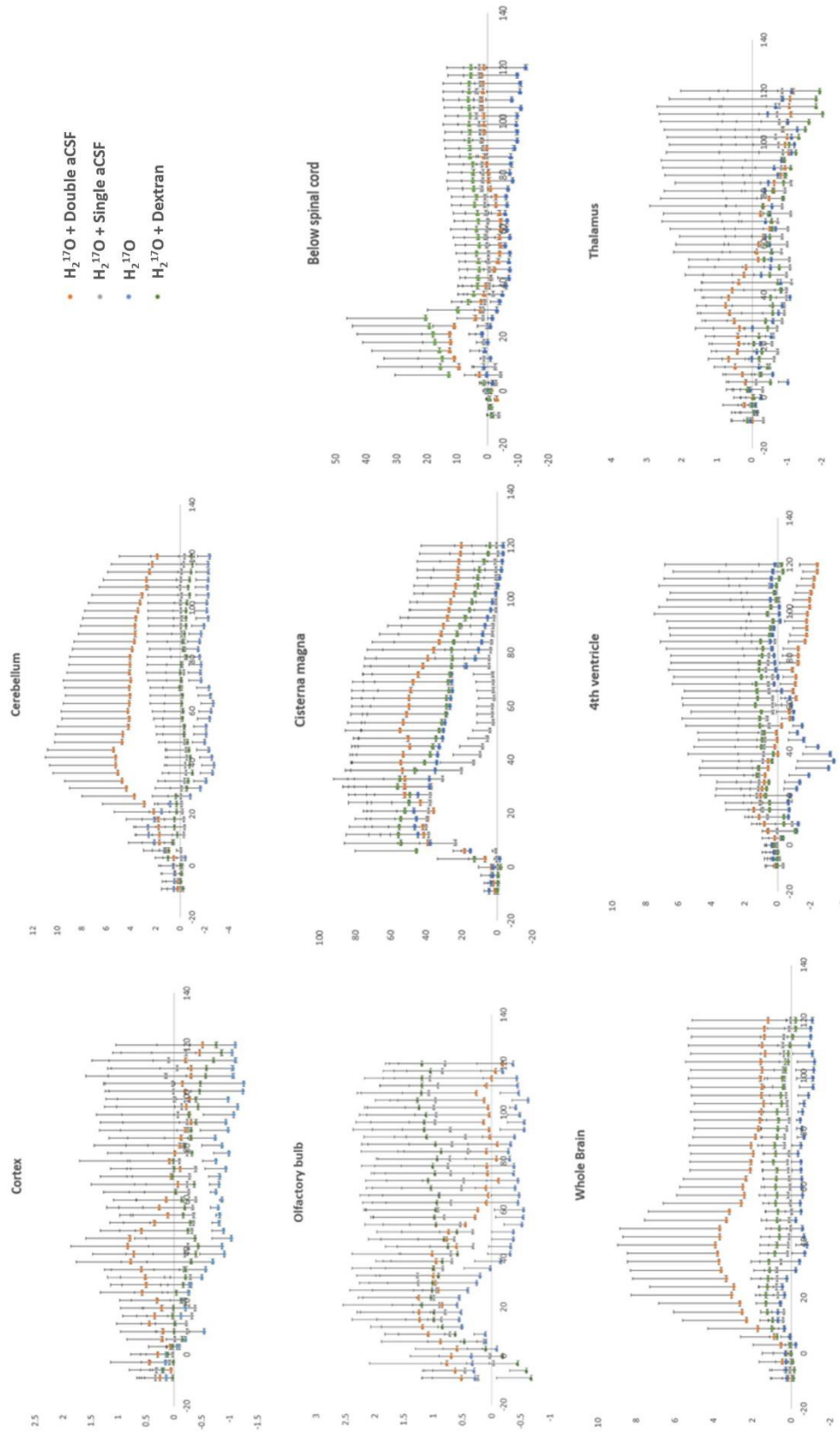


Figure 5-11: Percentage signal change plotted as a function of time for several brain regions.

5.3.3 Discussion

The challenge in detecting H_2^{17}O within the brain could be attributed to several factors, including the rapid washout of the tracer before its detection. It has been reported that the flow of the water tracer (H_2^{17}O) is faster than that of Gd-DTPA (Alshuhri et al., 2021). It could also arise from its rapid dispersion and dilution with CSF. As the tracer travels towards the brain, its concentration diminishes significantly, making its detection difficult. However, the presence of the tracer is evident from the pronounced signal change observed in the cisterna magna. Additionally, the cerebellum shows some uptake of H_2^{17}O due to its proximity to the cisterna magna. Nevertheless, as we move away from the cisterna magna towards the brain cortex, the H_2^{17}O signal diminishes rapidly. This decline in signal is expected, as the small amount of tracer administered (50 μl) becomes increasingly diluted with CSF, eventually dissipating.

In conclusion, despite diligent efforts made to optimize the image quality and enhance the signal from H_2^{17}O , the signal remains too weak to reliably conduct important studies, such as assessing the effects of AQP4 modulators on glymphatic function. Therefore, GBCAs were chosen over H_2^{17}O for subsequent experiments.

Chapter 6 The effect of a novel AQP4 facilitator, TGN-073, on glymphatic transport captured by diffusion MRI and DCE-MRI

The glymphatic system is a low resistance pathway, by which CSF enters the brain parenchyma along perivascular spaces via AQP4 water channels. It has been hypothesised that the resulting convective flow of the ISF provides an efficient mechanism for the removal of waste toxins from the brain. Therefore, enhancing AQP4 function might protect against neurodegenerative diseases such as AD. Here, different MRI techniques were employed to demonstrate that glymphatic function is enhanced by the novel AQP4 facilitator, TGN-073. This might aid in preventing or treating neurodegenerative diseases in which the AQP4 functionality is impaired.

6.1 Introduction

In humans, a quarter of the body's total energy expenditure is consumed by the brain, and around seven grams of waste solute are excreted every day (Nedergaard & Goldman, 2016). The clearance of metabolites, neurotransmitters and toxic macromolecules in an organised manner is necessary to maintain homeostasis, and prevent their accumulation and the associated initiation of pathologies. Conventionally, interstitial solutes were thought to be transported via diffusion, but recent evidence suggests an additional bulk flow of the ISF. The glymphatic (glial-lymphatic) model proposes that subarachnoid CSF is driven by arterial pulsation along the perivascular space surrounding penetrating arteries, with influx into the brain interstitium mediated by the astroglial water channel AQP4 (Iliff et al., 2012; Iliff, Wang, et al., 2013; Mestre, Tithof, et al., 2018). It is proposed that this influx results in a slow bulk flow of ISF, which then exits along perivenous spaces. This bulk flow provides a more efficient clearance mechanism

from the parenchyma than diffusion alone would. To date, glymphatic function has been implicated in the clearance of amyloid beta, tau, alpha synuclein and lactate (Lopes et al., 2022; Zhang et al., 2023; Iliff et al., 2014, 2012; Lundgaard et al., 2017). In addition, it is speculated to be involved in the clearance of other solutes that cannot be locally degraded or efflux across the blood brain barrier. It has been suggested that AQP4 water channels play a crucial role by facilitating water exchange (Mestre, Mori, et al., 2020).

AQP water channels are capable of bidirectional water movement across cell membranes. Water transported via these channels is governed by both hydraulic pressure and passive osmotic gradients. Thirteen types of AQPs have been verified as being distributed throughout the whole body of both rodents and humans. However, significant interest is directed at AQP4 due to its dense expression in the central nervous system. The distribution of AQP4 in astrocytic end feet is mainly at two regions, the perivascular space surrounding the cerebral vasculature, and the glia limitans externa underneath the pia mater (Huber, Igarashi, et al., 2018). Thirty-five per cent of the plasma membrane of the end feet of astrocytes is occupied by AQP4, in particular, the membrane facing the blood vasculature at the BBB (Amiry-Moghaddam et al., 2004; Papadopoulos & Verkman, 2013). Studies using AQP4 knockout mice have shown glymphatic function is mediated by AQP4, with both the influx of CSF and efflux of ISF diminished compared to wild types (Iliff et al., 2012). Further, it has been demonstrated that the loss of perivascular AQP4 localisation impairs glymphatic function (Plog & Nedergaard, 2018).

In several animal models of disease, glymphatic dysfunction has been identified. Ischaemic stroke in rodents has been associated with elevated glymphatic activity that might lead to the initiation of cerebral oedema (Mestre, Du, et al., 2020). In contrast, reduced glymphatic function has been observed in animal models of AD and traumatic brain injury (Iliff et al., 2014; Xu et al., 2015).

In-vivo human MR studies have demonstrated the presence of glymphatic function, showing brain-wide enrichment of intrathecally administered CSF tracer (Gadobutrol), with a dementia cohort exhibiting delayed tracer clearance (Ringstad et al., 2018). Moreover, dynamic ¹¹C-PiB PET has confirmed CSF-

mediated clearance deficits in patients with AD (Schubert et al., 2019; De Leon et al., 2017). Further, post-mortem studies of Alzheimer's patients have shown that AQP4 is upregulated (Moftakhar et al., 2010; Hoshi et al., 2012), with a loss of perivascular localisation (Zeppenfeld et al., 2017). These results indicate that altering AQP4 function pharmaceutically, by either facilitating or inhibiting water exchange, could aid in managing many neurological pathologies.

Earlier works have investigated the role of AQP4 in the brain either by inhibiting AQP4 pharmacologically or by genetically modifying rats and mice by deleting the AQP4 gene (Igarashi et al., 2011; Jerome Badaut et al., 2011; Manley et al., 2000). Using similar methods, later studies have investigated the role of AQP4 in the glymphatic system (Feng et al., 2020; Iliff et al., 2012; Xu et al., 2015; Harrison et al., 2020; E. Liu et al., 2020; Teng et al., 2018). Recently, it has been shown that a readthrough extended version (AQP4X) is exclusively perivascular and that A β clearance is reduced in AQP4X-specific knockout mice (Sapkota et al., 2022). Further, high-throughput screening has identified small molecule compounds that enhance readthrough of the AQP4 sequence (Sapkota et al., 2022).

In addition, a novel AQP4 facilitator (TGN-073) has been identified (Huber, Igarashi, et al., 2018). It has been postulated that ligand interaction with AQP4 leads to a conformational shift, especially in the protein loop spanning the H2 and HB helices increasing the channel diameter and increasing water flux (Kaptan et al., 2015). However, it is also possible that TGN-073 exerts an indirect effect on AQP4. For example, by impacting translational readthrough of AQP4 (Sapkota et al., 2022), by impacting subcellular localisation of AQP4 (Salman et al., 2022) or via some other unknown mechanism. Here we seek to investigate the effect of this novel AQP4 facilitator on the glymphatic transport in the normal rat brains using dynamic contrast-enhanced-MRI and assess changes in tissue water diffusivity using diffusion MRI.

6.2 Methods and Materials

6.2.1 Animals

Male Wistar rats were employed in this study (Charles River; aged: 20 to 24-weeks old, body weight: 300-380 g). Animal groups: vehicle (n=7), negative control aCSF (n=3) and TGN-073 treated group (n=7). Rats were randomly assigned to either the treated or the vehicle group. Two rats were excluded from the study, one vehicle and one TGN-073 treated, due to sudden death and unstable blood pressure, respectively. All animals were housed in the MRI unit one week prior the study for acclimatisation to reduce variabilities in results. Food and water access was *ad libitum*, and 12 h dark and 12 h light cycle was maintained. Humidity ($53 \pm 2\%$), ventilation and temperature ($21.5 \pm 0.5^\circ\text{C}$) were controlled automatically. The sample size was based on literature (Iliff, Lee, et al., 2013).

Heart rate, respiration rate and blood pressure were monitored throughout the experiments along with arterial blood gases. The rats' mean physiological signs were: respiration 65 ± 5 breaths per minute, heartbeats per minute 400 ± 50 and mean blood pressure 95 ± 5 mmHg. In addition, the core body temperature was monitored throughout the whole experiment and was maintained at $37.0 \pm 0.5^\circ\text{C}$ using a rectal thermocouple and controlled by a heating pad (Polystat® Cole-Parmer). At the end of scanning, animals were euthanised.

6.2.2 Drug Preparation

A detailed protocol for the preparation of the AQP4 facilitator TGN-073 is provided in the Methodology chapter, Section 3.6. In the TGN-073 treatment group, the drug was injected intraperitoneally using a 25G needle (200 mg/kg in 20 ml/kg body weight). This dose was selected based on the developer's original study (Huber, Igarashi, et al., 2018). Gamma-cyclodextrin (10 mM) and 5% DMSO were used to increase the solubility of TGN-073. Meanwhile, the vehicle group only received gamma-cyclodextrin and DMSO dissolved in distilled water. Both the treatment and vehicle groups received their respective injections 30 minutes before the start of the MRI study.

6.2.3 Animal Surgery

The study design is shown in Figure 6-1. Details regarding all surgical aspects can be found in the Methodology chapter. In summary, the anaesthetic regimen was as follows: initially, all rats were induced with 5% isoflurane inside an induction chamber using O₂ and N₂O as carrier gases (0.3 and 0.7 l/min respectively). Then, when the rats lost consciousness (i.e. did not respond to toe pinch) the animal was transferred onto facemask and isoflurane was reduced to 1.5%-2.5%, while keeping the same volume of O₂ and N₂O (ratio 30:70). Next the surgical areas were shaved and sterilised. The animal was then intubated via tracheotomy for artificial ventilation using a 13 G feeding tube and connected to a ventilator (Harvard Apparatus). A homeothermic blanket system with a rectal probe was used. Cannulation of the femoral artery was performed with polythene tubing PE-50 (diameters: 0.58 mm ID, 0.96 mm OD, Smith Medical International Ltd) and this was connected to a blood pressure transducer to measure arterial BP and HR continuously (Biopac Systems, MP100), and for the regular analysis of arterial blood gases and pH (epoc® Blood Analysis System, Siemens Healthineers). Parameters were maintained as follows: partial pressure of oxygen 90-110mmHg, partial pressure of carbon dioxide 35-45mmHg, pH 7.4 ± 0.1, and O₂ saturation: 97%-100%.

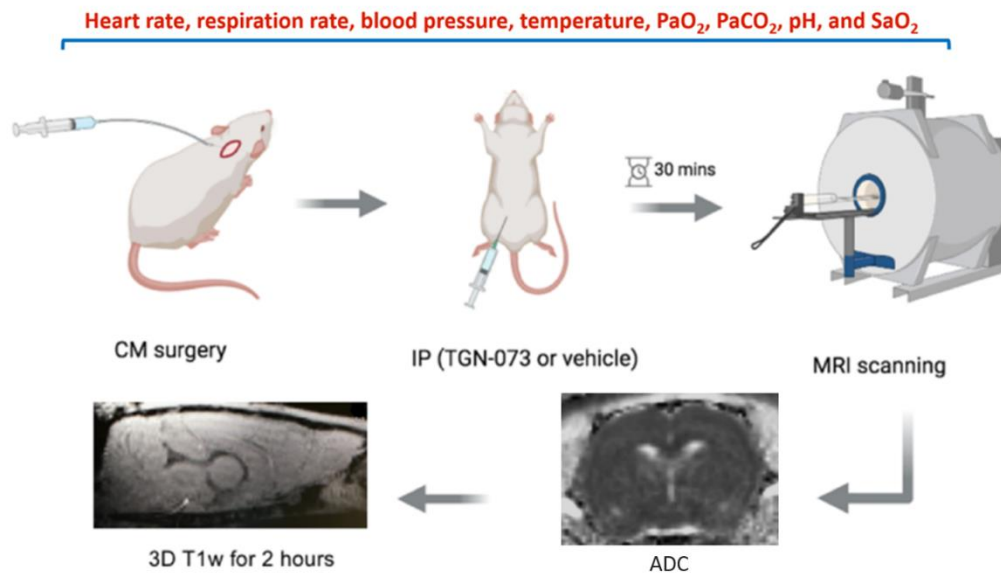


Figure 6-1: Study design (protocol). Cisterna magna cannulation then intraperitoneal injection of the drug; wait half an hour and start MRI scanning. CM: cisterna magna, IP: intraperitoneal, ADC: apparent diffusion coefficient, and MRI: magnetic resonance imaging.

Each rat was placed in the prone position in a stereotaxic frame, using tooth and ear bars for stabilisation with the head fixed to 45° (snout), Figure 6-2. After sterilising the area, to access the cisterna magna, a 3 cm skin incision was made in the midline of the dorsal neck to expose the occipital crest and dural membrane covering the cisterna magna. The muscles were separated to expose the atlanto-occipital membrane that overlays the dura mater. A custom-made cisterna magna cannula was connected to a polyethylene tube and filled with artificial CSF (aCSF: NaCl 140 mmol/L, NaH₂PO₄ 12 mmol/L, KCl 3 mmol/L, CaCl₂ 2.5 mmol/L, NaHCO₃ 12 mmol/L, pH 7.4) then advanced 2 mm into the subarachnoid space (i.e. cisterna magna space), Figure 6-2. The cannula was secured in place with super glue to avoid any movement or leakage. Then, the muscles and overlying skin were sutured to close the skull. Next, the animal was placed in the prone position in the cradle and moved to the MRI scanning room. The animal's physiology and vital signs were monitored continuously during the scanning with an MRI-compatible assembly.

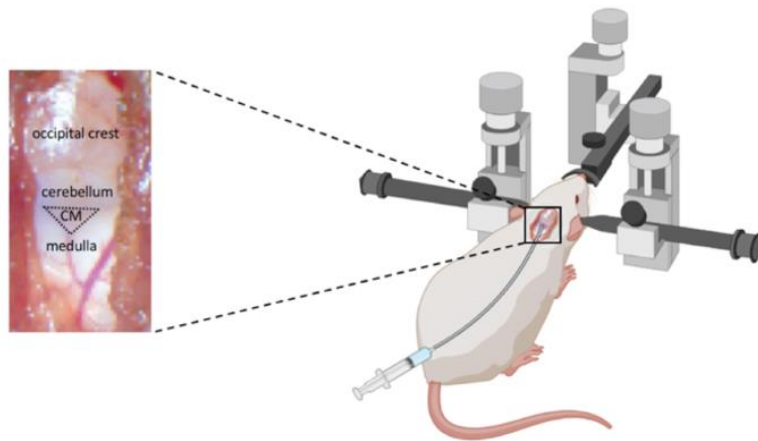


Figure 6-2: Cisterna magna cannulation. Rat was placed in the prone position in a stereotaxic frame, using tooth and ear bars for stabilisation with the head fixed to 45° (snout). A 3 cm skin incision was made in the midline of the dorsal neck to expose the occipital crest and dural membrane covering the cisterna magna. A custom-made CM cannula (22-gauge, 2 mm Tip PEEK, SAI Infusion Technologies, RCMC-03) was advanced 2 mm into the subarachnoid space (i.e. CM space). CM: cisterna magna.

6.2.4 Infusion Pump Setup

The polyethylene tube was filled with MRI contrast (Gd-DTPA) or aCSF and connected at one end of the cisterna magna cannula and the distal end was connected to a long line extending from the microinfusing pump. A total of 50 μl of the Gd-DTPA or aCSF was delivered intracisternally at an infusion rate of 1.6 μl per minute with total infusion time = 31 minutes. Details on setting up the infusion pump and determining the appropriate infusion rate are provided in the methodology chapter, Section 3.4.2.3.

6.2.5 Magnetic Resonance Imaging

All imaging was performed on a 7 Tesla preclinical MRI system (Bruker PharmaScan 7T/16) controlled by Paravision 5.1 software (Bruker Bio Spin, Ettlingen, Germany) and gradient coils with 9 cm inner diameter and a maximum strength of 300 mT/m. A surface coil with a four-channel phased array was used as the RF receiver coil and a volume (birdcage) coil with 72 mm inner diameter was used as RF transmitter. Ear and mouth bars were used for head stabilisation.

The scanning protocol was as follows: first, a localiser scan was performed to adjust the slice orientation and position. To investigate the effect of TGN-073 on the astrocytic microstructure, a diffusion-weighted echo planar imaging (DW-EPI) spin echo sequence was acquired before contrast agent administration. The scan parameters were TR = 4000 ms, TE = 23.2 ms, b-values (0, 1000) s/mm² along three orthogonal axes, diffusion time = 30 ms, NEX = 2, FOV = 2.50 x 2.50 cm, acquisition matrix = 96, slice thickness = 1.50 mm, number of contiguous slices = 8, acquisition time = 2 min 8 s, acquired in the coronal plane.

Next, a 3D T₁-weighted fast low angle shot (FLASH) sequence was used to image the transport of Gd-DTPA. The scan parameters were as follow: TR = 15 ms, TE = 3.1 ms, flip angle = 15°, NEX = 1, field of view = 3.0 x 3.0 x 3.0 cm, acquisition matrix size of 128 x 128 x 128 yielding an image resolution of 0.234 x 0.234 x 0.234 mm/pixel, acquisition time = 2 min 55 s, acquired in the sagittal plane. The scan protocol included five 3D T₁-weighted FLASH baseline scans. This was followed by the intrathecal infusion of paramagnetic contrast agent through the cannula in the cisterna magna; either Gd-DTPA (83 mM, molecular weight 938 Da, Magnevist® Bayer HealthCare Pharmaceuticals Inc.) or aCSF was used as a negative control, during the scan. After finishing the contrast infusion, the MRI scanning acquisitions continued for a total scanning time of two hours from the beginning of MRI contrast infusion. At the end of the study, the animal was euthanised with an overdose of isoflurane.

6.2.6 Data Analysis

To avoid bias, the coding of rats and data analysis were carried out in a blind fashion (i.e. the investigator was not aware whether rat received the drug or vehicle). All image data processing was performed using MATLAB software (MATLAB R2019a, MathWorks Ltd., UK); codes were developed in house. In brief, the DICOM format was used to process the MRI images. Brain extraction was achieved by applying a mask to remove non-brain tissue, which allowed for accurate brain co-registration. For spatial alignment, images were co-registered with rigid body transformation to the baseline image to correct for any inter-imaging head movement. Then, image smoothing was achieved by applying anisotropic diffusion filters to reduce noise.

A visual inspection was carried out to assure adequate pre-processing. Next, the averaged baseline image was subtracted from all of the time series images (i.e. after initiation of the contrast infusion). Then, subtracted images were divided by average baseline (image normalisation); this was carried out to correct for any signal variations due to nonuniform sensitivity of the surface RF receiver coil. The resulting value was then multiplied by 100 to find the percent change in signal intensity. Mean percentage signal intensity changes were extracted from ROIs drawn within the frontal cerebral cortex, cerebellum and whole brain. Plotting these percentage signal changes as a function of time, gave the TACs for each region.

The DWI-EPI images were analysed using image processing tools supplied by Bruker Paravision 5.1 software. Two animals (a drug treated and a vehicle) were excluded from the DWI calculations due to EPI artefacts in the Z-direction. Total animal numbers used for the DWI analysis were n= 6 drug, and n= 6 vehicle. The diffusion coefficient (D) was calculated:

$$D = -\frac{1}{b} \ln\left(\frac{S_{b1000}}{S_{b0}}\right) \quad \mathbf{6-1}$$

Where b is the b value, S_{b0} is the signal intensity with zero diffusion gradients (b=0), S_{b1000} is the signal intensity at a b value of 1000.

The apparent diffusion coefficient (ADC) was calculated from the average of three orthogonal directions:

$$ADC = \frac{(D_x + D_y + D_z)}{3} \quad \mathbf{6-2}$$

Where D_x is the diffusion coefficient in the x direction, D_y is the diffusion coefficient in the y direction, and D_z is the diffusion coefficient in the z direction. For each rat, the cerebral cortex, striatum and whole brain were manually segmented in the ADC map to find the average apparent diffusion coefficient values.

6.2.7 Statistical Analyses

Statistical analyses and graphs were plotted using MATLAB software (MATLAB R2019a, MathWorks Ltd., UK), codes developed in house, Excel 2016 (Microsoft Windows), and GraphPad Prism 9 (GraphPad Prism Software, California, USA). Statistical comparisons between the drug and vehicle groups were performed by repeated measures one-way ANOVA followed by Tukey's post hoc test to correct for multiple comparisons. A two-tailed unpaired (independent groups) student t-test was performed to study the ADC difference between the drug and vehicle groups. Data are presented here as mean \pm SD unless otherwise stated, with $P < 0.05$ considered to be statistically significant.

6.3 Results

Imaging the effect of the AQP4 facilitator, TGN-073, upon the glymphatic transport in rat brain was accomplished via intrathecal infusion of paramagnetic contrast agent Gd-DTPA. The images from serial 3D T_1 -weighted MRI clearly show more contrast uptake and deeper tissue penetration in the brain of the drug group compared to the vehicle group (Figure 6-3). This effect was markedly noticeable in the TAC of the prefrontal cortex, cerebellum, and whole brain (Figure 6-4a-c). The prefrontal cortex showed more than twofold higher contrast uptake in the treated group than the vehicle group (Figure 6-4a). The whole brain TAC of the TGN-073 treated animals revealed an increase of up to 41% in contrast enhancement compared to that of the vehicle group (Figure 6-4c). While the cerebellum showed higher difference between the groups, with a 70% increase in contrast enhancement in the treated group compared to the vehicle group (Figure 6-4b).

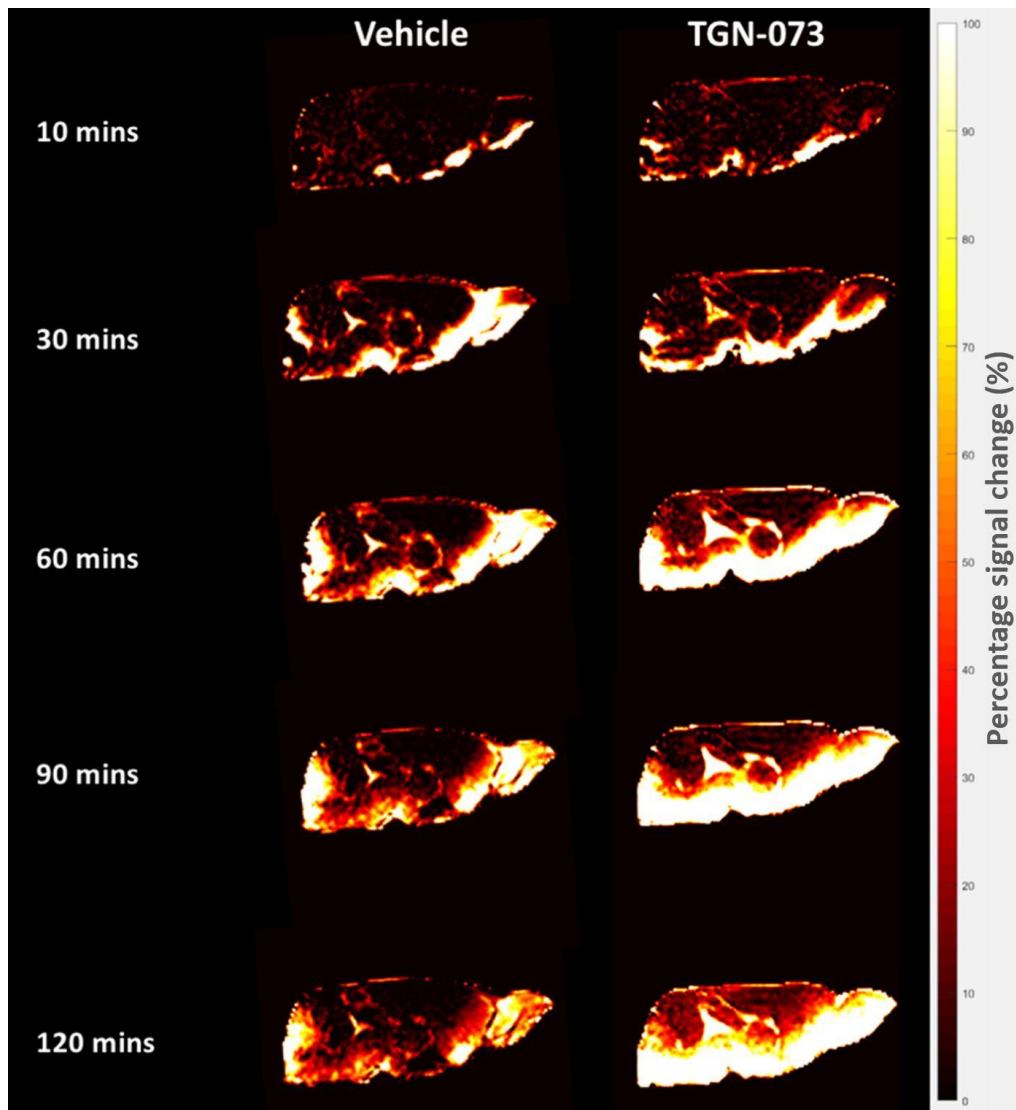


Figure 6-3: Serial MRI images in the sagittal plane of a single representative rat's brain. Using Gd-DTPA as the paramagnetic contrast agent reveals glymphatic transport, showing higher uptake and greater parenchymal penetration throughout the brain over a period of two hours in the animal treated with the AQP4 facilitator (TGN-073) compared to a vehicle-only treated rat. The time (in minutes) indicates the progression from the start of Gd-DTPA infusion.

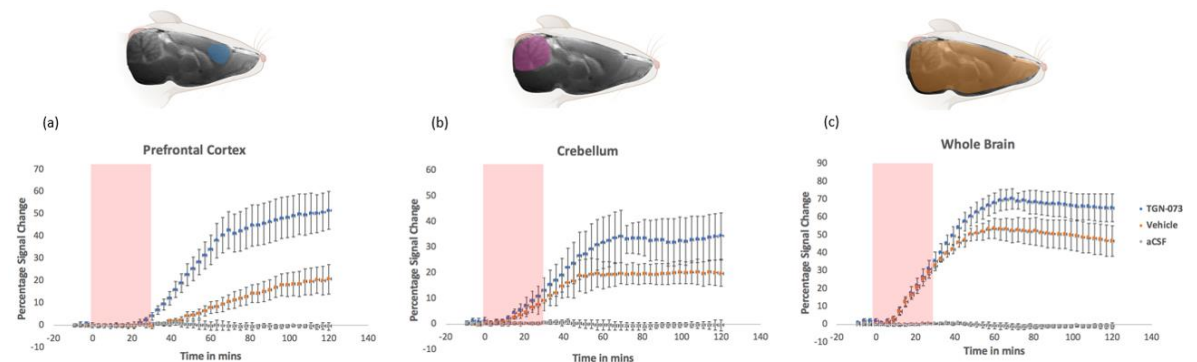


Figure 6-4: Averaged time activity curves (TAC) of three different regions of rats' brains. The percentage signal change is plotted as a function of time for the TGN-073 treated (n = 6, blue

circles), vehicles (n = 6, orange circles), and artificial CSF (n = 3, grey circles) in (a) prefrontal cortex, (b) cerebellum and (c) whole brain. Pink shading on graphs indicates the period of tracer infusion. Shading on the anatomical images of the brain illustrates the location of ROIs, blue: prefrontal cortex, purple: cerebellum and orange: whole brain.

In the prefrontal cortex, the contrast uptake was substantially greater in the TGN-073 group compared to vehicle ($51 \pm 8\%$ vs $20 \pm 6\%$, respectively; $P = 0.0001$). In the cerebellum, the contrast uptake was also substantially greater in the TGN-073 group compared to vehicle ($34 \pm 9\%$ vs $20 \pm 5\%$, respectively; $P = 0.0004$). For both the vehicle and TGN-073 treated groups, in the cerebellum the time activity curves showed a plateau after approximately one hour (Figure 6-4b). However, in the prefrontal cortex the TAC continued to increase right to the end of the 2 hour scanning period (Figure 6-4a).

The glymphatic transport and distribution in the brain is naturally heterogeneous (Figure 6-3). For instance, in TGN-073 treated group, T_1 -weighted MRI dynamic time series show heterogeneity in the arrival time of MRI tracer and maximum signal change in different brain regions. For the arrival time of the contrast in the TGN-073 group in TAC (Figure 6-4), the cerebral cortex signal started to increase after 30 min of starting the contrast infusion; meanwhile, the cerebellum signal started to increase just after 12 min of starting the infusion. The maximum percentage signal change was higher in the cerebral cortex than the cerebellum ($51 \pm 8\%$ vs $34 \pm 9\%$, respectively; $P < 0.001$). Thus, glymphatic transport differs in different brain territories.

Rats treated with TGN-073 showed increased water diffusion than those treated with vehicles (Figure 6-5). The boxplot of different ROIs in the brain reveals that ADC was higher in the TGN-073 treated group than in the vehicle group (Figure 6-5). Significant differences in ADC values were observed in the cerebral cortex (0.00074 vs 0.00070 mm^2/s ; $P < 0.05$), striatum (0.00074 vs 0.00069 mm^2/s ; $P < 0.05$), and whole brain (0.00079 vs 0.00074 mm^2/s ; $P < 0.05$).

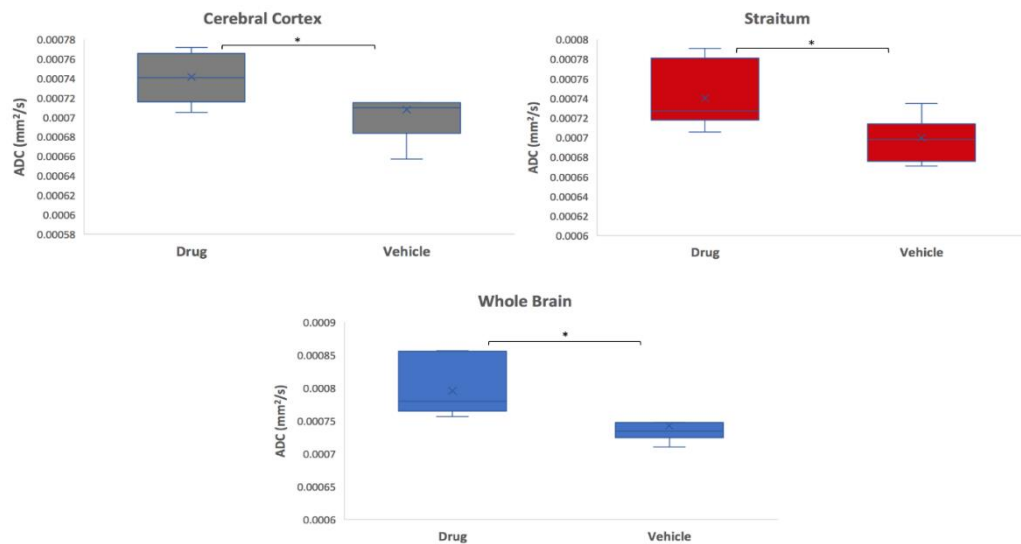


Figure 6-5: Boxplots of apparent diffusion coefficient in the cerebral cortex (grey), the striatum (red), and whole brain (blue). In each figure, left: TGN-073-treated group; right: vehicle group. Asterisks indicate significant differences: *P < 0.05.

6.4 Discussion

Reduced glymphatic activity is associated with several neurological disorders such as AD, traumatic brain injury and vascular dementia (Venkat et al., 2017; Iliff et al., 2014; Xu et al., 2015). In AD, it is speculated that the accumulation of harmful proteins (A β and tau) is the result of glymphatic dysfunction. For example, experiments have shown that injecting the striatum of AQP4^{-/-} mice with ¹²⁵I-A β ₁₋₄₀ results in a 55% inhibition in the clearance of A β compared to their wild-type counterparts (Iliff et al., 2012). Moreover, a 40% reduction in the clearance of ¹²⁵I-A β ₁₋₄₀ has been shown in the brain of aged mice, possibly due to reduced arterial pulsatility, along with changes in AQP4 expression (Kress et al., 2014). Therefore, pharmacological interventions that enhance water exchange through AQP4 and enhance clearance via glymphatic transport might be promising therapeutics for neurodegenerative diseases, by preventing the accumulation of harmful solutes in the brain. A previous study using intravenous injection of H₂¹⁷O has demonstrated that TGN-073 facilitates the transport of water through AQP4 channels across the blood brain barrier (Huber, Igarashi, et al., 2018). In this study, we sought to investigate the effect of TGN-073 on glymphatic transport. The contribution of the astrocytic water channel AQP4 to glymphatic transport is under considerable debate (Mestre et al., 2017; Xia et al., 2017; Murlidharan et

al., 2016; Smith & Verkman, 2018; Smith et al., 2017). This study was conducted to investigate the role of AQP4 by employing the novel AQP4 facilitator TGN-073 in normal rat brains.

Glymphatic transport was imaged using DCE-MRI with Gd-DTPA, where the contrast agent was slowly infused into the CSF at the cisterna magna. In the vehicle group the parenchymal uptake of Gd-DTPA shows a similar temporal distribution to that seen in previous studies (Iloff, Lee, et al., 2013; Alshuhri et al., 2021). In the cerebellum the TACs show a plateau after approximately one hour (Figure 6-4b). This can be explained by two key features. First, the cerebellum is adjacent to the infusion site of the cisterna magna, while it takes much longer for the contrast agent to reach more distal sites, e.g. the prefrontal cortex. Second, the high expression of AQP4 in the cerebellum (Hoddevik et al., 2017; Hubbard et al., 2015), could enable faster uptake and transport, reaching saturation sooner. Whereas, in the prefrontal cortex the TAC continued to increase right to the end of the 2 hour scanning period (Figure 6-4a).

Glymphatic transport was significantly enhanced in TGN-073-treated rats compared to vehicles (Figure 6-3). The brain of the treated group showed higher percentage signal change and deeper penetration of the contrast agent than the vehicle group. It has previously been reported that entry of tracers from the peri-arterial space to the surrounding brain interstitium was restricted based on molecular weight (Iloff, Lee, et al., 2013). Very large molecular weight tracers, like FITC-d2000 (MW 2,000 kDa), were confined to the peri-arterial spaces, but lower molecular weight tracers, including Texas Red-conjugated dextran (MW 3 kDa) and Alexa Fluor 647-conjugated ovalbumin (MW 45 kDa), quickly penetrated into the interstitium (Iloff et al., 2012). Given that the size of the narrowest part of the pore of AQP4 channel is around 2.8 Å (angstroms), just large enough to let water molecules pass through in a single file (Cui & Bastien, 2011; Halsey et al., 2018; Agre et al., 2002), it is clear that Gd-DTPA (938 Da) cannot pass through AQP4 channels. However, Gd-DTPA can penetrate the 20 nm cleft between overlapping astrocytic end feet, which entirely surround the cerebral vasculature (Mathiisen et al., 2010).

Given the above consideration, it is worth questioning how an AQP4 facilitator, e.g. TGN-073, could increase the rate at which Gd-DTPA penetrates the brain. We speculate that TGN-073 facilitates faster transport of water from the periarterial space into the brain interstitium, by lowering the resistance to flow. As a consequence, water flow (i.e. CSF flow) in the periarterial space would increase. As Gd-DTPA is dissolved in the CSF, and is transported with it, this in turn increases the rate at which Gd-DTPA can enter the interstitium.

Diffusion MRI is extremely sensitive to alterations in tissue microstructure and does not require any contrast agent. A number of studies have used diffusion MRI to investigate glymphatic transport (Demiral et al., 2019; Harrison et al., 2018; Sepehrband et al., 2019; Taoka et al., 2017). In addition, diffusion MRI has been used to study AQP expression and its relationship to several diseases (Badaut et al., 2014). Mukherjee et al. showed that AQP1 overexpression correlated with higher water diffusivity (Mukherjee et al., 2016). It was shown that the severity of hydrocephalus correlates with the ADC and AQP4 expression (Tourdias et al., 2009). Meanwhile, TBI rat models showed decreased water diffusivity after inducing small interfering RNAs to inhibit AQP4 (Fukuda et al., 2013).

Another study documented the reduction in water diffusivity in rodents' brains, and ADC values were reduced by 50% after acutely inhibiting AQP4 using RNA interference (Jerome Badaut et al., 2011). In line with these studies, our results show a significant increase in ADC values in the group given the AQP4 facilitator TGN-073. This may indicate that by increasing the flux of water through AQP4 channels, TGN-073 reduces restrictions to the diffusion of water molecules in the brain parenchyma. However, it is also possible that this increase in ADC is the result of increased brain water content rather than changes in water transport via AQP4. Previous studies have related ADC changes to changes in brain water content measured by wet/dry weights (Kuroiwa et al., 1998; Piepgras et al., 2001). However, in our case, given the relatively small changes in ADC (~6%) seen with TGN-073 and the variability of wet/dry measurements, it would be difficult to conclusively determine whether brain water content changes or not.

6.5 Conclusion

The glymphatic system is a low resistance pathway, in which cerebrospinal fluid enters the brain parenchyma along perivascular spaces via AQP4 channels. It has been hypothesised that the resulting convective transport of the interstitial fluid provides an efficient mechanism for the removal of waste toxins from the brain; this process is thought to be highly mediated by AQP4 water channels. Therefore, maintaining and supporting AQP4 function might protect against neurodegenerative diseases such as Alzheimer's disease. Here, DCE-MRI was employed to demonstrate that glymphatic transport is enhanced by an AQP4 facilitator, TGN-073. Further, diffusion MRI measurements demonstrated an increase in the diffusive transport of water in the brain of TGN-073 treated rats. Drugs like this novel AQP4 facilitator might hold a promising future in preventing, treating, or ameliorating neurodegenerative diseases in which the AQP4 functionality is impaired.

Chapter 7 AQP4 Staining Optimization

I undertook the challenge of initiating the Immunohistochemistry protocol for AQP4 staining using Immunofluorescence within our department, starting entirely from scratch. Within this chapter, each stage and detail of the process are covered. Together, the complexities will be navigated to establish the most effective method for staining AQP4. The goal was to refine the technique to its fullest potential, ensuring precision and reliability for the experiments that follow.

Dr. Karin Williams provided expert guidance during the histological staining process, including protocol optimisation and supervision.

7.1 Introduction

Histology and Immunohistochemistry (IHC) are the standard methods used to directly assess gross organ morphology, cell phenotype, and subcellular architecture (Bishop et al., 2018). IHC is an essential technique used to detect and visualize the distribution of specific antigens or proteins within cells and tissues. By utilizing labelled monoclonal or polyclonal antibodies that target these antigens or proteins, scientists can precisely identify and localize them, enabling detailed analysis of their density and distribution patterns within biological samples. Although the concept of IHC originated in the 1930s, the first study utilizing IHC techniques was not documented until 1941 (Coons et al., 1941).

IHC stands as the gold standard for identifying several pathological biomarkers, especially in the fields of neurology, oncology, and haematology (Duraiyan et al., 2012). By identifying the increase or decrease of disease targets, IHC is also utilised in pharmaceutical development to evaluate the effectiveness of new treatments (Harsh & Sugandha, 2012). In this chapter, the process of staining AQP4

water channels in the rat brain will be detailed. Beginning with brain fixation, followed by evaluating the effectiveness of the immunostaining technique. Furthermore, the optimization of antigen retrieval pH and antibody dilutions will be explored to ensure best results.

All materials were purchased from Sigma Aldrich and Abcam unless otherwise stated.

7.2 Fixation and preparation of brain sections

Following MRI scanning, the depth of anaesthesia was increased to achieve a deeper anaesthetic state (5% isoflurane). The rat underwent transcatheter perfusion with 200 mL of heparinized saline (1000 IU of heparin /100 mL of 0.9% saline) to eliminate blood from the circulatory system. This was followed by perfusion with 200 mL of 4% paraformaldehyde (PFA) fixative solution to preserve tissue structure. 4% PFA fixative solution was prepared in a fume hood by combining 80 g of PFA powder with 1.5 litres of distilled water, along with 95 mL of sodium dihydrogen orthophosphate (31.2 g/l) and 405 mL of disodium hydrogen orthophosphate (28.3 g/l). The mixture was stirred and heated until it reaches 60°C.

The transcatheter perfusion fixation technique employed utilized gravity to perfuse solutions through the aorta, ensuring thorough fixation of all body tissues, Figure 7-1. The solutions were suspended at a height that maintains a driving pressure similar to the rat's blood pressure, approximately 90 mmHg. After overnight post-fixation of the brains in 4% PFA at room temperature, they underwent dehydration by sequential immersion in increasing concentrations of ethanol to enable embedding with paraffin. The brains were then sectioned into 7-micrometer-thick coronal slices around -3 to -4 from bregma using a vibrating microtome. These slices were then mounted on poly-L-lysine-coated glass slides.

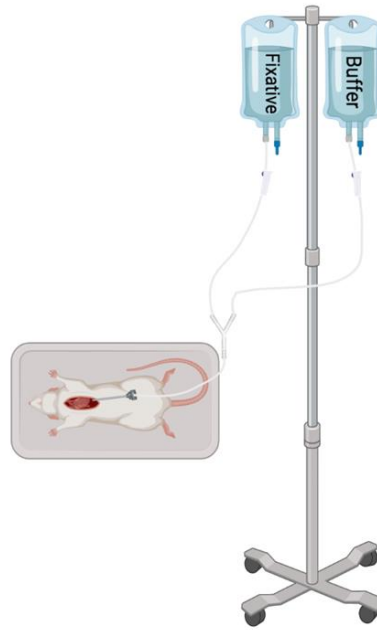


Figure 7-1: Gravity technique for transcatheter perfusion fixation.

7.3 First test run: Assessing technique validity

7.3.1 Introduction

In this experiment, immunofluorescence (IF) staining was conducted to visualize the widely expressed neuronal marker NeuN, utilizing an IHC protocol initially drafted for AQP4 staining. This approach served multiple purposes: firstly, it enabled the evaluation of the equipment required for the procedure and provided an overall appreciation of IHC staining technique. Additionally, it allowed addressing any technical issues before proceeding to stain AQP4 with costly antibodies. It's worth noting that NeuN antibodies were chosen due to their availability in our lab as surplus from prior studies.

7.3.2 Methods and materials

7.3.2.1 Deparaffinization and rehydration

After cutting brain slices and mounting them on poly-L-lysine-coated glass slides, the slides were placed in a metal rack and immersed in HistoClear for deparaffinization. They were immersed and gently agitated for three cycles in

separate containers of HistoClear, each for 5 minutes. To rehydrate the samples, the slides were then sequentially immersed and gently agitated in 100% ethanol twice for 5 minutes each, followed by 90% ethanol and then 70% ethanol, with 5 minutes duration for each step. Subsequently, the slides were rinsed in cold running tap water for about 5 minutes. Until ready to carry out antigen retrieval, the slides remained submerged in cold tap water. It is crucial to prevent the slides from drying out after this stage, as drying can result in substantial background staining due to nonspecific antibody binding.

7.3.2.2 Antigen retrieval

An acidic antigen retrieval solution was prepared in-house by dissolving 5.88 g of tri-sodium citrate in 2 litres of distilled water. Additionally, 1 mL of Tween-20 was added to the solution to enhance solubility. The pH was then adjusted to 6.0 by adding few drops of 4% HCl. The solution was then boiled in a pressure cooker. Rehydrated slides were subsequently immersed in the solution and heated to 121°C for 10 minutes. Following this, the slides were cooled by immersion in cold running tap water for 10-15 minutes.

7.3.2.3 Immunofluorescence staining

After the slides cooled down, they were washed twice in tris-buffered saline (TBS) for 5 minutes each. TBS was prepared in-house as follows: 12.2 g of Tris Base and 44 g of NaCl were dissolved in 500 mL of distilled water to obtain an initial solution. Then, 200 mL of this solution was diluted with 1800 mL of distilled water. Finally, 0.025% Triton X-100 was added to facilitate dissolution.

The slides were blocked using a blocking solution composed of TBS, 10% normal goat serum (NGS), and 5% bovine serum albumin (BSA). They were then incubated for 2 hours at room temperature in a humid chamber. The slides were subsequently drained and incubated overnight at 4°C in a humid chamber with the primary antibody Rabbit anti-NeuN (abcam, ab104225) diluted in blocking solution. The dilutions used were 1:1000, 1:700, and 1:500.

On the next day, after 2 washes, each lasting 5 minutes in TBS, slides were incubated with Alexa Fluor Plus 488 conjugated F(ab')₂-Goat anti-Rabbit IgG (H+L)

Cross-Adsorbed Secondary Antibody (Thermofisher scientific A48282, 1:500) diluted in blocking solution. The incubation lasted for 1 hour at room temperature in a humid chamber. To ensure protection from light-induced degradation, tin foil was used to cover the slides, and the lab lights were lowered. Following incubation, slides were washed in TBS (3 cycles, each for 5 minutes). Finally, the slides were mounted using either Vectashield mounting medium without DAPI (Vector Laboratories, Inc., Burlingame, CA 94010, USA, H-1400) or Fluoroshield mounting medium with DAPI (Sigma-Aldrich, USA, 1:2000). Slides were coverslipped and varnished to seal them.

7.3.2.4 Imaging and analysis

Once the slides were dried, imaging began. The distribution of neurons within the brain slices was visualized using both a fluorescence microscope and a confocal laser scanning microscope (Leica). Exposure intensity and levels were established and maintained constant throughout the investigation. Images were analysed using ImageJ software (NIH).

7.3.3 Results and conclusion

The brain slices did not exhibit proper staining, and no specific bindings were observed as depicted in Figure 7-2. Possible causes for this outcome include protocol issues, such as inadequate dewaxing, or antibody-related issues, potentially due to prolonged storage or expiration. However, the protocol follows a rigorous dewaxing regimen, minimizing the likelihood of protocol-related issues. Therefore, either the primary, secondary antibodies, or both may not be functioning effectively.

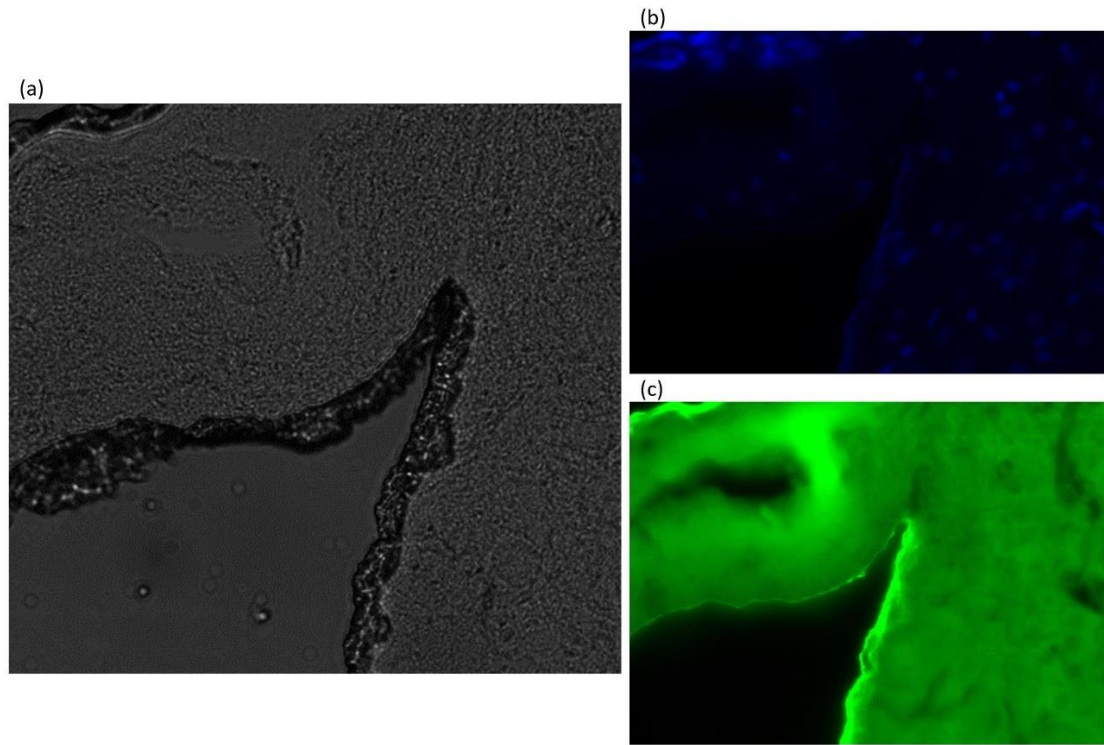


Figure 7-2: a. A grayscale microscopic image of the rat brain section in coronal orientation. b. The same microscopic image utilizes the blue channel to visualize DAPI staining, revealing the successful staining of cell nuclei within the brain section. c. The same microscopic image utilizes the green channel to visualize fluorescence emitted by immunofluorescence Alexa Fluor 488, which is supposed to stain neurons. However, the image appears smeared due to nonspecific staining.

Following the unsuccessful immunofluorescence staining of brain neurons, the next approach was to switch to 3,3'-Diaminobenzidine (DAB) staining to assess the validity of the antibodies. The decision to transition to DAB staining was based on its several advantages, including its high sensitivity for detecting low levels of protein expression, cost-effectiveness, resilience to heat and light, and long-term storage capability.

7.4 Second test run: Assessing the validity of antibodies

7.4.1 Introduction

Here, the quality of the primary antibody, Rabbit anti-NeuN, was assessed by conducting DAB staining with two different secondary antibodies. One secondary antibody had been stored in the facility for more than two years, while the other was fresh. The primary objective was to determine whether the issue lay with the primary or secondary antibody.

The hypothesis was as follows: if staining occurred with the fresh secondary antibody but not the old one, it would suggest that the primary antibody was functional, and the issue stemmed from the old secondary antibody. However, if neither the old nor the fresh secondary antibody yielded staining, it would indicate that the primary antibody was non-functional.

7.4.2 Methods and materials

7.4.2.1 Deparaffinization and rehydration

In this run, some protocol improvements were implemented, including minor adjustments to the deparaffinization/rehydration cycles and ethanol concentrations. Specifically, HistoClear was replaced with xylene for deparaffinization. Slides underwent two cycles of immersion and gentle agitation in separate containers of xylene, each for 5 minutes. Additionally, the rehydration process was more rigorous. Samples were sequentially immersed and gently agitated in 100% ethanol, 95% ethanol, and 70% ethanol, with each step lasting 5 minutes and repeated twice. Afterward, the slides were immersed in cool tap water for about 5 minutes or until ready to carry out antigen retrieval.

Antigen retrieval was performed similarly to the process described in the first run (Section 7.3.2.2).

7.4.2.2 DAB staining

After cooling down following antigen retrieval, the slides underwent two 5-minute washes in TBS each. They were then blocked using peroxidase blocking solution (Dako) and incubated for 15 minutes at room temperature in a humid chamber. Following this, the slides underwent two 5-minute washes in TBS before being drained and dried around sections to prevent extra dilution of the antibodies. Subsequently, the slides were incubated overnight at 4°C in a humid chamber with the primary antibody Rabbit anti-NeuN. The primary antibody was diluted in the blocking solution (TBS, 10% NGS, and 5% BSA) at a dilution of 1:1000.

The next day, after two 5-minute washes in TBS, the slides were drained, dried around sections, and incubated with the secondary antibody, Polyclonal Goat Anti-

Rabbit Immunoglobulins conjugated with horseradish peroxidase (HRP) (Dako EnVision+ System- HRP, Labelled Polymer) diluted 1:500 in the blocking solution. This incubation lasted for 1 hour at room temperature in a humid chamber. Following incubation, the slides underwent two 5-minute washes in TBS. To label HRP, DAB solution was applied to brain sections (1 mL TBS + 25 microliters DAB (Dako)). After two minutes, the slides were immersed in tap water. Subsequently, the slides were counterstained with haematoxylin, dehydrated with gradual ethanol (70%, 90%, 100%), and then cleared in xylene. Finally, the slides were coverslipped with permount mounting medium.

7.4.2.3 Imaging and analysis

Neuronal distribution within the brain sections was visualized under a bright field microscope (VWR). The exposure intensity and level were established and kept constant for the course of the investigation.

7.4.3 Results and conclusion

The aim of this run was to determine whether the issue resided with the primary or secondary antibody. The brain sections stained with the old secondary antibody failed to exhibit NeuN staining of brain neurons, as evidenced in Figure 7-3b. In contrast, brain sections stained with the fresh secondary antibody displayed clear NeuN staining of brain neurons, as shown in Figure 7-3a. This observation provides compelling evidence supporting the integrity of the staining protocol and the functionality of the antibodies. Consequently, we proceeded with optimizing AQP4 staining using the high-cost antibodies.

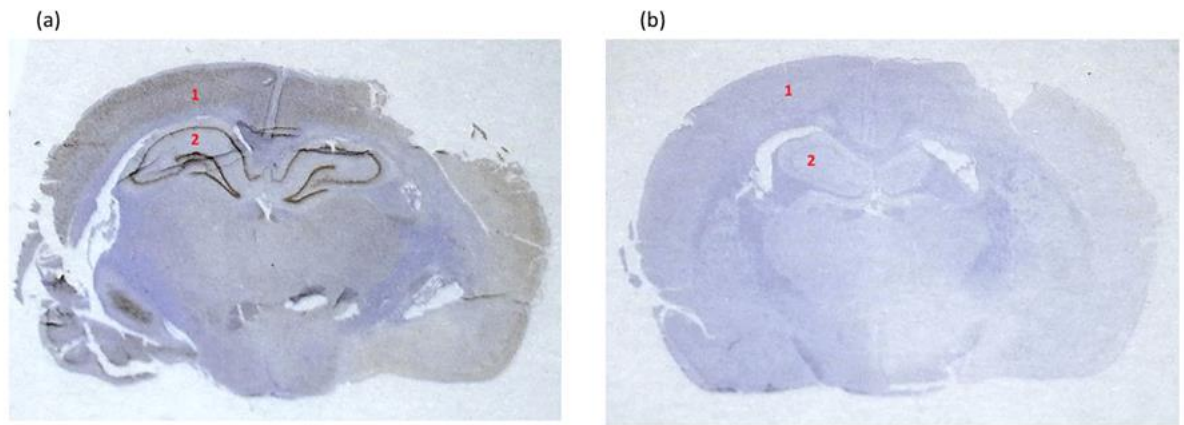


Figure 7-3: DAB staining of rat brain sections. a. rat brain section was stained with the anti-NeuN primary antibody and a fresh secondary antibody conjugated with horseradish peroxidase, resulting in clear staining of neurons with DAB (brown colour). **b.** rat brain section stained with the same anti-NeuN primary antibody but using an old secondary antibody conjugated with horseradish peroxidase, with no observable staining of neurons. Both images were counterstained with haematoxylin to highlight cell nuclei (purple colour). Brain regions are denoted as follows: 1. cerebral cortex, and 2. hippocampus.

7.5 Third test run: Optimizing AQP4 antibody dilution factor and antigen retrieval pH

7.5.1 Introduction

In this experiment, DAB staining was performed to visualize AQP4 water channels in rat brain. The objectives were to determine the optimal pH for antigen retrieval solution (pH 6 vs. 9) and the most effective AQP4 antibody dilution factor (1:1000 vs. 1:2000). Additionally, kidney sections were included in the experiment. This decision was based on the high expression of AQP4 in the collecting ducts and renal tubules of mammalian kidneys (Matsuzaki et al., 2017; Van Hoek et al., 2000). Notably, studies involving AQP4 knockout mice have shown a significant reduction in water permeability in the inner medullary collecting duct (Chou et al., 1998; Ma et al., 1997). Therefore, kidney sections were utilized as positive controls for AQP4 staining.

7.5.2 Methods and materials

Control brain and kidney sections were utilized in this experiment. The kidney underwent the same process of paraformaldehyde fixation and paraffin

embedding as the brains, see section 7.2. Additionally, the kidney sections were cut to a similar thickness as the brain sections (7 micron). The orientation of kidney sections was axial, and slices were collected from the widest part of the kidney, specifically the middle part. A total of 4 brain sections and 4 kidney sections were used, resulting in 8 slides in total, as shown in Figure 7-4. Deparaffinization and rehydration were performed similarly to the previous run, as described in Section 7.4.2.1.

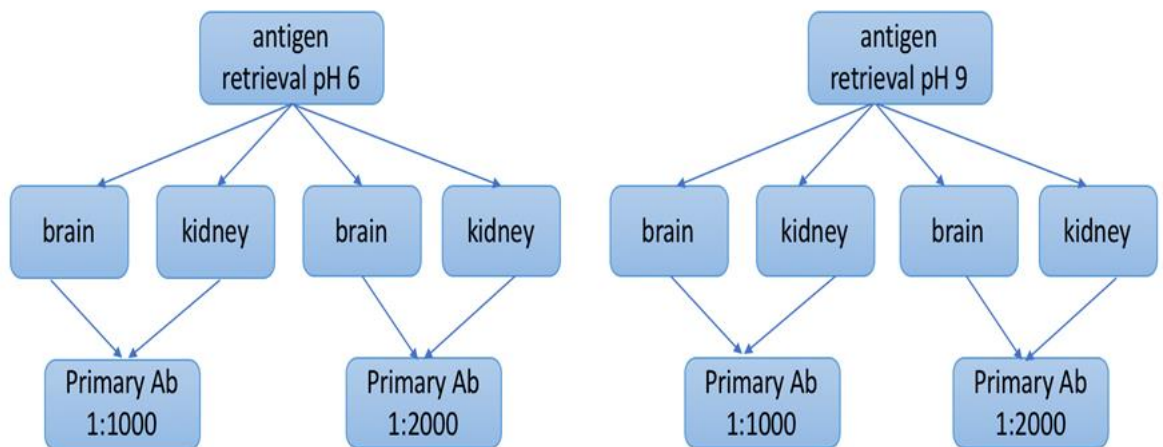


Figure 7-4: The diagram illustrates the allocation of slides to different antigen retrieval solutions and AQP4 antibody dilution factors. Ab: antibody.

7.5.2.1 Antigen retrieval

Two antigen retrieval solutions with different pH levels were utilized. One solution was the antigen retrieval solution prepared in-house with a pH of 6, while the other one was a commercially available solution with a pH of 9 (Dako Target Retrieval Solution, pH 9 (10x)). The boiling process remained consistent with previous procedures 7.3.2.2. Two brain and two kidney slides were immersed in each solution.

7.5.2.2 DAB staining

Similar to the previous run, Section 7.4.2.2, with some exceptions. The changes employed here were as follows: a different primary antibody was utilized to stain for AQP4 instead of neurons. Specifically, Rabbit anti-Aquaporin 4 antibody

(abcam, ab128906) was used. Additionally, antibody diluent (Dako, S0809) was used instead of the blocking solution to dilute the antibodies. Furthermore, two dilution factors were used for the AQP4 antibody: 1:1000 and 1:2000, as illustrated in Figure 7-4.

7.5.2.3 Imaging and analysis

AQP4 distribution within the brain and kidney sections was visualized under a bright field microscope and a slide scanner (Leica). The exposure intensity and level were established and kept constant for the course of the investigation.

7.5.3 Results and conclusion

Initially, slides were imaged using the department's microscope, as shown in Figure 7-5. However, the image quality was found to be unsatisfactory. Therefore, the slides were sent to another department for imaging using a slide scanner, offering a larger field of view and enhanced resolution, as illustrated in Figure 7-6. In evaluating the antigen retrieval pH, brain AQP4 staining showed superior quality with reduced nonspecific binding at pH 6 compared to pH 9. Overall, optimal brain AQP4 staining with minimal background staining was achieved with an antibody dilution factor of 1:2000 at an antigen retrieval pH 6 for DAB stain (delineated by the red square in Figure 7-6). Consequently, these conditions were employed in the subsequent run for immunofluorescence staining of AQP4.

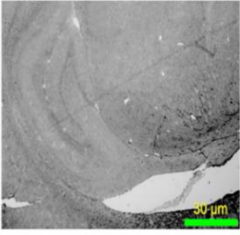
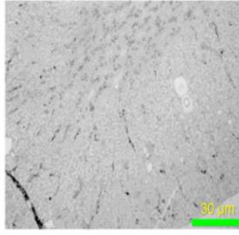
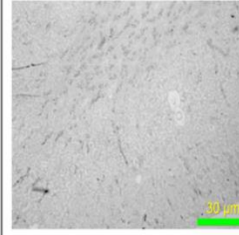
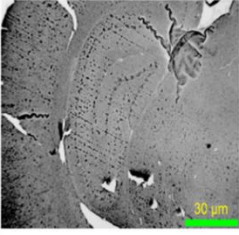
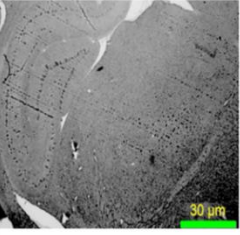
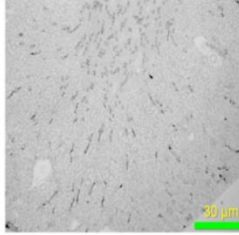
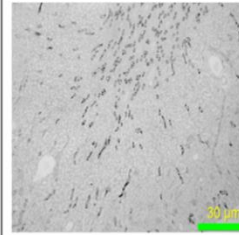
Antigen retrieval pH	Brain		Kidney	
	Primary Ab 1:1000	Primary Ab 1:2000	Primary Ab 1:1000	Primary Ab 1:2000
pH 6				
pH 9				

Figure 7-5: Images were obtained using a standard microscope.

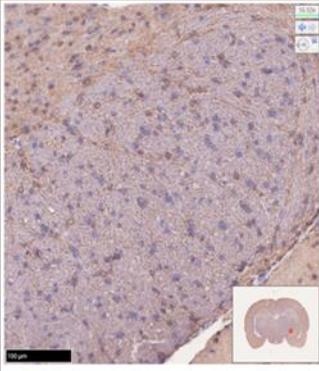
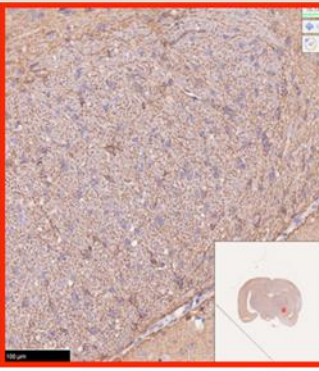
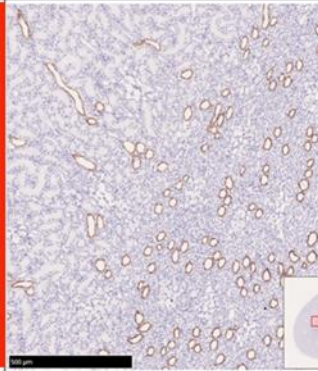
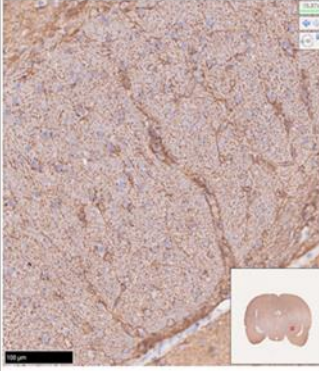
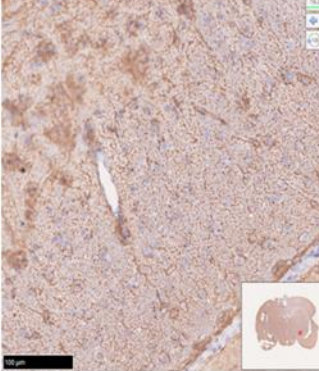
Antigen retrieval pH	Brain		kidney
	Primary Ab 1:1000	Primary Ab 1:2000	Primary Ab 1:2000
pH 6			
pH 9			

Figure 7-6: Images were obtained using a slide scanner. The brain images were zoomed in on the substantia nigra, while the kidney images were zoomed in on the convoluted tubules and

collecting ducts of the nephron. The brown colour represents DAB staining of AQP4, while the purple colour, resulting from haematoxylin staining, highlights cell nuclei.

7.6 Fourth test run: Retest the optimized protocol using immunofluorescence.

7.6.1 Introduction

The aim here was to implement all the refinements made thus far and transition to immunofluorescence staining for AQP4 instead of DAB. This change aligns with the intention to use immunofluorescence in the experiments detailed in the following chapters, as it offers superior capabilities for quantitative analysis and provides higher spatial resolution compared to DAB staining.

7.6.2 Methods and materials

In this run, only the antigen retrieval solution with a pH of 6 was used. Two dilution factors for the primary AQP4 antibody, 1:2000 and 1:5000, were evaluated. The dilution factor for the secondary antibody remained at 1:500, consistent with all previous runs. Two brain and two kidney sections were stained, totalling four slides, as illustrated in Figure 7-7.

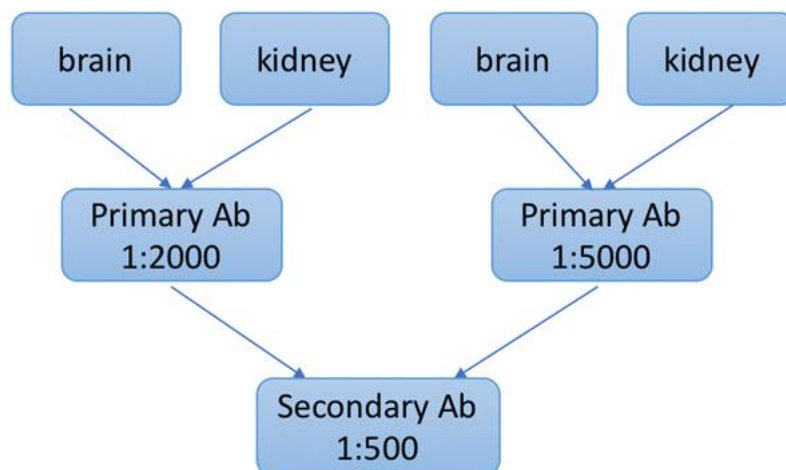


Figure 7-7: The diagram illustrates the allocation of slides to different AQP4 antibody dilution factors. Ab: antibody.

7.6.2.1 Immunofluorescence staining

Deparaffinization and rehydration were conducted as outlined in Section 7.4.2.1, while antigen retrieval was performed according to the process described in Section 7.3.2.2. After cooling down following antigen retrieval, the slides underwent two 5-minute washes in TBS each. Subsequently, the slides were incubated overnight at 4°C in a humid chamber with the primary antibody (Rabbit anti-Aquaporin 4 antibody) diluted in Dako antibody diluent. Two dilution factors were tested: 1:2000 and 1:5000, as illustrated in Figure 7-7.

The next day, after two 5-minute washes in TBS, the slides were then incubated for 1 hour at room temperature in a humid chamber with Goat Anti-Rabbit IgG H&L (Alexa Fluor 488) Secondary Antibody (ab150077, 1:500) diluted in Dako antibody diluent. Care was taken not to expose the slides to light after applying the secondary antibody. Following incubation, the slides underwent two 5-minute washes in TBS.

Lastly, the slides were mounted using mounting medium with DAPI (ProLong™ Diamond Antifade Mountant with DAPI, Cat# P36962, Thermo Fisher Scientific). The slides were then cover-slipped (22 x 50 mm) and sealed with CoverGrip™ Coverslip Sealant (Cat# 23005, Biotium, CA, USA).

7.6.2.2 Imaging and analysis

AQP4 distribution within brain and kidney sections was visualized using a Zeiss LSM 710 Confocal Laser Scanning Microscope equipped with Zen software. Exposure intensity and level were established and maintained constant throughout the investigation. Image analysis was performed using ImageJ software (NIH) and QuPath v0.4.3.

7.6.3 Results and conclusion

Both the brain and kidney sections displayed very low fluorescence signals, with the brain exhibiting the weakest signal (Figure 7-8). This was likely attributed to the high dilution factors used (1:2000 and 1:5000), which are commonly suitable for DAB staining. As mentioned earlier, DAB staining is known for its higher sensitivity compared to immunofluorescence staining.

DAB staining is less affected by high dilution factors compared to immunofluorescence staining. This is because DAB staining depends on the enzymatic reaction between the HRP enzyme conjugated to the secondary antibody and the DAB substrate, which can still occur even at high dilution factors for the primary antibody. In contrast, immunofluorescence staining depends on the binding of fluorophore-conjugated secondary antibodies to the primary antibodies bound to the target antigen/protein. If the primary antibody is diluted too much, there may be insufficient binding sites for the secondary antibody, resulting in reduced fluorescence signal.

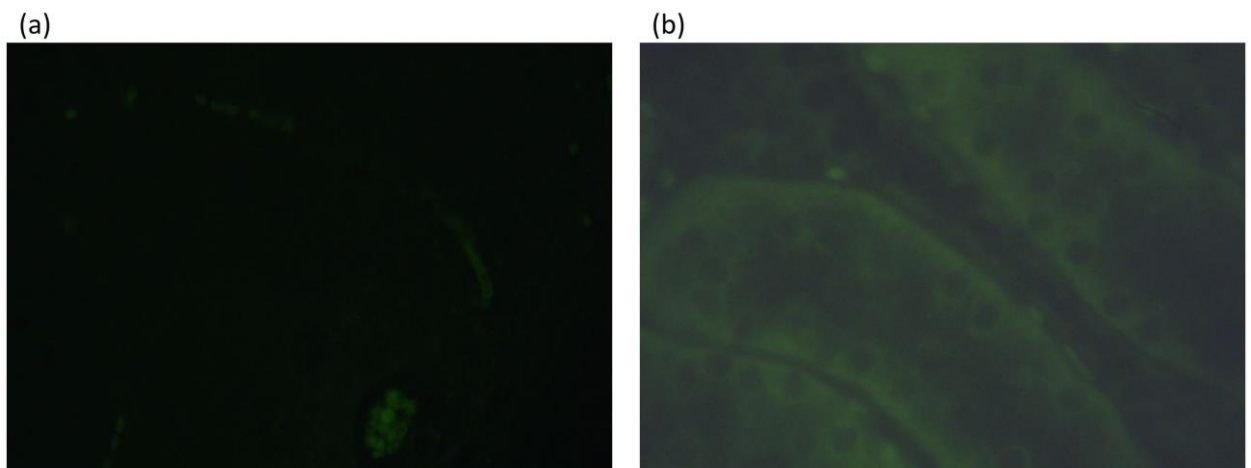


Figure 7-8: Immunofluorescence staining of AQP4 using Alexa Fluor 488 (green) in (a) brain and (b) kidney sections from rat.

7.7 Fifth test run: Decreasing AQP4 antibody dilution

This experiment closely resembled the previous run in all aspects. The only difference was that lower AQP4 antibody dilution factors were tested: 1:200 and 1:400. The immunofluorescence staining resulted in notably robust signals across both dilutions, as depicted in Figure 7-9. Specifically, the 1:400 dilution exhibited superior fluorescence intensity compared to other dilution. This finding holds significant implications for subsequent experiments, wherein the 1:400 served as the preferred dilution factor for AQP4 antibody.

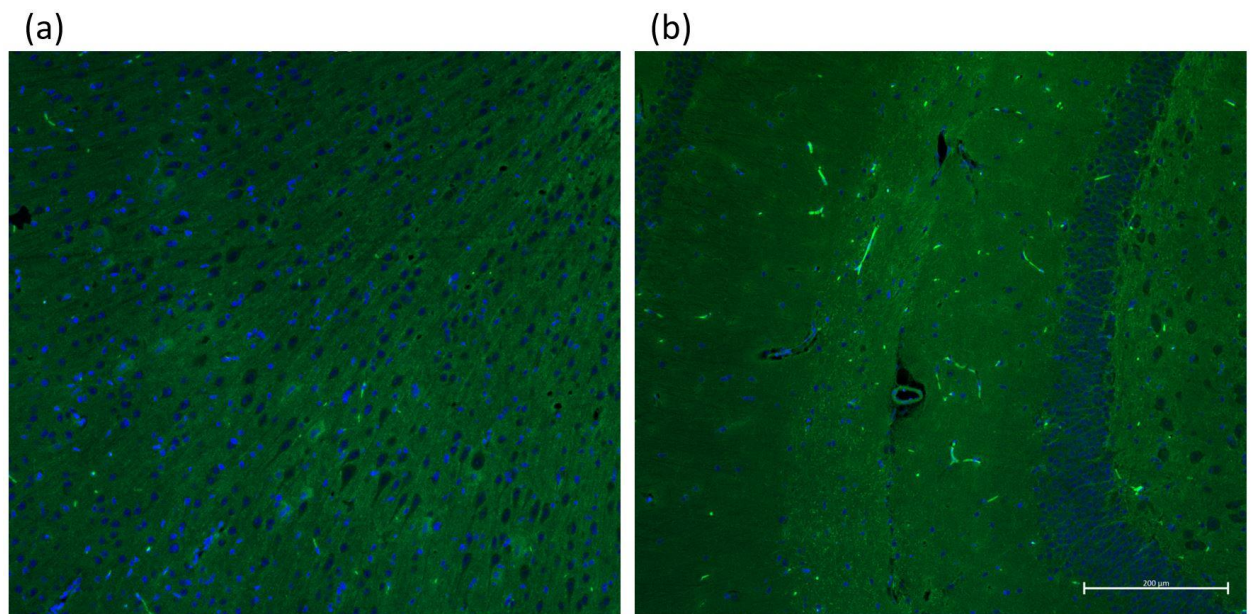


Figure 7-9: Immunofluorescence staining illustrates the distribution of AQP4 in the hippocampal region of rat brain sections. The bright green signal (Alexa Fluor 488) indicates perivascular localization of AQP4 around blood vessels, while cell nuclei are counterstained with DAPI (blue). Figure (a) and (b) show staining with 1:200 and 1:400 primary antibody dilutions, respectively. The observed perivascular streaks and punctate signals suggest high AQP4 expression along astrocytic endfeet surrounding vessels, consistent with its role in glymphatic fluid transport. Notably, the AQP4 signal appeared more distinct and better defined at the 1:400 dilution, indicating enhanced specificity and reduced background staining compared to the 1:200 dilution. Scale bar = 200 μ m.

In conclusion, after a series of comprehensive tests and refinements, the optimal protocol for staining AQP4 using immunofluorescence was successfully identified. This refined protocol was employed in the following experiments to visualize and evaluate the distribution of AQP4 in rat brains following the administration of AQP4 modulator drugs.

Chapter 8 Exploring the Impact of TGN-073 and TGN-020 on AQP4 Water Channels and Brain Microstructure

The study in Chapter 6 demonstrated that the pharmacological AQP4 facilitator TGN-073 significantly enhances glymphatic transport, as observed using contrast-enhanced MRI. However, the invasive nature of this technique, requiring cisterna magna cannulation for CSF contrast infusion, prompted the need for non-invasive alternatives. In this study, two non-invasive MRI sequences, diffusion MRI and T₂ mapping, were employed to investigate the effects of two putative AQP4 modulators: the facilitator TGN-073 and the inhibitor TGN-020. This was followed by immunofluorescence labelling of AQP4, using the method developed in the previous chapter. This comprehensive approach allowed for the assessment of their impact on brain microstructure, water dynamics, and AQP4 expression.

8.1 Introduction

Water is essential for all living organisms and is indispensable for life. It plays a critical role in numerous biological processes, including homeostasis and cell osmotic balance. These processes are regulated by AQP water channels, first discovered by Preston and Agre in 1991 (Preston & Agre, 1991). AQPs are vital membrane proteins found throughout the bodies of most organisms. Composed of six transmembrane helices, they form pores in the cell membrane. There are over 150 known types of AQPs across all species, including plants, bacteria, and fungi, but only 13 types are found in mammals (Meli et al., 2018). These proteins can exist as monomers, dimers, or tetramers. AQP4, in particular, is abundant in the brain and is organized as tetramers with a molecular size of 30 kDa (Meli et al., 2018).

Brain AQP4s facilitate water movement between four fluid compartments: CSF, ISF, intracellular fluid (ICF), and blood circulation. AQP4 plays an important role in the rapid volume regulation of astrocytes (Ikeshima-Kataoka, 2016). This role is evidenced by the inhibition of astrocyte volume changes in the absence of AQP4 (Thrane et al., 2011). At the BBB, approximately 50% of astrocytic endfeet are covered with AQP4, and nearly 99% of the brain vasculature is ensheathed by astrocyte endfeet (Nagelhus et al., 1998; Mathiisen et al., 2010).

The role of AQP4 in the glymphatic system remains a topic of debate in current literature, with arguments both supporting and questioning its importance (Iliff & Simon, 2019; Pedersen et al., 2023; Smith & Verkman, 2019). Nonetheless, rodents lacking AQP4 have shown significantly better survival rates and outcomes, along with reduced cerebral oedema, compared to wild-type rodents in several neurological disorders, including water intoxication (Manley et al., 2000), ischemic stroke (Manley et al., 2000; Yao, Derugin, et al., 2015; Hirt et al., 2017), spinal cord injuries (Saadoun et al., 2008), and meningitis (Papadopoulos & Verkman, 2005). Conversely, the absence of AQP4 in mice with induced intracerebral haemorrhage resulted in more severe damage, such as increased oedema formation, BBB disruption, and neuronal death, compared to wild-type mice (Tang et al., 2010). Additionally, APP/PS1 mouse models lacking AQP4 exhibited exacerbated AB deposition compared to those with AQP4 (Xu et al., 2015). These experiments underscore the critical role of AQP4 in brain injuries and oedema formation, highlighting the importance of these channels in AB clearance and their potential as therapeutic targets.

Pharmacologically altering AQP4 could aid in managing various neurological conditions. Enhancing AQP4 activity may benefit AD, while inhibition of AQP4 could help in ischemic stroke. It has been demonstrated that TGN-020 decreases glymphatic transport, whereas our previous research showed that TGN-073 increases glymphatic transport (Alghanimy et al., 2023; Alshuhri et al., 2021). Commonly, the glymphatic system and AQP4 function have been studied using invasive imaging techniques like two-photon microscopy and MRI with intrathecal contrast, which are unsuitable for clinical use. Therefore, this study aimed to use non-invasive imaging techniques to assess the effects of potential AQP4 modulators on the rat brain. Diffusion and T₂ mapping were employed to assess

the impact of TGN-073 and TGN-020 on brain microstructure and water exchange. A novel diffusion MRI technique was utilized with long diffusion times, up to 1400 ms, to increase sensitivity to diffusion processes influenced by AQP4 activity, including water diffusion over longer distances that may involve crossing AQP4 channels, Figure 8-1. Additionally, histological changes in AQP4 expression were evaluated through immunofluorescence staining.

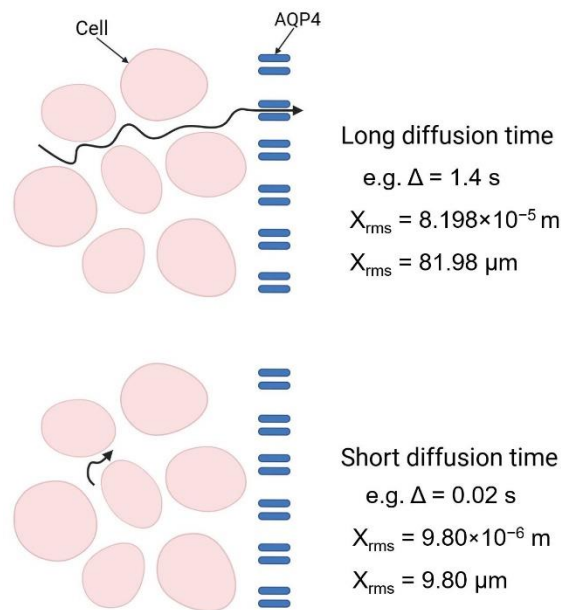


Figure 8-1: Top image: the longer diffusion time allows water molecules to travel greater distances, increasing the likelihood of interactions with structures such as cell membranes and AQP4 channels. Bottom image: with a shorter diffusion time, water molecules have less opportunity to move and interact with cellular structures. The Root Mean Square Displacement (X_{rms}) was calculated using the equation $X_{rms} = \sqrt{6D\Delta}$, where D is the diffusion coefficient ($0.8 \times 10^{-9} \text{ m}^2 \text{ s}^{-1}$) and Δ is the diffusion time.

8.2 Materials and methods

8.2.1 Animals

Male Wistar rats (Charles River) aged 20 to 24 weeks and weighing 300-350 g were utilized in this study. The animals were divided into three groups: vehicle ($n = 7$), TGN-073 treated group ($n = 6$), and TGN-020 treated group ($n = 6$). Rats were randomly assigned to each group. However, one rat from the vehicle group was excluded due to sudden death, resulting in a total of 18 rats included in the study. All animals underwent a one-week acclimatization period in the MRI unit prior to the study to minimize result variabilities. Environmental parameters, including

humidity, ventilation, and temperature, were automatically controlled. The sample size was determined based on existing literature (Iloff, Lee, et al., 2013).

The rats' arterial blood gases and physiological parameters, including heart rate, respiration rate, and blood pressure, were continuously monitored throughout the experiments. The rats exhibited the following mean physiological values: respiration rate = 65 ± 5 breaths per minute, heart rate = 350 ± 50 beats per minute, and mean blood pressure = 90 ± 10 mmHg. Core body temperature was closely monitored and maintained at $37.0 \pm 0.5^\circ\text{C}$ using a rectal thermocouple and controlled by a heating pad (Thermo Scientific NESLAB RTE-7 Circulating Bath, NIST, US). Following the scanning sessions, the animals' brains were dissected for histological examination.

8.2.2 Study design

The study design is shown in Figure 8-2. The anaesthetic regimen was as follows: initially, all rats were induced with 5% isoflurane in an induction chamber using O_2 and N_2O as carrier gases (0.3 and 0.7 L/min, respectively). Once the rats lost consciousness (i.e. did not respond to a toe pinch), they were transferred to a facemask and the isoflurane concentration was reduced to 1.5% - 2.5%, while maintaining the same O_2 and N_2O volumes (30:70 ratio). The animal was intubated via tracheotomy for artificial ventilation using a 13G feeding tube and connected to a ventilator. A homeothermic blanket system with a rectal probe was used to maintain the animal's body temperature. Femoral artery cannulation was performed using polythene tubing. This tubing was connected to a blood pressure transducer for continuous monitoring of arterial BP and HR, as well as for periodic analysis of arterial blood gases and pH. The parameters were maintained within the following ranges: partial pressure of oxygen 90-110 mmHg, partial pressure of carbon dioxide 35-45 mmHg, pH 7.4 ± 0.1 , and oxygen saturation 97%-100%. For detailed information on these surgical procedures, please refer to Chapter 3. The animal was then placed in the prone position in a cradle and transferred to the MRI scanning room. Throughout the scanning, the animal's physiology and vital signs were continuously monitored and maintained stable using an MRI-compatible setup.

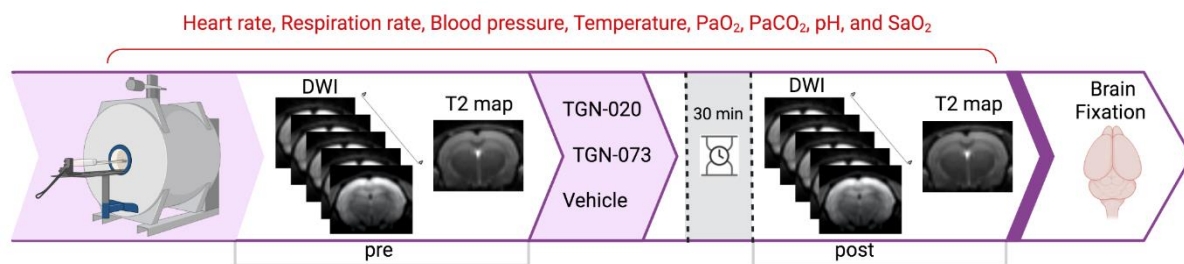


Figure 8-2: Study Protocol: The study involved an initial baseline MRI scan, followed by an intraperitoneal injection of either the drug or vehicle. After a waiting period of 30 minutes, a second MRI scan was performed. Following the imaging, the rats' brains were fixed for immunofluorescence staining. DWI: Diffusion weighted imaging.

8.2.3 Drug Preparation

Preparation of the drugs is described in Section 3.6. In the treatment groups receiving TGN-073 and TGN-020, the drugs were administered intraperitoneally using a 25G needle, 30 minutes before the MRI rescans (at a dose of 200 mg/kg in 20 ml/kg body weight). Meanwhile, the vehicle group received only gamma-cyclodextrin and DMSO dissolved in distilled water.

8.2.4 Magnetic Resonance Imaging Protocols

All imaging was conducted using a 7 Tesla preclinical MRI system (Bruker BioSpec 7 T/30) controlled by Paravision 6.0.1 software (Bruker Bio Spin, Ettlingen, Germany), equipped with gradient coils featuring a 114 mm inner diameter and a maximum strength of 440 mT/m. A surface coil with a four-channel phased array served as the RF receiver coil, while a volume (birdcage) coil with a 72 mm inner diameter served as the RF transmitter. Head stabilization was achieved using ear and mouth bars. Initially, a localizer scan was performed to adjust the slice orientation and position.

For diffusion images, due to the use of long observation times, up to 1400 ms, stimulated echo (STE) was used instead of the standard spin echo to minimise signal loss. For further details on STE, refer to Chapter 2, Section 2.6.5. Imaging parameters for diffusion weighted echo planar imaging (DW-EPI) STE scan were: TR = 4000 ms, TE = 24.53 ms, 4 b-values ranging from 0 to 1000 s/mm² along the

X direction, NEX = 2 , flip angle = 90° , FOV = 4 cm, acquisition matrix = 96, slice thickness = 2 mm, slice gap = 2 mm, slice orientation: coronal, number of slices = 3, acquisition time \approx 3 minutes. Data were acquired for nine diffusion times (Δ): 20, 100, 200, 400, 600, 800, 1000, 1200, and 1400 ms.

MSME sequence was utilized for T_2 mapping with the following parameters: TR = 8000 ms, TE = 20 ms, NEX = 1, flip angle = 90° , number of echoes (echo images) = 35, slice thickness = 1.5 mm, echo spacing = 20 ms, FOV = 40 x 40 mm, matrix size = 96 x 96, resulting in a resolution = 0.417 x 0.417 mm, and total scan time = 9 minutes and 12 seconds. Following imaging completion, animals were immediately sacrificed to collect brain tissue samples for immunohistochemistry. Euthanasia was performed by deeply anesthetizing the rats using 4% isoflurane, followed by transcardial perfusion fixation.

8.2.5 Immunohistochemistry

For details on AQP4 immunofluorescence staining, please refer to Chapter 7. Briefly, rats were transcardially perfused with heparinized saline (200 mL) followed by 4% PFA (200 mL). After isolation and post-fixation of the brains in 4% PFA overnight at room temperature, the brains were dehydrated to enable embedding with paraffin. Six serial coronal brain sections (7 micro-meter thickness) utilizing a vibrating microtome for each animal were collected at a distance of around -4.5 mm from the bregma, according to the rat brain atlas published by Paxinos and Watson fourth edition (1998). After rehydration, heat-induced antigen retrieval was performed using citrate buffer, pH = 6 at 121°C for 10 minutes to enhance the immunostaining signal. Slices were incubated with primary antibody, Rabbit Anti-Aquaporin 4 (abcam, ab128906 1:400) diluted in antibody diluent (Dako, S0809) overnight at 4°C . The next day, slices were incubated with Alexa Fluor Plus 488 conjugated F(ab')₂-Goat anti-Rabbit IgG (H&L) Cross-Adsorbed Secondary Antibody, (abcam, ab150077, 1:500) diluted in antibody diluent. Incubate for 1 hour at room temperature. The antibodies were protected from light at all times. Slices were mounted with ProLong™ Diamond Antifade Mountant with DAPI, (Catalog number: P36962, Thermo Fisher Scientific). Rat brains were imaged using a confocal microscope at 10× 20× and 40× primary objective power (Zeiss LSM 710 Confocal Laser Scanning Microscope) utilizing Zen

software. Representative images were captured at 40× magnification utilizing Leica slide scanner microscope. Two separate runs of immunofluorescence staining were conducted to evaluate protocol reproducibility and account for any technical or experimental variabilities. Additionally, staining several brains in each group accounted for any biological variabilities.

8.2.6 Data analysis

All MRI images in this study were analysed using MATLAB software (MATLAB R2019a, MathWorks Ltd., UK); the codes were developed in-house.

For the STE-DW-EPI image analysis, the diffusion coefficient (D) along the x-axis was calculated for each voxel by fitting the data using the following equation:

$$S = S_0 e^{-bD} \quad \mathbf{8-1}$$

where

$$b = \gamma^2 G^2 \delta^2 \left(\Delta - \frac{\delta}{3} \right) \quad \mathbf{8-2}$$

Where S_0 is the signal intensity with zero diffusion gradients ($b = 0$), S is the signal intensity after applying the diffusion gradients, b is the b-value (s/mm^2), G is the gradient strength, Δ is the diffusion time, γ is the gyromagnetic ratio, and δ is the duration of the gradient. Images after drug injection were co-registered to the pre-injection images using rigid transformation. For each rat, the ROI in the cerebral cortex was manually segmented in the DWI to calculate the average diffusion coefficient values. The cortex was chosen due to its proximity to the MRI coil, which provided the highest SNR. These values were then normalized by dividing by the baseline values, which were obtained at a diffusion time of 20 ms. The diffusion coefficients were normalized to account for inherent inter-subject variability in diffusion values, allowing for a more accurate comparison of treatment effects across subjects.

To measure T_2 values, signal decay curves were fitted using the following equation:

$$S = S_0 e^{\frac{-t}{T_2}} + c \quad \mathbf{8-3}$$

Where S_0 is the initial signal intensity, S is the signal intensity at time t , T_2 is the transvers relaxation time, and c is a baseline offset. T_2 map images after drug injection were co-registered with the pre-injection images using rigid transformation. ROIs were delineated on the coronal images of the brain. For each rat, the cerebral cortex, hippocampus, and thalamus were manually segmented to calculate the average T_2 values. Figure 8-4d highlights the location of the ROIs.

For immunohistochemistry, immunofluorescence sections were scanned to visualize AQP4 distribution within the rat brains. Image analysis was conducted using QuPath 0.4.3 software. The exposure intensity and level were established and kept constant throughout the investigation to ensure consistency. QuPath's annotation tools were used to identify and quantify AQP4-positive signals. The 'Object Classification' tool was then employed to differentiate between background fluorescence and specific AQP4 labelling based on pixel intensity thresholds and object size parameters. To assess the level of AQP4 expression in different brain regions, the 'Measurement' tool was used to calculate the average fluorescence intensity of the AQP4 emission channels within the classified AQP4-positive objects. To account for inter-slice variability, the percentage of AQP4 coverage was quantified for three slices per animal, and these values were averaged to obtain a single representative value per animal. The averaged value was then used for statistical comparison between the TGN-073 recipient group (n=6), the TGN-020 recipient group (n=6), and the vehicle recipient group (n=6). To evaluate AQP4 expression with preserved polarity, the calculation involved determining the percentage of the total field of view where pixel intensity matched or exceeded that of the perivascular endfeet within the image area. Animals were coded, and data analysis was carried out in a blinded fashion to reduce bias.

8.2.7 Statistical analysis

Statistical analyses and graphs were generated using MATLAB software (MATLAB R2019a, MathWorks Ltd., UK), Excel 2016 (Microsoft Windows), and GraphPad Prism 10 (GraphPad Prism Software, California, USA). Statistical comparisons

between two groups were performed using paired two-tailed Student's t-test. For comparisons involving three groups, a one-way ANOVA was performed, followed by Tukey's multiple comparison post hoc test. Comparisons between data collected before and after drug administration at different diffusion times were performed using repeated measures ANOVA, followed by Tukey's post hoc test to correct for multiple comparisons. Data are presented as mean \pm SD unless otherwise stated. The statistical significance is indicated as follows: *: $P < 0.05$, **: $P < 0.01$, ***: $P < 0.001$, and ****: $P < 0.0001$.

8.3 Results

8.3.1 No significant change in diffusion values was observed after administering AQP4 drugs

To investigate the impact of AQP4 drugs (TGN-073 and TGN-020) on brain microstructure non-invasively, DW-EPI with stimulated echo sequence was performed using nine different diffusion times, ranging from 20 to 1400 milliseconds. The goal was to assess changes in water diffusion within brain tissue following drug administration. Three animal groups were studied: Vehicle, TGN-073, and TGN-020. Each group underwent DW-EPI scans before and 30 minutes after IP injection of the respective treatment. Across all groups, an overall decrease in water diffusion was observed as the diffusion time increased. However, there was no statistically significant change in water diffusivity following drug administration, Figure 8-3. This suggests that under normal conditions, modulation of AQP4 by TGN-073 or TGN-020 does not significantly impact water diffusion within brain tissue.

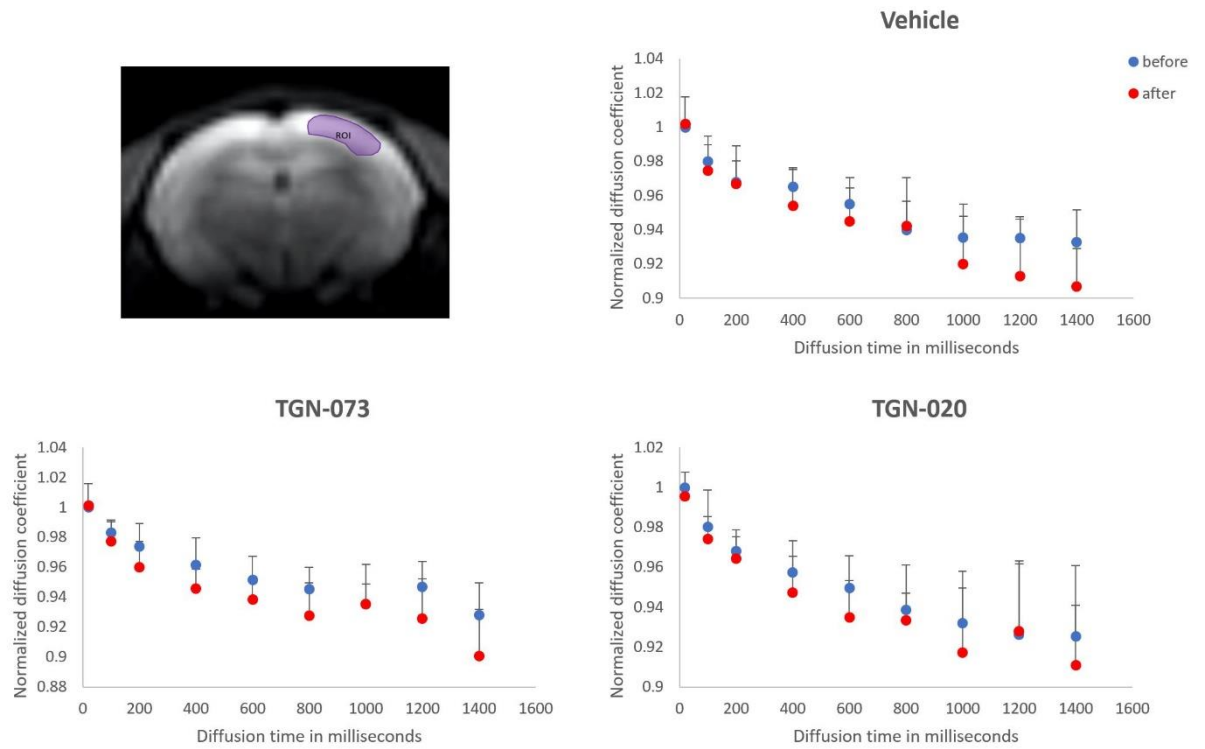


Figure 8-3: Normalized diffusion coefficient values within the brain cortex across a range of diffusion times spanning from 20 to 1400 milliseconds, for TGN-073, TGN-020, and vehicle groups. Blue circles: before drug administration, and red circles: after drug administration.

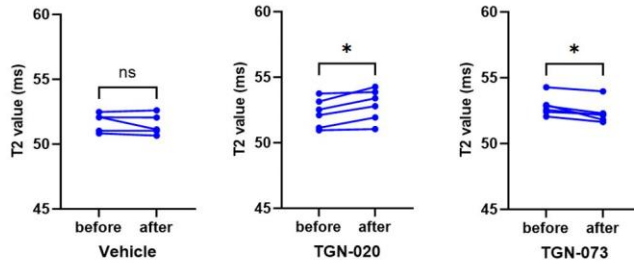
8.3.2 Inhibition of AQP4 resulted in increased brain T_2 values, whereas enhancement of AQP4 led to reduced brain T_2 values

T_2 maps were utilized to detect changes in water content and exchange in the brain (see Figure 8-4). All ROIs exhibited a tendency towards higher T_2 values following AQP4 inhibition and lower T_2 values following AQP4 facilitation. Significant reduction in T_2 values, in cerebral cortex ($P= 0.0141$), hippocampus ($P= 0.0478$), and thalamus ($P= 0.0314$) after TGN-073 administration. In contrast, significant increase in T_2 values, in cerebral cortex ($P= 0.0158$), hippocampus ($P= 0.0474$), and thalamus ($P= 0.0471$) after TGN-020 administration. Yet, no significant difference was shown after vehicle administration in all brain regions ($P > 0.05$).

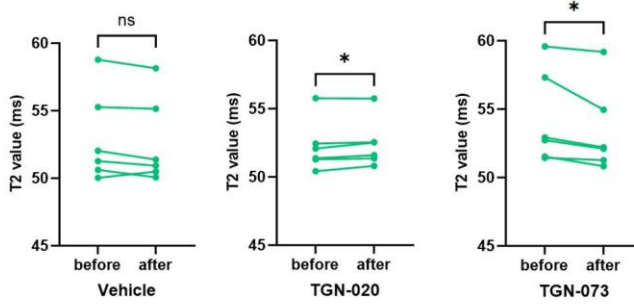
To further investigate the impact of AQP4 modulation on brain tissue water dynamics, a comparative analysis of T_2 values across treatment groups, focusing solely on post-treatment data was conducted (Figure 8-5). Unlike the within-

subject comparisons performed in Figure 8-4, this analysis focuses on between-group comparisons, allowing for the assessment of the effects of AQP4 facilitation and inhibition against vehicles. Notably, no statistically significant differences in T_2 values were observed between the groups in the cerebral cortex and hippocampus. However, a significant increase in T_2 values was detected in the thalamus of TGN-020-treated rats compared to vehicles ($p < 0.05$), suggesting an elevated water content in this region following AQP4 inhibition. No significant differences were identified between vehicle and TGN-073-treated groups in any ROI ($P > 0.05$). These findings indicate that while AQP4 modulation induces significant changes in water dynamics within individual brain regions, as evidenced by the pre- versus post-treatment comparisons in Figure 8-4, the comparison of post-treatment T_2 values between groups highlights potential region-specific effects of the treatments.

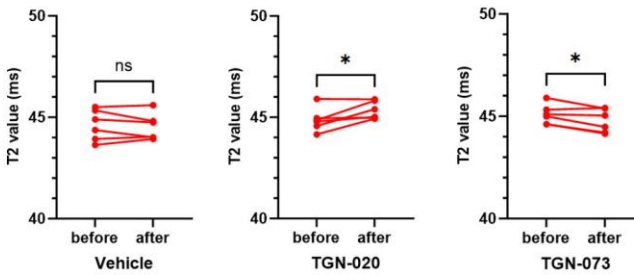
(a) Cerebral cortex



(b) Hippocampus



(c) Thalamus



(d)

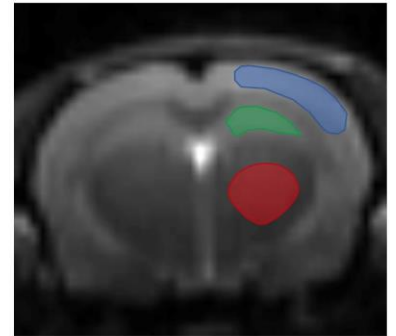


Figure 8-4: In the TGN-020 treated group, T_2 values exhibited significant increases, whereas in the TGN-073 treated group, significant decreases were observed in several brain regions. Figure d shows the locations of the ROIs.

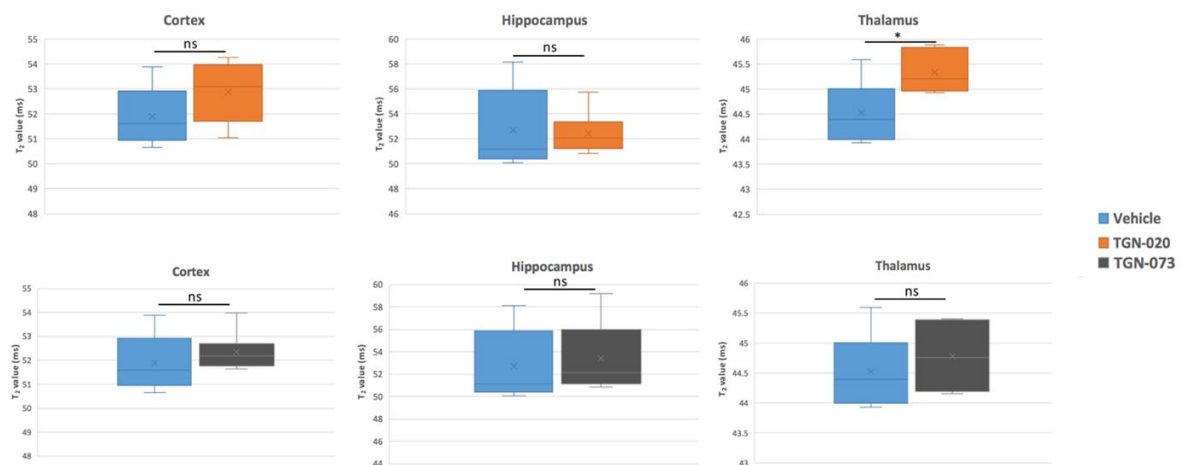


Figure 8-5: T_2 values compared across treatment groups (Vehicle vs TGN-020, and Vehicle vs TGN-073) for the same ROIs as in Fig. 8.4. Unlike Fig. 8.4, which focused on within-group comparisons before and after treatment, this figure presents between-group comparisons.

Statistical analysis revealed no significant differences in T_2 values in the Cortex and Hippocampus across groups, but a significant difference ($P < 0.05$) was identified in the Thalamus between Vehicle and TGN-020 recipients. The locations of the ROIs are shown in Figure 8.4d. Data are presented as box plots showing median, interquartile range, and whiskers representing minimum and maximum values.

8.3.3 AQP4 expression in the brain increased with TGN-073 treatment, whereas decreased with TGN-020 treatment

The impact of TGN-073 and TGN-020 on AQP4 expression in rat brains was evaluated using immunofluorescence staining (Figure 8-6 and Figure 8-7). The findings revealed that administration of TGN-073, an AQP4 facilitator, led to upregulation of AQP4 expression compared to vehicle-treated rats. In contrast, the use of TGN-020, an AQP4 inhibitor, resulted in downregulation of AQP4 expression, although not a complete diminishment, compared to vehicle-treated rats.

In the violin plots, Figure 8-8, the cortex exhibited the most pronounced differences in AQP4 expression among the treatment groups. Specifically, AQP4 expression in the cortex was significantly reduced in the TGN-020 group compared to both the vehicle and TGN-073 groups ($P < 0.05$ and $P < 0.0001$, respectively). Conversely, AQP4 expression was significantly increased in the TGN-073 group compared to the vehicle and TGN-020 groups ($P < 0.05$ and $P < 0.0001$, respectively). Similarly, in the hippocampus and thalamus, AQP4 expression showed a similar pattern of differences between the groups as observed in the cortex, although statistical significance was only observed when comparing TGN-073 to TGN-020 ($P < 0.05$).

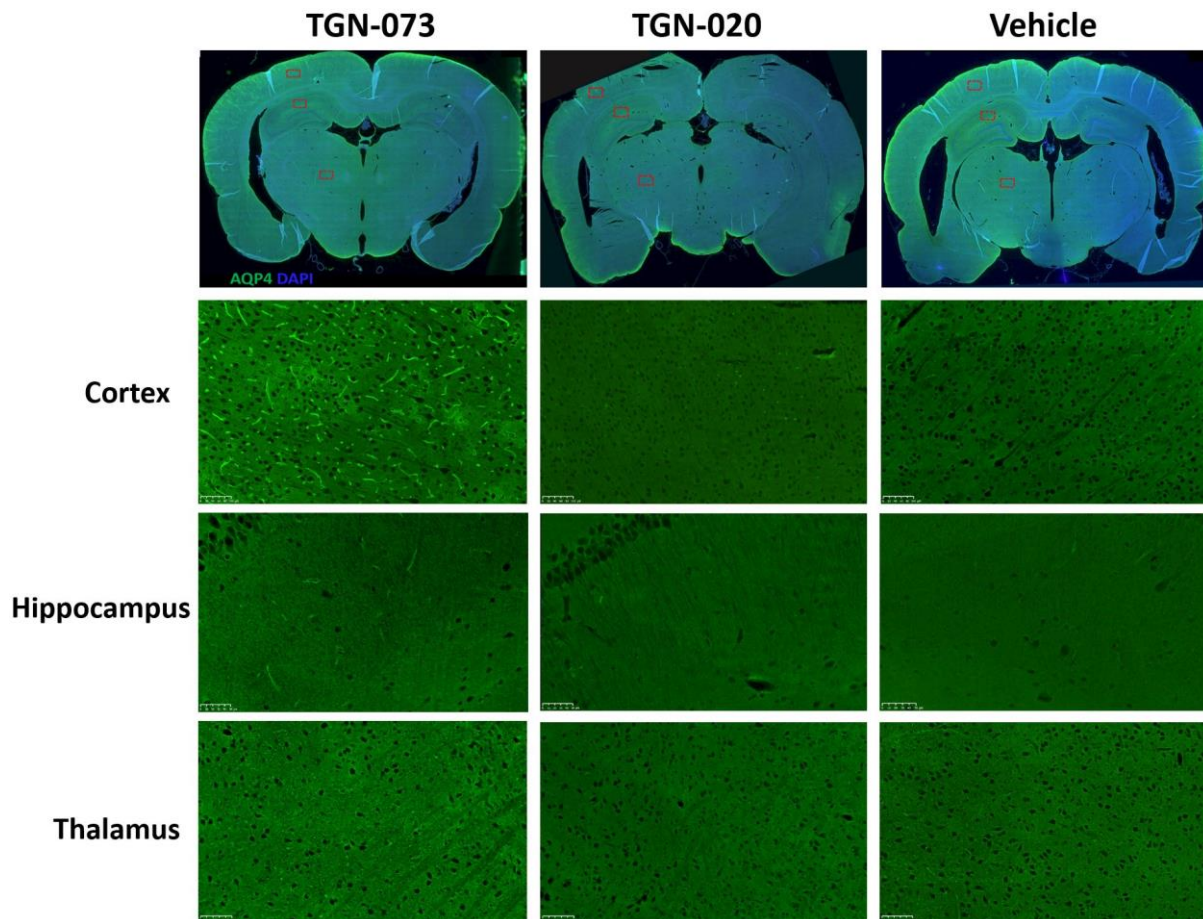


Figure 8-6: AQP4 immunofluorescence staining was performed in the rat brain using Alexa Fluor 488 (green) and nuclear counterstaining with DAPI (blue). Images captured at 40x magnification. Scale bars: Cortex and thalamus, 100 μm ; hippocampus, 50 μm .

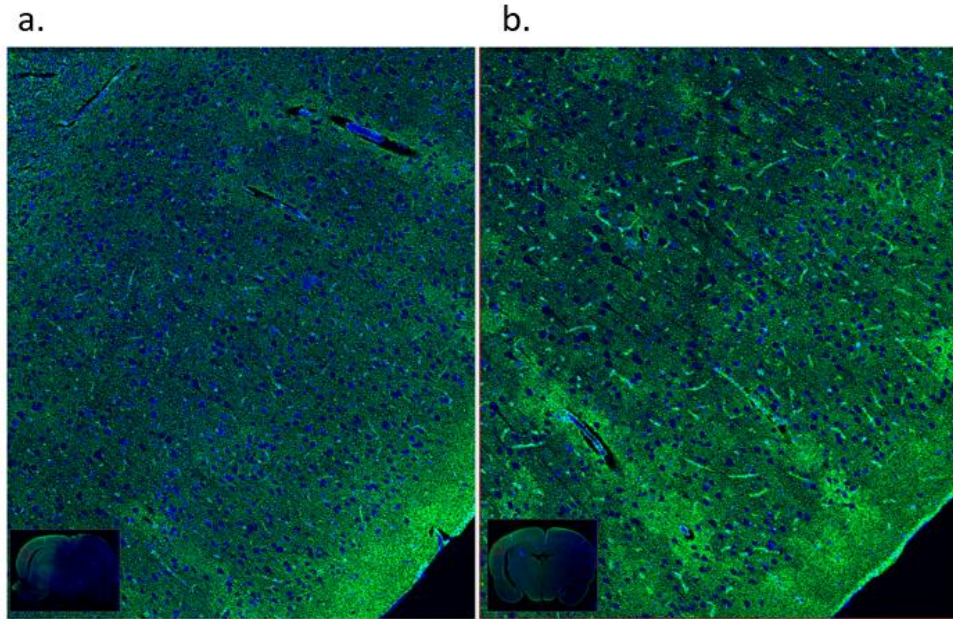


Figure 8-7: AQP4 Immunofluorescence staining of rat brain. The figure displays a larger field of view of the brain cortex. Panels depict: a. TGN-020 recipient, b. TGN-073 recipient. Images were captured at 20x magnification.

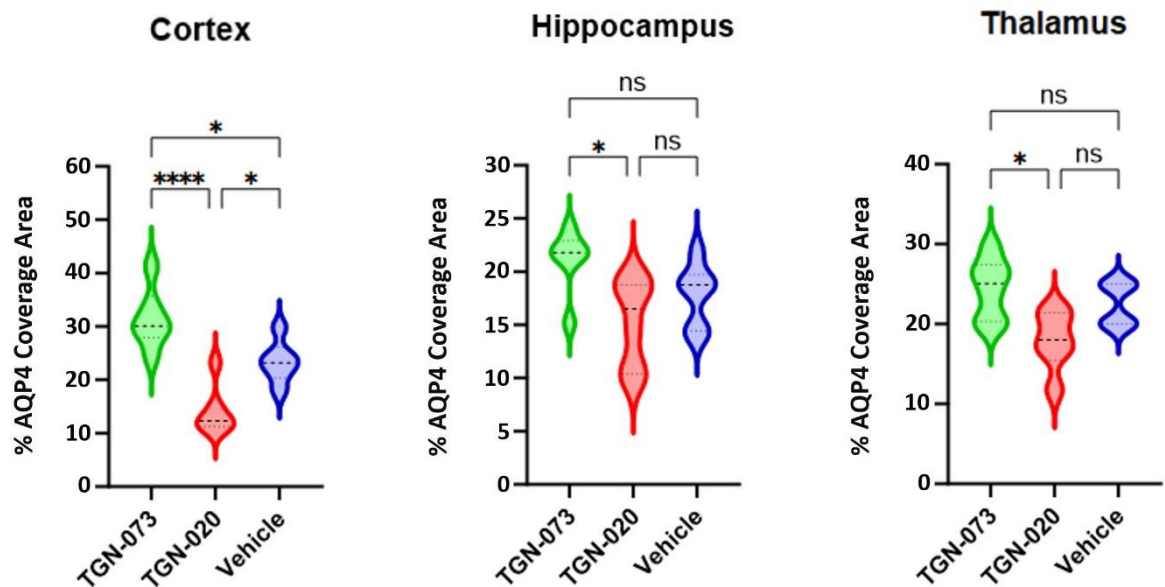


Figure 8-8: (The violin plots represent the percentage of AQP4 coverage area in different brain regions. The TGN-073 recipient group (n=6) is represented by green, the TGN-020 recipient group (n=6) by red, and the vehicle recipient group (n=6) by blue. * indicates $P < 0.05$, and **** indicates $P < 0.0001$.

8.4 Discussion

Dysregulation of AQP4 expression is associated with various neurological disorders, including AD, PD, cerebral oedema, and hematoma (Potokar et al., 2016; Lan et al., 2016; Sun et al., 2016; Zhang et al., 2011; Badaut et al., 2007; Chiu et al., 2013; Brissaud et al., 2010). Therefore, an in-depth study of these water channels is crucial for understanding their roles in these conditions. This study aimed to investigate the effects of pharmacological modulation of AQP4 on the glymphatic system and brain microstructure using advanced non-invasive MRI techniques and immunofluorescence staining. Our findings provide valuable insights into the role of AQP4 in the glymphatic system and highlight its potential as a therapeutic target for neurological disorders. Despite the important role of AQP4 in water transport and homeostasis, our STE-DW-EPI results showed no significant change in the diffusion coefficient along the x-axis across all observation times in any of the treatment groups. This suggests that neither the facilitation nor inhibition of AQP4 activity significantly alters brain microstructure within the timeframe of the study (i.e. 30 minutes after drug administration). This is an important observation as it implies that short-term modulation of AQP4 does not disrupt the structural integrity of brain tissue in normal animals, which is a positive indication for the potential therapeutic use of AQP4 modulators.

In contrast, T_2 mapping revealed significant changes associated with AQP4 modulation. T_2 values positively correlate with water content and negatively with water exchange (Chou et al., 2009). Specifically, TGN-073 administration resulted in a significant reduction in T_2 values, indicative of enhanced water exchange and potentially more efficient glymphatic clearance. Conversely, TGN-020 administration led to an increase in T_2 values, suggesting impaired water exchange. These results underscore the critical role of AQP4 in regulating water movement between brain tissue compartments and highlight its influence on brain water homeostasis. Immunofluorescence staining further corroborated these findings, showing that TGN-073 significantly upregulated AQP4 expression, whereas TGN-020 caused notable downregulation. This differential expression of AQP4 aligns with the observed changes in T_2 values, reinforcing the idea that AQP4 activity directly impacts brain water dynamics.

Our findings are consistent with prior research demonstrating that AQP4 plays a crucial role in facilitating the clearance of interstitial solutes and maintaining fluid homeostasis within the brain. For instance, Ohene et al. employed a multi-TE ASL MRI method to assess water permeability across the blood-brain interface in mouse brains. By calculating the exchange time, they observed a 31% increase in exchange time in AQP4 knockout mice compared to wild-type counterparts. This substantial difference suggests a reduction in water exchange in AQP4 knockout mice, highlighting the importance of AQP4 in regulating water dynamics (Ohene et al., 2019). In contrast to wild-type rats, AQP4 knockout rats displayed a significantly prolonged half-life of ISF in the thalamus, alongside a reduction in the clearance coefficient (Teng et al., 2018). Our findings support these observations, as an elevation in T_2 values across different brain regions was demonstrated following pharmacological inhibition of AQP4, indicating a decline in water exchange between tissue compartments. T_2 relaxation times are influenced by the behaviour of water molecules within tissues, serving as indicators of water mobility and exchange dynamics. Regions characterized by restricted water mobility typically exhibit longer T_2 times, whereas those with greater water exchange exhibit shorter T_2 times (Jiang et al., 2023; Whittall et al., 1997). Utilizing T_2 mapping MRI provides researchers and healthcare practitioners with invaluable insights into tissue properties, particularly water content, and the dynamics of water exchange across various anatomical regions.

AQP4 is a potential therapeutic target due to its involvement in several neurological disorders. AQP4 knockout mice, for instance, exhibit reduced astrocytic water permeability and show better outcomes and lower morbidity compared to wild-type mice in various neurological injuries (Papadopoulos & Verkman, 2007; Manley et al., 2000; Yao, Uchida, et al., 2015). In ischemic stroke models, AQP4 knockout mice demonstrate lower cerebral cytotoxic oedema formation than wild-type mice (Manley et al., 2000; Solenov et al., 2004; Verkman, 2012). However, in conditions involving vasogenic oedema, such as subarachnoid haemorrhage, ischemic stroke, and brain tumours—where the integrity of the BBB is compromised—the deletion of AQP4 exacerbates the problem (Bloch et al., 2005; Tait et al., 2010; E. Liu et al., 2020; Verkman, 2012). These findings indicate that AQP4 has a dual role, both harmful and beneficial. It

acts as a two-way water channel: during cytotoxic oedema, it increases intracellular water flux and retention, contributing to oedema progression (Hirt et al., 2017), whereas during vasogenic oedema, it assists in the removal of excess water (Saadoun & Papadopoulos, 2010; Papadopoulos et al., 2004). Several studies have suggested that the resolution of vasogenic oedema is correlated with higher AQP4 expression (J Badaut et al., 2011; Jerome Badaut et al., 2011; Fukuda et al., 2012; Meng et al., 2004; Tourdias et al., 2009; Abir-Awan et al., 2019; Verkman et al., 2017; Tang & Yang, 2016).

The role of AQP4 in the glymphatic system for facilitating fluid movement and exchange has been demonstrated by several studies using various methods of genetic deletion of AQP4 (Iloff et al., 2012; Murlidharan et al., 2016; Plog et al., 2015; Achariyar et al., 2016; Lundgaard et al., 2017). However, AQP4 knockout animals, i.e., genetically modified animals, suffer from serious abnormalities, including impairments in vision, hearing, and memory (Li et al., 2002; Li & Verkman, 2001; Fan et al., 2013; Rosu et al., 2020). Therefore, pharmacological inhibition of AQP4 might be a more viable option for scientific research. Previous studies have demonstrated that TGN-020 inhibits AQP4 through the intracellular ubiquitin proteasome system, both in vitro and in vivo (Rosu et al., 2020; Huber et al., 2009; Harrison et al., 2020). The Half-maximal inhibitory concentration (IC₅₀) was found to be 3 μ M (Huber et al., 2009). Moreover, TGN-020 led to a downregulation of glymphatic function and inhibited the exchange between CSF and ISF (Rosu et al., 2020; Pirici et al., 2017). Similar to AQP4 knockout animals, treatment with TGN-020 results in smaller cerebral cytotoxic oedema following ischemic injuries (Pirici et al., 2017; Igarashi et al., 2011; Popescu et al., 2017; Sun et al., 2022). TGN-020 may exhibit neuroprotective effects following neurological insult. In a recent mouse study, TGN-020 was found to alleviate cell apoptosis and inflammation induced by cerebral ischemia-reperfusion injuries (Li et al., 2023). This effect was attributed to TGN-020's suppression of the ERK1/2 pathway (Li et al., 2023). On the other hand, TGN-073 enhances water transport through AQP4 channels across the BBB (Huber, Igarashi, et al., 2018). Moreover, TGN-073 has been shown to enhance glymphatic function (Alghanimy et al., 2023). In agreement with these findings, administration of TGN-020 resulted in decreased water exchange and AQP4 expression, whereas administration of TGN-073 led to increased water exchange and AQP4 expression.

In Chapter 6, rats treated with TGN-073 exhibited significantly higher water diffusion compared to vehicle-treated rats ($p < 0.05$). This finding was consistent even when analysing diffusion coefficients along the x-direction alone. It is important to note that a relatively short diffusion time of 30 ms was used in that chapter. In this chapter, we did not use a 30 ms diffusion time; the closest time point was 20 ms. At this 20 ms time point, we observed an increase in diffusion values after TGN-073 administration (0.000676 vs. 0.000668), but this increase did not reach statistical significance ($p = 0.2$). The differences between these findings may be attributed to the variation in diffusion times. Additionally, other methodological differences between the two experiments may have contributed to the observed discrepancies, such as the use of different MRI scanners (Bruker PharmaScan vs Bruker BioSpec).

Our study has several implications for the therapeutic modulation of AQP4. The ability of TGN-073 to enhance AQP4 expression and facilitate water exchange could be beneficial in conditions characterized by impaired glymphatic clearance, such as AD and PD (Pedersen et al., 2023; Hoshi et al., 2017; Cui et al., 2021). Conversely, TGN-020's ability to reduce AQP4 expression and hinder water exchange could be useful in conditions where reducing brain oedema is desirable, such as after a stroke or traumatic brain injuries (X. Liu et al., 2021; Zhang et al., 2020).

8.5 Conclusion

This study highlights the capability of TGN-020 and TGN-073 to modulate AQP4 expression. While no observable effects on water diffusion were detected, even at extended diffusion times, significant alterations in brain water dynamics were found, as evidenced by changes in T_2 values. Our findings indicate that TGN-073 has the potential to enhance AQP4 expression, while TGN-020 can reduce it. These results support the potential of AQP4-targeting therapeutic approaches in managing neurological conditions characterized by dysregulated AQP4 expression. Future studies should explore the long-term effects of AQP4 modulation and its therapeutic potential in various neurological conditions.

Chapter 9 The Effect of AQP4 Facilitator TGN-073 on the BCAS Rat Model

This final study aims to extend findings from normal rats to bilateral common carotid artery stenosis (BCAS) models, testing whether the positive impact of the TGN-073 observed in normal rats can improve glymphatic transport in these models. To our knowledge, this is the first study to investigate the effects of TGN-073 in cerebral hypoperfusion rat models. The study evaluates glymphatic transport using DCE-MRI and AQP4 expression through immunofluorescence staining. A small number of animals were used in this study due to challenges encountered during the implementation of the new BCAS model at the university. These challenges are discussed later in this chapter.

9.1 Introduction

Among developed nations, vascular diseases rank as the second most prevalent cause of dementia, following AD (Wallin & Blennow, 1993). Vascular cognitive impairment (VCI) encompasses various forms of cognitive decline associated with cerebrovascular diseases, including post-stroke dementia, vascular mild cognitive impairment, and vascular dementia (Lansdell & Dorrance, 2022). Vascular dementia, in particular, has garnered significant attention due to the prevalence of small vessel diseases in the elderly and its similarity to AD in terms of gradual cognitive decline. Cerebral hypoperfusion (i.e. inadequate oxygen supply to the brain) is a common feature associated with small vessel diseases, contributing to the cognitive impairments seen in vascular dementia (Sarti et al., 2002).

Deciphering the precise cause-and-effect relationship of vascular dementia in humans poses a challenge due to the influence of additional factors such as degenerative processes and ageing, which can impact cognitive abilities.

Nevertheless, experimental studies utilizing models featuring consistent and moderate reduction of blood flow to the brain offer valuable insights into clarifying this relationship.

In 1994, a prolonged cerebral hypoperfusion rat model, induced by bilateral common carotid artery occlusion (BCAO), was established to evaluate persistent ischaemic white matter lesions. This BCAO model exhibited glial activation and white matter alterations similar to those observed in human white matter damage (Wakita et al., 1994). However, the impairment of the visual pathway due to occlusion of the ophthalmic arteries, along with sporadic involvement of the cerebral cortices could compromise cognitive and behavioural evaluations in both mouse and rat BCAO models (Sarti et al., 2002; Ishikawa et al., 2023).

On the other hand, the chronic cerebral hypoperfusion model using BCAS was introduced as a model of vascular dementia in 2004 in mice and in 2015 in rats to study white matter lesions. Unlike the BCAO model, the BCAS mouse model avoids damage to grey matter structures and minimally impacts the visual tract, providing a more reliable platform for assessing cognitive and behavioural outcomes (Shibata et al., 2004; Li et al., 2015).

Chronic cerebral hypoperfusion induced by BCAS has been shown to exacerbate A β accumulation in AD mouse models, such as APP-Tg mice (Kitaguchi et al., 2009; Yamada et al., 2011). Moreover, tau transgenic mice subjected to the BCAS procedure exhibited higher levels of phosphorylated tau compared to those undergoing a sham procedure (Shimada et al., 2019). Similarly, PD mouse models experienced worsened cognitive deficits due to BCAS (Tang et al., 2017). In another study, spontaneous hypertensive rats that underwent the BCAS operation using ameroid constrictors showed white matter injuries and memory deficits, akin to pathologies found in subcortical ischaemic vascular dementia patients (Kitamura et al., 2016). The BCAS model effectively induces cerebral hypoperfusion, exacerbating neurodegenerative pathology and cognitive deficits across various disease models.

In this study, glymphatic influx in a rat model of BCAS was investigated using MRI enhanced with intracisternal gadolinium infusion. Cerebral blood flow (CBF) was

measured before and after BCAS induction. Additionally, the effect of the AQP4 facilitator TGN-073 on glymphatic flow in these models was evaluated. Finally, immunofluorescence staining of AQP4 was performed to assess the impact of BCAS on AQP4 expression and to evaluate the potential benefits of TGN-073.

9.2 Materials and methods

9.2.1 Animals

Wistar Kyoto rats, bred in-house at the animal facility of the University of Glasgow, were used in this experiment. The rats, weighing between 270 and 320 g, were divided into three groups and randomly assigned as follows: BCAS-operated rats treated with TGN-073 (n = 4), BCAS-operated rats treated with vehicle (n = 4), and sham-operated rats (n = 2). The animals had ad libitum access to food and water and were maintained under a 12-hour light-dark cycle. Physiological parameters and blood gases of the animals were continuously monitored and maintained within normal ranges, as detailed in Chapter 3. Parameters were maintained as follows: mean blood pressure 97 ± 5 mmHg, partial pressure of oxygen 100 ± 5 mmHg, partial pressure of carbon dioxide 38 ± 3 mmHg, pH 7.4 ± 0.1 , and O₂ saturation: 97 ± 2 %. The study design is illustrated in Figure 9-1.

9.2.2 Animal surgeries

First day: Rats were anesthetized with isoflurane delivered via intubation using a ventilator, maintaining a concentration of 1.5-2.5%. BCAS surgery was conducted by placing ligatures around both common carotid arteries. Detailed surgical methods are described in Chapter 3. Briefly, the right common carotid artery was exposed, and a blunt needle (27-gauge, 0.5 cm length) was positioned adjacent to it. The artery and the needle were securely tied together using two 4-0 silk sutures, spaced 1-2 mm apart. The needle was then carefully extracted to induce stenosis, effectively narrowing the artery to match the needle diameter of 0.41 mm. The same procedure was repeated on the left common carotid artery. Sham-operated rats underwent the same procedure, except the arteries were not ligated. Rats in the treatment group received immediate intraperitoneal

injections of TGN-073 (200 mg/kg) following the BCAS surgery. Next, the rats were allowed to recover for 24 hours and were closely monitored for the first 3 hours post-surgery. For further details, please refer to Chapter 3. All animals recovered well, as indicated by normal behavioural assessments, with weight loss not exceeding 5%.

On the second day, the rats underwent physical and behavioural assessments to evaluate their health and neurological conditions. If any rats showed severe distress or abnormalities, they were immediately euthanized and excluded from the study. Following this, the rats were anesthetized with 1.5-2.5% isoflurane. A tracheotomy was performed to enable artificial ventilation, and femoral artery cannulation was conducted for continuous blood pressure monitoring and regular gas analysis. Detailed procedures are available in Chapter 3. A tracheotomy was chosen on the second day instead of intubation for two primary reasons: first, because the animals were not intended to recover at the end of the day's procedures, making tracheotomy suitable; and second, to minimize potential airway irritation or trauma associated with repeated intubation. Additionally, rats underwent cisterna magna cannulation, as outlined in Chapter 3, Section 3.4.2, to allow the infusion of MRI contrast media Gd-DTPA into the CSF for direct visualization of glymphatic transport. A closed-end polyethylene tube, filled with 50 μ l of Gd-DTPA and connected to the infusion pump, was then attached to the cannula.



Figure 9-1: study protocol timeline.

9.2.3 Magnetic Resonance Imaging

All imaging in this experiment was performed on a 7 Tesla preclinical MRI system (Bruker Biospec 7T/30) controlled by Paravision 6.0.1 software (Bruker BioSpin,

Ettlingen, Germany). Head stabilization was achieved using ear and mouth bars. Physiological parameters were continuously monitored with MRI-compatible equipment and maintained within normal ranges.

CBF was measured using pulsed arterial spin labelling (PASL) with a Flow-sensitive Alternating Inversion Recovery (FAIR) echo planar imaging (EPI) sequence. Imaging parameters were as follows: coronal slice thickness = 3 mm, number of slices = 1, flip angle = 90°, TE = 35 ms, TR = 6000 ms, number of averages = 8, field of view = 25 × 25 mm, acquisition matrix size = 96 × 96, yielding an image resolution of 0.26 × 0.26 mm/pixel, and a scan time of 9 min 36 s. Inversion times (TI) were 50, 108, 235, 510, 1106, and 2400 ms, with two inversion modes: selective and non-selective inversions. The inversion slab thickness was 5 mm, with slice package margins of 1 mm.

CBF maps were constructed using the Image Sequence Analysis (ISA) tool package (Paravision 6.0.1, Bruker). CBF was calculated according to the following equation (Detre et al., 1992):

$$CBF = \left(\left(\frac{1}{T_{1 \text{ selective}}} \right) - \left(\frac{1}{T_{1 \text{ nonselective}}} \right) \right) * \lambda \quad 9-1$$

Where $T_{1 \text{ selective}}$ is the T1 relaxation time measured with selective inversion (labelled), $T_{1 \text{ nonselective}}$ is the T1 relaxation time measured with non-selective inversion (control), and λ is the blood/tissue water partition coefficient, typically around 0.9 mL/g. CBF is expressed in unites of mL/100 g/min. However, CBF values in this study are presented as a percentage change from baseline.

For DCE-MRI, the protocol followed procedures outlined in Chapter 6. Briefly, a 3D T1-weighted FLASH sequence was used to dynamically capture the transport of Gd-DTPA. Prior to contrast infusion, three baseline scans were acquired. Subsequently, 50 µl of Gd-DTPA was intrathecally infused at a rate of 1.6 µl per minute over 31 minutes. MRI scanning continued for two hours post-infusion

initiation. Image processing was consistent with those detailed in Chapter 6. Percentage signal change ($\% \Delta S_{(i,j,k)}$) was calculated using the formula:

$$\% \Delta S_{(i,j,k)} = \left(\frac{post_{(i,j,k)} - base_{(i,j,k)}}{base_{(i,j,k)}} \right) * 100 \quad 9-2$$

Where (i, j, k) represents the voxel location. Mean percentage signal changes from baseline were extracted from ROIs delineated within the cerebral cortex, cerebellum, fourth ventricle, thalamus, and whole brain. These values were plotted over time to generate TACs for each region.

9.2.4 Immunohistochemistry

AQP4 immunofluorescence staining and analysis followed the protocol outlined in Chapter 8, with minor differences in the imaging protocol. Briefly, rats were perfused with heparinized saline followed by 4% paraformaldehyde. Brains were post-fixed overnight, dehydrated, and embedded in paraffin. After rehydration, antigen retrieval was performed using citrate buffer. Slices were then incubated overnight at 4°C with Rabbit Anti-Aquaporin 4 primary antibody, followed by incubation with Alexa Fluor Plus 488-conjugated secondary antibody for 1 hour at room temperature. Finally, slices were mounted using ProLong™ Diamond Antifade Mountant with DAPI and imaged at 40× magnification using a Zeiss LSM 710 Confocal Microscope with Zen software. Image analysis utilized QuPath 0.4.3 software. To ensure consistency, exposure intensity and levels were established and maintained throughout the investigation. AQP4 expression was quantified by measuring the area occupied by AQP4 relative to the total area of the region of interest.

9.2.5 Statistical analysis

Statistical analyses and graphs were generated using MATLAB software (MathWorks), in-house developed scripts, Excel 2016, and GraphPad Prism 10. Repeated measures one-way ANOVA followed by Tukey's post hoc test was used

for statistical comparisons between groups to evaluate the evolution of Gd-DTPA. A two-tailed paired Student's t-test was conducted to analyse the difference in CBF before and after surgery. One-way ANOVA followed by Tukey's post hoc test was used for comparisons of AQP4 expression. Data are presented as mean \pm SD unless otherwise stated, with $P < 0.05$ considered statistically significant.

9.3 Results

9.3.1 Cerebral blood flow reduction observed following BCAS in a pilot study

As a pilot study with single animals per group (Figure 9-2), CBF was assessed using ASL-MRI before and 24 hours after BCAS or sham surgery in three groups: sham-operated animal (n=1), BCAS-operated animal that received a vehicle (n=1), and BCAS-operated animal that received TGN-073 (n=1). In the sham-operated animal, a modest 9.06% decrease in CBF from baseline was observed, which is expected as cerebral perfusion remained largely unaffected. Conversely, the vehicle-treated animal post-BCAS exhibited a drastic 89.58% reduction in CBF, confirming the successful induction of cerebral hypoperfusion in this preliminary assessment. Notably, the animal receiving TGN-073 following BCAS showed a markedly less severe reduction in CBF, at 34.67% from baseline, suggesting a potentially mitigating effect of TGN-073 on the extent of cerebral hypoperfusion in this model. However, these findings are limited by the single animals per group and require further validation through studies with larger cohorts.

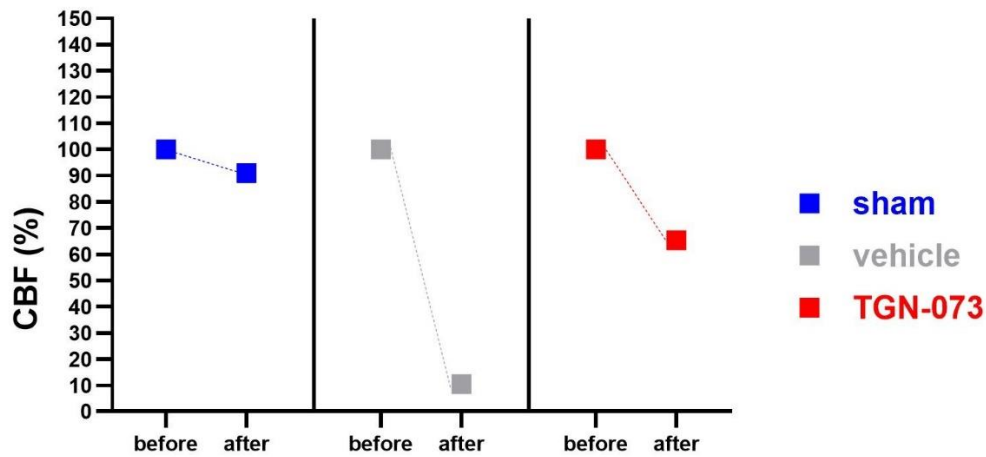


Figure 9-2: CBF measured using ASL-MRI before and 24 hours after BCAS or sham surgery. CBF values are presented as percentages, normalized to baseline (pre-surgery) measurements set at 100%. Blue squares represent sham-operated animals, grey squares represent BCAS-operated animals that received a vehicle, and red squares represent BCAS-operated animals that received TGN-073.

9.3.2 AQP4 facilitator enhanced the glymphatic function in BCAS rats

BCAS rats treated with the AQP4 facilitator TGN-073 exhibited higher uptake and greater parenchymal penetration of Gd-DTPA compared to those treated with a vehicle, suggesting enhanced glymphatic transport. This was demonstrated by the temporal evolution of 3D T1-weighted MRI of rat brains enhanced with the paramagnetic contrast agent Gd-DTPA, administered via intrathecal infusion, (Figure 9-3). TACs for various regions of interest in rat brains further support these findings. The percentage signal change is plotted over a period of two hours for BCAS rats treated with TGN-073, BCAS rats treated with a vehicle, and sham rats, (Figure 9-4). The TACs revealed significantly higher brain uptake of Gd-DTPA in all brain regions in BCAS rats treated with TGN-073 compared to those treated with a vehicle. The statistical significances are as follows: Cerebral Cortex ($P < 0.0001$), Cerebellum ($P < 0.0001$), Thalamus ($P < 0.0001$), Fourth Ventricle ($P < 0.0001$), and Whole Brain ($P = 0.0001$). The fastest arrival time of Gd-DTPA was observed in the cerebellum at 15 minutes from the start of the infusion, likely due to its proximity to the infusion site. In contrast, the slowest arrival time was noted in the thalamus at 36 minutes from the start of the infusion. After a two-hour scanning period following contrast infusion onset, both brain images and data curves clearly demonstrate minimal uptake of Gd-DTPA in the cerebral cortex and

thalamus of BCAS rats that received vehicle compared to those that received TGN-073 treatment ($13 \pm 4\%$ vs. $93 \pm 37\%$ and $6 \pm 2\%$ vs. $55 \pm 17\%$, respectively). These results indicate that TGN-073 improves glymphatic transport and could play a therapeutic role in conditions characterized by impaired CBF and glymphatic dysfunction, such as those induced by chronic cerebral hypoperfusion.

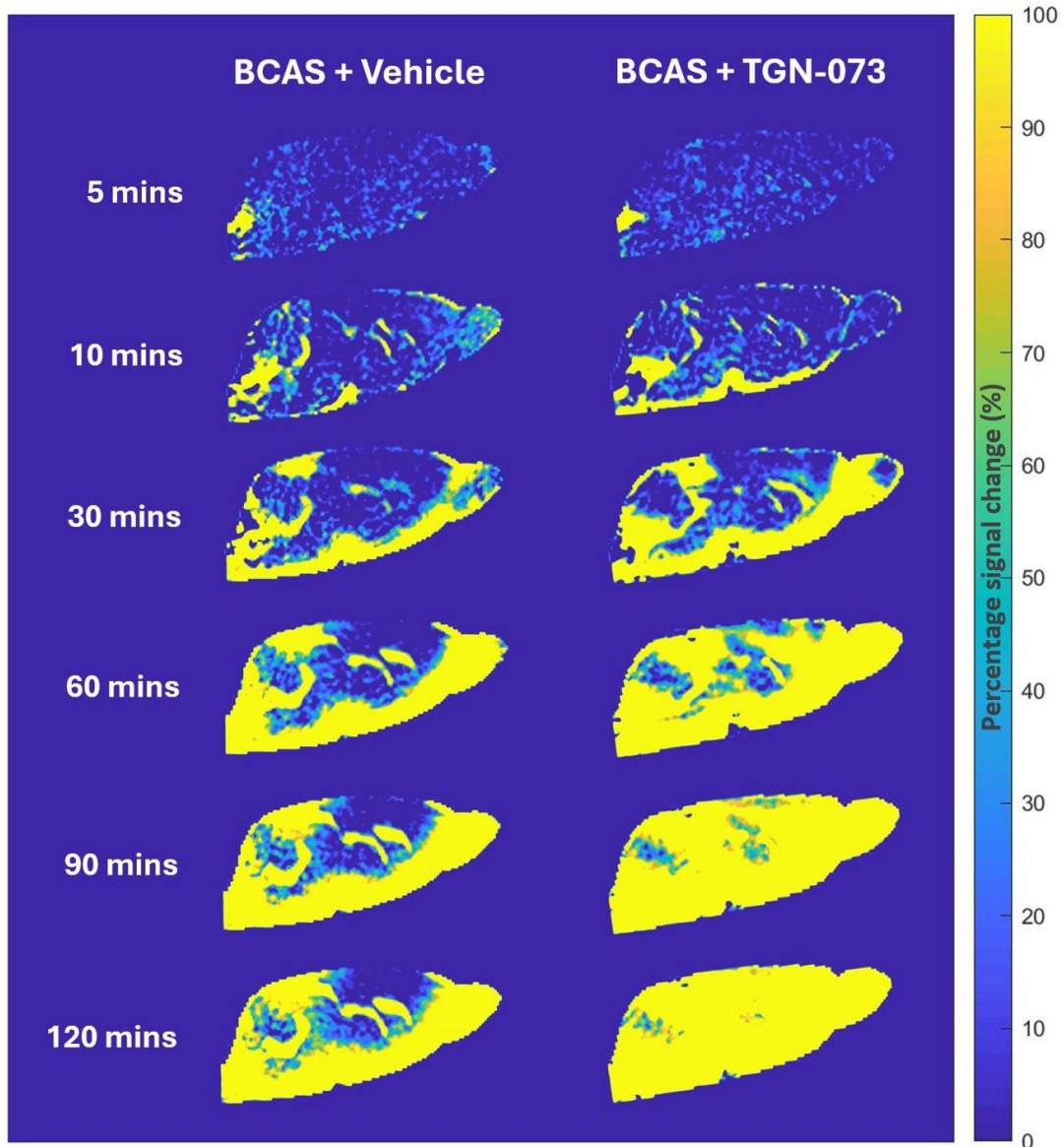


Figure 9-3: Serial T1-weighted MRI images in the sagittal plane of rat brains following the BCAS procedure reveal glymphatic transport using Gd-DTPA as the paramagnetic contrast agent. Over a period of two hours, BCAS-operated rats treated with the AQP4 facilitator TGN-073 exhibited higher uptake and greater parenchymal penetration of Gd-DTPA compared to those treated with a vehicle. The times (in minutes) represent changes from the start of the Gd-DTPA infusion.

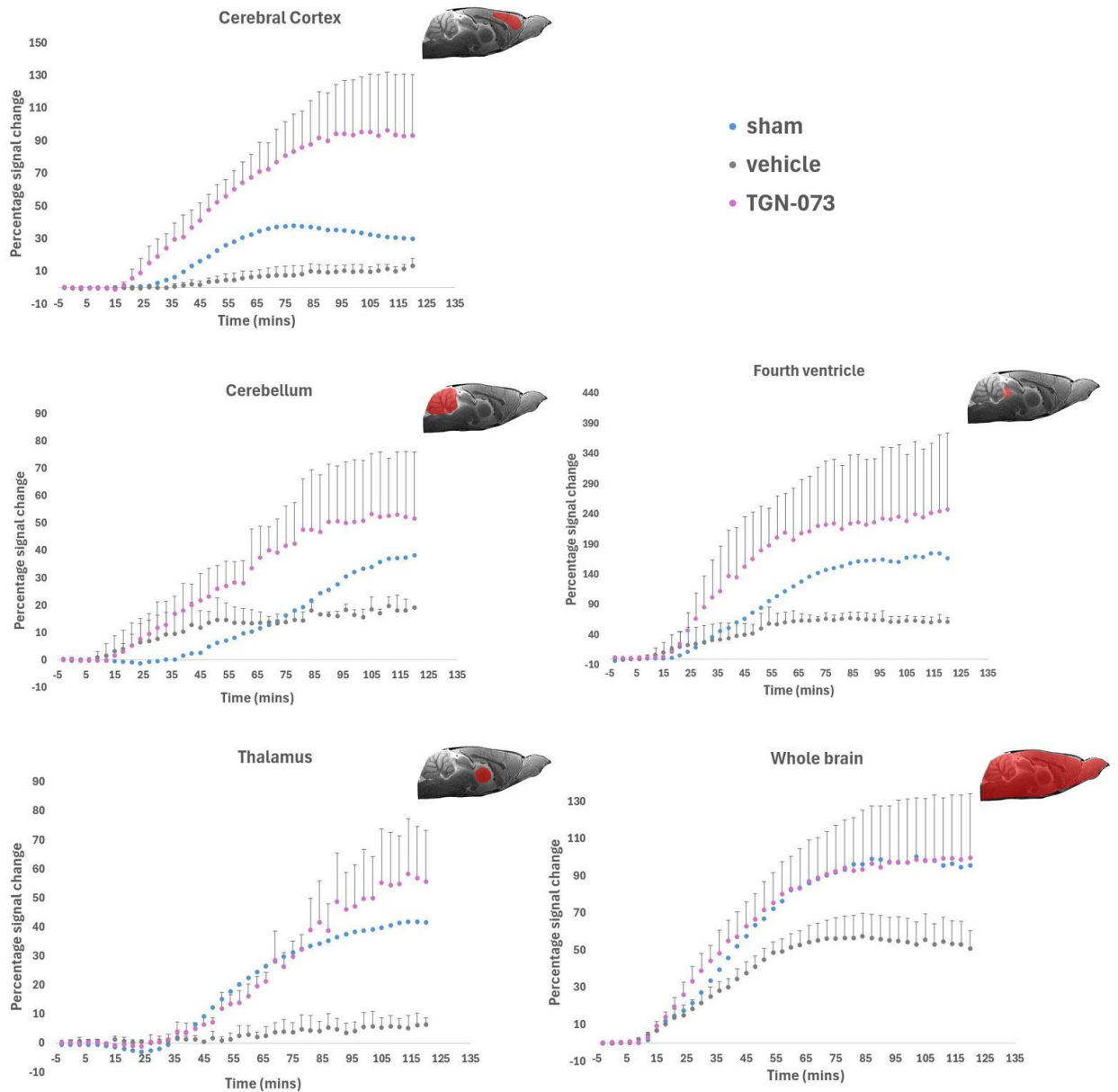


Figure 9-4: Time-activity curves (TAC) of several regions of interest (ROIs) in rat brains. The percentage signal change is plotted as a function of time for BCAS-operated rats treated with TGN-073 (n = 3, pink circles), BCAS-operated rats treated with vehicle (n = 3, grey circles), and sham-operated rats (n = 1, blue circles). Red shading on the brain images indicates the locations of the ROIs.

9.3.3 AQP4 expression rescued by TGN-073 after BCAS induction

AQP4 expression in rat brains was evaluated using immunofluorescence staining, as shown in Figure 9-5. BCAS significantly reduced AQP4 expression, whereas treatment with TGN-073 effectively restored and enhanced AQP4 expression. Quantification of AQP4 expression in various brain regions, depicted in Figure 9-6,

demonstrated that BCAS markedly decreased AQP4 levels. However, TGN-073 treatment preserved AQP4 expression, particularly in the hippocampus, where AQP4 expression was more than eight-fold higher (25.4% vs. 3.2%, $P < 0.0001$), followed by the cortex, where AQP4 expression was more than five-fold higher (46.7% vs. 8.3%, $P < 0.0001$) compared to BCAS rats that received the vehicle.

A significant reduction in AQP4 expression in the cortex was observed in the vehicle-treated BCAS group compared to the sham group ($P < 0.001$). BCAS also led to a significant decrease in AQP4 expression in the hippocampus of vehicle-treated BCAS rats compared to the sham group ($P < 0.01$). While the reduction in AQP4 expression in the thalamus of vehicle-treated BCAS rats did not reach statistical significance compared to the sham group, TGN-073 treatment significantly increased AQP4 expression compared to vehicle-treated BCAS rats ($P < 0.01$).

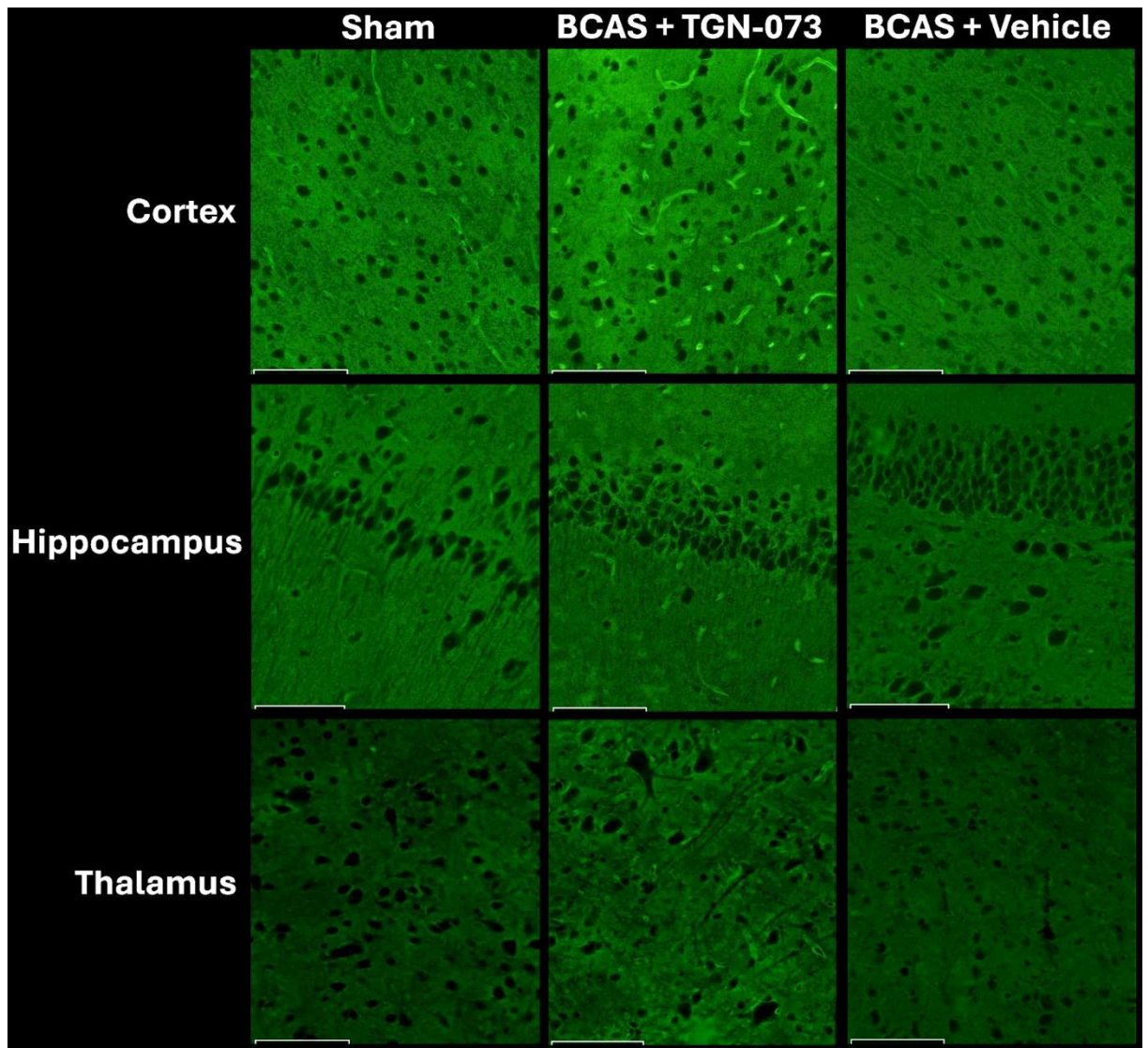


Figure 9-5: AQP4 immunofluorescence staining was performed on rat brain sections using Alexa Fluor 488 (green) to visualize AQP4 expression. Images were captured at 40x magnification using a confocal laser scanning microscope. Scale bars represent 100 μm . Representative images show the localization and distribution of AQP4 in the cerebral cortex, hippocampus, and thalamus, highlighting differences in expression among TGN-073 treated BCAS, vehicle BCAS, and sham groups.

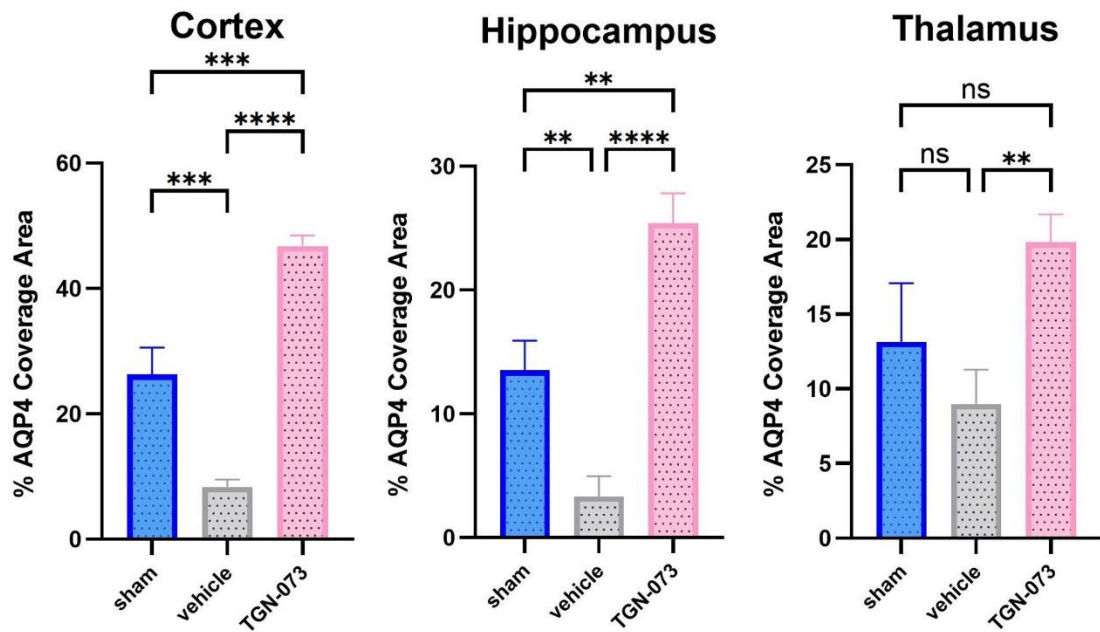


Figure 9-6: The bar charts represent the percentage of AQP4 coverage area in different brain regions. Blue bars indicate sham animals, grey bars indicate BCAS animals that received a vehicle, and pink bars indicate BCAS animals treated with TGN-073. Statistical significance is indicated as follows: ** $P < 0.01$, *** $P < 0.001$, and **** $P < 0.0001$.

9.4 Discussion

The brain's substantial metabolic demands require efficient cerebral circulation to ensure an adequate supply of oxygen and glucose. Cerebrovascular pathologies, such as cerebral hypoperfusion, disrupt this balance, leading to a mismatch between metabolic supply and demand, which can result in various brain injuries and diseases, including stroke, vascular dementia, and other neurodegenerative conditions (Lansdell & Dorrance, 2022). To our knowledge, this is the first study to evaluate glymphatic transport in BCAS rat models and to assess the impact of an AQP4 facilitator in this context. We successfully induced cerebral hypoperfusion via BCAS, as evidenced by the significant reduction in CBF. Furthermore, we demonstrated glymphatic dysfunction and altered AQP4 expression resulting from BCAS, and showed that the AQP4 facilitator could ameliorate these effects. This work highlights the potential of AQP4 facilitators to mitigate the adverse effects of cerebral hypoperfusion.

The potential connection between glymphatic dysfunction and cerebral hypoperfusion in humans has been investigated using diffusion tensor imaging (DTI) to assess glymphatic system activity in adults with moyamoya disease (Hara

et al., 2023). DTI measured diffusivity along the perivascular space (ALPS index), serving as a non-invasive proxy for glymphatic function. Moyamoya disease is a rare cerebrovascular condition characterized by the gradual narrowing of arteries and hemodynamic disruption. The findings indicated reduced perivascular space diffusivity in patients with moyamoya disease, suggesting potential glymphatic dysfunction. This impairment might be correlated with the extent of hemodynamic disturbances and cognitive dysfunction in these patients (Hara et al., 2023). Moreover, a recent study showed that BCAS significantly diminished the influx of CSF tracers into the brain parenchyma in mice (Li et al., 2022). In agreement with these findings, our data demonstrated that glymphatic function was significantly reduced in rat models following BCAS, as evidenced by MRI enhanced with intracisternal gadolinium infusion.

Studies have demonstrated that carotid stenosis diminishes cerebral perfusion, leading to increased A β accumulation, which ultimately contributes to the development of cerebral microinfarcts, cerebral amyloid angiopathy (CAA) and dementia (Okamoto et al., 2012; Salvadores et al., 2017). Following the BCAS procedure in mouse models, CBF measured by Laser Speckle Blood Flow Imaging (LSBFI) dropped to approximately 69% of the baseline within 10 minutes. After one month, CBF partially recovered to 84% of the baseline (Ihara et al., 2014). Similarly, Laser-Doppler Flowmetry (LDF) revealed a significant reduction in CBF of up to 70% two hours post-BCAS, with partial recovery noted at 24 hours, although CBF levels remained significantly lower than controls (Shibata et al., 2004). Both LSBFI and LDF are considered invasive due to the requirement of a cranial burr hole or partial skull removal. In contrast, ASL-MRI is a non-invasive technique that uses blood as an endogenous tracer. Post-BCAS, an ASL-MRI study has shown significant reductions in cortical and subcortical CBF in mice (Hattori et al., 2016). Additionally, CBF in the corpus callosum and thalamus dropped to 50-60% of baseline levels following BCAS (Kitamura et al., 2017). Here, ASL-MRI was employed in a pilot study to measure CBF before and 24 hours after BCAS surgery. Consistent with previous studies, BCAS resulted in a substantial drop in CBF. However, further replicates are required to confirm this finding.

CBF is presented as percent change from baseline (pre-surgical) values, normalized to 100%, to mitigate the impact of inherent inter-subject variability in

baseline CBF given the variability associated with ASL-MRI measurements and biological systems. This normalization allows for a more direct assessment of the relative changes in cerebral perfusion induced by the surgical interventions (BCAS or sham) and pharmacological treatment (TGN-073) within each animal. Furthermore, the use of percent change facilitates a clearer visualization and interpretation of the surgical and treatment effects on cerebral perfusion, independent of the initial physiological state of each animal.

The simplified CBF quantification model used in this study is limited as it does not account for the potential for arterial transit artefacts. As well as the transit time of labelled blood from the labelling region to the imaging slice. This assumes instantaneous arrival of labelled water, which is not typically accurate and can lead to underestimation of CBF, particularly in conditions with altered haemodynamics such as the chronic cerebral hypoperfusion induced by BCAS. The model also assumes a uniform and fixed blood-brain partition coefficient (λ) for water, which can vary across tissue types and physiological states. However, a value of approximately 0.9 g/mL is often used for grey matter, the region employed for our CBF calculation. Furthermore, it doesn't explicitly correct for T_1 relaxation of blood during the labelling and image acquisition process, potentially underestimating CBF, especially with longer delays. Despite these limitations, this model was employed as a foundational approach to provide a relative index of CBF changes within our pilot study, offering a straightforward method to assess the impact of BCAS and TGN-073 on cerebral perfusion within the constraints of our initial investigation and limited sample size.

A smaller number of animals was utilized in this study due to various challenges encountered during its execution. This study newly established within our university, which naturally encountered logistical challenges. Obtaining approval from biological services entailed an extensive wait of approximately six months, significantly delaying the commencement of research activities. The optimization and training required for surgical procedures consumed considerable time as well. Additionally, the project licenses underwent amendments, necessitating further approval before proceeding. These factors collectively restricted the ability to conduct a study with a larger cohort of animals, compelling us to proceed with a proof-of-concept approach. Furthermore, I took the initiative to train my fellow

students in performing immunohistology and AQP4 staining, aiming to pass on knowledge and ensure the continuity of the studies. Despite the limitations imposed by circumstances beyond our control, this study represents a crucial first step in laying the groundwork for future investigations in our research domain.

9.5 Conclusion

This study aimed to translate findings from healthy rat models to disease conditions, specifically testing the impact of the AQP4 facilitator TGN-073 in cerebral hypoperfusion induced by BCAS. Immunofluorescence staining of AQP4 revealed significant reductions in expression post-BCAS, which were effectively reversed by TGN-073 treatment. Although based on a single animal per group, the data suggest that the TGN-073 treated BCAS rat demonstrated improved CBF compared to the vehicle-treated BCAS rat. Moreover, enhanced Gd-DTPA uptake and deeper tissue penetration in TGN-073-treated BCAS rats compared to vehicle-treated BCAS rats underscored its potential in augmenting glymphatic transport. These findings suggest promising therapeutic implications for TGN-073 in mitigating cerebral hypoperfusion-associated impairments in glymphatic function. Moving forward, future research should explore the long-term effects and applications of TGN-073 in neuroprotective strategies.

Chapter 10 General discussion

10.1 Summary

The glymphatic system, suggested to rely heavily on AQP4 water channels, plays a pivotal role in removing brain metabolites and solutes. Harmful protein aggregation is a key feature that manifests in many neurodegenerative disorders, including but not limited to, AD, PD, and amyotrophic lateral sclerosis. This suggests that defects in glymphatic clearance might be associated with these pathologies (van Es et al., 2017; Sevigny et al., 2017; Peng et al., 2018). Therefore, pharmacological interventions that enhance water exchange through AQP4 might help prevent the accumulation of harmful solutes in the brain. Our aim was to develop and validate innovative preclinical MRI techniques to investigate the glymphatic system and evaluate the impact of novel drugs targeting AQP4, such as the AQP4 facilitator TGN-073. This novel drug has the potential to enhance glymphatic function and improve brain clearance.

Our findings from both invasive and non-invasive MRI imaging, as detailed in Chapters 6 and 8, demonstrated the beneficial impact of TGN-073 on enhancing glymphatic function. Additionally, we used immunofluorescence to stain AQP4 and observed a significant increase in AQP4 expression following TGN-073 administration. Moreover, we evaluated the effect of this AQP4 facilitator in a recently established rat model implemented in our department. This model involves inducing bilateral carotid artery stenosis, a surgical procedure that narrows the carotid arteries to induce cerebral hypoperfusion. This approach allows us to mimic certain aspects of human diseases, such as vascular dementia, providing valuable insights into disease mechanisms and potential therapeutic interventions.

We successfully generated and imaged BCAS rat models and modulated AQP4 expression in these models. TGN-073 effectively rescued AQP4 expression and enhanced glymphatic transport in these models. These findings highlight the potential of TGN-073 as a therapeutic agent for conditions associated with glymphatic dysfunction or altered AQP4 expression, such as AD, traumatic brain injury, and other neurodegenerative disorders. By improving glymphatic function,

TGN-073 could mitigate disease progression and enhance the quality of life for affected patients.

10.2 Limitation

Although this thesis has produced promising results underscoring the crucial role of AQP4 in glymphatic transport, it is essential to address several limitations identified during the course of this research. First, cisterna magna cannulation may negatively impact glymphatic flow, potentially introducing uncertainty. Studies suggest that puncturing the cisterna magna significantly inhibits perivascular CSF influx into brain tissue (Iliff et al., 2012; Mestre, Mori, et al., 2020). Thrane et al. demonstrated that this procedure inhibits the movement of perivascular lipids (Thrane et al., 2013). Furthermore, Lundgaard et al. reported impaired brain lactate clearance following suppression of the glymphatic system due to cisterna magna puncture (Lundgaard et al., 2017). To minimise these effects, we employed a custom-made cannula with a closed end and immediately secured in place with Vetbond glue to prevent CSF leakage and maintain stable intracranial pressure.

Second, the use of isoflurane for anaesthesia has been reported to negatively impact glymphatic flow. In contrast, ketamine/xylazine enhances the glymphatic system by increasing perivascular CSF influx (Hablitz et al., 2019). However, one major obstacle that prevented us from using ketamine/xylazine was its negative impact on cardiac and respiratory systems when used in high doses, especially considering the prolonged imaging sessions required for MRI (Giroux et al., 2015). Furthermore, Liu et al. demonstrated that, compared to wakefulness, anaesthesia-induced sleep increases CSF production rates. Notably, the effect of isoflurane on CSF production was 33% greater than that of ketamine/xylazine (G. Liu et al., 2020). Since CSF production is one of the suggested driving forces for glymphatic transport (Rasmussen et al., 2018; Smets et al., 2023), this finding suggests that isoflurane might still offer some advantages despite its overall negative impact on glymphatic flow.

Third, cisterna magna cannulation is a delicate procedure, and failing to correctly inject into the cisterna magna can introduce significant variability in the results (Xavier et al., 2018; Lee et al., 2015). To ensure accuracy, correct cannula

positioning in all animals was verified by observing the pulsation of CSF and confirming the cannula placement in T₂-weighted images, as illustrated in Chapter 3. Fourth, MRI imaging was restricted to two hours after starting the MRI contrast agent infusion due to potential adverse reactions and disruptions in normal physiological parameters that could arise from longer scan durations. Consequently, it was not feasible to observe the washout of the contrast agents from the brain parenchyma.

Fifth, the use of Gd-DTPA as an MRI contrast agent has faced criticism due to concerns about its deposition in the brain and the potential for de-chelation (Taoka & Naganawa, 2018; Kanda et al., 2014, 2015, 2016). In humans, administering GBCA intrathecally in large amounts can lead to severe side effects, including seizures, unconsciousness, and death (Kapoor et al., 2010; Besteher et al., 2020; Provenzano et al., 2019). However, small-dose intrathecal injections of GBCA have not induced harmful side effects, such as in cases of suspected CSF leakage (Eide & Ringstad, 2019b; Eide et al., 2018; Ringstad et al., 2018, 2017; Eide & Ringstad, 2019a; He et al., 2018; Edeklev et al., 2019). Moreover, a systematic review encompassing 53 studies indicated that the intrathecal administration of MRI contrast agents in small doses is associated with the lowest incidence of adverse events (Patel et al., 2020).

Sixth, our study exclusively utilized male rats, which limits our ability to assess potential gender differences in glymphatic functionality. Nonetheless, female rats may exhibit protective mechanisms mediated by oestrogen following neurological insults, which could confound our findings. Additionally, fluctuations in oestrogen levels throughout the menstrual cycle might introduce variability, influencing the accuracy and interpretation of our results (Ding et al., 2014).

Seventh, regarding immunohistology, it is crucial to recognize that fixation and dehydration can alter tissue samples, leading to discrepancies between their in vivo and fixed states. For example, Mestre et al. demonstrated that perivascular spaces collapse significantly when transcardially perfused with 4% paraformaldehyde. In live mice, cross-sectional imaging showed that the perivascular space is approximately 1.4 times larger than the surrounding artery, but this proportion reduces to 0.14 after fixation (Mestre, Tithof, et al., 2018).

However, our primary goal for brain fixation is to quantify AQP4 expression rather than to measure perivascular spaces.

Finally, no behavioural tests were conducted in our BCAS model. However, our study focused on the acute effects, and previous studies indicated that short-term BCAS induction in mice may not lead to significant declines in memory and cognition (Miyanojara et al., 2018; Coltman et al., 2011; Ahn et al., 2016). For example, Miyamoto et al. demonstrated that young mice subjected to a two-week period of reduced CBF did not exhibit impairments in spatial working memory, as assessed by Y-maze tests (Miyamoto et al., 2013).

10.3 Future work

In future research, exploring the effect of AQP4 facilitators like TGN-073 in AD models with disrupted AQP4 function holds significant promise. Rodent models offer the advantage of accelerated life cycles, allow comprehensive investigations across multiple stages of life within a condensed timeframe. For instance, AD rodent models simulate up to two decades of human ageing in only 1 to 2 years, encompassing all the stages of AD, from prodromal, mild cognitive impairment to advanced AD stages (Dickie et al., 2021). Recent findings indicate that AD mouse models exhibiting depolarised AQP4, due to the absence of *Snta1*, experience increased AB accumulation in the brain and cerebral vessels (Pedersen et al., 2023). Evaluating TGN-073 in these models could elucidate its potential to enhance AB clearance, offering new therapeutic strategies. Furthermore, in conditions such as cerebral microinfarcts where transient AQP4 depolarisation returns to normal a month after the insult, TGN-073 might preserve AQP4 function and accelerate recovery processes (Wang et al., 2012).

Future studies should investigate the impact of TGN-073 on cerebral stroke. Interestingly, TGN-073 has shown an analgesic effect, potentially due to its role in maintaining AQP4 integrity following neurological insults, suggesting a beneficial impact post-stroke (Huber, Kwee, et al., 2018). After haemorrhagic stroke, AQP4 expression in periarterial spaces is significantly higher than in perivenous spaces. Additionally, periarterial AQP4 expression is elevated following haemorrhagic stroke compared to the sham group, possibly contributing to

oedema formation (E. Liu et al., 2021). TGN-073 may increase AQP4 expression in the perivenous spaces to compensate for the elevation of AQP4 in the periarterial spaces, thereby preventing oedema formation by facilitating the clearance of excess fluid and preventing its accumulation in the interstitial space.

Previous research using mouse models demonstrated that carotid artery ligation resulted in a 50% reduction in arterial pulsatility and inhibition of perivascular CSF-ISF exchange. Conversely, the administration of dobutamine, an inotropic adrenergic agonist, led to a 60% increase in arterial pulsatility associated with enhanced glymphatic function (Iloff, Wang, et al., 2013). Therefore, it is worthwhile to use dobutamine in BCAS rat models to assess its effects on glymphatic clearance, AQP4 expression, and CBF. This approach could improve outcomes in conditions involving cerebral hypoperfusion.

Healthy lifestyle and non-invasive interventions may preserve glymphatic function and AQP4 expression in BCAS rats. Physical exercise and good sleep patterns are particularly beneficial for maintaining a healthy glymphatic system, especially in ageing brains (Shokri-Kojori et al., 2018; Eide et al., 2021; Abbott et al., 2018; He et al., 2017). Exercise has also been shown to ameliorate AD (Y. Liu et al., 2020; Liu et al., 2022). A recent study explored the protective impact of scalp mechanical stimulation (SMS) against cerebral oedema in rats with cerebral hypoperfusion (Tan et al., 2023). SMS significantly enhanced CBF and decreased brain water content in two-vessel carotid artery occlusion rats. This treatment also reduced cell apoptosis and the expression of proteins related to cerebral oedema, such as GFAP compared to untreated group. This technique holds promise as a simple approach to preventing ischemic stroke and cognitive impairment.

Environmental enrichment strategies have demonstrated positive effects on cerebral hypoperfusion in mouse models by reducing white matter pathologies and improving working memory (Hase et al., 2018). Additionally, intermittent fasting has been shown to enhance spatial working memory in cerebral hypoperfusion models compared to ad libitum feeding (Andika et al., 2021). We recommend further investigation into the combined effects of one or more of these non-invasive interventions augmented with TGN-073 in BCAS rat models. Future research should assess whether these interventions can mitigate cognitive

impairments and pathological changes associated with cerebral hypoperfusion. Such studies could provide valuable insights into potential therapeutic strategies for conditions involving glymphatic dysfunction and altered AQP4 expression.

References

- Abbott, N.J. (2004) 'Evidence for bulk flow of brain interstitial fluid: significance for physiology and pathology', *Neurochemistry international*, 45(4), pp. 545-552.
- Abbott, N.J., Pizzo, M.E., Preston, J.E., Janigro, D. & Thorne, R.G. (2018) 'The role of brain barriers in fluid movement in the CNS: is there a 'glymphatic' system?', *Acta neuropathologica*, 135pp. 387-407.
- Abir-Awan, M., Kitchen, P., Salman, M.M., Conner, M.T., Conner, A.C. & Bill, R.M. (2019) 'Inhibitors of mammalian aquaporin water channels', *International journal of molecular sciences*, 20(7), p. 1589.
- Absinta, M., Ha, S.-K., Nair, G., Sati, P., Luciano, N.J., Palisoc, M., Louveau, A., Zaghoul, K.A., Pittaluga, S. & Kipnis, J. (2017) 'Human and nonhuman primate meninges harbor lymphatic vessels that can be visualized noninvasively by MRI', *elife*, 6p. e29738.
- Achariyar, T.M., Li, B., Peng, W., Verghese, P.B., Shi, Y., McConnell, E., Benraiss, A., Kasper, T., Song, W. & Takano, T. (2016) 'Glymphatic distribution of CSF-derived apoE into brain is isoform specific and suppressed during sleep deprivation', *Molecular neurodegeneration*, 11(1), pp. 1-20.
- Agre, P. (2006) 'The aquaporin water channels', *Proceedings of the American Thoracic Society*, 3(1), pp. 5-13.
- Agre, P., King, L.S., Yasui, M., Guggino, W.B., Ottersen, O.P., Fujiyoshi, Y., Engel, A. & Nielsen, S. (2002) 'Aquaporin water channels-from atomic structure to clinical medicine', *The Journal of physiology*, 542(1), pp. 3-16.
- Ahn, S.M., Kim, Y.R., Kim, H.N., Shin, Y.-I., Shin, H.K. & Choi, B.T. (2016) 'Electroacupuncture ameliorates memory impairments by enhancing oligodendrocyte regeneration in a mouse model of prolonged cerebral hypoperfusion', *Scientific Reports*, 6(1), p. 28646.
- Albargothy, N.J., Johnston, D.A., MacGregor-Sharp, M., Weller, R.O., Verma, A., Hawkes, C.A. & Carare, R.O. (2018) 'Convective influx/glymphatic system: tracers injected into the CSF enter and leave the brain along separate periarterial basement membrane pathways', *Acta neuropathologica*, 136pp. 139-152.
- Alghanimy, A., Martin, C., Gallagher, L. & Holmes, W.M. (2023) 'The effect of a novel AQP4 facilitator, TGN-073, on glymphatic transport captured by diffusion MRI and DCE-MRI', *PLOS ONE*, 18(3), pp. e0282955-.
- Alghanimy, A., Work, L.M. & Holmes, W.M. (2024) 'The Glymphatic System and Multiple Sclerosis: An Evolving Connection', *Multiple Sclerosis and Related Disorders*, p. 105456.
- Alperin, N., Bagci, A.M., Lee, S.H. & Lam, B.L. (2016) 'Automated quantitation of spinal CSF volume and measurement of craniospinal CSF redistribution following lumbar withdrawal in idiopathic intracranial hypertension', *American Journal of Neuroradiology*, 37(10), pp. 1957-1963.
- Alshuhri, M.S., Gallagher, L., McCabe, C. & Holmes, W.M. (2020) 'Change in CSF dynamics responsible for ICP elevation after ischemic stroke in rats: a new mechanism for unexplained END?', *Translational Stroke Research*, 11pp. 310-318.
- Alshuhri, M.S., Gallagher, L., Work, L.M. & Holmes, W.M. (2021) 'Direct imaging of glymphatic transport using H₂¹⁷O MRI', *JCI insight*,

- Amiry-Moghaddam, M., Frydenlund, D.S. & Ottersen, O.P. (2004) 'Anchoring of aquaporin-4 in brain: molecular mechanisms and implications for the physiology and pathophysiology of water transport', *Neuroscience*, 129(4), pp. 997-1008.
- Andel, R., Crowe, M., Pedersen, N.L., Fratiglioni, L., Johansson, B. & Gatz, M. (2008) 'Physical exercise at midlife and risk of dementia three decades later: a population-based study of Swedish twins', *The Journals of Gerontology Series A: Biological Sciences and Medical Sciences*, 63(1), pp. 62-66.
- Andica, C., Kamagata, K., Takabayashi, K., Kikuta, J., Kaga, H., Someya, Y., Tamura, Y., Kawamori, R., Watada, H. & Taoka, T. (2023) 'Neuroimaging findings related to glymphatic system alterations in older adults with metabolic syndrome', *Neurobiology of Disease*, 177p. 105990.
- Andika, F.R., Yoon, J.-H., Kim, G.S. & Jeong, Y. (2021) 'Intermittent fasting alleviates cognitive impairments and hippocampal neuronal loss but enhances astrogliosis in mice with subcortical vascular dementia', *The Journal of Nutrition*, 151(3), pp. 722-730.
- Arras, M., Autenried, P., Rettich, A., Spaeni, D. & Rüllicke, T. (2001) 'Optimization of intraperitoneal injection anesthesia in mice: drugs, dosages, adverse effects, and anesthesia depth', *Comparative medicine*, 51(5), pp. 443-456.
- Asgari, M., De Zélicourt, D. & Kurtcuoglu, V. (2016) 'Glymphatic solute transport does not require bulk flow', *Scientific reports*, 6(1), p. 38635.
- Asgari, M., De Zélicourt, D. & Kurtcuoglu, V. (2015) 'How astrocyte networks may contribute to cerebral metabolite clearance', *Scientific reports*, 5(1), p. 15024.
- Aspelund, A., Antila, S., Proulx, S.T., Karlsen, T.V., Karaman, S., Detmar, M., Wiig, H. & Alitalo, K. (2015) 'A dural lymphatic vascular system that drains brain interstitial fluid and macromolecules.', *The Journal of experimental medicine*, 212(7), pp. 991-999.
- Association, A. (2018) '2018 Alzheimer's disease facts and figures', *Alzheimer's & Dementia*, 14(3), pp. 367-429.
- Avram, A. (2011) *Diffusion Tensor Imaging of Myelin Water*. [Online].
- Badaut, Jerome, Ashwal, S., Adami, A., Tone, B., Recker, R., Spagnoli, D., Ternon, B. & Obenaus, A. (2011) 'Brain water mobility decreases after astrocytic aquaporin-4 inhibition using RNA interference.', *Journal of cerebral blood flow and metabolism : official journal of the International Society of Cerebral Blood Flow and Metabolism*, 31(3), pp. 819-831.
- Badaut, J, Ashwal, S. & Obenaus, A. (2011) 'Aquaporins in cerebrovascular disease: a target for treatment of brain edema', *Cerebrovascular Diseases*, 31(6), pp. 521-531.
- Badaut, J., Ashwal, S., Tone, B., Regli, L., Tian, H.R. & Obenaus, A. (2007) 'Temporal and regional evolution of aquaporin-4 expression and magnetic resonance imaging in a rat pup model of neonatal stroke', *Pediatric Research*, 62(3), pp. 248-254.
- Badaut, J., Fukuda, A.M., Jullienne, A. & Petry, K.G. (2014) 'Aquaporin and brain diseases', *Biochimica et Biophysica Acta (BBA)-General Subjects*, 1840(5), pp. 1554-1565.
- Bae, Y.J., Choi, B.S., Kim, J.-M., Choi, J.-H., Cho, S.J. & Kim, J.H. (2021) 'Altered glymphatic system in idiopathic normal pressure hydrocephalus', *Parkinsonism & Related Disorders*, 82pp. 56-60.
- Bakker, E.N.T.P., Bacskai, B.J., Arbel-Ornath, M., Aldea, R., Bedussi, B., Morris, A.W.J., Weller, R.O. & Carare, R.O. (2016) 'Lymphatic clearance of the

- brain: perivascular, paravascular and significance for neurodegenerative diseases', *Cellular and molecular neurobiology*, 36pp. 181-194.
- Balbi, M., Ghosh, M., Longden, T.A., Vega, M.J., Gesierich, B., Hellal, F., Lourbopoulos, A., Nelson, M.T. & Plesnila, N. (2015) 'Dysfunction of Mouse Cerebral Arteries during Early Aging', *Journal of Cerebral Blood Flow & Metabolism*, 35(9), pp. 1445-1453.
- Barberger-Gateau, P., Raffaitin, C., Letenneur, L., Berr, C., Tzourio, C., Dartigues, J.-F. & Alpérovitch, A. (2007) 'Dietary patterns and risk of dementia: the Three-City cohort study', *Neurology*, 69(20), pp. 1921-1930.
- Battal, B., Kocaoglu, M., Bulakbasi, N., Husmen, G., Tuba Sanal, H. & Tayfun, C. (2011) 'Cerebrospinal fluid flow imaging by using phase-contrast MR technique', *The British journal of radiology*, 84(1004), pp. 758-765.
- Bedussi, B., Almasian, M., de Vos, J., VanBavel, E. & Bakker, E.N.T.P. (2018) 'Paravascular spaces at the brain surface: Low resistance pathways for cerebrospinal fluid flow', *Journal of Cerebral Blood Flow & Metabolism*, 38(4), pp. 719-726.
- Bedussi, B., van Lier, M.G.J.T.B., Bartstra, J.W., de Vos, J., Siebes, M., VanBavel, E. & Bakker, E.N.T.P. (2015) 'Clearance from the mouse brain by convection of interstitial fluid towards the ventricular system.', *Fluids and barriers of the CNS*, 12p. 23.
- Bedussi, B., van der Wel, N.N., de Vos, J., van Veen, H., Siebes, M., VanBavel, E. & Bakker, E.N.T.P. (2017) 'Paravascular channels, cisterns, and the subarachnoid space in the rat brain: a single compartment with preferential pathways', *Journal of Cerebral Blood Flow & Metabolism*, 37(4), pp. 1374-1385.
- Beitz, E., Pavlovic-Djuranovic, S., Yasui, M., Agre, P. & Schultz, J.E. (2004) 'Molecular dissection of water and glycerol permeability of the aquaglyceroporin from *Plasmodium falciparum* by mutational analysis', *Proceedings of the National Academy of Sciences of the United States of America*, 101(5), pp. 1153 LP - 1158.
- Benveniste, H., Lee, H., Ding, F., Sun, Q., Al-Bizri, E., Makaryus, R., Probst, S., Nedergaard, M., Stein, E.A. & Lu, H. (2017) 'Anesthesia with dexmedetomidine and low-dose isoflurane increases solute transport via the glymphatic pathway in rat brain when compared with high-dose isoflurane', *Anesthesiology*, 127(6), pp. 976-988.
- Benveniste, H., Liu, X., Koundal, S., Sanggaard, S., Lee, H. & Wardlaw, J. (2019) 'The Glymphatic System and Waste Clearance with Brain Aging: A Review', *Gerontology*, 65(2), pp. 106-119.
- Berezuk, C., Ramirez, J., Gao, F., Scott, C.J.M., Huroy, M., Swartz, R.H., Murray, B.J., Black, S.E. & Boulous, M.I. (2015) 'Virchow-Robin spaces: correlations with polysomnography-derived sleep parameters', *Sleep*, 38(6), pp. 853-858.
- Besteher, B., Chung, H.-Y., Mayer, T.E., Witte, O.W., Kirchhof, K. & Schwab, M. (2020) 'Acute encephalopathy and cardiac arrest induced by intrathecal gadolinium administration', *Clinical Neuroradiology*, 30pp. 629-631.
- Bianchi, V.E., Herrera, P.F. & Laura, R. (2021) 'Effect of nutrition on neurodegenerative diseases. A systematic review', *Nutritional neuroscience*, 24(10), pp. 810-834.
- Bishop, D.P., Cole, N., Zhang, T., Doble, P.A. & Hare, D.J. (2018) 'A guide to integrating immunohistochemistry and chemical imaging', *Chemical Society Reviews*, 47(11), pp. 3770-3787.
- Bloch, O., Papadopoulos, M.C., Manley, G.T. & Verkman, A.S. (2005) 'Aquaporin-4 gene deletion in mice increases focal edema associated with

- staphylococcal brain abscess', *Journal of neurochemistry*, 95(1), pp. 254-262.
- Bordoni, L., Thoren, A.E., Gutiérrez-Jiménez, E., Åbjørsbråten, K.S., Bjørnstad, D.M., Tang, W., Stern, M., Østergaard, L., Nagelhus, E.A. & Frische, S. (2023) 'Deletion of aquaporin-4 improves capillary blood flow distribution in brain edema', *Glia*, 71(11), pp. 2559-2572.
- Bossy, B., Perkins, G. & Bossy-Wetzel, E. (2008) 'Clearing the brain's cobwebs: the role of autophagy in neuroprotection', *Current neuropharmacology*, 6(2), pp. 97-101.
- Bradbury, M.W.B. & Cserr, H.F. (1985) 'Drainage of cerebral interstitial fluid and of cerebrospinal fluid into lymphatics', *Experimental biology of the lymphatic circulation*, 9pp. 355-394.
- Branger, P., Arenaza-Urquijo, E.M., Tomadesso, C., Mézenge, F., André, C., de Flores, R., Mutlu, J., de La Sayette, V., Eustache, F. & Chételat, G. (2016) 'Relationships between sleep quality and brain volume, metabolism, and amyloid deposition in late adulthood', *Neurobiology of aging*, 41pp. 107-114.
- Brightman, M.W. (2002) 'The brain's interstitial clefts and their glial walls', *Journal of neurocytology*, 31pp. 595-603.
- Brissaud, O., Villega, F., Pieter Konsman, J., Sanchez, S., Raffard, G., Franconi, J.-M., Chateil, J.-F. & Bouzier-Sore, A.-K. (2010) 'Short-term effect of erythropoietin on brain lesions and aquaporin-4 expression in a hypoxic-ischemic neonatal rat model assessed by magnetic resonance diffusion weighted imaging and immunohistochemistry', *Pediatric Research*, 68(2), pp. 123-127.
- Brown, R., Benveniste, H., Black, S.E., Charpak, S., Dichgans, M., Joutel, A., Nedergaard, M., Smith, K.J., Zlokovic, B. V & Wardlaw, J.M. (2018) 'Understanding the role of the perivascular space in cerebral small vessel disease', *Cardiovascular research*, 114(11), pp. 1462-1473.
- Del Brutto, O.H., Mera, R.M., Del Brutto, V.J. & Castillo, P.R. (2019) 'Enlarged basal ganglia perivascular spaces and sleep parameters. A population-based study', *Clinical neurology and neurosurgery*, 182pp. 53-57.
- Butler, A.B., Dacey, R.G., Maffeo, C.J., Mann, J.D., Johnson, R.N. & Bass, N.H. (1983) 'Mechanisms of cerebrospinal fluid absorption in normal and pathologically altered arachnoid villi', *Neurobiology of Cerebrospinal Fluid* 2, pp. 707-726.
- Cacciaguerra, L., Carotenuto, A., Pagani, E., Mistri, D., Radaelli, M., Martinelli, V., Filippi, M. & Rocca, M.A. (2022) 'Magnetic resonance imaging evaluation of perivascular space abnormalities in neuromyelitis optica', *Annals of Neurology*, 92(2), pp. 173-183.
- Cahalan, M.D. & Parker, I. (2005) 'Close encounters of the first and second kind: T-DC and T-B interactions in the lymph node', in *Seminars in immunology*. [Online]. 2005 Elsevier. pp. 442-451.
- Cai, X., Chen, Z., He, C., Zhang, P., Nie, K., Qiu, Y., Wang, Limin, Wang, Lijuan, Jing, P. & Zhang, Y. (2023) 'Diffusion along perivascular spaces provides evidence interlinking compromised glymphatic function with aging in Parkinson's disease', *CNS Neuroscience & Therapeutics*, 29(1), pp. 111-121.
- Cai, X., Qiao, J., Kulkarni, P., Harding, I.C., Ebong, E. & Ferris, C.F. (2020) 'Imaging the effect of the circadian light-dark cycle on the glymphatic system in awake rats', *Proceedings of the National Academy of Sciences*, 117(1), pp. 668-676.
- Callaghan, P.T. (1993) *Principles of nuclear magnetic resonance microscopy*. Clarendon press.

- Calon, F. & Cole, G. (2007) 'Neuroprotective action of omega-3 polyunsaturated fatty acids against neurodegenerative diseases: evidence from animal studies', *Prostaglandins, Leukotrienes and Essential Fatty Acids*, 77(5-6), pp. 287-293.
- Cao, J., Yao, D., Li, R., Guo, X., Hao, J., Xie, M., Li, J., Pan, D., Luo, X. & Yu, Z. (2022) 'Digoxin ameliorates glymphatic transport and cognitive impairment in a mouse model of chronic cerebral hypoperfusion', *Neuroscience Bulletin*, pp. 1-19.
- Carare, R.O., Bernardes-Silva, M., Newman, T.A., Page, A.M., Nicoll, J.A.R., Perry, V.H. & Weller, R.O. (2008) 'Solutes, but not cells, drain from the brain parenchyma along basement membranes of capillaries and arteries: significance for cerebral amyloid angiopathy and neuroimmunology', *Neuropathology and applied neurobiology*, 34(2), pp. 131-144.
- Carnevale, D., Perrotta, M., Lembo, G. & Trimarco, B. (2016) 'Pathophysiological links among hypertension and Alzheimer's disease', *High Blood Pressure & Cardiovascular Prevention*, 23pp. 3-7.
- Carotenuto, A., Cacciaguerra, L., Pagani, E., Preziosa, P., Filippi, M. & Rocca, M.A. (2022) 'Glymphatic system impairment in multiple sclerosis: relation with brain damage and disability', *Brain*, 145(8), pp. 2785-2795.
- Cercignani, M., Dowell, N.G. & Tofts, P.S. (2018) *Quantitative MRI of the brain: principles of physical measurement*.
- Chazen, J.L., Dyke, J.P., Holt, R.W., Horky, L., Pauplis, R.A., Hesterman, J.Y., Mozley, D.P. & Verma, A. (2017) 'Automated segmentation of MR imaging to determine normative central nervous system cerebrospinal fluid volumes in healthy volunteers', *Clinical imaging*, 43pp. 132-135.
- Chiu, C., Miller, M.C., Caralopoulos, I.N., Worden, M.S., Brinker, T., Gordon, Z.N., Johanson, C.E. & Silverberg, G.D. (2012) 'Temporal course of cerebrospinal fluid dynamics and amyloid accumulation in the aging rat brain from three to thirty months', *Fluids and Barriers of the CNS*, 9(1), pp. 1-8.
- Chiu, C.-D., Chen, C.-C. V, Shen, C.-C., Chin, L.-T., Ma, H.-I., Chuang, H.-Y., Cho, D.-Y., Chu, C.-H. & Chang, C. (2013) 'Hyperglycemia exacerbates intracerebral hemorrhage via the downregulation of aquaporin-4: temporal assessment with magnetic resonance imaging', *Stroke*, 44(6), pp. 1682-1689.
- Chou, C.L., Ma, T., Yang, B., Knepper, M.A. & Verkman, A.S. (1998) 'Fourfold reduction of water permeability in inner medullary collecting duct of aquaporin-4 knockout mice', *American Journal of Physiology-Cell Physiology*, 274(2), pp. C549-C554.
- Chou, M.C., Tsai, P.H., Huang, G.S., Lee, H.S., Lee, C.H., Lin, M.H., Lin, C.Y. & Chung, H.W. (2009) 'Correlation between the MR T2 value at 4.7 T and relative water content in articular cartilage in experimental osteoarthritis induced by ACL transection', *Osteoarthritis and Cartilage*, 17(4), pp. 441-447.
- Chung, S.J., Yoo, H.S., Shin, N.-Y., Park, Y.W., Lee, H.S., Hong, J.-M., Kim, Y.J., Lee, S.-K., Lee, P.H. & Sohn, Y.H. (2021) 'Perivascular spaces in the basal ganglia and long-term motor prognosis in newly diagnosed Parkinson disease', *Neurology*, 96(16), pp. e2121-e2131.
- Coltman, R., Spain, A., Tsenkina, Y., Fowler, J.H., Smith, J., Scullion, G., Allerhand, M., Scott, F., Kalaria, R.N. & Ihara, M. (2011) 'Selective white matter pathology induces a specific impairment in spatial working memory', *Neurobiology of aging*, 32(12), pp. 2324-e7.

- Coons, A.H., Creech, H.J. & Jones, R.N. (1941) 'Immunological properties of an antibody containing a fluorescent group.', *Proceedings of the society for experimental biology and medicine*, 47(2), pp. 200-202.
- Croci, M., Vinje, V. & Rognes, M.E. (2019) 'Uncertainty quantification of parenchymal tracer distribution using random diffusion and convective velocity fields', *Fluids and Barriers of the CNS*, 16pp. 1-21.
- Cserr, H.F., Cooper, D.N. & Milhorat, T.H. (1977) 'Flow of cerebral interstitial fluid as indicated by the removal of extracellular markers from rat caudate nucleus', *Experimental Eye Research*, 25pp. 461-473.
- Cserr, H.F., Cooper, D.N., Suri, P.K. & Patlak, C.S. (1981) 'Efflux of radiolabeled polyethylene glycols and albumin from rat brain', *American Journal of Physiology-Renal Physiology*, 240(4), pp. F319-F328.
- Cserr, H.F., Harling-Berg, C.J. & Knopf, P.M. (1992) 'Drainage of brain extracellular fluid into blood and deep cervical lymph and its immunological significance', *Brain pathology*, 2(4), pp. 269-276.
- Cserr, H.F. & Ostrach, L.H. (1974) 'Bulk flow of interstitial fluid after intracranial injection of Blue Dextran 2000', *Experimental Neurology*, 45(1), pp. 50-60.
- Cui, H., Wang, W., Zheng, X., Xia, D., Liu, H., Qin, C., Tian, H. & Teng, J. (2021) 'Decreased AQP4 expression aggravates α -synuclein pathology in Parkinson's disease mice, possibly via impaired glymphatic clearance', *Journal of Molecular Neuroscience*, pp. 1-14.
- Cui, Y. & Bastien, D.A. (2011) 'Water transport in human aquaporin-4: molecular dynamics (MD) simulations', *Biochemical and biophysical research communications*, 412(4), pp. 654-659.
- Damkier, H.H., Brown, P.D. & Praetorius, J. (2013) 'Cerebrospinal fluid secretion by the choroid plexus', *Physiological reviews*, 93(4), pp. 1847-1892.
- Davson, H. & Segal, M.B. (1996) 'Physiology of the CSF and blood-brain barriers', (No Title),
- Deane, R., Bell, R.D., Sagare, A. & Zlokovic, B. V (2009) 'Clearance of amyloid- β peptide across the blood-brain barrier: implication for therapies in Alzheimer's disease', *CNS & Neurological Disorders-Drug Targets (Formerly Current Drug Targets-CNS & Neurological Disorders)*, 8(1), pp. 16-30.
- Debaker, C., Djemai, B., Ciobanu, L., Tsurugizawa, T. & Le Bihan, D. (2020) 'Diffusion MRI reveals in vivo and non-invasively changes in astrocyte function induced by an aquaporin-4 inhibitor', *PloS one*, 15(5), p. e0229702.
- Demiral, Ş.B., Tomasi, D., Sarlls, J., Lee, H., Wiers, C.E., Zehra, A., Srivastava, T., Ke, K., Shokri-Kojori, E. & Freeman, C.R. (2019) 'Apparent diffusion coefficient changes in human brain during sleep-Does it inform on the existence of a glymphatic system?', *Neuroimage*, 185pp. 263-273.
- Detre, J.A., Leigh, J.S., Williams, D.S. & Koretsky, A.P. (1992) 'Perfusion imaging', *Magnetic resonance in medicine*, 23(1), pp. 37-45.
- Dichgans, M. & Leys, D. (2017) 'Vascular cognitive impairment', *Circulation research*, 120(3), pp. 573-591.
- Dickie, B.R., Boutin, H., Parker, G.J.M. & Parkes, L.M. (2021) 'Alzheimer's disease pathology is associated with earlier alterations to blood-brain barrier water permeability compared with healthy ageing in TgF344-AD rats', *NMR in Biomedicine*, 34(7), p. e4510.
- Ding, D., Starke, R.M., Dumont, A.S., Owens, G.K., Hasan, D.M., Chalouhi, N., Medel, R. & Lin, C.-L. (2014) 'Therapeutic Implications of Estrogen for Cerebral Vasospasm and Delayed Cerebral Ischemia Induced by Aneurysmal Subarachnoid Hemorrhage' John H Zhang (ed.), *BioMed Research International*, 2014p. 727428.

- Ding, G., Chopp, M., Li, L., Zhang, L., Davoodi-Bojd, E., Li, Q., Zhang, Z. & Jiang, Q. (2018) 'MRI investigation of glymphatic responses to Gd-DTPA infusion rates', *Journal of neuroscience research*, 96(12), pp. 1876-1886.
- Donahue, E.K., Murdos, A., Jakowec, M.W., Sheikh-Bahaei, N., Toga, A.W., Petzinger, G.M. & Sepehrband, F. (2021) 'Global and regional changes in perivascular space in idiopathic and familial Parkinson's disease', *Movement Disorders*, 36(5), pp. 1126-1136.
- Duraiyan, J., Govindarajan, R., Kaliyappan, K. & Palanisamy, M. (2012) 'Applications of immunohistochemistry', *Journal of pharmacy & bioallied sciences*, 4(Suppl 2), p. S307.
- Durand-Fardel, M. (1843) *Traite du ramollissement du cerveau*. Baillière.
- Dyke, J.P., Xu, H.S., Verma, A., Voss, H.U. & Chazen, J.L. (2020) 'MRI characterization of early CNS transport kinetics post intrathecal gadolinium injection: Trends of subarachnoid and parenchymal distribution in healthy volunteers', *Clinical Imaging*, 68pp. 1-6.
- Edeklev, C.S., Halvorsen, M., Løvland, G., Vatnehol, S.A.S., Gjertsen, Ø., Nedregård, B., Sletteberg, R., Ringstad, G. & Eide, P.K. (2019) 'Intrathecal use of gadobutrol for glymphatic MR imaging: prospective safety study of 100 patients', *American Journal of Neuroradiology*, 40(8), pp. 1257-1264.
- Eide, P.K. & Ringstad, G. (2019a) 'Delayed clearance of cerebrospinal fluid tracer from entorhinal cortex in idiopathic normal pressure hydrocephalus: a glymphatic magnetic resonance imaging study', *Journal of Cerebral Blood Flow & Metabolism*, 39(7), pp. 1355-1368.
- Eide, P.K. & Ringstad, G. (2019b) 'In vivo imaging of molecular clearance from human entorhinal cortex: a possible method for preclinical testing of dementia', *Gerontology and Geriatric Medicine*, 5p. 2333721419889739.
- Eide, P.K. & Ringstad, G. (2015) 'MRI with intrathecal MRI gadolinium contrast medium administration: a possible method to assess glymphatic function in human brain', *Acta radiologica open*, 4(11), p. 2058460115609635.
- Eide, P.K., Vatnehol, S.A.S., Emblem, K.E. & Ringstad, G. (2018) 'Magnetic resonance imaging provides evidence of glymphatic drainage from human brain to cervical lymph nodes', *Scientific reports*, 8(1), p. 7194.
- Eide, P.K., Vinje, V., Pripp, A.H., Mardal, K.-A. & Ringstad, G. (2021) 'Sleep deprivation impairs molecular clearance from the human brain', *Brain*, 144(3), pp. 863-874.
- Eidsvaag, V.A., Enger, R., Hansson, H., Eide, P.K. & Nagelhus, E.A. (2017) 'Human and mouse cortical astrocytes differ in aquaporin-4 polarization toward microvessels', *Glia*, 65(6), pp. 964-973.
- van Es, M.A., Hardiman, O., Chio, A., Al-Chalabi, A., Pasterkamp, R.J., Veldink, J.H. & Van den Berg, L.H. (2017) 'Amyotrophic lateral sclerosis', *The Lancet*, 390(10107), pp. 2084-2098.
- Faber, W.M. (1937) 'The nasal mucosa and the subarachnoid space', *American Journal of Anatomy*, 62(1), pp. 121-148.
- Faghih, M.M. & Sharp, M.K. (2018) 'Is bulk flow plausible in perivascular, paravascular and paravenous channels?', *Fluids and Barriers of the CNS*, 15(1), p. 17.
- Faghih, M.M. & Sharp, M.K. (2021) 'Mechanisms of tracer transport in cerebral perivascular spaces', *Journal of biomechanics*, 118p. 110278.
- Fan, Y., Liu, M., Wu, X., Wang, F., Ding, J., Chen, J. & Hu, G. (2013) 'Aquaporin-4 promotes memory consolidation in Morris water maze', *Brain Structure and Function*, 218(1), pp. 39-50.
- Farr, G.W., Hall, C.H., Farr, S.M., Wade, R., Detzel, J.M., Adams, A.G., Buch, J.M., Beahm, D.L., Flask, C.A. & Xu, K. (2019) 'Functionalized

- phenylbenzamides inhibit aquaporin-4 reducing cerebral edema and improving outcome in two models of CNS injury', *Neuroscience*, 404pp. 484-498.
- Feng, W., Zhang, Y., Wang, Z., Xu, H., Wu, T., Marshall, C., Gao, J. & Xiao, M. (2020) 'Microglia prevent beta-amyloid plaque formation in the early stage of an Alzheimer's disease mouse model with suppression of glymphatic clearance', *Alzheimer's research & therapy*, 12(1), pp. 1-15.
- Ford, A.H., Hankey, G.J., Yeap, B.B., Golledge, J., Flicker, L. & Almeida, O.P. (2018) 'Hearing loss and the risk of dementia in later life', *Maturitas*, 112pp. 1-11.
- Fournier, A.P., Gauberti, M., Quenault, A., Vivien, D., Macrez, R. & Docagne, F. (2018) 'Reduced spinal cord parenchymal cerebrospinal fluid circulation in experimental autoimmune encephalomyelitis', *Journal of Cerebral Blood Flow & Metabolism*, 39(7), pp. 1258-1265.
- Frost, S., Guymer, R., Zaw Aung, K., Lance Macaulay, S., R Sohrabi, H., Bourgeat, P., Salvado, O., C Rowe, C., Ames, D. & L Masters, C. (2016) 'Alzheimer's disease and the early signs of age-related macular degeneration', *Current Alzheimer Research*, 13(11), pp. 1259-1266.
- Fukuda, A.M., Adami, A., Pop, V., Bellone, J.A., Coats, J.S., Hartman, R.E., Ashwal, S., Obenaus, A. & Badaut, J. (2013) 'Posttraumatic reduction of edema with aquaporin-4 RNA interference improves acute and chronic functional recovery', *Journal of Cerebral Blood Flow & Metabolism*, 33(10), pp. 1621-1632.
- Fukuda, A.M., Pop, V., Spagnoli, D., Ashwal, S., Obenaus, A. & Badaut, J. (2012) 'Delayed increase of astrocytic aquaporin 4 after juvenile traumatic brain injury: possible role in edema resolution?', *Neuroscience*, 222pp. 366-378.
- Gabr, R.E., Lincoln, J.A., Hasan, K.M. & Kramer, L.A. (2023) 'Functional assessment of the dural lymphatic vessels using dynamic contrast MRI in multiple sclerosis', *Brain and Behavior*, p. e3042.
- Gentile, M.T., Poulet, R., Di Pardo, A., Cifelli, G., Maffei, A., Vecchione, C., Passarelli, F., Landolfi, A., Carullo, P. & Lembo, G. (2009) 'B-Amyloid deposition in brain is enhanced in mouse models of arterial hypertension', *Neurobiology of aging*, 30(2), pp. 222-228.
- Georgiopoulos, C., Tisell, A., Holmgren, R.T., Eleftheriou, A., Rydja, J., Lundin, F. & Tobieson, L. (2023) 'Noninvasive assessment of glymphatic dysfunction in idiopathic normal pressure hydrocephalus with diffusion tensor imaging', *Journal of Neurosurgery*, 1(aop), pp. 1-9.
- Giroux, M.-C., Hélie, P., Burns, P. & VaChon, P. (2015) 'Anesthetic and pathological changes following high doses of ketamine and xylazine in Sprague Dawley rats', *Experimental animals*, 64(3), pp. 253-260.
- Gomez, D.G., Ehrmann, J.E., Potts, D.G., Pavese, A.M. & Gilanian, A. (1983) 'The arachnoid granulations of the newborn human: an ultrastructural study', *International Journal of Developmental Neuroscience*, 1(2), pp. 139-147.
- Gomez, D.G. & Potts, D.G. (1977) 'Effects of pressure on the arachnoid villus', *Experimental Eye Research*, 25pp. 117-125.
- Gomez, D.G., Potts, G., Deonarine, V. & Reilly, K.F. (1973) 'Effects of pressure gradient changes on the morphology of arachnoid villi and granulations of the monkey', *Laboratory investigation; a journal of technical methods and pathology*, 28(6), pp. 648-657.
- Gorelick, P.B., Scuteri, A., Black, S.E., DeCarli, C., Greenberg, S.M., Iadecola, C., Launer, L.J., Laurent, S., Lopez, O.L. & Nyenhuis, D. (2011) 'Vascular contributions to cognitive impairment and dementia: a statement for

- healthcare professionals from the American Heart Association/American Stroke Association', *stroke*, 42(9), pp. 2672-2713.
- Govindarajan, B.R., Sharma, P.K., Polaka, Y., Pujitha, S. & Natarajan, P. (2024) 'The Role of Phase-Contrast MRI in Diagnosing Cerebrospinal Fluid Flow Abnormalities', *Cureus*, 16(3), .
- Hablitz, L.M., Vinitsky, H.S., Sun, Q., Staeger, F.F., Sigurdsson, B., Mortensen, K.N., Lilius, T.O. & Nedergaard, M. (2019) 'Increased glymphatic influx is correlated with high EEG delta power and low heart rate in mice under anesthesia.', *Science advances*, 5(2), p. eaav5447.
- Halsey, A.M., Conner, A.C., Bill, R.M., Logan, A. & Ahmed, Z. (2018) 'Aquaporins and their regulation after spinal cord injury', *Cells*, 7(10), p. 174.
- Hara, S., Kikuta, J., Takabayashi, K., Kamagata, K., Hayashi, S., Inaji, M., Tanaka, Y., Hori, M., Ishii, K. & Nariai, T. (2023) *Diffusivity Along the Perivascular Space is Decreased and Related to Hypoperfusion in Adult Moyamoya disease*,
- Hardy, J. & Selkoe, D.J. (2002) 'The amyloid hypothesis of Alzheimer's disease: progress and problems on the road to therapeutics', *science*, 297(5580), pp. 353-356.
- Harrison, I.F., Ismail, O., Machhada, A., Colgan, N., Ohene, Y., Nahavandi, P., Ahmed, Z., Fisher, A., Meftah, S. & Murray, T.K. (2020) 'Impaired glymphatic function and clearance of tau in an Alzheimer's disease model', *Brain*, 143(8), pp. 2576-2593.
- Harrison, I.F., Siow, B., Akilo, A.B., Evans, P.G., Ismail, O., Ohene, Y., Nahavandi, P., Thomas, D.L., Lythgoe, M.F. & Wells, J.A. (2018) 'Non-invasive imaging of CSF-mediated brain clearance pathways via assessment of perivascular fluid movement with diffusion tensor MRI.', *eLife*, 7.
- Harsh, M. & Sugandha, M. (2012) 'Essential pathology for dental students', *infectious and parasitic diseases*, pp. 172-173.
- Hase, Y., Craggs, L., Hase, M., Stevenson, W., Slade, J., Chen, A., Liang, D., Ennaceur, A., Oakley, A. & Ihara, M. (2018) 'The effects of environmental enrichment on white matter pathology in a mouse model of chronic cerebral hypoperfusion', *Journal of Cerebral Blood Flow & Metabolism*, 38(1), pp. 151-165.
- Hattori, Y., Enmi, J., Iguchi, S., Saito, S., Yamamoto, Y., Nagatsuka, K., Iida, H. & Ihara, M. (2016) 'Substantial reduction of parenchymal cerebral blood flow in mice with bilateral common carotid artery stenosis', *Scientific reports*, 6(1), p. 32179.
- Hauglund, N.L., Pavan, C. & Nedergaard, M. (2020) 'Cleaning the sleeping brain- the potential restorative function of the glymphatic system', *Current Opinion in Physiology*, 15pp. 1-6.
- Hayes, C.E., Edelstein, W.A., Schenck, J.F., Mueller, O.M. & Eash, M. (1985) 'An efficient, highly homogeneous radiofrequency coil for whole-body NMR imaging at 1.5 T', *Journal of Magnetic Resonance (1969)*, 63(3), pp. 622-628.
- He, F.-F., Li, L., Liu, M.-J., Zhong, T.-D., Zhang, Q.-W. & Fang, X.-M. (2018) 'Targeted epidural blood patch treatment for refractory spontaneous intracranial hypotension in China', *Journal of Neurological Surgery Part B: Skull Base*, 79(03), pp. 217-223.
- He, P., Shi, L., Li, Y., Duan, Q., Qiu, Y., Feng, S., Gao, Y., Luo, Y., Ma, G. & Zhang, Y. (2023) 'The Association of the Glymphatic Function with Parkinson's Disease Symptoms: Neuroimaging Evidence from Longitudinal and Cross-Sectional Studies', *Annals of Neurology*,

- He, X., Liu, D., Zhang, Q., Liang, F., Dai, G., Zeng, J., Pei, Z., Xu, G. & Lan, Y. (2017) 'Voluntary exercise promotes glymphatic clearance of amyloid beta and reduces the activation of astrocytes and microglia in aged mice', *Frontiers in molecular neuroscience*, 10p. 144.
- Helakari, H., Korhonen, V., Holst, S.C., Piispala, J., Kallio, M., Väyrynen, T., Huotari, N., Raitamaa, L., Tuunanen, J. & Kananen, J. (2022) 'Human NREM sleep promotes brain-wide vasomotor and respiratory pulsations', *Journal of Neuroscience*, 42(12), pp. 2503-2515.
- Henkelman, R.M., Stanisiz, G.J. & Graham, S.J. (2001) 'Magnetization transfer in MRI: a review', *NMR in Biomedicine: An International Journal Devoted to the Development and Application of Magnetic Resonance In Vivo*, 14(2), pp. 57-64.
- Hennig, J., Nauerth, A. & Friedburg, H. (1986) 'RARE imaging: a fast imaging method for clinical MR', *Magnetic resonance in medicine*, 3(6), pp. 823-833.
- Hirt, L., Fukuda, A.M., Ambadipudi, K., Rashid, F., Binder, D., Verkman, A., Ashwal, S., Obenaus, A. & Badaut, J. (2017) 'Improved long-term outcome after transient cerebral ischemia in aquaporin-4 knockout mice', *Journal of Cerebral Blood Flow & Metabolism*, 37(1), pp. 277-290.
- Hladky, S.B. & Barrand, M.A. (2014) 'Mechanisms of fluid movement into, through and out of the brain: evaluation of the evidence.', *Fluids and barriers of the CNS*, 11(1), p. 26.
- Hoddevik, E.H., Khan, F.H., Rahmani, S., Ottersen, O.P., Boldt, H.B. & Amiry-Moghaddam, M. (2017) 'Factors determining the density of AQP4 water channel molecules at the brain-blood interface', *Brain Structure and Function*, 222(4), pp. 1753-1766.
- Van Hoek, A.N., Ma, T., Yang, B., Verkman, A.S. & Brown, D. (2000) 'Aquaporin-4 is expressed in basolateral membranes of proximal tubule S3 segments in mouse kidney', *American Journal of Physiology - Renal Physiology*, 278(2 47-2), pp. 310-316.
- von Holstein-Rathlou, S., Petersen, N.C. & Nedergaard, M. (2018) 'Voluntary running enhances glymphatic influx in awake behaving, young mice', *Neuroscience letters*, 662pp. 253-258.
- Holter, K.E., Kehlet, B., Devor, A., Sejnowski, T.J., Dale, A.M., Omholt, S.W., Ottersen, O.P., Nagelhus, E.A., Mardal, K.-A. & Pettersen, K.H. (2017) 'Interstitial solute transport in 3D reconstructed neuropil occurs by diffusion rather than bulk flow.', *Proceedings of the National Academy of Sciences of the United States of America*, 114(37), pp. 9894-9899.
- Holth, J.K., Fritschi, S.K., Wang, C., Pedersen, N.P., Cirrito, J.R., Mahan, T.E., Finn, M.B., Manis, M., Geerling, J.C. & Fuller, P.M. (2019) 'The sleep-wake cycle regulates brain interstitial fluid tau in mice and CSF tau in humans', *Science*, 363(6429), pp. 880-884.
- Holth, J.K., Patel, T.K. & Holtzman, D.M. (2017) 'Sleep in Alzheimer's disease-beyond amyloid', *Neurobiology of sleep and circadian rhythms*, 2pp. 4-14.
- Hoshi, A., Tsunoda, A., Tada, M., Nishizawa, M., Ugawa, Y. & Kakita, A. (2017) 'Expression of aquaporin 1 and aquaporin 4 in the temporal neocortex of patients with Parkinson's disease', *Brain Pathology*, 27(2), pp. 160-168.
- Hoshi, A., Yamamoto, T., Shimizu, K., Ugawa, Y., Nishizawa, M., Takahashi, H. & Kakita, A. (2012) 'Characteristics of aquaporin expression surrounding senile plaques and cerebral amyloid angiopathy in Alzheimer disease', *Journal of Neuropathology & Experimental Neurology*, 71(8), pp. 750-759.
- Hubbard, J.A., Hsu, M.S., Seldin, M.M. & Binder, D.K. (2015) 'Expression of the astrocyte water channel aquaporin-4 in the mouse brain', *ASN neuro*, 7(5), p. 1759091415605486.

- Huber, V.J., Igarashi, H., Ueki, S., Kwee, I.L. & Nakada, T. (2018) 'Aquaporin-4 facilitator TGN-073 promotes interstitial fluid circulation within the blood-brain barrier: [17 O]H₂O JVCPE MRI study', *NeuroReport*, 29(9), pp. 697-703.
- Huber, V.J., Kwee, I.L. & Nakada, T. (2018) 'Aquaporin-4 facilitator TGN-073 demonstrates novel analgesic activity', *bioRxiv*, pp. 6-7.
- Huber, V.J., Tsujita, M. & Nakada, T. (2009) 'Identification of Aquaporin 4 inhibitors using in vitro and in silico methods', *Bioorganic and Medicinal Chemistry*, 17(1), pp. 411-417.
- Hutton, D., Fadelalla, M.G., Kanodia, A.K. & Hossain-Ibrahim, K. (2022) 'Choroid plexus and CSF: an updated review', *British Journal of Neurosurgery*, 36(3), pp. 307-315.
- Igarashi, H., Huber, V.J., Tsujita, M. & Nakada, T. (2011) 'Pretreatment with a novel aquaporin 4 inhibitor, TGN-020, significantly reduces ischemic cerebral edema', *Neurological Sciences*, 32(1), pp. 113-116.
- Igarashi, H., Tsujita, M., Kwee, I.L. & Nakada, T. (2014) 'Water influx into cerebrospinal fluid is primarily controlled by aquaporin-4, not by aquaporin-1: 17O JVCPE MRI study in knockout mice', *NeuroReport*, 25(1), pp. 39-43.
- Ihara, M., Taguchi, A., Maki, T., Washida, K. & Tomimoto, H. (2014) 'A mouse model of chronic cerebral hypoperfusion characterizing features of vascular cognitive impairment', *Cerebral Angiogenesis: Methods and Protocols*, pp. 95-102.
- Ikeshima-Kataoka, H. (2016) 'Neuroimmunological implications of AQP4 in astrocytes', *International journal of molecular sciences*, 17(8), p. 1306.
- Iliff, J. & Simon, M. (2019) 'CrossTalk proposal: The glymphatic system supports convective exchange of cerebrospinal fluid and brain interstitial fluid that is mediated by perivascular aquaporin-4', *Journal of Physiology*, 597(17), pp. 4417-4419.
- Iliff, J.J., Chen, M.J., Plog, B.A., Zeppenfeld, D.M., Soltero, M., Yang, L., Singh, I., Deane, R. & Nedergaard, M. (2014) 'Impairment of glymphatic pathway function promotes tau pathology after traumatic brain injury.', *The Journal of neuroscience : the official journal of the Society for Neuroscience*, 34(49), pp. 16180-16193.
- Iliff, J.J., Lee, H., Yu, M., Feng, T., Logan, J., Nedergaard, M. & Benveniste, H. (2013) 'Brain-wide pathway for waste clearance captured by contrast-enhanced MRI.', *The Journal of clinical investigation*, 123(3), pp. 1299-1309.
- Iliff, J.J., Wang, M., Liao, Y., Plogg, B.A., Peng, W., Gundersen, G.A., Benveniste, H., Vates, G.E., Deane, R., Goldman, S.A., Nagelhus, E.A. & Nedergaard, M. (2012) 'A Paravascular Pathway Facilitates CSF Flow Through the Brain Parenchyma and the Clearance of Interstitial Solutes, Including Amyloid B', *Science Translational Medicine*, 4(147), pp. 147ra111 LP-147ra111.
- Iliff, J.J., Wang, M., Zeppenfeld, D.M., Venkataraman, A., Plog, B.A., Liao, Y., Deane, R. & Nedergaard, M. (2013) 'Cerebral arterial pulsation drives paravascular CSF-interstitial fluid exchange in the murine brain', *Journal of Neuroscience*, 33(46), pp. 18190-18199.
- Ishida, K., Misawa, K., Nishimura, H., Hirata, T., Yamamoto, M. & Ota, N. (2020) '5-Caffeoylquinic acid ameliorates cognitive decline and reduces AB deposition by modulating AB clearance pathways in APP/PS2 transgenic mice', *Nutrients*, 12(2), p. 494.

- Ishikawa, H., Shindo, A., Mizutani, A., Tomimoto, H., Lo, E.H. & Arai, K. (2023) *A brief overview of a mouse model of cerebral hypoperfusion by bilateral carotid artery stenosis*,
- Jessen, N.A., Munk, A.S.F., Lundgaard, I. & Nedergaard, M. (2015) 'The Glymphatic System: A Beginner's Guide', *Neurochemical Research*, 40(12), pp. 2583-2599.
- Jiang, D., Gou, Y., Wei, Z., Hou, X., Yedavalli, V. & Lu, H. (2023) 'Quantification of T1 and T2 of subarachnoid CSF: Implications for water exchange between CSF and brain tissues', *Magnetic Resonance in Medicine*,
- Jin, B.-J., Smith, A.J. & Verkman, A.S. (2016) 'Spatial model of convective solute transport in brain extracellular space does not support a "glymphatic" mechanism', *Journal of General Physiology*, 148(6), pp. 489-501.
- Johnston, M., Zakharov, A., Papaiconomou, C., Salmasi, G. & Armstrong, D. (2004) 'Evidence of connections between cerebrospinal fluid and nasal lymphatic vessels in humans, non-human primates and other mammalian species', *Cerebrospinal fluid research*, 1pp. 1-13.
- Joseph, C.R., Benhatzel, C.M., Stern, L.J., Hopper, O.M. & Lockwood, M.D. (2020) 'Pilot study utilizing MRI 3D TGSE PASL (arterial spin labeling) differentiating clearance rates of labeled protons in the CNS of patients with early Alzheimer disease from normal subjects', *Magnetic Resonance Materials in Physics, Biology and Medicine*, 33pp. 559-568.
- Ju, Y.-E.S., Ooms, S.J., Sutphen, C., Macauley, S.L., Zangrilli, M.A., Jerome, G., Fagan, A.M., Mignot, E., Zempel, J.M. & Claassen, J.A.H.R. (2017) 'Slow wave sleep disruption increases cerebrospinal fluid amyloid- β levels', *Brain*, 140(8), pp. 2104-2111.
- Kalmijn, S., Launer, L.J., Ott, A., Witteman, J.C.M., Hofman, A. & Breteler, M.M.B. (1997) 'Dietary fat intake and the risk of incident dementia in the Rotterdam Study', *Annals of neurology*, 42(5), pp. 776-782.
- Kamagata, K., Andica, C., Takabayashi, K., Saito, Y., Taoka, T., Nozaki, H., Kikuta, J., Fujita, S., Hagiwara, A. & Kamiya, K. (2022) 'Association of MRI indices of glymphatic system with amyloid deposition and cognition in mild cognitive impairment and Alzheimer disease', *Neurology*, 99(24), pp. e2648-e2660.
- Kanda, T., Fukusato, T., Matsuda, M., Toyoda, K., Oba, H., Kotoku, J., Haruyama, T., Kitajima, K. & Furui, S. (2015) 'Gadolinium-based contrast agent accumulates in the brain even in subjects without severe renal dysfunction: evaluation of autopsy brain specimens with inductively coupled plasma mass spectroscopy', *Radiology*, 276(1), pp. 228-232.
- Kanda, T., Ishii, K., Kawaguchi, H., Kitajima, K. & Takenaka, D. (2014) 'High signal intensity in the dentate nucleus and globus pallidus on unenhanced T1-weighted MR images: relationship with increasing cumulative dose of a gadolinium-based contrast material', *Radiology*, 270(3), pp. 834-841.
- Kanda, T., Oba, H., Toyoda, K., Kitajima, K. & Furui, S. (2016) 'Brain gadolinium deposition after administration of gadolinium-based contrast agents', *Japanese journal of radiology*, 34(1), pp. 3-9.
- Kang, J.-E., Lim, M.M., Bateman, R.J., Lee, J.J., Smyth, L.P., Cirrito, J.R., Fujiki, N., Nishino, S. & Holtzman, D.M. (2009) 'Amyloid- β dynamics are regulated by orexin and the sleep-wake cycle', *Science*, 326(5955), pp. 1005-1007.
- Kant, S., Stopa, E.G., Johanson, C.E., Baird, A. & Silverberg, G.D. (2018) 'Choroid plexus genes for CSF production and brain homeostasis are altered in Alzheimer's disease', *Fluids and Barriers of the CNS*, 15pp. 1-10.

- Kapoor, R., Liu, J., Devasenapathy, A. & Gordin, V. (2010) 'Gadolinium encephalopathy after intrathecal gadolinium injection', *Pain Physician*, 13(5), p. E321.
- Kaptan, S., Assentoft, M., Schneider, H.P., Fenton, R.A., Deitmer, J.W., MacAulay, N. & de Groot, B.L. (2015) 'H95 is a pH-dependent gate in aquaporin 4', *Structure*, 23(12), pp. 2309-2318.
- Karimy, J.K., Kahle, K.T., Kurland, D.B., Yu, E., Gerzanich, V. & Simard, J.M. (2015) 'A novel method to study cerebrospinal fluid dynamics in rats', *Journal of neuroscience methods*, 241pp. 78-84.
- Kaur, J., Davoodi-Bojd, E., Fahmy, L.M., Zhang, L., Ding, G., Hu, J., Zhang, Z., Chopp, M. & Jiang, Q. (2020) 'Magnetic resonance imaging and modeling of the glymphatic system'. *Diagnostics* 10 (6).
- Kedarasetti, R.T., Drew, P.J. & Costanzo, F. (2020) 'Arterial pulsations drive oscillatory flow of CSF but not directional pumping', *Scientific reports*, 10(1), p. 10102.
- Keith Sharp, M., Carare, R.O. & Martin, B.A. (2019) 'Dispersion in porous media in oscillatory flow between flat plates: applications to intrathecal, periarterial and paraarterial solute transport in the central nervous system', *Fluids and Barriers of the CNS*, 16(1), pp. 1-17.
- Key, A. (1875) *Studien in der Anatomie des Nervensystems und des Bindegewebes: 1. Hälfte*. Vol. 1. Samson & Wallin.
- Khodabakhshi, Z., Gabrys, H., Wallimann, P., Guckenberger, M., Andratschke, N. & Tanadini-Lang, S. (2024) 'Magnetic resonance imaging radiomic features stability in brain metastases: impact of image preprocessing, image-, and feature-level harmonization', *Physics and Imaging in Radiation Oncology*, 30p. 100585.
- Kido, D.K., Gomez, D.G., Pavese Jr, A.M. & Potts, D.G. (1976) 'Human spinal arachnoid villi and granulations', *Neuroradiology*, 11(5), pp. 221-228.
- Kim, H.G., Shin, N.-Y., Nam, Y., Yun, E., Yoon, U., Lee, H.S. & Ahn, K.J. (2022) 'MRI-visible dilated perivascular space in the brain by age: The human connectome project', *Radiology*, 306(3), p. e213254.
- Kitaguchi, H., Tomimoto, H., Ihara, M., Shibata, M., Uemura, K., Kalaria, R.N., Kihara, T., Asada-Utsugi, M., Kinoshita, A. & Takahashi, R. (2009) 'Chronic cerebral hypoperfusion accelerates amyloid β deposition in APPSwInd transgenic mice', *Brain research*, 1294pp. 202-210.
- Kitamura, A., Manso, Y., Duncombe, J., Searcy, J., Koudelka, J., Binnie, M., Webster, S., Lennen, R., Jansen, M. & Marshall, I. (2017) 'Long-term cilostazol treatment reduces gliovascular damage and memory impairment in a mouse model of chronic cerebral hypoperfusion', *Scientific reports*, 7(1), p. 4299.
- Kitamura, A., Saito, S., Maki, T., Oishi, N., Ayaki, T., Hattori, Y., Yamamoto, Y., Urushitani, M., Kalaria, R.N. & Fukuyama, H. (2016) 'Gradual cerebral hypoperfusion in spontaneously hypertensive rats induces slowly evolving white matter abnormalities and impairs working memory', *Journal of Cerebral Blood Flow & Metabolism*, 36(9), pp. 1592-1602.
- Kiviniemi, V., Wang, X., Korhonen, V., Keinanen, T., Tuovinen, T., Autio, J., LeVan, P., Keilholz, S., Zang, Y.-F., Hennig, J. & Nedergaard, M. (2016) 'Ultra-fast magnetic resonance encephalography of physiological brain activity - Glymphatic pulsation mechanisms?', *Journal of cerebral blood flow and metabolism : official journal of the International Society of Cerebral Blood Flow and Metabolism*, 36(6), pp. 1033-1045.

- Koh, L., Zakharov, A. & Johnston, M. (2005) 'Integration of the subarachnoid space and lymphatics: is it time to embrace a new concept of cerebrospinal fluid absorption?', *Cerebrospinal fluid research*, 2pp. 1-11.
- Koundal, S., Elkin, R., Nadeem, S., Xue, Y., Constantinou, S., Sanggaard, S., Liu, X., Monte, B., Xu, F. & Van Nostrand, W. (2020) 'Optimal mass transport with lagrangian workflow reveals advective and diffusion driven solute transport in the glymphatic system', *Scientific reports*, 10(1), p. 1990.
- Kress, B.T., Iliff, J.J., Xia, M., Wang, M., Wei, H.S., Zeppenfeld, D., Xie, L., Kang, H., Xu, Q., Liew, J.A., Plog, B.A., Ding, F., Deane, R. & Nedergaard, M. (2014) 'Impairment of paravascular clearance pathways in the aging brain.', *Annals of neurology*, 76(6), pp. 845-861.
- Krueger, J.M., Frank, M.G., Wisor, J.P. & Roy, S. (2016) 'Sleep function: Toward elucidating an enigma'. *Sleep Medicine Reviews* 28 p.pp. 46-54.
- Kudo, K., Harada, T., Kameda, H., Uwano, I., Yamashita, F., Higuchi, S., Yoshioka, K. & Sasaki, M. (2018) 'Indirect Proton MR Imaging and Kinetic Analysis of (17)O-Labeled Water Tracer in the Brain.', *Magnetic resonance in medical sciences : MRMS : an official journal of Japan Society of Magnetic Resonance in Medicine*, 17(3), pp. 223-230.
- Kuroiwa, T., Nagaoka, T., Ueki, M., Yamada, I., Miyasaka, N. & Akimoto, H. (1998) 'Different apparent diffusion coefficient: water content correlations of gray and white matter during early ischemia', *Stroke*, 29(4), pp. 859-865.
- Kwee, I.L., Igarashi, H., Suzuki, Y., Ueki, S. & Huber, V.J. (2020) 'Aquaporin4 facilitator decreases insoluble amyloid b of 5XFAD mouse brain', *Alzheimer's & Dementia*, 16.
- Kylkilahti, T.M., Berends, E., Ramos, M., Shanbhag, N.C., Töger, J., Markenroth Bloch, K. & Lundgaard, I. (2021) 'Achieving brain clearance and preventing neurodegenerative diseases—A glymphatic perspective', *Journal of Cerebral Blood Flow & Metabolism*, 41(9), pp. 2137-2149.
- Lan, Y.-L., Zhao, J., Ma, T. & Li, S. (2016) 'The potential roles of aquaporin 4 in Alzheimer's disease', *Molecular neurobiology*, 53(8), pp. 5300-5309.
- Lansdell, T.A. & Dorrance, A.M. (2022) 'Chronic cerebral hypoperfusion in male rats results in sustained HPA activation and hyperinsulinemia', *American Journal of Physiology - Endocrinology and Metabolism*, 322(1), pp. E24-E33.
- Lee, H., Xie, L., Yu, M., Kang, H., Feng, T., Deane, R., Logan, J., Nedergaard, M. & Benveniste, H. (2015) 'The Effect of Body Posture on Brain Glymphatic Transport.', *The Journal of neuroscience : the official journal of the Society for Neuroscience*, 35(31), pp. 11034-11044.
- Lee, H., Xu, F., Liu, X., Koundal, S., Zhu, X., Davis, J., Yanez, D., Schrader, J., Stanisavljevic, A. & Rothman, D.L. (2021) 'Diffuse white matter loss in a transgenic rat model of cerebral amyloid angiopathy', *Journal of Cerebral Blood Flow & Metabolism*, 41(5), pp. 1103-1118.
- De Leon, M.J., Li, Y., Okamura, N., Tsui, W.H., Saint-Louis, L.A., Glodzik, L., Osorio, R.S., Fortea, J., Butler, T., Pirraglia, E., Fossati, S., Kim, H.J., Carare, R.O., Nedergaard, M., Benveniste, H. & Rusinek, H. (2017) 'Cerebrospinal fluid clearance in Alzheimer disease measured with dynamic PET', *Journal of Nuclear Medicine*, 58(9), pp. 1471-1476.
- Levendowski, D.J., Gamaldo, C., St Louis, E.K., Ferini-Strambi, L., Hamilton, J.M., Salat, D., Westbrook, P.R. & Berka, C. (2019) 'Head position during sleep: potential implications for patients with neurodegenerative disease', *Journal of Alzheimer's Disease*, 67(2), pp. 631-638.
- Levitt, M.H. (2013) *Spin dynamics: basics of nuclear magnetic resonance*. John Wiley & Sons.

- Li, J., Patil, R. V & Verkman, A.S. (2002) 'Mildly abnormal retinal function in transgenic mice without Muller cell aquaporin-4 water channels', *Investigative ophthalmology & visual science*, 43(2), pp. 573-579.
- Li, J. & Verkman, A.S. (2001) 'Impaired hearing in mice lacking aquaporin-4 water channels', *Journal of Biological Chemistry*, 276(33), pp. 31233-31237.
- Li, M., Kitamura, A., Beverley, J., Koudelka, J., Duncombe, J., Lennen, R., Jansen, M.A., Marshall, I., Platt, B., Wiegand, U.K., Carare, R.O., Kalaria, R.N., Iliff, J.J. & Horsburgh, K. (2022) 'Impaired Glymphatic Function and Pulsation Alterations in a Mouse Model of Vascular Cognitive Impairment', *Frontiers in Aging Neuroscience*, 13.
- Li, N., Gu, Z., Li, Y., Fu, X., Wang, J. & Bai, H. (2015) 'A modified bilateral carotid artery stenosis procedure to develop a chronic cerebral hypoperfusion rat model with an increased survival rate', *Journal of Neuroscience Methods*, 255pp. 115-121.
- Li, X., Xie, Z., Zhou, Q., Tan, X., Meng, W., Pang, Y., Huang, L., Ding, Z., Hu, Y., Li, R., Huang, G. & Li, H. (2023) 'TGN-020 Alleviate Inflammation and Apoptosis After Cerebral Ischemia-Reperfusion Injury in Mice Through Glymphatic and ERK1/2 Signaling Pathway', *Molecular Neurobiology*,
- Lilius, T.O., Blomqvist, K., Hauglund, N.L., Liu, G., Stæger, F.F., Bærentzen, S., Du, T., Ahlström, F., Backman, J.T. & Kalso, E.A. (2019) 'Dexmedetomidine enhances glymphatic brain delivery of intrathecally administered drugs', *Journal of Controlled Release*, 304pp. 29-38.
- Lim, J. & Dinges, D.F. (2010) 'A meta-analysis of the impact of short-term sleep deprivation on cognitive variables.', *Psychological bulletin*, 136(3), p. 375.
- Liu, E., Peng, X., Ma, H., Zhang, Yan, Yang, X., Zhang, Yixuan, Sun, L. & Yan, J. (2021) 'The Involvement of Aquaporin-4 in the Interstitial Fluid Drainage Impairment Following Subarachnoid Hemorrhage', *Frontiers in Aging Neuroscience*, 12(January), pp. 1-11.
- Liu, E., Sun, L., Zhang, Y., Wang, A. & Yan, J. (2020) 'Aquaporin4 knockout aggravates early brain injury following subarachnoid hemorrhage through impairment of the glymphatic system in rat brain', in *Subarachnoid Hemorrhage*. [Online]. Springer. pp. 59-64.
- Liu, G., Mestre, H., Sweeney, A.M., Sun, Q., Weikop, P., Du, T. & Nedergaard, M. (2020) 'Direct Measurement of Cerebrospinal Fluid Production in Mice', *Cell Reports*, 33(12), .
- Liu, S., Sun, X., Ren, Q., Chen, Y., Dai, T., Yang, Y., Gong, G., Li, W., Zhao, Y., Meng, X., Lin, P. & Yan, C. (2023) 'Glymphatic dysfunction in patients with early-stage amyotrophic lateral sclerosis', *Brain*, p. awad274.
- Liu, X., Xie, Y., Wan, X., Wu, J., Fan, Z. & Yang, L. (2021) 'Protective effects of aquaporin-4 deficiency on longer-term neurological outcomes in a mouse model', *Neurochemical Research*, 46(6), pp. 1380-1389.
- Liu, Y., Feng, W., Hu, P., Zhai, S., Zhang, R., Li, Q., Marsahall, C., Xiao, M. & Wu, T. (2020) *Beneficial effects of voluntary exercise therapy on an Alzheimer's mouse model are dependent on aquaporin 4-mediated glymphatic transport*,
- Liu, Y., Hu, P.-P., Zhai, S., Feng, W.-X., Zhang, R., Li, Q., Marshall, C., Xiao, M. & Wu, T. (2022) 'Aquaporin 4 deficiency eliminates the beneficial effects of voluntary exercise in a mouse model of Alzheimer's disease', *Neural Regeneration Research*, 17(9), p. 2079.
- Lopes, D.M., Llewellyn, S.K. & Harrison, I.F. (2022) 'Propagation of tau and a-synuclein in the brain: therapeutic potential of the glymphatic system', *Translational Neurodegeneration*, 11(1), pp. 1-23.

- Loughrey, D.G., Kelly, M.E., Kelley, G.A., Brennan, S. & Lawlor, B.A. (2018) 'Association of age-related hearing loss with cognitive function, cognitive impairment, and dementia: a systematic review and meta-analysis', *JAMA otolaryngology-head & neck surgery*, 144(2), pp. 115-126.
- Louveau, A., Plog, B.A., Antila, S., Alitalo, K., Nedergaard, M. & Kipnis, J. (2017) 'Understanding the functions and relationships of the glymphatic system and meningeal lymphatics', *The Journal of clinical investigation*, 127(9), pp. 3210-3219.
- Louveau, A., Smirnov, I., Keyes, T.J., Eccles, J.D., Rouhani, S.J., Peske, J.D., Derecki, N.C., Castle, D., Mandell, J.W., Lee, K.S., Harris, T.H. & Kipnis, J. (2015) 'Structural and functional features of central nervous system lymphatic vessels.', *Nature*, 523(7560), pp. 337-341.
- Love, S. & Miners, J.S. (2016) 'Cerebrovascular disease in ageing and Alzheimer's disease', *Acta neuropathologica*, 131pp. 645-658.
- Lu, M., Lee, M.D., Smith, B.L., Jung, J.S., Agre, P., Verdijk, M.A., Merckx, G., Rijss, J.P. & Deen, P.M. (1996) 'The human AQP4 gene: definition of the locus encoding two water channel polypeptides in brain.', *Proceedings of the National Academy of Sciences*, 93(20), pp. 10908-10912.
- Lundgaard, I., Li, B., Xie, L., Kang, H., Sanggaard, S., Haswell, J.D.R., Sun, W., Goldman, S., Blekot, S. & Nielsen, M. (2015) 'Direct neuronal glucose uptake heralds activity-dependent increases in cerebral metabolism', *Nature communications*, 6(1), p. 6807.
- Lundgaard, I., Lu, M.L., Yang, E., Peng, W., Mestre, H., Hitomi, E., Deane, R. & Nedergaard, M. (2017) 'Glymphatic clearance controls state-dependent changes in brain lactate concentration', *Journal of Cerebral Blood Flow & Metabolism*, 37(6), pp. 2112-2124.
- Ma, Q., Ineichen, B. V, Detmar, M. & Proulx, S.T. (2017) 'Outflow of cerebrospinal fluid is predominantly through lymphatic vessels and is reduced in aged mice', *Nature communications*, 8(1), p. 1434.
- Ma, Q., Ries, M., Decker, Y., Müller, A., Riner, C., Bücker, A., Fassbender, K., Detmar, M. & Proulx, S.T. (2019) 'Rapid lymphatic efflux limits cerebrospinal fluid flow to the brain', *Acta Neuropathologica*, 137(1), pp. 151-165.
- Ma, T., Yang, B., Gillespie, A., Carlson, E.J., Epstein, C.J. & Verkman, A.S. (1997) 'Generation and phenotype of a transgenic knockout mouse lacking the mercurial-insensitive water channel aquaporin-4', *Journal of Clinical Investigation*, 100(5), pp. 957-962.
- Ma, X., Li, S., Li, C., Wang, R., Chen, M., Chen, H. & Su, W. (2021) 'Diffusion tensor imaging along the perivascular space index in different stages of Parkinson's disease', *Frontiers in Aging Neuroscience*, 13p. 773951.
- Ma, Y., Smith, D., Hof, P.R., Foerster, B., Hamilton, S., Blackband, S.J., Yu, M. & Benveniste, H. (2008) 'In vivo 3D digital atlas database of the adult C57BL/6J mouse brain by magnetic resonance microscopy', *Frontiers in neuroanatomy*, 2p. 175.
- Mader, S. & Brimberg, L. (2019) 'Aquaporin-4 water channel in the brain and its implication for health and disease', *Cells*, 8(2), p. 90.
- Magendie, F. (1842) 'Recherches physiologiques et cliniques sur le liquide céphalo-rachidien ou cérébro-spinal', (*No Title*),
- Manley, G.T., Fujimura, M., Ma, T., Noshita, N., Filiz, F., Bollen, A.W., Chan, P. & Verkman, A.S. (2000) 'Aquaporin-4 deletion in mice reduces brain edema after acute water intoxication and ischemic stroke.', *Nature medicine*, 6(2), pp. 159-163.

- Mathiisen, T.M., Lehre, K.P., Danbolt, N.C. & Ottersen, O.P. (2010) 'The perivascular astroglial sheath provides a complete covering of the brain microvessels: an electron microscopic 3D reconstruction', *Glia*, 58(9), pp. 1094-1103.
- Matin, N., Fisher, C., Jackson, W.F. & Dorrance, A.M. (2016) 'Bilateral common carotid artery stenosis in normotensive rats impairs endothelium-dependent dilation of parenchymal arterioles', *American Journal of Physiology-Heart and Circulatory Physiology*, 310(10), pp. H1321-H1329.
- Matsuzaki, T., Yaguchi, T., Shimizu, K., Kita, A., Ishibashi, K. & Takata, K. (2017) 'The distribution and function of aquaporins in the kidney: resolved and unresolved questions', *Anatomical Science International*, 92(2), pp. 187-199.
- Mawuenyega, K.G., Sigurdson, W., Ovod, V., Munsell, L., Kasten, T., Morris, J.C., Yarasheski, K.E. & Bateman, R.J. (2010) 'Decreased clearance of CNS β -amyloid in Alzheimer's disease', *Science*, 330(6012), p. 1774.
- May, C., Kaye, J.A., Atack, J.R., Schapiro, M.B., Friedland, R.P. & Rapoport, S.I. (1990) 'Cerebrospinal fluid production is reduced in healthy aging', *Neurology*, 40(3 Part 1), p. 500.
- McComb, J.G. (1983) 'Recent research into the nature of cerebrospinal fluid formation and absorption', *Journal of neurosurgery*, 59(3), pp. 369-383.
- McKnight, C.D., Trujillo, P., Lopez, A.M., Petersen, K., Considine, C., Lin, Y.-C., Yan, Y., Kang, H., Donahue, M.J. & Claassen, D.O. (2021) 'Diffusion along perivascular spaces reveals evidence supportive of glymphatic function impairment in Parkinson disease', *Parkinsonism & related disorders*, 89pp. 98-104.
- McRobbie, D.W., Moore, E.A., Graves, M.J. & Prince, M.R. (2017) *MRI from Picture to Proton*. Cambridge university press.
- Meiboom, S. (1961) 'Nuclear magnetic resonance study of the proton transfer in water', *The Journal of Chemical Physics*, 34(2), pp. 375-388.
- Meli, R., Pirozzi, C. & Pelagalli, A. (2018) 'New perspectives on the potential role of aquaporins (AQPs) in the physiology of inflammation', *Frontiers in physiology*, 9p. 101.
- Meng, S., Qiao, M., Lin, L., Del Bigio, M.R., Tomanek, B. & Tuor, U.I. (2004) 'Correspondence of AQP4 expression and hypoxic-ischaemic brain oedema monitored by magnetic resonance imaging in the immature and juvenile rat', *European Journal of Neuroscience*, 19(8), pp. 2261-2269.
- Menick, B.J. (2001) 'Phase-contrast magnetic resonance imaging of cerebrospinal fluid flow in the evaluation of patients with Chiari I malformation', *Neurosurgical Focus*, 11(1), pp. 1-4.
- Da Mesquita, S., Fu, Z. & Kipnis, J. (2018) 'The Meningeal Lymphatic System: A New Player in Neurophysiology', *Neuron*, 100(2), pp. 375-388.
- Mestre, H., Du, T., Sweeney, A.M., Liu, G., Samson, A.J., Peng, W., Mortensen, K.N., Stæger, F.F., Bork, P.A.R., Bashford, L., Toro, E.R., Tithof, J., Kelley, D.H., Thomas, J.H., Hjorth, P.G., Martens, E.A., Mehta, R.I., Solis, O., Blinder, P., et al. (2020) 'Cerebrospinal fluid influx drives acute ischemic tissue swelling', *Science*, 7171(January), p. eaax7171.
- Mestre, H., Hablitz, L.M., Xavier, A.L.R., Feng, W., Zou, W., Pu, T., Monai, H., Murlidharan, G., Rivera, R.M.C., Simon, M.J., Pike, M.M., Plá, V., Du, T., Kress, B.T., Wang, X., Plog, B.A., Thrane, A.S., Lundgaard, I., Abe, Y., et al. (2018) 'Aquaporin-4-dependent glymphatic solute transport in the rodent brain', *eLife*, 7pp. 1-31.

- Mestre, H., Kostrikov, S., Mehta, R.I. & Nedergaard, M. (2017) 'Perivascular spaces, glymphatic dysfunction, and small vessel disease', *Clinical science*, 131(17), pp. 2257-2274.
- Mestre, H., Mori, Y. & Nedergaard, M. (2020) 'The Brain's Glymphatic System: Current Controversies', *Trends in Neurosciences*, 43(7), pp. 458-466.
- Mestre, H., Tithof, J., Du, T., Song, W., Peng, W., Sweeney, A.M., Olveda, G., Thomas, J.H., Nedergaard, M. & Kelley, D.H. (2018) 'Flow of cerebrospinal fluid is driven by arterial pulsations and is reduced in hypertension', *Nature communications*, 9(1), pp. 1-9.
- Meyer, R.E. & Fish, R.E. (2005) 'A review of tribromoethanol anesthesia for production of genetically engineered mice and rats', *Lab Animal*, 34(10), pp. 47-52.
- Miyamoto, N., Pham, L.-D.D., Hayakawa, K., Matsuzaki, T., Seo, J.H., Magnain, C., Ayata, C., Kim, K.-W., Boas, D. & Lo, E.H. (2013) 'Age-related decline in oligodendrogenesis retards white matter repair in mice', *Stroke*, 44(9), pp. 2573-2578.
- Miyanohara, J., Kakae, M., Nagayasu, K., Nakagawa, T., Mori, Y., Arai, K., Shirakawa, H. & Kaneko, S. (2018) 'TRPM2 channel aggravates CNS inflammation and cognitive impairment via activation of microglia in chronic cerebral hypoperfusion', *Journal of Neuroscience*, 38(14), pp. 3520-3533.
- Mobasher, A. & Marples, D. (2004) 'Expression of the AQP-1 water channel in normal human tissues: a semiquantitative study using tissue microarray technology', *American Journal of Physiology-Cell Physiology*, 286(3), pp. C529-C537.
- Moftakhar, P., Lynch, M.D., Pomakian, J.L. & Vinters, H. V (2010) 'Aquaporin expression in the brains of patients with or without cerebral amyloid angiopathy', *Journal of Neuropathology & Experimental Neurology*, 69(12), pp. 1201-1209.
- Mollanji, R., Papaiconomou, C., Boulton, M., Midha, R. & Johnston, M. (2001) 'Comparison of cerebrospinal fluid transport in fetal and adult sheep', *American Journal of Physiology-Regulatory, Integrative and Comparative Physiology*, 281(4), pp. R1215-R1223.
- Moran, M., Lynch, C.A., Walsh, C., Coen, R., Coakley, D. & Lawlor, B.A. (2005) 'Sleep disturbance in mild to moderate Alzheimer's disease', *Sleep medicine*, 6(4), pp. 347-352.
- Morawska, M.M., Moreira, C.G., Ginde, V.R., Valko, P.O., Weiss, T., Büchele, F., Imbach, L.L., Masneuf, S., Kollarik, S. & Prymaczok, N. (2021) 'Slow-wave sleep affects synucleinopathy and regulates proteostatic processes in mouse models of Parkinson's disease', *Science translational medicine*, 13(623), p. eabe7099.
- Morris, M.C., Evans, D.A., Tangney, C.C., Bienias, J.L. & Wilson, R.S. (2005) 'Fish consumption and cognitive decline with age in a large community study', *Archives of neurology*, 62(12), pp. 1849-1853.
- Mortensen, K.N., Sanggaard, S., Mestre, H., Lee, H., Kostrikov, S., Xavier, A.L.R., Gjedde, A., Benveniste, H. & Nedergaard, M. (2019) 'Impaired glymphatic transport in spontaneously hypertensive rats', *Journal of Neuroscience*, 39(32), pp. 6365-6377.
- Mukherjee, A., Wu, D., Davis, H.C. & Shapiro, M.G. (2016) 'Non-invasive imaging using reporter genes altering cellular water permeability', *Nature communications*, 7(1), pp. 1-9.
- Murlidharan, G., Crowther, A., Reardon, R.A., Song, J. & Asokan, A. (2016) 'Glymphatic fluid transport controls paravascular clearance of AAV vectors from the brain', *JCI insight*, 1(14), .

- Naganawa, S., Nakane, T., Kawai, H. & Taoka, T. (2019) 'Age Dependence of Gadolinium Leakage from the Cortical Veins into the Cerebrospinal Fluid Assessed with Whole Brain 3D-real Inversion Recovery MR Imaging.', *Magnetic resonance in medical sciences : MRMS : an official journal of Japan Society of Magnetic Resonance in Medicine*, 18(2), pp. 163-169.
- Naganawa, S., Nakane, T., Kawai, H. & Taoka, T. (2017) 'Gd-based Contrast Enhancement of the Perivascular Spaces in the Basal Ganglia.', *Magnetic resonance in medical sciences : MRMS : an official journal of Japan Society of Magnetic Resonance in Medicine*, 16(1), pp. 61-65.
- Nagelhus, E.A., Veruki, M.L., Torp, R., Haug, F.-M., Laake, J.H., Nielsen, S., Agre, P. & Ottersen, O.P. (1998) 'Aquaporin-4 water channel protein in the rat retina and optic nerve: polarized expression in Müller cells and fibrous astrocytes', *Journal of Neuroscience*, 18(7), pp. 2506-2519.
- Nedergaard, M. (2013) 'Neuroscience. Garbage truck of the brain.', *Science (New York, N.Y.)*, 340(6140), pp. 1529-1530.
- Nedergaard, M. & Goldman, S.A. (2016) 'BRAIN DRAIN.', *Scientific American*, 314(3), pp. 44-49.
- Nedergaard, M. & Goldman, S.A. (2020) 'Glymphatic failure as a final common pathway to dementia', *Science*, 370(6512), pp. 50-56.
- Neely, J.D., Amiry-Moghaddam, M., Ottersen, O.P., Froehner, S.C., Agre, P. & Adams, M.E. (2001) 'Syntrophin-dependent expression and localization of Aquaporin-4 water channel protein', *Proceedings of the National Academy of Sciences*, 98(24), pp. 14108-14113.
- Nielsen, S., Nagelhus, E.A., Amiry-Moghaddam, M., Bourque, C., Agre, P. & Ottersen, O.P. (1997) 'Specialized membrane domains for water transport in glial cells: high-resolution immunogold cytochemistry of aquaporin-4 in rat brain', *Journal of Neuroscience*, 17(1), pp. 171-180.
- Nilsson, C., Stahlberg, F., Thomsen, C., Henriksen, O., Herning, M. & Owman, C. (1992) 'Circadian variation in human cerebrospinal fluid production measured by magnetic resonance imaging', *American Journal of Physiology-Regulatory, Integrative and Comparative Physiology*, 262(1), pp. R20-R24.
- Ohene, Y., Harrison, I.F., Nahavandi, P., Ismail, O., Bird, E. V., Ottersen, O.P., Nagelhus, E.A., Thomas, D.L., Lythgoe, M.F. & Wells, J.A. (2019) 'Non-invasive MRI of brain clearance pathways using multiple echo time arterial spin labelling: an aquaporin-4 study.', *NeuroImage*, 188pp. 515-523.
- Okamoto, Y., Yamamoto, T., Kalaria, R.N., Senzaki, H., Maki, T., Hase, Y., Kitamura, A., Washida, K., Yamada, M. & Ito, H. (2012) 'Cerebral hypoperfusion accelerates cerebral amyloid angiopathy and promotes cortical microinfarcts', *Acta neuropathologica*, 123pp. 381-394.
- Opel, R.A., Christy, A., Boespflug, E.L., Weymann, K.B., Case, B., Pollock, J.M., Silbert, L.C. & Lim, M.M. (2019) 'Effects of traumatic brain injury on sleep and enlarged perivascular spaces', *Journal of Cerebral Blood Flow & Metabolism*, 39(11), pp. 2258-2267.
- Opitz, A., Falchier, A., Linn, G.S., Milham, M.P. & Schroeder, C.E. (2017) 'Limitations of ex vivo measurements for in vivo neuroscience', *Proceedings of the National Academy of Sciences*, 114(20), pp. 5243-5246.
- Orešković, D. & Klarica, M. (2010) 'The formation of cerebrospinal fluid: nearly a hundred years of interpretations and misinterpretations', *Brain research reviews*, 64(2), pp. 241-262.
- Oshio, K., Watanabe, H., Song, Y., Verkman, A.S. & Manley, G.T. (2005) 'Reduced cerebrospinal fluid production and intracranial pressure in mice lacking choroid plexus water channel Aquaporin-1', *The FASEB journal*, 19(1), pp. 76-78.

- Pang, Y., Malyarenko, D.I., Wilmes, L.J., Devaraj, A., Tan, E.T., Marinelli, L., Endt, A. vom, Peeters, J., Jacobs, M.A. & Newitt, D.C. (2022) 'Long-term stability of gradient characteristics warrants model-based correction of diffusion weighting bias', *Tomography*, 8(1), .
- Papadopoulos, M.C., Manley, G.T., Krishna, S. & Verkman, A.S. (2004) 'Aquaporin-4 facilitates reabsorption of excess fluid in vasogenic brain edema', *The FASEB journal*, 18(11), pp. 1291-1293.
- Papadopoulos, M.C. & Verkman, A.S. (2013) 'Aquaporin water channels in the nervous system', *Nature Reviews Neuroscience*, 14(4), pp. 265-277.
- Papadopoulos, M.C. & Verkman, A.S. (2007) 'Aquaporin-4 and brain edema', *Pediatric nephrology*, 22(6), pp. 778-784.
- Papadopoulos, M.C. & Verkman, A.S. (2005) 'Aquaporin-4 gene disruption in mice reduces brain swelling and mortality in pneumococcal meningitis', *Journal of Biological Chemistry*, 280(14), pp. 13906-13912.
- Papaiconomou, C., Bozanovic-Sosic, R., Zakharov, A. & Johnston, M. (2002) 'Does neonatal cerebrospinal fluid absorption occur via arachnoid projections or extracranial lymphatics?', *American Journal of Physiology-Regulatory, Integrative and Comparative Physiology*, 283(4), pp. R869-R876.
- Pardridge, W.M. (2016) 'CSF, blood-brain barrier, and brain drug delivery', *Expert opinion on drug delivery*, 13(7), pp. 963-975.
- Patel, M., Atyani, A., Salameh, J.-P., McInnes, M. & Chakraborty, S. (2020) 'Safety of intrathecal administration of gadolinium-based contrast agents: a systematic review and meta-analysis', *Radiology*, 297(1), pp. 75-83.
- Patterson, B.W., Elbert, D.L., Mawuenyega, K.G., Kasten, T., Ovod, V., Ma, S., Xiong, C., Chott, R., Yarasheski, K. & Sigurdson, W. (2015) 'Age and amyloid effects on human central nervous system amyloid-beta kinetics', *Annals of neurology*, 78(3), pp. 439-453.
- Pedersen, T.J., Keil, S.A., Han, W., Wang, M.X. & Iliff, J.J. (2023) 'The effect of aquaporin-4 mis-localization on A β deposition in mice', *Neurobiology of Disease*, 181.
- Peng, C., Gathagan, R.J., Covell, D.J., Medellin, C., Stieber, A., Robinson, J.L., Zhang, B., Pitkin, R.M., Olufemi, M.F. & Luk, K.C. (2018) 'Cellular milieu imparts distinct pathological α -synuclein strains in α -synucleinopathies', *Nature*, 557(7706), pp. 558-563.
- Peng, W., Achariyar, T.M., Li, B., Liao, Y., Mestre, H., Hitomi, E., Regan, S., Kasper, T., Peng, S., Ding, F., Benveniste, H., Nedergaard, M. & Deane, R. (2016) 'Suppression of glymphatic fluid transport in a mouse model of Alzheimer's disease.', *Neurobiology of disease*, 93pp. 215-225.
- Peng, W., Yuan, Y., Lei, J., Zhao, Y., Li, Y., Qu, Q. & Wang, J. (2025) 'Long-Term High-Fat Diet Impairs AQP4-Mediated Glymphatic Clearance of Amyloid Beta', *Molecular Neurobiology*, 62(1), pp. 1079-1093.
- Piegras, A., Elste, V., Frietsch, T., Schmiedek, P., Reith, W. & Schilling, L. (2001) 'Effect of moderate hypothermia on experimental severe subarachnoid hemorrhage, as evaluated by apparent diffusion coefficient changes', *Neurosurgery*, 48(5), pp. 1128-1135.
- Pirici, I., Balsanu, T.A., Bogdan, C., Margaritescu, C., Divan, T., Vitalie, V., Mogoanta, L., Pirici, D., Carare, R.O. & Muresanu, D.F. (2017) 'Inhibition of aquaporin-4 improves the outcome of ischaemic stroke and modulates brain paravascular drainage pathways', *International journal of molecular sciences*, 19(1), p. 46.
- Pittock, S.J. & Lucchinetti, C.F. (2016) 'Neuromyelitis optica and the evolving spectrum of autoimmune aquaporin-4 channelopathies: a decade later', *Annals of the new York Academy of Sciences*, 1366(1), pp. 20-39.

- Plog, B.A., Dashnaw, M.L., Hitomi, E., Peng, W., Liao, Y., Lou, N., Deane, R. & Nedergaard, M. (2015) 'Biomarkers of traumatic injury are transported from brain to blood via the glymphatic system', *Journal of Neuroscience*, 35(2), pp. 518-526.
- Plog, B.A. & Nedergaard, M. (2018) 'The Glymphatic System in Central Nervous System Health and Disease: Past, Present, and Future', *Annual Review of Pathology: Mechanisms of Disease*, 13pp. 379-394.
- Pollay, M. (2010) 'The function and structure of the cerebrospinal fluid outflow system', *Cerebrospinal fluid research*, 7pp. 1-20.
- Pomilio, C., Pavia, P., Gorjod, R.M., Vinuesa, A., Alaimo, A., Galvan, V., Kotler, M.L., Beauquis, J. & Saravia, F. (2016) 'Glial alterations from early to late stages in a model of Alzheimer's disease: Evidence of autophagy involvement in A β internalization', *Hippocampus*, 26(2), pp. 194-210.
- Popescu, E.S., Pirici, I., Ciurea, R.N., Balseanu, T.-A., Catalin, B., Margaritescu, C., Mogoanta, L., Hostiuc, S. & Pirici, D. (2017) 'Three-dimensional organ scanning reveals brain edema reduction in a rat model of stroke treated with an aquaporin 4 inhibitor', *Rom. J. Morphol. Embryol*, 58pp. 59-66.
- Potokar, M., Jorgačevski, J. & Zorec, R. (2016) 'Astrocyte aquaporin dynamics in health and disease', *International journal of molecular sciences*, 17(7), p. 1121.
- Preston, G.M. & Agre, P. (1991) 'Isolation of the cDNA for erythrocyte integral membrane protein of 28 kilodaltons: member of an ancient channel family', *Proceedings of the National Academy of Sciences*, 88(24), pp. 11110-11114.
- Preston, G.M., Carroll, T.P., Guggino, W.B. & Agre, P. (1992) 'Appearance of water channels in *Xenopus* oocytes expressing red cell CHIP28 protein', *Science*, 256(5055), pp. 385-387.
- Proulx, S.T. (2021) 'Cerebrospinal fluid outflow: a review of the historical and contemporary evidence for arachnoid villi, perineural routes, and dural lymphatics', *Cellular and Molecular Life Sciences*, 78(6), pp. 2429-2457.
- Provenzano, D.A., Pellis, Z. & DeRiggi, L. (2019) 'Fatal gadolinium-induced encephalopathy following accidental intrathecal administration: a case report and a comprehensive evidence-based review', *Regional Anesthesia & Pain Medicine*, 44(7), pp. 721-729.
- Purdon, P.L., Sampson, A., Pavone, K.J. & Brown, E.N. (2015) 'Clinical electroencephalography for anesthesiologists: part I: background and basic signatures', *Anesthesiology*, 123(4), pp. 937-960.
- Puwarawuttipanit, W., Bragg, A.D., Frydenlund, D.S., Mylonakou, M.-N., Nagelhus, E.A., Peters, M.F., Kotchabhakdi, N., Adams, M.E., Froehner, S.C. & Haug, F.-M. (2006) 'Differential effect of α -syntrophin knockout on aquaporin-4 and Kir4.1 expression in retinal macroglial cells in mice', *Neuroscience*, 137(1), pp. 165-175.
- Raghunandan, A., Ladron-de-Guevara, A., Tithof, J., Mestre, H., Du, T., Nedergaard, M., Thomas, J.H. & Kelley, D.H. (2021) 'Bulk flow of cerebrospinal fluid observed in periarterial spaces is not an artifact of injection', *Elife*, 10p. e65958.
- Ramirez, J., Berberian, S.A., Breen, D.P., Gao, F., Ozzoude, M., Adamo, S., Scott, C.J.M., Berezuk, C., Yhap, V. & Mestre, T.A. (2022) 'Small and Large Magnetic Resonance Imaging-Visible Perivascular Spaces in the Basal Ganglia of Parkinson's Disease Patients', *Movement Disorders*, 37(6), pp. 1304-1309.
- Ramirez, J., Berezuk, C., McNeely, A.A., Scott, C.J.M., Gao, F. & Black, S.E. (2015) 'Visible Virchow-Robin spaces on magnetic resonance imaging of Alzheimer's disease patients and normal elderly from the Sunnybrook Dementia Study', *Journal of Alzheimer's Disease*, 43(2), pp. 415-424.

- Rash, J.E., Yasumura, T., Hudson, C.S., Agre, P. & Nielsen, S. (1998) 'Direct immunogold labeling of aquaporin-4 in square arrays of astrocyte and ependymocyte plasma membranes in rat brain and spinal cord', *Proceedings of the National Academy of Sciences*, 95(20), pp. 11981-11986.
- Rasmussen, M.K., Mestre, H. & Nedergaard, M. (2018) 'The glymphatic pathway in neurological disorders', *The Lancet Neurology*, 17(11), pp. 1016-1024.
- Rechtschaffen, A., Gilliland, M.A., Bergmann, B.M. & Winter, J.B. (1983) 'Physiological correlates of prolonged sleep deprivation in rats', *Science*, 221(4606), pp. 182-184.
- Reddy, O.C. & van der Werf, Y.D. (2020) 'The sleeping brain: Harnessing the power of the glymphatic system through lifestyle choices'. *Brain Sciences* 10 (11) p.pp. 1-16.
- Ren, H., Luo, C., Feng, Y., Yao, X., Shi, Z., Liang, F., Kang, J.X., Wan, J., Pei, Z. & Su, H. (2017) 'Omega-3 polyunsaturated fatty acids promote amyloid- β clearance from the brain through mediating the function of the glymphatic system', *The FASEB Journal*, 31(1), pp. 282-293.
- Rennels, M.L., Gregory, T.F., Blaumanis, O.R., Fujimoto, K. & Grady, P.A. (1985) 'Evidence for a "Paravascular" fluid circulation in the mammalian central nervous system, provided by the rapid distribution of tracer protein throughout the brain from the subarachnoid space', *Brain Research*, 326(1), pp. 47-63.
- Rey, J. & Sarntinoranont, M. (2018) 'Pulsatile flow drivers in brain parenchyma and perivascular spaces: a resistance network model study', *Fluids and Barriers of the CNS*, 15(1), pp. 1-11.
- Ries, M. & Sastre, M. (2016) 'Mechanisms of A β clearance and degradation by glial cells', *Frontiers in aging neuroscience*, 8p. 160.
- Ringstad, G., Valnes, L.M., Dale, A.M., Pripp, A.H., Vatnehol, S.-A.S., Emblem, K.E., Mardal, K.-A. & Eide, P.K. (2018) 'Brain-wide glymphatic enhancement and clearance in humans assessed with MRI', *JCI insight*, 3(13), .
- Ringstad, G., Vatnehol, S.A.S. & Eide, P.K. (2017) 'Glymphatic MRI in idiopathic normal pressure hydrocephalus', *Brain*, 140(10), pp. 2691-2705.
- Robbins, R., Quan, S.F., Weaver, M.D., Bormes, G., Barger, L.K. & Czeisler, C.A. (2021) 'Examining sleep deficiency and disturbance and their risk for incident dementia and all-cause mortality in older adults across 5 years in the United States', *Aging (Albany NY)*, 13(3), p. 3254.
- Robin, C. (1859) 'Recherches sur quelques particularites de la structure des capillaires de l'encephale', *J Physiol Homme Animaux*, 2p. 537.
- Rogers, B.P., Blaber, J., Welch, E.B., Ding, Z., Anderson, A.W. & Landman, B.A. (2017) 'Stability of gradient field corrections for quantitative diffusion MRI', in *Medical imaging 2017: physics of medical imaging*. [Online]. 2017 SPIE. pp. 1272-1278.
- Rosu, G.C., Catalin, B., Balseanu, T.A., Laurentiu, M., Claudiu, M., Kumar-Singh, S. & Daniel, P. (2020) 'Inhibition of Aquaporin 4 Decreases Amyloid A β 40 Drainage Around Cerebral Vessels', *Molecular Neurobiology*, 57(11), pp. 4720-4734.
- Saadoun, S., Bell, B.A., Verkman, A.S. & Papadopoulos, M.C. (2008) 'Greatly improved neurological outcome after spinal cord compression injury in AQP4-deficient mice', *Brain*, 131(4), pp. 1087-1098.
- Saadoun, S. & Papadopoulos, M.C. (2010) 'Aquaporin-4 in brain and spinal cord oedema', *Neuroscience*, 168(4), pp. 1036-1046.
- Sales, C.P., Carvalho, H. de A., Taverna, K.C., Pastorello, B.F., Rubo, R.A., Borgonovi, A.F., Stuart, S.R. & Rodrigues, L.N. (2016) 'Avaliação do uso de diferentes agentes de contraste em ressonância magnética como fontes

- falsas em planejamentos de braquiterapia guiados por imagem', *Radiologia Brasileira*, 49(3), pp. 165-169.
- Salman, M.M., Kitchen, P., Halsey, A., Wang, M.X., Törnroth-Horsefield, S., Conner, A.C., Badaut, J., Iliff, J.J. & Bill, R.M. (2022) *Emerging roles for dynamic aquaporin-4 subcellular relocalization in CNS water homeostasis*.
- Salvadores, N., Searcy, J.L., Holland, P.R. & Horsburgh, K. (2017) 'Chronic cerebral hypoperfusion alters amyloid- β peptide pools leading to cerebral amyloid angiopathy, microinfarcts and haemorrhages in Tg-SwDI mice', *Clinical science*, 131(16), pp. 2109-2123.
- Samadi, M., Moradi, S., Moradinazar, M., Mostafai, R. & Pasdar, Y. (2019) 'Dietary pattern in relation to the risk of Alzheimer's disease: a systematic review', *Neurological Sciences*, 40pp. 2031-2043.
- Sapkota, D., Florian, C., Doherty, B.M., White, K.M., Reardon, K.M., Ge, X., Garbow, J.R., Yuede, C.M., Cirrito, J.R. & Dougherty, J.D. (2022) 'Aqp4 stop codon readthrough facilitates amyloid- β clearance from the brain', *Brain*, 145(9), pp. 2982-2990.
- Sarti, C., Pantoni, L., Bartolini, L. & Inzitari, D. (2002) 'Cognitive impairment and chronic cerebral hypoperfusion: what can be learned from experimental models', *Journal of the neurological sciences*, 203pp. 263-266.
- Scarmeas, N., Luchsinger, J.A., Schupf, N., Brickman, A.M., Cosentino, S., Tang, M.X. & Stern, Y. (2009) 'Physical activity, diet, and risk of Alzheimer disease', *Jama*, 302(6), pp. 627-637.
- Schmid-Schonbein, G.W. (1990) 'Microlymphatics and lymph flow', *Physiological reviews*, 70(4), pp. 987-1028.
- Schubert, J.J., Veronese, M., Marchitelli, L., Bodini, B., Tonietto, M., Stankoff, B., Brooks, D.J., Bertoldo, A., Edison, P. & Turkheimer, F.E. (2019) 'Dynamic 11C-PIB PET shows cerebrospinal fluid flow alterations in Alzheimer disease and multiple sclerosis', *Journal of Nuclear Medicine*, 60(10), pp. 1452-1460.
- Sepehrband, F., Cabeen, R.P., Choupan, J., Barisano, G., Law, M., Toga, A.W. & Initiative, A.D.N. (2019) 'Perivascular space fluid contributes to diffusion tensor imaging changes in white matter', *Neuroimage*, 197pp. 243-254.
- Sevigny, J., Chiao, P., Bussière, T., Weinreb, P.H., Williams, L., Maier, M., Dunstan, R., Salloway, S., Chen, T. & Ling, Y. (2017) 'Addendum: The antibody aducanumab reduces A β plaques in Alzheimer's disease', *Nature*, 546(7659), p. 564.
- Shaw, P.J., Tononi, G., Greenspan, R.J. & Robinson, D.F. (2002) 'Stress response genes protect against lethal effects of sleep deprivation in *Drosophila*', *Nature*, 417(6886), pp. 287-291.
- Shen, T., Yue, Y., Ba, F., He, T., Tang, X., Hu, X., Pu, J., Huang, C., Lv, W. & Zhang, B. (2022) 'Diffusion along perivascular spaces as marker for impairment of glymphatic system in Parkinson's disease', *NPJ Parkinson's disease*, 8(1), p. 174.
- Shen, T., Yue, Y., Zhao, S., Xie, J., Chen, Y., Tian, J., Lv, W., Lo, C.-Y.Z., Hsu, Y.-C. & Kober, T. (2021) 'The role of brain perivascular space burden in early-stage Parkinson's disease', *NPJ Parkinson's disease*, 7(1), p. 12.
- Shibata, M., Ohtani, R., Ihara, M. & Tomimoto, H. (2004) 'White matter lesions and glial activation in a novel mouse model of chronic cerebral hypoperfusion', *Stroke*, 35(11), pp. 2598-2603.
- Shibata, M., Yamada, S., Kumar, S.R., Calero, M., Bading, J., Frangione, B., Holtzman, D.M., Miller, C.A., Strickland, D.K. & Ghiso, J. (2000) 'Clearance of Alzheimer's amyloid- β 1-40 peptide from brain by LDL receptor-related

- protein-1 at the blood-brain barrier', *The Journal of clinical investigation*, 106(12), pp. 1489-1499.
- Shimada, T., Shindo, A., Matsuyama, H., Yata, K., Niwa, A., Sasaki, R., Ayaki, T., Maki, T., Wakita, H. & Tomimoto, H. (2019) 'Chronic cerebral hypoperfusion upregulates leptin receptor expression in astrocytes and tau phosphorylation in tau transgenic mice', *Neuroscience letters*, 704pp. 133-140.
- Shokri-Kojori, E., Wang, G.-J., Wiers, C.E., Demiral, S.B., Guo, M., Kim, S.W., Lindgren, E., Ramirez, V., Zehra, A. & Freeman, C. (2018) 'β-Amyloid accumulation in the human brain after one night of sleep deprivation', *Proceedings of the National Academy of Sciences*, 115(17), pp. 4483-4488.
- Si, X., Guo, T., Wang, Z., Fang, Y., Gu, L., Cao, L., Yang, W., Gao, T., Song, Z. & Tian, J. (2022) 'Neuroimaging evidence of glymphatic system dysfunction in possible REM sleep behavior disorder and Parkinson's disease', *npj Parkinson's Disease*, 8(1), p. 54.
- Silva, I., Silva, J., Ferreira, R. & Trigo, D. (2021) 'Glymphatic system, AQP4, and their implications in Alzheimer's disease', *Neurological research and practice*, 3pp. 1-9.
- Simka, M., Czaja, J. & Kowalczyk, D. (2019) 'Collapsibility of the internal jugular veins in the lateral decubitus body position: a potential protective role of the cerebral venous outflow against neurodegeneration', *Medical Hypotheses*, 133p. 109397.
- Skucas, V.A., Mathews, I.B., Yang, J., Cheng, Q., Treister, A., Duffy, A.M., Verkman, A.S., Hempstead, B.L., Wood, M.A. & Binder, D.K. (2011) 'Impairment of select forms of spatial memory and neurotrophin-dependent synaptic plasticity by deletion of glial aquaporin-4', *Journal of Neuroscience*, 31(17), pp. 6392-6397.
- Smets, N.G., Strijkers, G.J., Vinje, V. & Bakker, E.N.T.P. (2023) 'Cerebrospinal fluid turnover as a driver of brain clearance', *NMR in Biomedicine*,
- Smith, A.J., Jin, B.-J., Ratelade, J. & Verkman, A.S. (2014) 'Aggregation state determines the localization and function of M1-and M23-aquaporin-4 in astrocytes', *Journal of Cell Biology*, 204(4), pp. 559-573.
- Smith, A.J. & Verkman, A.S. (2019) 'Going against the flow: Interstitial solute transport in brain is diffusive and aquaporin-4 independent', *The Journal of physiology*, 597(17), p. 4421.
- Smith, A.J. & Verkman, A.S. (2018) 'The "glymphatic" mechanism for solute clearance in Alzheimer's disease: game changer or unproven speculation?', *The FASEB Journal*, 32(2), p. 543.
- Smith, A.J., Yao, X., Dix, J.A., Jin, B.-J. & Verkman, A.S. (2017) 'Test of the "glymphatic" hypothesis demonstrates diffusive and aquaporin-4-independent solute transport in rodent brain parenchyma.', *eLife*, 6.
- Solenov, E., Watanabe, H., Manley, G.T. & Verkman, A.S. (2004) 'Sevenfold-reduced osmotic water permeability in primary astrocyte cultures from AQP-4-deficient mice, measured by a fluorescence quenching method', *American Journal of Physiology-Cell Physiology*, 286(2), pp. C426-C432.
- Song, H., Ruan, Z., Gao, L., Lv, D., Sun, D., Li, Z., Zhang, R., Zhou, X., Xu, H. & Zhang, J. (2022) 'Structural network efficiency mediates the association between glymphatic function and cognition in mild VCI: a DTI-ALPS study', *Frontiers in Aging Neuroscience*, 14p. 974114.
- Spector, R., Robert Snodgrass, S. & Johanson, C.E. (2015) 'A balanced view of the cerebrospinal fluid composition and functions: Focus on adult humans.', *Experimental neurology*, 273pp. 57-68.

- Stejskal, E.O. & Tanner, J.E. (1965) 'Spin diffusion measurements: Spin echoes in the presence of a time-dependent field gradient', *The Journal of Chemical Physics*, 42(1), pp. 288-292.
- Steward, C., Venkatraman, V., Lui, E., Malpas, C., Ellis, K., O'Brien, T., Lautenschlager, N. & Desmond, P. (2019) 'Reproducibility of the diffusion of the perivascular space in older adults with dementia', in *Proc 27th Annual Meeting ISMRM, Montreal*. [Online]. 2019 p. 3425.
- Stuckenschneider, T., Askew, C.D., Rüdiger, S., Polidori, M.C., Abeln, V., Vogt, T., Krome, A., Olde Rikkert, M., Lawlor, B. & Schneider, S. (2018) 'Cardiorespiratory fitness and cognitive function are positively related among participants with mild and subjective cognitive impairment', *Journal of Alzheimer's Disease*, 62(4), pp. 1865-1875.
- Sun, B.-L., Wang, L., Yang, T., Sun, J., Mao, L., Yang, M., Yuan, H., Colvin, R.A. & Yang, X. (2018) 'Lymphatic drainage system of the brain: a novel target for intervention of neurological diseases', *Progress in neurobiology*, 163pp. 118-143.
- Sun, C., Lin, L., Yin, L., Hao, X., Tian, J., Zhang, X., Ren, Y., Li, C. & Yang, Y. (2022) 'Acutely Inhibiting AQP4 With TGN-020 Improves Functional Outcome by Attenuating Edema and Peri-Infarct Astroglia After Cerebral Ischemia', *Frontiers in Immunology*, 13(May), pp. 1-10.
- Sun, H., Liang, R., Yang, B., Zhou, Y., Liu, M., Fang, F., Ding, J., Fan, Y. & Hu, G. (2016) 'Aquaporin-4 mediates communication between astrocyte and microglia: Implications of neuroinflammation in experimental Parkinson's disease', *Neuroscience*, 317pp. 65-75.
- Sundaram, S., Hughes, R.L., Peterson, E., Müller-Oehring, E.M., Brontë-Stewart, H.M., Poston, K.L., Faerman, A., Bhowmick, C. & Schulte, T. (2019) 'Establishing a framework for neuropathological correlates and glymphatic system functioning in Parkinson's disease', *Neuroscience & Biobehavioral Reviews*, 103pp. 305-315.
- Syková, E. & Nicholson, C. (2008) 'Diffusion in brain extracellular space', *Physiological reviews*, 88(4), pp. 1277-1340.
- T O'Brien, J. & Thomas, A. (2015) 'Vascular dementia', *The Lancet*, 386(10004), pp. 1698-1706.
- Taylor, D.R., Roy, A., Regatte, R.R., Charagundla, S.R., McLaughlin, A.C., Leigh, J.S. & Reddy, R. (2003) 'Indirect 17(O)-magnetic resonance imaging of cerebral blood flow in the rat.', *Magnetic resonance in medicine*, 49(3), pp. 479-487.
- Tait, M.J., Saadoun, S., Bell, B.A., Verkman, A.S. & Papadopoulos, M.C. (2010) 'Increased brain edema in aqp4-null mice in an experimental model of subarachnoid hemorrhage', *Neuroscience*, 167(1), pp. 60-67.
- Tan, Y., Zhang, H., Zhang, C., Chen, W., Peng, T., Liu, Z., Wang, X., Zhang, P., Jin, L.L. & Hua, Q. (2023) 'Scalp mechanical stimulation alleviates cerebral hypoperfusion in rats with 2-VO by controlling cerebral edema', *Journal of Traditional Chinese Medical Sciences*,
- Tang, G. & Yang, G.-Y. (2016) 'Aquaporin-4: A potential therapeutic target for cerebral edema', *International journal of molecular sciences*, 17(10), p. 1413.
- Tang, H., Gao, Y., Zhang, Q., Nie, K., Zhu, R., Gao, L., Feng, S., Wang, L., Zhao, J. & Huang, Z. (2017) 'Chronic cerebral hypoperfusion independently exacerbates cognitive impairment within the pathopoiesis of Parkinson's disease via microvascular pathologies', *Behavioural Brain Research*, 333pp. 286-294.

- Tang, Y., Wu, P., Su, J., Xiang, J., Cai, D. & Dong, Q. (2010) 'Effects of Aquaporin-4 on edema formation following intracerebral hemorrhage', *Experimental neurology*, 223(2), pp. 485-495.
- Taoka, T., Ito, R., Nakamichi, R., Kamagata, K., Sakai, M., Kawai, H., Nakane, T., Abe, T., Ichikawa, K. & Kikuta, J. (2022) 'Reproducibility of diffusion tensor image analysis along the perivascular space (DTI-ALPS) for evaluating interstitial fluid diffusivity and glymphatic function: Changes in Alps index on Multiple condition acquisition experiment (CHAMONIX) study', *Japanese journal of radiology*, 40(2), pp. 147-158.
- Taoka, T., Jost, G., Frenzel, T., Naganawa, S. & Pietsch, H. (2018) 'Impact of the Glymphatic System on the Kinetic and Distribution of Gadodiamide in the Rat Brain: Observations by Dynamic MRI and Effect of Circadian Rhythm on Tissue Gadolinium Concentrations.', *Investigative radiology*, 53(9), pp. 529-534.
- Taoka, T., Masutani, Y., Kawai, H., Nakane, T., Matsuoka, K., Yasuno, F., Kishimoto, T. & Naganawa, S. (2017) 'Evaluation of glymphatic system activity with the diffusion MR technique: diffusion tensor image analysis along the perivascular space (DTI-ALPS) in Alzheimer's disease cases', *Japanese journal of radiology*, 35pp. 172-178.
- Taoka, T. & Naganawa, S. (2018) 'Gadolinium-based Contrast Media, Cerebrospinal Fluid and the Glymphatic System: Possible Mechanisms for the Deposition of Gadolinium in the Brain', *Magnetic resonance in medical sciences: MRMS: an official journal of Japan Society of Magnetic Resonance in Medicine*, 17(2), pp. 111-119.
- Taoka, T. & Naganawa, S. (2020) 'Glymphatic imaging using MRI', *Journal of Magnetic Resonance Imaging*, 51(1), pp. 11-24.
- Taoka, T. & Naganawa, S. (2021) 'Imaging for central nervous system (CNS) interstitial fluidopathy: disorders with impaired interstitial fluid dynamics'. *Japanese Journal of Radiology* 39 (1).
- Teng, Z., Wang, A., Wang, P., Wang, R., Wang, W. & Han, H. (2018) 'The effect of aquaporin-4 knockout on interstitial fluid flow and the structure of the extracellular space in the deep brain', *Aging and Disease*, 9(5), pp. 808-816.
- Thangavel, K. & Saritaş, E.Ü. (2017) 'Aqueous paramagnetic solutions for MRI phantoms at 3 T: A detailed study on relaxivities', *Turkish Journal of Electrical Engineering and Computer Sciences*, 25(3), pp. 2108-2121.
- Theologou, M., Natsis, K., Kouskouras, K., Chatzinikolaou, F., Varoutis, P., Skoulios, N., Tsitouras, V. & Tsonidis, C. (2022) 'Cerebrospinal fluid homeostasis and hydrodynamics: A review of facts and theories', *European Neurology*, 85(4), pp. 313-325.
- Thorne, R.G. & Nicholson, C. (2006) 'In vivo diffusion analysis with quantum dots and dextrans predicts the width of brain extracellular space', *Proceedings of the National Academy of Sciences*, 103(14), pp. 5567-5572.
- Thrane, A.S., Rappold, P.M., Fujita, T., Torres, A., Bekar, L.K., Takano, T., Peng, W., Wang, F., Thrane, V.R., Enger, R., Haj-Yasein, N.N., Skare, Ø., Holen, T., Klungland, A., Ottersen, O.P., Nedergaard, M. & Nagelhus, E.A. (2011) 'Critical role of aquaporin-4 (AQP4) in astrocytic Ca²⁺ signaling events elicited by cerebral edema', *Proceedings of the National Academy of Sciences of the United States of America*, 108(2), pp. 846-851.
- Thrane, V.R., Thrane, A.S., Plog, B.A., Thiyagarajan, M., Iff, J.J., Deane, R., Nagelhus, E.A. & Nedergaard, M. (2013) 'Paravascular microcirculation facilitates rapid lipid transport and astrocyte signaling in the brain', *Scientific reports*, 3(1), p. 2582.

- Tourdias, T., Dragonu, I., Fushimi, Y., Deloire, M.S.A., Boiziau, C., Brochet, B., Moonen, C., Petry, K.G. & Dousset, V. (2009) 'Aquaporin 4 correlates with apparent diffusion coefficient and hydrocephalus severity in the rat brain: A combined MRI-histological study', *NeuroImage*, 47(2), pp. 659-666.
- Tradtrantip, L., Jin, B.-J., Yao, X., Anderson, M.O. & Verkman, A.S. (2017) 'Aquaporin-targeted therapeutics: state-of-the-field', *Aquaporins*, pp. 239-250.
- Trillo-Contreras, J.L., Ramírez-Lorca, R., Villadiego, J. & Echevarría, M. (2022) 'Cellular distribution of brain aquaporins and their contribution to cerebrospinal fluid homeostasis and hydrocephalus', *Biomolecules*, 12(4), p. 530.
- Turner, L. (1958) 'The structure and relationships of arachnoid granulations', in *Ciba Foundation Symposium-The Cerebrospinal Fluid: Production, Circulation and Absorption*. [Online]. 1958 Wiley Online Library. pp. 32-54.
- Ueno, M., Chiba, Y., Murakami, R., Matsumoto, K., Kawachi, M. & Fujihara, R. (2016) 'Blood-brain barrier and blood-cerebrospinal fluid barrier in normal and pathological conditions', *Brain tumor pathology*, 33pp. 89-96.
- Ulmer, J.L., Mathews, V.P., Hamilton, C.A., Elster, A.D. & Moran, P.R. (1996) 'Magnetization transfer or spin-lock? An investigation of off-resonance saturation pulse imaging with varying frequency offsets.', *American journal of neuroradiology*, 17(5), pp. 805-819.
- Vandebroek, A. & Yasui, M. (2020) 'Regulation of AQP4 in the central nervous system', *International Journal of Molecular Sciences*, 21(5), pp. 17-19.
- van Veluw, S.J., Hou, S.S., Calvo-Rodriguez, M., Arbel-Ornath, M., Snyder, A.C., Frosch, M.P., Greenberg, S.M. & Bacskai, B.J. (2020) 'Vasomotion as a driving force for paravascular clearance in the awake mouse brain', *Neuron*, 105(3), pp. 549-561.
- Venkat, P., Chopp, M., Zacharek, A., Cui, C., Zhang, L., Li, Q., Lu, M., Zhang, T., Liu, A. & Chen, J. (2017) 'White matter damage and glymphatic dysfunction in a model of vascular dementia in rats with no prior vascular pathologies', *Neurobiology of aging*, 50pp. 96-106.
- Vergheze, J.P., Terry, A., de Natale, E.R. & Politis, M. (2022) 'Research Evidence of the Role of the Glymphatic System and Its Potential Pharmacological Modulation in Neurodegenerative Diseases', *Journal of Clinical Medicine*, 11(23), p. 6964.
- Verkman, A.S. (2012) 'Aquaporins in clinical medicine', *Annual review of medicine*, 63pp. 303-316.
- Verkman, A.S. (2013) 'Diffusion in the extracellular space in brain and tumors.', *Physical biology*, 10(4), p. 45003.
- Verkman, A.S., Anderson, M.O. & Papadopoulos, M.C. (2014) 'Aquaporins: important but elusive drug targets', *Nature reviews Drug discovery*, 13(4), pp. 259-277.
- Verkman, A.S., Smith, A.J., Phuan, P., Tradtrantip, L. & Anderson, M.O. (2017) 'The aquaporin-4 water channel as a potential drug target in neurological disorders', *Expert opinion on therapeutic targets*, 21(12), pp. 1161-1170.
- Vilor-Tejedor, N., Ciampa, I., Operto, G., Falcón, C., Suárez-Calvet, M., Crous-Bou, M., Shekari, M., Arenaza-Urquijo, E.M., Milà-Alomà, M. & Grau-Rivera, O. (2021) 'Perivascular spaces are associated with tau pathophysiology and synaptic dysfunction in early Alzheimer's continuum', *Alzheimer's research & therapy*, 13(1), pp. 1-13.
- Vindedal, G.F., Thoren, A.E., Jensen, V., Klungland, A., Zhang, Y., Holtzman, M.J., Ottersen, O.P. & Nagelhus, E.A. (2016) 'Removal of aquaporin-4 from

- glial and ependymal membranes causes brain water accumulation', *Molecular and Cellular Neuroscience*, 77pp. 47-52.
- Vinje, V., Eklund, A., Mardal, K.-A., Rognes, M.E. & Støverud, K.-H. (2020) 'Intracranial pressure elevation alters CSF clearance pathways', *Fluids and Barriers of the CNS*, 17pp. 1-19.
- Virchow, R. (1851) 'Ueber die Erweiterung kleinerer Gefäße', *Virchows Archiv*, 3(3), pp. 427-462.
- Visanji, N.P., Lang, A.E. & Munoz, D.G. (2018) 'Lymphatic vasculature in human dural superior sagittal sinus: implications for neurodegenerative proteinopathies', *Neuroscience Letters*, 665pp. 18-21.
- Wakita, H., Tomimoto, H., Akiguchi, I. & Kimura, J. (1994) 'Glial activation and white matter changes in the rat brain induced by chronic cerebral hypoperfusion: an immunohistochemical study', *Acta neuropathologica*, 87pp. 484-492.
- Wallin, A. & Blennow, K. (1993) 'Heterogeneity of vascular dementia: mechanisms and subgroups', *Journal of geriatric psychiatry and neurology*, 6(3), pp. 177-188.
- Walter, B.A., Valera, V.A., Takahashi, S. & Ushiki, T. (2006) 'The olfactory route for cerebrospinal fluid drainage into the peripheral lymphatic system', *Neuropathology and applied neurobiology*, 32(4), pp. 388-396.
- Walz, T., Smith, B.L., Zeidel, M.L., Engel, A. & Agre, P. (1994) 'Biologically active two-dimensional crystals of aquaporin CHIP.', *Journal of Biological Chemistry*, 269(3), pp. 1583-1586.
- Wang, Jianping, Fu, X., Jiang, C., Yu, L., Wang, M., Han, W., Liu, L. & Wang, Jian (2014) 'Bone marrow mononuclear cell transplantation promotes therapeutic angiogenesis via upregulation of the VEGF-VEGFR2 signaling pathway in a rat model of vascular dementia', *Behavioural brain research*, 265pp. 171-180.
- Wang, M., Iliff, J.J., Liao, Y., Chen, M.J., Shinseki, M.S., Venkataraman, A., Cheung, J., Wang, W. & Nedergaard, M. (2012) 'Cognitive deficits and delayed neuronal loss in a mouse model of multiple microinfarcts', *Journal of Neuroscience*, 32(50), pp. 17948-17960.
- Wang, M.-L., Yu, M.-M., Wei, X.-E., Li, W.-B., Li, Y.-H. & Initiative, A.D.N. (2021) 'Association of enlarged perivascular spaces with AB and tau deposition in cognitively normal older population', *Neurobiology of Aging*, 100pp. 32-38.
- Weed, L.H. (1914) 'Studies on Cerebro-Spinal Fluid. No. III: The pathways of escape from the Subarachnoid Spaces with particular reference to the Arachnoid Villi', *The Journal of medical research*, 31(1), p. 51.
- Weishaupt, D., Köchli, V.D. & Marinček, B. (2003) *How does MRI work?*
- Welch, K. & FRIEDMAN, V. (1960) 'The cerebrospinal fluid valves', *Brain*, 83(3), pp. 454-469.
- Welch, K. & Pollay, M. (1961) 'Perfusion of particles through arachnoid villi of the monkey', *American Journal of Physiology-Legacy Content*, 201(4), pp. 651-654.
- Westbrook, C. & Talbot, J. (2018) *MRI in Practice*. John Wiley & Sons.
- Whittall, K.P., MacKay, A.L., Graeb, D.A., Nugent, R.A., Li, D.K.B. & Paty, D.W. (1997) 'In vivo measurement of T2 distributions and water contents in normal human brain', *Magnetic Resonance in Medicine*, 37(1), pp. 34-43.
- Winer, J.R., Mander, B.A., Helfrich, R.F., Maass, A., Harrison, T.M., Baker, S.L., Knight, R.T., Jagust, W.J. & Walker, M.P. (2019) 'Sleep as a Potential Biomarker of Tau and β -Amyloid Burden in the Human Brain', *The Journal of Neuroscience*, 39(32), p. 6315.

- Woollam, D.H.M. & Millen, J.W. (1955) 'The perivascular spaces of the mammalian central nervous system and their relation to the perineuronal and subarachnoid spaces', *Journal of anatomy*, 89(Pt 2), p. 193.
- Wyss-Coray, T., Loike, J.D., Brionne, T.C., Lu, E., Anankov, R., Yan, F., Silverstein, S.C. & Husemann, J. (2003) 'Adult mouse astrocytes degrade amyloid- β in vitro and in situ', *Nature medicine*, 9(4), pp. 453-457.
- Xavier, A.L.R., Hauglund, N.L., von Holstein-Rathlou, S., Li, Q., Sanggaard, S., Lou, N., Lundgaard, I. & Nedergaard, M. (2018) 'Cannula implantation into the cisterna magna of rodents', *Journal of visualized experiments: JoVE*, (135), .
- Xia, M., Yang, L., Sun, G., Qi, S. & Li, B. (2017) 'Mechanism of depression as a risk factor in the development of Alzheimer's disease: the function of AQP4 and the glymphatic system', *Psychopharmacology*, 234(3), pp. 365-379.
- Xie, L., Kang, H., Xu, Q., Chen, M.J., Liao, Y., Thiyagarajan, M., O'Donnell, J., Christensen, D.J., Nicholson, C., Iliff, J.J., Takano, T., Deane, R. & Nedergaard, M. (2013) 'Sleep drives metabolite clearance from the adult brain.', *Science (New York, N.Y.)*, 342(6156), pp. 373-377.
- Xu, K., Zhang, J., Xing, C., Xu, X., Yin, X., Wu, Y., Chen, X. & Chen, Y. (2023) 'Evaluation of glymphatic system activity by diffusion tensor image analysis along the perivascular space in presbycusis', *CNS Neuroscience & Therapeutics*,
- Xu, Z., Xiao, N., Chen, Y., Huang, H., Marshall, C., Gao, J., Cai, Z., Wu, T., Hu, G. & Xiao, M. (2015) 'Deletion of aquaporin-4 in APP/PS1 mice exacerbates brain AB accumulation and memory deficits', *Molecular Neurodegeneration*, 10(1), pp. 1-16.
- Xue, Y., Liu, X., Koundal, S., Constantinou, S., Dai, F., Santambrogio, L., Lee, H. & Benveniste, H. (2020) 'In vivo T1 mapping for quantifying glymphatic system transport and cervical lymph node drainage', *Scientific Reports*, 10(1), p. 14592.
- Yamada, M., Ihara, M., Okamoto, Y., Maki, T., Washida, K., Kitamura, A., Hase, Y., Ito, H., Takao, K. & Miyakawa, T. (2011) 'The influence of chronic cerebral hypoperfusion on cognitive function and amyloid B metabolism in APP overexpressing mice', *PloS one*, 6(1), p. e16567.
- Yamada, S., Miyazaki, M., Yamashita, Y., Ouyang, C., Yui, M., Nakahashi, M., Shimizu, S., Aoki, I., Morohoshi, Y. & McComb, J.G. (2013) 'Influence of respiration on cerebrospinal fluid movement using magnetic resonance spin labeling', *Fluids and Barriers of the CNS*, 10(1), pp. 1-7.
- Yang, G., Deng, N., Liu, Y., Gu, Y. & Yao, X. (2020) 'Evaluation of glymphatic system using diffusion MR technique in T2DM cases', *Frontiers in human neuroscience*, 14p. 300.
- Yang, J., Lunde, L.K., Nuntagij, P., Oguchi, T., Camassa, L., Nilsson, L.N.G., Lannfelt, L., Xu, Y., Amiry-Moghaddam, M. & Ottersen, O.P. (2011) 'Loss of astrocyte polarization in the tg-ArcSwe mouse model of Alzheimer's disease', *Journal of Alzheimer's Disease*, 27(4), pp. 711-722.
- Yang, L., Kress, B.T., Weber, H.J., Thiyagarajan, M., Wang, B., Deane, R., Benveniste, H., Iliff, J.J. & Nedergaard, M. (2013) 'Evaluating glymphatic pathway function utilizing clinically relevant intrathecal infusion of CSF tracer', *Journal of translational medicine*, 11(1), pp. 1-9.
- Yao, X., Derugin, N., Manley, G.T. & Verkman, A.S. (2015) 'Reduced brain edema and infarct volume in aquaporin-4 deficient mice after transient focal cerebral ischemia', *Neuroscience letters*, 584pp. 368-372.
- Yao, X., Uchida, K., Papadopoulos, M.C., Zador, Z., Manley, G.T. & Verkman, A.S. (2015) 'Mildly reduced brain swelling and improved neurological

- outcome in aquaporin-4 knockout mice following controlled cortical impact brain injury', *Journal of neurotrauma*, 32(19), pp. 1458-1464.
- Yasui, M., Hazama, A., Kwon, T.-H., Nielsen, S., Guggino, W.B. & Agre, P. (1999) 'Rapid gating and anion permeability of an intracellular aquaporin', *Nature*, 402(6758), pp. 184-187.
- Yin, M., Pu, T., Wang, L., Marshall, C., Wu, T. & Xiao, M. (2018) 'Astroglial water channel aquaporin 4-mediated glymphatic clearance function: a determined factor for time-sensitive treatment of aerobic exercise in patients with Alzheimer's disease', *Medical Hypotheses*, 119pp. 18-21.
- Yokota, H., Vijayasarathi, A., Cekic, M., Hirata, Y., Linetsky, M., Ho, M., Kim, W. & Salamon, N. (2019) 'Diagnostic performance of glymphatic system evaluation using diffusion tensor imaging in idiopathic normal pressure hydrocephalus and mimickers', *Current Gerontology and Geriatrics Research*, 2019pp. 1-10.
- Yukutake, Y., Hirano, Y., Suematsu, M. & Yasui, M. (2009) 'Rapid and reversible inhibition of aquaporin-4 by zinc', *Biochemistry*, 48(51), pp. 12059-12061.
- Yukutake, Y. & Yasui, M. (2010) 'Regulation of water permeability through aquaporin-4', *Neuroscience*, 168(4), pp. 885-891.
- Zador, Z., Stiver, S., Wang, V. & Manley, G.T. (2009) 'Role of aquaporin-4 in cerebral edema and stroke', *Handbook of experimental pharmacology*, (190), pp. 159-170.
- Zeidel, M.L., Nielsen, S., Smith, B.L., Ambudkar, S. V, Maunsbach, A.B. & Agre, P. (1994) 'Ultrastructure, pharmacologic inhibition, and transport selectivity of aquaporin CHIP in proteoliposomes', *Biochemistry*, 33(6), pp. 1606-1615.
- Zeppenfeld, D.M., Simon, M., Haswell, J.D., D'Abreo, D., Murchison, C., Quinn, J.F., Grafe, M.R., Woltjer, R.L., Kaye, J. & Iliff, J.J. (2017) 'Association of perivascular localization of aquaporin-4 with cognition and Alzheimer disease in aging brains', *JAMA neurology*, 74(1), pp. 91-99.
- Zhang, E., Wan, X., Yang, L., Wang, D., Chen, Z., Chen, Y., Liu, M., Zhang, G., Wu, J., Han, H. & Fan, Z. (2020) 'Omega-3 Polyunsaturated Fatty Acids Alleviate Traumatic Brain Injury by Regulating the Glymphatic Pathway in Mice', *Frontiers in Neurology*, 11(July), pp. 1-10.
- Zhang, J., Li, Y., Chen, Z., Dang, H., Ding, J., Fan, Y. & Hu, G. (2013) 'Glia protein aquaporin-4 regulates aversive motivation of spatial memory in Morris water maze', *CNS neuroscience & therapeutics*, 19(12), pp. 937-944.
- Zhang, Y., Zhang, C., He, X.-Z., Li, Z.-H., Meng, J.-C., Mao, R.-T., Li, X., Xue, R., Gui, Q. & Zhang, G.-X. (2023) 'Interaction Between the Glymphatic System and α -Synuclein in Parkinson's Disease', *Molecular Neurobiology*, pp. 1-14.
- Zhang, Y.W., Li, H.T., Hu, J., Lin, Y., Hou, J.M. & Wu, W.J. (2011) 'Correlation analysis between the expression of aquaporin 4 and magnetic resonance imaging of brain tissue in severely scalded rabbit with brain edema during early stage', *Zhonghua Shao Shang za zhi= Zhonghua Shaoshang Zazhi= Chinese Journal of Burns*, 27(6), pp. 441-445.
- Zhou, Y., Cai, J., Zhang, W., Gong, X., Yan, S., Zhang, K., Luo, Z., Sun, J., Jiang, Q. & Lou, M. (2020) 'Impairment of the glymphatic pathway and putative meningeal lymphatic vessels in the aging human', *Annals of neurology*, 87(3), pp. 357-369.
- Zhu, X.-H. & Chen, W. (2017) 'In vivo(17)O MRS imaging - Quantitative assessment of regional oxygen consumption and perfusion rates in living brain.', *Analytical biochemistry*, 529pp. 171-178.

- Zhu, X.H., Zhang, N., Zhang, Y., Zhang, X., Ugurbil, K. & Chen, W. (2005) 'In vivo 170 NMR approaches for brain study at high field', *NMR in Biomedicine*, 18(2), pp. 83-103.
- Zlokovic, B. V (2011) 'Neurovascular pathways to neurodegeneration in Alzheimer's disease and other disorders', *Nature Reviews Neuroscience*, 12(12), pp. 723-738.
- Zlokovic, B. V, Deane, R., Sagare, A.P., Bell, R.D. & Winkler, E.A. (2010) 'Low-density lipoprotein receptor-related protein-1: a serial clearance homeostatic mechanism controlling Alzheimer's amyloid β -peptide elimination from the brain', *Journal of neurochemistry*, 115(5), pp. 1077-1089.

